

1 LEVERAGING MULTI-MESSENGER ASTROPHYSICS FOR DARK MATTER SEARCHES

By

Daniel Nicholas Salazar-Gallegos

A DISSERTATION

Submitted to
Michigan State University
in partial fulfillment of the requirements
for the degree of

Physics—Doctor of Philosophy
Computational Mathematics in Science and Engineering—Dual Major

Today

ABSTRACT

3 I did Dark Matter with HAWC and IceCube. I also used Graph Neural Networks

⁴ Copyright by

⁵ DANIEL NICHOLAS SALAZAR-GALLEGOS

⁶ Today

ACKNOWLEDGMENTS

8 I love my friends. Thanks to everyone that helped me figure this out. Amazing thanks to the people
9 at LANL who supported me. Eames, etc Dinner Parties Jenny and her child Kaydince Kirsten, Pat,
10 Andrea Family. You're so far but so critical to my formation. Unconditional love. Roommate

TABLE OF CONTENTS

12	LIST OF TABLES	vii
13	LIST OF FIGURES	ix
14	LIST OF ABBREVIATIONS	xviii
15	CHAPTER 1 INTRODUCTION	1
16	CHAPTER 2 DARK MATTER IN THE COSMOS	2
17	2.1 Introduction	2
18	2.2 Dark Matter Basics	3
19	2.3 Evidence for Dark Matter	4
20	2.4 Searching for Dark Matter: Particle DM	11
21	2.5 Sources for Indirect Dark Matter Searches	16
22	2.6 Multi-Messenger Dark Matter	18
23	CHAPTER 3 HIGH ALTITUDE WATER CHERENKOV (HAWC) OBSERVATORY	21
24	3.1 The Detector	21
25	3.2 Events Reconstruction and Data Acquisition	21
26	3.3 Remote Monitoring	21
27	CHAPTER 4 ICECUBE NEUTRINO OBSERVATORY	22
28	4.1 The Detector	22
29	4.2 Events Reconstruction and Data Acquisition	22
30	4.3 Northern Test Site	22
31	CHAPTER 5 GLORY DUCK: MULTI-WAVELENGTH SEARCH FOR DARK MATTER ANNIHILATION TOWARDS DWARF SPHEROIDAL GALAXIES	23
32	5.1 Introduction	23
33	5.2 Dataset and Background	25
34	5.3 Analysis	27
35	5.4 Likelihood Methods	31
36	5.5 HAWC Results	38
37	5.6 Glory Duck Combined Results	40
38	5.7 HAWC Systematics	45
39	5.8 J -factor distributions	47
40	5.9 Discussion and Conclusions	53
43	CHAPTER 6 MULTITHREADING HAWC ANALYSES FOR DARK MATTER SEARCHES	57
44	6.1 Introduction	57
45	6.2 Dataset and Background	57
46	6.3 Analysis	59

48	6.4 Likelihood Methods	63
49	6.5 Computational Methods: Multithreading	63
50	6.6 Analysis Results	69
51	6.7 Systematics	74
52	6.8 Conclusion and Discussion	74
53	CHAPTER 7 HEAVY DARK MATTER ANNIHILATION SEARCH WITH ICE-CUBE'S NORTH SKY TRACK DATA	76
55	7.1 Introduction	76
56	7.2 Dataset and Background	77
57	7.3 Analysis	78
58	7.4 Likelihood Methods	87
59	7.5 Background Simulation	87
60	7.6 Signal Recovery	88
61	7.7 Systematics	89
62	7.8 Conclusions	89
63	CHAPTER 8 NU DUCK	112
64	APPENDIX A MULTI-EXPERIMENT SUPPLEMENTARY FIGURES	113
65	APPENDIX B MULTITHREADING DARK MATTER ANALYSES SUPPLEMENTARY MATERIAL	114
66	B.1 Remaining Spectral Models	114
67	B.2 <code>mpu_analysis.py</code>	115
68	B.3 Comparison with Glory Duck	124
70	APPENDIX C ICECUBE HEAVY DARK MATTER ANALYSIS SUPPLEMENTARY MATERIAL	127
72	C.1 Docker Image for Oscillating Neutrino Spectra	127
73	C.2 Spline Fitting Statuses	130
74	C.3 Neutrino Composite Spectra	131
75	C.4 Segue 1 And Ursa Major II Signal Recovery	132
76	BIBLIOGRAPHY	133

LIST OF TABLES

<p>78 Table 5.1 Summary of the relevant properties of the dSphs used in the present work. Column 1 lists the dSphs. Columns 2 and 3 present their heliocentric distance and galactic coordinates, respectively. Columns 4 and 5 report the J-factors of each source given from the \mathcal{GS} and \mathcal{B} independent studies and their estimated $\pm 1\sigma$ uncertainties. The values $\log_{10} J$ (\mathcal{GS} set) [45] correspond to the mean J-factor values for a source extension truncated at the outermost observed star. The values $\log_{10} J$ (\mathcal{B} set) [49] are provided for a source extension at the tidal radius of each dSph. Bolded sources are within HAWC's field of view and provided to the Glory Duck analysis.</p> <p>87 Table 5.2 Summary of dSph observations by each experiment used in this work. A ‘-’ indicates the experiment did not observe the dSph for this study. For Fermi-LAT, the exposure at 1 GeV is given. For HAWC, $\Delta\theta$ is the absolute difference between the source declination and HAWC latitude. HAWC is more sensitive to sources with smaller $\Delta\theta$. For IACTs, we show the zenith angle range, the total exposure, the energy range, the angular radius θ of the signal or ON region, the ratio of exposures between the background-control (OFF) and signal (ON) regions (τ), and the significance of gamma-ray excess in standard deviations, σ.</p> <p>96 Table 6.1 Summary of the relevant properties of the dSphs used in the present work. Column 1 lists the dSphs. Columns 2 and 3 present their heliocentric distance and galactic coordinates, respectively. Column 4 reports the J-factors of each source given from the \mathcal{LS} studies and estimated $\pm 1\sigma$ uncertainties. The values $\log_{10} J$ (\mathcal{LS} set) [66] correspond to the mean J-factor values for a source extension truncated at 0.5°.</p> <p>102 Table 6.2 Timing summaries for analyses for serial and multithreaded processes. M tasks is the number of functional-parallel tasks ran for the computation. $T_{p,c}$ is a single run time in hours:minutes:seconds for runs utilizing p nodes and c threads. Runs are run interactively on the same computer to maximize consistency. Empty entries are indicated with ‘-’. (.) entries are estimated entries extrapolated from data earlier in the column.</p> <p>108 Table 6.3 Speed up summaries for analyses for serial and multithreaded processes. M tasks is the number of functional-parallel tasks ran for the computation. $S_{p,c}$ is a single speedup comparison for runs utilizing p nodes and c threads. [.] are the estimated speedups calculated from Tab. 6.2, Eq. (6.7), and Eq. (6.4). Empty entries are indicated with ‘-’.</p>	<p>32</p> <p>33</p> <p>63</p> <p>67</p> <p>69</p>
---	---

113	Table 7.1 Spline err tolerances used for input in particle physics component to Eq. (7.1).	
114	Column 1 is the DM annihilation channel being fit. Columns 2, 3, and 4	
115	are the tolerances for "GOOD" (pass), "OK" requires inspection, and "FAIL"	
116	(tune and refit) respectively. Column 5 has the X ranges over which the error	
117	is evaluated. MAX/MIN $[\cdot, \cdot]$ takes the maximum or minimum of the two	
118	enclosed values.	84
119	Proof I know how to include	

LIST OF FIGURES

<p>121 Figure 2.1 Rotation curve fit to NGC 6503 from [7]. Dashed line is the contribution 122 from visible matter. Dotted curves are from gas. Dash-dot curves are from 123 dark matter (DM). Solid line is the composite contribution from all matter 124 and DM sources. Data are indicated with bold dots with error bars. Data 125 agree strongly with a matter + DM composite prediction.</p> <p>126 Figure 2.2 Light from distant galaxy is bent in unique ways depending on the distribution 127 of mass between the galaxy and Earth. Yellow dashed lines indicate where 128 the light would have gone if the matter were not present [8].</p> <p>129 Figure 2.3 (left) Optical image of galactic cluster 1E0657-558. (right) X-ray image of the 130 cluster with redder meaning hotter and higher baryon density. (both) Green 131 contours are reconstruction of gravity contours from weak lensing. White 132 rings are the best fit mass maxima at 68.3%, 95.5%, and 99.7% confidence. 133 The matter maxima of the clusters are clearly separated from x-ray maxima. [9]</p> <p>134 Figure 2.4 Plank CMB sky. Sky map features small variations in temperature in primor- 135 dial light. These anisotropies are used to make inferences about the universe's 136 energy budget and developmental history. [10]</p> <p>137 Figure 2.5 Observed Cosmic Microwave Background power spectrum as a function of 138 multipole moment from Plank [10]. Blue line is best fit model from ΛCDM. 139 Red points and lines are data and error, respectively.</p> <p>140 Figure 2.6 Predicted power spectra of CMB for different $\Omega_m h^2$ values for fixed baryon 141 density from [11]. (left) Low $\Omega_m h^2$ increases the prominence of first and 142 second peaks. (middle) $\Omega_m h^2$ is most similar to the observed power spectrum. 143 The second and third peaks are similar in height. (right) $\Omega_m h^2$ is large which 144 suppresses the first peak and raises the prominence of the third peak.</p> <p>145 Figure 2.7 The Standard Model (SM) of particle physics. Figure taken from http://www.quantumdiaries.org/2014/03/14/the-standard-model-a-beautiful-but-flawed-theory/</p> <p>148 Figure 2.8 Simplified Feynman diagram demonstrating with different ways DM can 149 interact with SM particles. The 'X's refer to the DM particles whereas the 150 SM refer to fundamental particles in the SM. The large circle in the center 151 indicates the vertex of interaction and is purposely left vague. The colored 152 arrows refer to different directions of time as well as their respective labels. 153 The arrows indicate the initial and final state of the DM -SM interaction in time.</p>	<p style="text-align: right;">5</p> <p style="text-align: right;">7</p> <p style="text-align: right;">8</p> <p style="text-align: right;">9</p> <p style="text-align: right;">10</p> <p style="text-align: right;">10</p> <p style="text-align: right;">12</p> <p style="text-align: right;">13</p>
---	---

154	Figure 2.9 A single jet event in ATLAS detector from 2017 [16]. Jet momentum was 155 observed to be 1.9 TeV. Missing transverse momentum was observed to be 156 1.9 TeV compared to the initial transverse momentum of the event was 0. 157 Implied MET is traced by a red dashed line in event display.	14
158	Figure 2.10 More detailed pseudo-Feynman diagram of particle cascade from dark matter 159 annihilation into 2 quarks. The quarks hadronize and down to stable particles 160 like γ or the anti-proton (p^-). Diagram pulled from ICRC 2021 presentation 161 on DM annihilation search [17].	15
162	Figure 2.11 Dark Matter (DM) decay spectrum for $b\bar{b}$ initial state and γ final state. Redder 163 spectra are for larger DM masses. Bluer spectra are light DM masses. x is a 164 unitless factor defined as the ratio of the mass of DM, m_χ , and the final state 165 particle energy E_γ . Figure from [19].	17
166	Figure 2.12 Different dark matter density profiles compared. Some models produce ex- 167 ceptionally large densities at small r [20].	18
168	Figure 2.13 The Milky Way Galaxy in photons (γ) and neutrinos (ν) [22]. The Galactic 169 center is at $l=0^\circ$ and is the brightest region in all panels. (top) An Optical 170 color image of the Milky Way galaxy seen from Earth. Clouds of gas and dust 171 obscure some light from stars. (2nd down) Integrated flux of γ -rays observed 172 by the Fermi-LAT telescope [23]. (middle) Expected neutrino emission 173 that corresponds with Fermi-LAT observations. (2nd up) Expected neutrino 174 emission profile after considering detector systematics of IceCube. (bottom) 175 Observed neutrino emission from region of the galactic plane. Substantial 176 neutrino emission was detected.	19
177	Figure 2.14 Dark Matter annihilation spectra for different final state particle and standard 178 model annihilation channels [24]. Photons (red), e^\pm (green), \bar{p} (blue), ν (black).	20
179	Figure 5.1 Sensitivities of five gamma-ray experiments compared to percentages of the 180 Crab nebula's emission and dark matter annihilation. Solid lines present 181 estimated sensitivities to power law spectra [FACT CHECK THIS] for each 182 experiment. Green lines are Fermi-LAT sensitivities where lighter green is 183 the sensitivity to the galactic center and dark green is its sensitivity to higher 184 declinations. Orange, red, and purple solid lines represent the MAGIC, HESS, 185 and VERITAS 50 hour sensitivities respectively. The maroon and brown lines 186 are the HAWC 1 year and 5 year sensitivities. Across four decades of gamma- 187 ray energy, these experiments have similar sensitivities on the order 10^{-12} 188 $\text{erg cm}^{-2}\text{s}^{-1}$. The dotted lines are estimated dark matter fluxes assuming 189 $m_\chi = 5 \text{ TeV}$ DM annihilating to bottom quarks (red), tau leptons (blue), 190 and W bosons (green). Faded gray lines outline percentage flux of the Crab 191 nebula. Figure is an augmented version of [25]	24

192	Figure 5.2	Effect of Electroweak (EW) corrections on expected DM annihilation spectrum for $\chi\chi \rightarrow W^-W^+$. Solid lines are spectral models that consider EW corrections. Dash-dot lines are spectral models without EW corrections. Red lines are models for $M_\chi = 1$ TeV. Blue lines represent models for $M_\chi = 100$ TeV. All models are sourced from the PPPC4DMID [44].	28
197	Figure 5.3	$\frac{dJ}{d\Omega}$ maps for Segue1 (top) and Coma Berenices (bottom). Origin is centered on the specific dwarf spheroidal galaxies (dSph). X and Y axes are the angular separation from the center of the dwarf. Profile is truncated at the scale radius. Plots of the remaining 11 dSph HAWC studied are linked in Fig. A.1.	30
201	Figure 5.4	Illustration of the combination technique showing a comparison between $-2 \ln \lambda$ provided by four instruments (colored lines) from the observation of the same dSph without any J nuisance and their sum, <i>i.e.</i> the resulting combined likelihood (thin black line). According to the test statistics of Equation (5.7), the intersection of the likelihood profiles with the line $-2 \ln \lambda = 2.71$ indicates the 95% C.L. upper limit on $\langle \sigma v \rangle$. The combined likelihood (thin black line) shows a smaller value of upper limit on $\langle \sigma v \rangle$ than those derived by individual instruments. We also show how the uncertainties on the J factor effects the combined likelihood and degrade the upper limit on $\langle \sigma v \rangle$ (thick black line). All likelihood profiles are normalized so that the global minimum $\widehat{\langle \sigma v \rangle}$ is 0. We note that each profile depends on the observational conditions in which a target object was observed. The sensitivity of a given instrument can be degraded and the upper limits less constraining if the observations are performed in non-optimal conditions such as a high zenith angle or a short exposure time.	36
216	Figure 5.5	39
217	Figure 5.6	HAWC TS values for best fit $\langle \sigma v \rangle$ versus m_χ for seven SM annihilation channels with J factors from \mathcal{GS} . The solid black line shows the combined best fit TS values. The colored, dashed lines are the TS values for each of the 13 sources HAWC studied.	40
221	Figure 5.7	HAWC Brazil bands at 95% confidence level on $\langle \sigma v \rangle$ versus DM mass for seven annihilation channels with J -factors from \mathcal{GS} [55]. The solid line represents the combined limit from 13 dSphs. The dashed line is the expected limit. The green band is the 68% containment. The yellow band is the 95% containment.	41

226	Figure 5.8	Upper limits at 95% confidence level on $\langle \sigma v \rangle$ in function of the DM mass for 227 eight annihilation channels, using the set of J factors from Ref. [55] (\mathcal{GS} set 228 in Table 5.1). The black solid line represents the observed combined limit, 229 the black dashed line is the median of the null hypothesis corresponding 230 to the expected limit, while the green and yellow bands show the 68% and 231 95% containment bands. Combined upper limits for each individual detector 232 are also indicated as solid, colored lines. The value of the thermal relic 233 cross-section in function of the DM mass is given as the red dotted-dashed 234 line [56].	42
235	Figure 5.9	Same as Fig. 5.8, using the set of J factors from Ref. [49, 57] (\mathcal{B} set in Table 5.1).	43
236	Figure 5.10	Comparisons of the combined limits at 95% confidence level for each of the 237 eight annihilation channels when using the J factors from Ref. [55] (\mathcal{GS} set in 238 Table 5.1), plain lines, and the J factor from Ref. [49, 57] (\mathcal{B} set in Table 5.1), 239 dashed lines. The cross-section given by the thermal relic is also indicated [56].	45
240	Figure 5.11	Comparisons of the combined limits at 95% confidence level for a point source 241 analysis and extended source using [55] \mathcal{GS} J-factor distributions and PPPC 242 [44] annihilation spectra. Shown are the limits for Segue1 which will have 243 the most significant impact on the combined limit. 6 of the 7 DM annihilation 244 channels are shown. Solid lines are extended source studies. Dashed lines 245 are point source studies. Overall, the extended source analysis improves the 246 limit by a factor of 2.	47
247	Figure 5.12	Same as Fig. 5.11 on Coma Berenices. This dSph also contributes signifi- 248 cantly to the limit. The limits are identical in this case.	48
249	Figure 5.13	Comparison of combined limits when correcting for HAWC's pointing sys- 250 tematic. All DM annihilation channels are shown. The solid black line is the 251 ratio between published limit to the declination corrected limit. The blue solid 252 line or "Combined_og" represented the limits computed for Glory Duck. The 253 solid orange line or "Combined_ad" represented the limits computed after 254 correcting for the pointing systematic.	49
255	Figure 5.14	Differential map of dJ/Ω from model built in Section 5.8.1 and profiles 256 provided directly from authors. (Top) Differential from Segue1. (bottom) 257 Differential from Coma Berenices. Note that their scales are not the same. 258 Segue1 shows the deepest discrepancies which is congruent with its large 259 uncertainties. Both models show anuli where unique models become apparent.	50

260	Figure 5.15 HAWC limits for Coma Berenices (top) and Segue1 (bottom) for two different 261 map sets. Blue lines are limits calculated on maps with poor model repre- 262 sentation. Orange lines are limits calculated on spatial profiles provided by 263 the authors of [45]. Black line is the ratio of the poor spatial model limits to 264 the corrected spatial models. The left y-axis measures $\langle \sigma v \rangle$ for the blue and 265 orange lines. The right y-axis measures the ratio and is unitless.	51
266	Figure 5.16 Comparisons between the J -factors versus the angular radius for the com- 267 putation of J factors from Ref. [55] (\mathcal{GS} set in Table 5.1) in blue and for 268 the computation from Ref. [49, 57] (\mathcal{B} set in Tab. 5.1) in orange. The solid 269 lines represent the central value of the J -factors while the shaded regions 270 correspond to the 1σ standard deviation.	53
271	Figure 5.17 Comparisons between the J -factors versus the angular radius for the computa- 272 tion of J factors from Ref. [55] (\mathcal{GS} set in Tab. 5.1) in blue and for the 273 computation from Ref. [49, 57] (\mathcal{B} set in Tab. 5.1) in orange. The solid 274 lines represent the central value of the J -factors while the shaded regions 275 correspond to the 1σ standard deviation.	54
276	Figure 6.1 Spectral hypotheses from PPPC [44] and HDM [65] for DM annihilation: 277 $\chi\chi \rightarrow W^-W^+$. Solid lines are spectral models with EW corrections from the 278 PPPC. Dash-dot lines are spectral models from HDM. Red lines are models 279 for $M_\chi = 1$ TeV. Blue lines represent models for $M_\chi = 100$ TeV.	59
280	Figure 6.2 Photon spectra for $\chi\chi \rightarrow \gamma\gamma$ (left) and $\chi\chi \rightarrow ZZ$ (right) after Gaussian 281 convolution of line features. Both spectra have δ -features at photon energies 282 equal to the DM mass. Bluer lines are annihilation spectra with lower DM 283 mass. Redder lines are spectra from larger DM mass. All spectral models are 284 sourced from the Heavy Dark Matter models [65]. Axes are drawn roughly 285 according to the energy sensitivity of HAWC.	60
286	Figure 6.3 $\frac{dJ}{d\Omega}$ maps for Coma Berenices, Draco, Segue1, and Sextans. Columns are 287 divided for the $\pm 1\sigma$ uncertainties in $dJ/d\Omega$ around the mean value from \mathcal{LS} 288 [66]. Origin is centered on the specific dwarf spheroidal galaxies (dSph). θ 289 and ϕ axes are the angular separation from the center of the dwarf. Profiles 290 are truncated at 1° and flattened beyond.	62
291	Figure 6.4 Infographic on how jobs and DM computation was organized in Section 5.3. 292 Jobs were built for each permutation of CHANS and SOURCES shown by the 293 left block in the figure. Each job, which took on the order 2 hrs to compute, 294 had the following work flow: 1. Import HAWC analysis software, 2 min to 295 run. 2. Load HAWC count maps, 5 min to run. 3. Load HAWC energy and 296 spatial resolutions, 4 min. 5. Load DM spatial source templates and spectral 297 models, less than 1 s. 6. Perform likelihood fit on data and model, about 8 298 min per DM mass. 7. Write results to file, less than 1s.	64

299	Figure 6.5	Graphic of Gustafson parallel coding pattern. f_s is the fraction of a program, 300 in time, spent on serial computation. f_p is the fraction of computing time 301 that is parallelizable. T_p is the total time for a parallel program to run. T_1 is 302 the total time for a parallel program to run if only 1 processor is allocated. 303 P_N is the N -th processor where it's row is the computation the processor 304 performs. The Gustafson pattern is most similar to what is implemented for 305 this analysis. Figure is pulled from [68].	65
306	Figure 6.6	Task chart for one multithreaded job developed for this project. Green blocks 307 indicate a shared resource across the threads AND computation performed 308 serially. Red blocks indicate functional parallel processing within each thread. 309 3 threads are represented here, yet many more can be employed during the 310 full analysis. Jobs are defined by the SOURCE as these require unique maps 311 to be loaded into the likelihood estimator. The m_χ , CHAN, and $\langle\sigma v\rangle$ variables 312 are entered into the thread pool and allocated as evenly as possible across the 313 threads.	67
314	Figure 6.7	HAWC upper limits at 95% confidence level on $\langle\sigma v\rangle$ versus m_χ for $\chi\chi \rightarrow b\bar{b}$, $t\bar{t}$, $u\bar{u}$, $d\bar{d}$, $s\bar{s}$, $c\bar{c}$, gg , W^+W^- , and hh . Limits are with \mathcal{LS} J-factors 315 [66]. The solid line represents the observed combined limit. Dashed lines 316 represent limits from individual dSphs.	70
318	Figure 6.8	HAWC upper limits at 95% confidence level on $\langle\sigma v\rangle$ versus m_χ for $\chi\chi \rightarrow \nu_e \bar{\nu}_e$, $\nu_\mu \bar{\nu}_\mu$, $\nu_\tau \bar{\nu}_\tau$, $e\bar{e}$, $\mu\bar{\mu}$, $\tau\bar{\tau}$, $\gamma\gamma$ and ZZ . Limits use \mathcal{LS} J-factors [66]. The 319 solid line represents the observed combined limit. Dashed lines represent 320 limits from individual dSphs.	71
322	Figure 6.9	HAWC TS values for best fit $\langle\sigma v\rangle$ versus m_χ for SM annihilation channels: 323 $\chi\chi \rightarrow b\bar{b}$, $t\bar{t}$, $u\bar{u}$, $d\bar{d}$, $s\bar{s}$, $c\bar{c}$, gg , W^+W^- , and hh . Limits use \mathcal{LS} J-factors. 324 The solid black line shows the combined best fit TS values. The colored, 325 dashed lines are the TS values from each dSph.	72
326	Figure 6.10	HAWC TS values for best fit $\langle\sigma v\rangle$ versus m_χ for SM annihilation channels: 327 $\chi\chi \rightarrow \nu_e \bar{\nu}_e$, $\nu_\mu \bar{\nu}_\mu$, $\nu_\tau \bar{\nu}_\tau$, $e\bar{e}$, $\mu\bar{\mu}$, $\tau\bar{\tau}$, $\gamma\gamma$ and ZZ . Limits use \mathcal{LS} J-factors. 328 The solid black line shows the combined best fit TS values. The colored, 329 dashed lines are the TS values from each dSph.	73
330	Figure 6.11	Comparison of HAWC limits from this analysis to Glory Duck (Fig. 5.5) 331 for 3 dSphs and 3 DM annihilation channels: $b\bar{b}$, $\tau\bar{\tau}$, and $e\bar{e}$. Each sector 332 shows the 95% confidence limit from Glory Duck (blue line) and this analysis 333 (orange line) in the top plot. The lower plot features the ratio in log scale of 334 Glory Duck to this analysis in a red solid line. Horizontal dashed lines are 335 for ratios of 1.0 (black) and $\sqrt{2}$ (blue). Ratios larger than 1.0 are for limits 336 smaller, or stricter, than Glory Duck. Ratios larger than $\sqrt{2}$ indicates limits 337 are stricter than a simple doubling of the Glory Duck data.	75

338	Figure 7.1	Neutrino spectra at production (left panels) and after oscillation at Earth 339 (right panels). Blue, orange, and green lines are the ν_e , ν_μ , and ν_τ spectra 340 respectively. Top panels show the spectra in $\frac{dN}{dE}$. Lower panels plot the flavor 341 ratio to $\nu_e + \nu_\mu + \nu_\tau$. SM annihilation channels $b\bar{b}$, $\tau\bar{\tau}$, and $\nu_\mu\bar{\nu}_\mu$ are shown 342 for $M_\chi = 1$ PeV, TeV, and EeV.	80
343	Figure 7.2	Signal recovery for 100 TeV DM annihilation into $\nu_\mu\bar{\nu}_\mu$ for a source at Dec 344 = 16.06°. n_{inj} is the number of injected signal events in simulation. n_s is 345 the number of reconstructed signal events from the simulation. Although 346 the uncertainties are small and tight, the reconstructed n_s are systematically 347 underestimated.	81
348	Figure 7.3	Left panel shows the two kernels overlaying the original spectrum from 349 χ arony after propagation to Earth [71]. The vertical red line indicates where 350 the original neutrino line is maximized. Blue line is the output from χ aroy. 351 Green line is the spectrum after convolution with a flat kernel. Orange line 352 is the spectrum after Gaussian convolution. Right panel shows the signal 353 recovery of the spectral model using the Gaussian kernel with parameters 354 enumerated above.	82
355	Figure 7.4	Example spline that failed the fit. Failed splined are corrected on a case by 356 case basis unless the SM channel has a systematic problem fitting the splines. 357 In this case, I made a bookkeeping error and loaded the incorrect spectral model	84
358	Figure 7.5	Summary of input spectral models that were smoothed with Gaussian kernel. 359 Spectral models are for $\chi\chi \rightarrow e\bar{e}$, $\mu\bar{\mu}\tau\bar{\tau}$, $\nu_e\bar{\nu}_e$, $\nu_\mu\bar{\nu}_\mu$, and $\nu_\tau\bar{\nu}_\tau$. These spectra 360 are the composite ($\nu_\mu + \nu_\tau$) of neutrino flavors. Every spectral model used for 361 this analysis is featured as a colored solid line. Bluer lines are for lower DM 362 mass spectral models. DM masses range from 681 GeV to 100 PeV. HDM 363 [65], χ aroy [71], and Photospline [75] are used to generate these spectra. 364 Energy (x-axis) was chosen to roughly represent the energy sensitivity of NST. .	85
365	Figure 7.6	Test statistic (TS) distributions for Segue 1 and $\chi\chi \rightarrow b\bar{b}$. Each subplot, 366 except the final, is the TS distribution for a specific DM mass listed in the 367 subplot. Orange dashed lines are the traces for a χ^2 distribution with 1 degree 368 of freedom. $\epsilon[\cdot]$ is the fraction of trials smaller than the bracketed value. The 369 final subplot plots the all DM spectral models, similar to Fig. 7.5, used as 370 input for the TS distributions.	91
371	Figure 7.7	Same as Fig. 7.6 for Segue 1 $\chi\chi \rightarrow \tau\bar{\tau}$	92
372	Figure 7.8	Same as Fig. 7.6 for Segue 1 $\chi\chi \rightarrow \nu_\mu\bar{\nu}_\mu$	93
373	Figure 7.9	Same as Fig. 7.6 for Ursa Major II 1 $\chi\chi \rightarrow b\bar{b}$	94
374	Figure 7.10	Same as Fig. 7.6 for Ursa Major II 1 $\chi\chi \rightarrow \tau\bar{\tau}$	95

375	Figure 7.11 Same as Fig. 7.6 for Ursa Major II 1 $\chi\chi \rightarrow \nu_\mu\bar{\nu}_\mu$	96
376	Figure 7.12 Same as Fig. 7.6 for 15, \mathcal{GS} J -factor, stacked sources and $\chi\chi \rightarrow b\bar{b}$	97
377	Figure 7.13 Same as Fig. 7.6 for 15, \mathcal{GS} J -factor, stacked sources and $\chi\chi \rightarrow t\bar{t}$	98
378	Figure 7.14 Same as Fig. 7.6 for 15, \mathcal{GS} J -factor, stacked sources and $\chi\chi \rightarrow u\bar{u}$	99
379	Figure 7.15 Same as Fig. 7.6 for 15, \mathcal{GS} J -factor, stacked sources and $\chi\chi \rightarrow d\bar{d}$	100
380	Figure 7.16 Same as Fig. 7.6 for 15, \mathcal{GS} J -factor, stacked sources and $\chi\chi \rightarrow e\bar{e}$	101
381	Figure 7.17 Same as Fig. 7.6 for 15, \mathcal{GS} J -factor, stacked sources and $\chi\chi \rightarrow \mu\bar{\mu}$	102
382	Figure 7.18 Same as Fig. 7.6 for 15, \mathcal{GS} J -factor, stacked sources and $\chi\chi \rightarrow \tau\bar{\tau}$	103
383	Figure 7.19 Same as Fig. 7.6 for 15, \mathcal{GS} J -factor, stacked sources and $\chi\chi \rightarrow W^+W^-$	104
384	Figure 7.20 Same as Fig. 7.6 for 15, \mathcal{GS} J -factor, stacked sources and $\chi\chi \rightarrow ZZ$	105
385	Figure 7.21 Same as Fig. 7.6 for 15, \mathcal{GS} J -factor, stacked sources and $\chi\chi \rightarrow \nu_e\bar{\nu}_e$	106
386	Figure 7.22 Same as Fig. 7.6 for 15, \mathcal{GS} J -factor, stacked sources and $\chi\chi \rightarrow \nu_\mu\bar{\nu}_\mu$	107
387	Figure 7.23 Signal Recovery study for an analysis with 15 stacked sources using the \mathcal{GS} J -factors [45]. Each panel block represents 14 studies for DM mass ranging between 1 TeV and 20 PeV and one annihilation channel. Panel block is for $t\bar{t}$. Each panel block features every spectral model used as input in the bottom-right subpanel. The remaining panels show n_{inj} as the number of signal events injected into background simulation. Whereas, n_s is the number of signal events recovered from analyzing the injected simulation. Blue line represents the median values of 100 simulations. Light blue bands show the 1σ statistical uncertainty around the median.	108
396	Figure 7.24 Same as Fig. 7.23 but for $\chi\chi \rightarrow b\bar{b}$ (top) and $\nu_\mu\bar{\nu}_\mu$ (bottom).	109
397	Figure 7.25 Words. I predict Icecube Sensitivities weeee	110
398	Figure 7.26 Words. I predict Icecube Sensitivities weeee	111
399	Figure A.1 Sister figure to Figure 5.3. Sources in the first row from left to right: Bootes I, Canes Venatici I, II. In second row: Draco, Hercules, Leo I. In the first row: Leo II, Leo IV, Sextans. In the final row: Ursa Major I, Ursa Major II.	113

402	Figure B.1 Sister figure to Figure 6.2 for remaining SM primary annihilation channels 403 studied for this thesis. These did not require any post generation smoothing 404 and so are directly pulled from [65] with a binning scheme most helpful for a 405 HAWC analysis.	114
406	Figure B.2 TODO: fill this out	124
407	Figure B.3 TODO: fill this out	125
408	Figure B.4 TODO: fill this out	126
409	Figure C.1 Current status of spline tables according to constraints defined by Tab. 7.1. 410 Green splines are splines that passed under the GOOD tolerance. Yellow 411 are splines that are OK. Red are splines that FAIL. All yellow splines were 412 inspected individually before running the analysis. Splines were made for the 413 μ (PID 14; top panel) flavor and τ (PID 16; bottom panel) neutrino flavors.	130
414	Figure C.2 Sister figure to Fig. 7.5 for annihilation channels that did not require kernel 415 smoothing. These spectra are the composite ($\nu_\mu + \nu_\tau$) of neutrino flavors. 416 Every spectral model used for this analysis is featured as a colored solid line. 417 Bluer lines are for lower DM mass spectral models. DM masses range from 418 681 GeV to 100 PeV.	131
419	Figure C.3 TODO: Fill this out eventually. I think I want all the plots generated 420 first[NEEDS A SOURCE][FACT CHECK THIS]	132

LIST OF ABBREVIATIONS

- 422 **MSU** Michigan State University
423 **LANL** Los Alamos National Laboratory
424 **DM** Dark Matter
425 **SM** Standard Model
426 **HAWC** High Altitude Water Cherenkov Observatory
427 **dSph** Dwarf Spheroidal Galaxy

CHAPTER 1

INTRODUCTION

429 Is the text not rendering right? Ah ok it knows im basically drafting the doc still

CHAPTER 2

430

DARK MATTER IN THE COSMOS

431 **2.1 Introduction**

432 The dark matter problem can be summarized in part by the following thought experiment.

433 Let us say you are the teacher for an elementary school classroom. You take them on a field
434 trip to your local science museum and among the exhibits is one for mass and weight. The exhibit
435 has a gigantic scale, and you come up with a fun problem for your class.

436 You ask your class, "What is the total weight of the classroom? Give your best estimation to
437 me in 30 minutes, and then we'll check your guess on the scale. If your guess is within 10% of the
438 right answer, we will stop for ice cream on the way back."

439 The students are ecstatic to hear this, and they get to work. The solution is some variation of
440 the following strategy. The students should give each other their weight or best guess if they do
441 not know. Then, all they must do is add each student's weight and get a grand total for the class.

442 The measurement on the giant scale should show the true weight of the class. When comparing
443 the measured weight to your estimation, multiply the measurement by 1.0 ± 0.1 to get the $\pm 10\%$
444 tolerances for your estimation.

445 Two of your students, Sandra and Mario, return to you with a solution.

446 They say, "We weren't sure of everyone's weight. We used 65 lbs. for the people we didn't
447 know and added everyone who does know. There are 30 of us, and we got 2,000 lbs.! That's a ton!"

448 You estimated 1,900 lbs. assuming the average weight of a student in your class was 60 lbs.
449 So, you are pleased with Sandra's and Mario's answer. You instruct your students to all gather on
450 the giant scale and read off the weight together. To all your surprise, the scale reads *10,000 lbs.*!
451 10,000 is significantly more than a 10% error from 2,000. In fact, it is approximately 5 times more
452 massive than either your or your students' estimates. You think to yourself and conclude there
453 must be something wrong with the scale. You ask an employee to check the scale and verify it is
454 well calibrated. They confirm that the scale is in working order. You weigh a couple of students
455 individually to assess that the scale is well calibrated. Sandra weighs 59 lbs., and Mario weighs

456 62 lbs., typical weights for their age. You then weigh each student individually and see that their
457 weights individually do not deviate greatly from 60 lbs. So, where does all the extra weight come
458 from?

459 This thought experiment serves as an analogy to the Dark Matter problem. The important
460 substitution to make however is to replace the students with stars and the classroom with a galaxy,
461 say the Milky Way. Individually the mass of stars is well measured and defined with the Sun as our
462 nearest test case. However, when we set out to measure the mass of a collection of stars as large as
463 galaxies, our well-motivated estimation is wildly incorrect. There simply is no way to account for
464 this discrepancy except without some unseen, or dark, contribution to mass and matter in galaxies.
465 I set out in my thesis to narrow the possibilities of what this Dark Matter could be.

466 This chapter is organized like the following... **TODO: Text should look like ... Chapter x has**
467 **blah blah blah.**

468 2.2 Dark Matter Basics

469 Presently, a more compelling theory of cosmology that includes Dark Matter (DM) in order
470 to explain a variety of observations is Λ Cold Dark Matter, or Λ CDM. I present the evidence
471 supporting Λ CDM in Section 2.3 yet discuss the conclusions of the Λ CDM model here. According
472 to Λ CDM fit to observations on the Cosmic Microwave Background (CMB), DM is 26.8% of the
473 universe's current energy budget. Baryonic matter, stuff like atoms, gas, and stars, contributes to
474 4.9% of the universe's current energy budget [1, 2, 3].

475 DM is dark; it does not interact readily with light at any wavelength. DM also does not interact
476 noticeably with the other standard model forces (Strong and Weak) at a rate that is readily observed
477 [3]. DM is cold, which is to say that the average velocity of DM is below relativistic speeds [1].
478 'Hot' DM would not likely manifest the dense structures we observe like galaxies, and instead
479 would produce much more diffuse galaxies than what is observed [3, 1]. DM is old; it played a
480 critical role in the formation of the universe and the structures within it [1, 2].

481 Observations of DM have so far been only gravitational. The parameter space available to what
482 DM could be therefore is extremely broad. The broad DM parameter space is iteratively tested in

483 DM searches by supposing a hypothesis that has not yet been ruled out and performing observations
484 to test them. When the observations yield a null result, the parameter space is constrained further.
485 I present some approaches for DM searches in Section 2.4.

486 **2.3 Evidence for Dark Matter**

487 Dark Matter (DM) has been a looming problem in physics for almost 100 years. Anomalies
488 have been observed by astrophysicists in galactic dynamics as early as 1933 when Fritz Zwicky
489 noticed unusually large velocity dispersion in the Coma cluster. Zwicky's measurement was the
490 first recorded to use the Virial theorem to measure the mass fraction of visible and invisible matter
491 in celestial bodies [4]. From Zwicky in [5], "*If this would be confirmed, we would get the surprising*
492 *result that dark matter is present in much greater amount than luminous matter.*" Zwicky's and
493 others' observation did not instigate a crisis in astrophysics because the measurements did not
494 entirely conflict with their understanding of galaxies [4]. In 1978, Rubin, Ford, and Norbert
495 measured rotation curves for ten spiral galaxies [6]. Rubin et al.'s 1978 publication presented a
496 major challenge to the conventional understanding of galaxies that could no longer be dismissed by
497 measurement uncertainties. Evidence has been mounting ever since for this exotic form of matter.
498 The following subsections provide three compelling pieces of evidence in support of the existence
499 of DM.

500 **2.3.1 First Clues: Stellar Velocities**

501 Zwicky, and later Rubin, measured the stellar velocities of various galaxies to estimate their
502 virial mass. The Virial Theorem upon which these observations are interpreted is written as

$$2T + V = 0. \quad (2.1)$$

503 Where T is the kinetic energy and V is the potential energy in a self-gravitating system. The
504 classical Newton's law of gravity from stars and gas was used for gravitational potential modeled in
505 the observed galaxies:

$$V = -\frac{1}{2} \sum_i \sum_{j \neq i} \frac{m_i m_j}{r_{ij}}. \quad (2.2)$$

506 Zwicky et al. measured just the velocities of stars apparent in optical wavelengths [5]. Rubin et al.
 507 added by measuring the velocity of the hydrogen gas via the 21 cm emission line of Hydrogen [6].
 508 The velocities of the stars and gas are used to infer the total mass of galaxies and galaxy clusters
 509 via Equation (2.1). An inferred mass is obtained from the luminosity of the selected sources. The
 510 two inferences are compared to each other as a luminosity to mass ratio which typically yielded [1]

$$\frac{M}{L} \sim 400 \frac{M_{\odot}}{L_{\odot}} \quad (2.3)$$

511 M_{\odot} and L_{\odot} referring to stellar mass and stellar luminosity, respectively. These ratios clearly indicate
 512 a discrepancy in apparent light and mass from stars and gas and their velocities.

513 Rubin et al. [6] demonstrated that the discrepancy was unlikely to be an underestimation of
 514 the mass of the stars and gas. The inferred "dark" mass was up to 5 times more than the luminous
 515 mass. This dark mass also needed to extend well beyond the extent of the luminous matter.

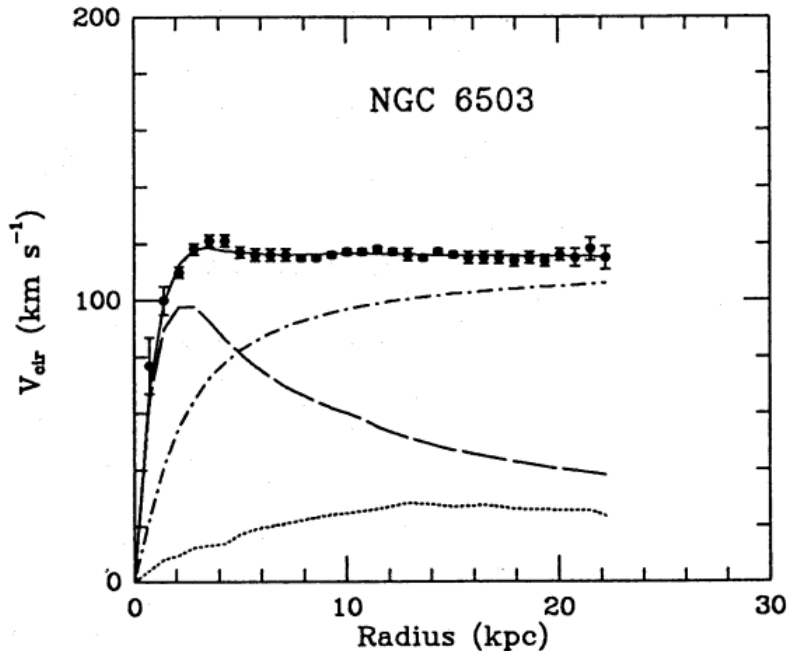


Figure 2.1 Rotation curve fit to NGC 6503 from [7]. Dashed line is the contribution from visible matter. Dotted curves are from gas. Dash-dot curves are from dark matter (DM). Solid line is the composite contribution from all matter and DM sources. Data are indicated with bold dots with error bars. Data agree strongly with a matter + DM composite prediction.

516 Figure 2.1 features one of many rotation curves plotted from the stellar velocities within galaxies.

517 The measured rotation curves mostly feature a flattening of velocities at higher radius which is not
518 expected if the gravity was only coming from gas and luminous matter. The extension of the
519 flat velocity region also indicates that the DM is distributed far from the center of the galaxy.
520 Modern velocity measurements include significantly larger objects, galactic clusters, and smaller
521 objects, dwarf galaxies. Yet, measurements along this regime are leveraging the Virial theorem
522 with Newtonian potential energies. We know Newtonian gravity is not a comprehensive description
523 of gravity. New observational techniques have been developed since 1978, and those are discussed
524 in the following sections.

525 **2.3.2 Evidence for Dark Matter: Gravitational Lensing**

526 Modern evidence for dark matter comes from new avenues beyond stellar velocities. Grav-
527 itational lensing from DM is a new channel from general relativity. General relativity predicts
528 aberrations in light caused by massive objects. In recent decades we have been able to measure the
529 lensing effects from compact objects and DM halos. Figure 2.2 shows how different massive ob-
530 jects change the final image of a faraway galaxy resulting from gravitational lensing. Gravitational
531 lensing developed our understanding of dark matter in two important ways.

532 Gravitational lensing provides additional compelling evidence for DM. The observation of two
533 merging galactic clusters in 2006, shown in Figure 2.3, provided a compelling argument for DM
534 outside the Standard Model. These clusters merged recently in astrophysical time scales. Galaxies
535 and star cluster have mostly passed by each other as the likelihood of their collision is low. Therefore,
536 these massive objects will mostly track the highest mass, dark and/or baryonic, density. Yet, the
537 intergalactic gas is responsible for the majority of the baryonic mass in the systems [4]. These gas
538 bodies will not phase through and will heat up as they collide together. The hot gas is located via
539 x-ray emission from the cluster. Two observations of the clusters were performed independently of
540 each other.

541 The first was the lensing of light around the galaxies due to their gravitational influences.
542 When celestial bodies are large enough, the gravity they exert bends space and time itself. The
543 warped space-time lenses light and will deflect in an analogous way to how glass lenses will bend

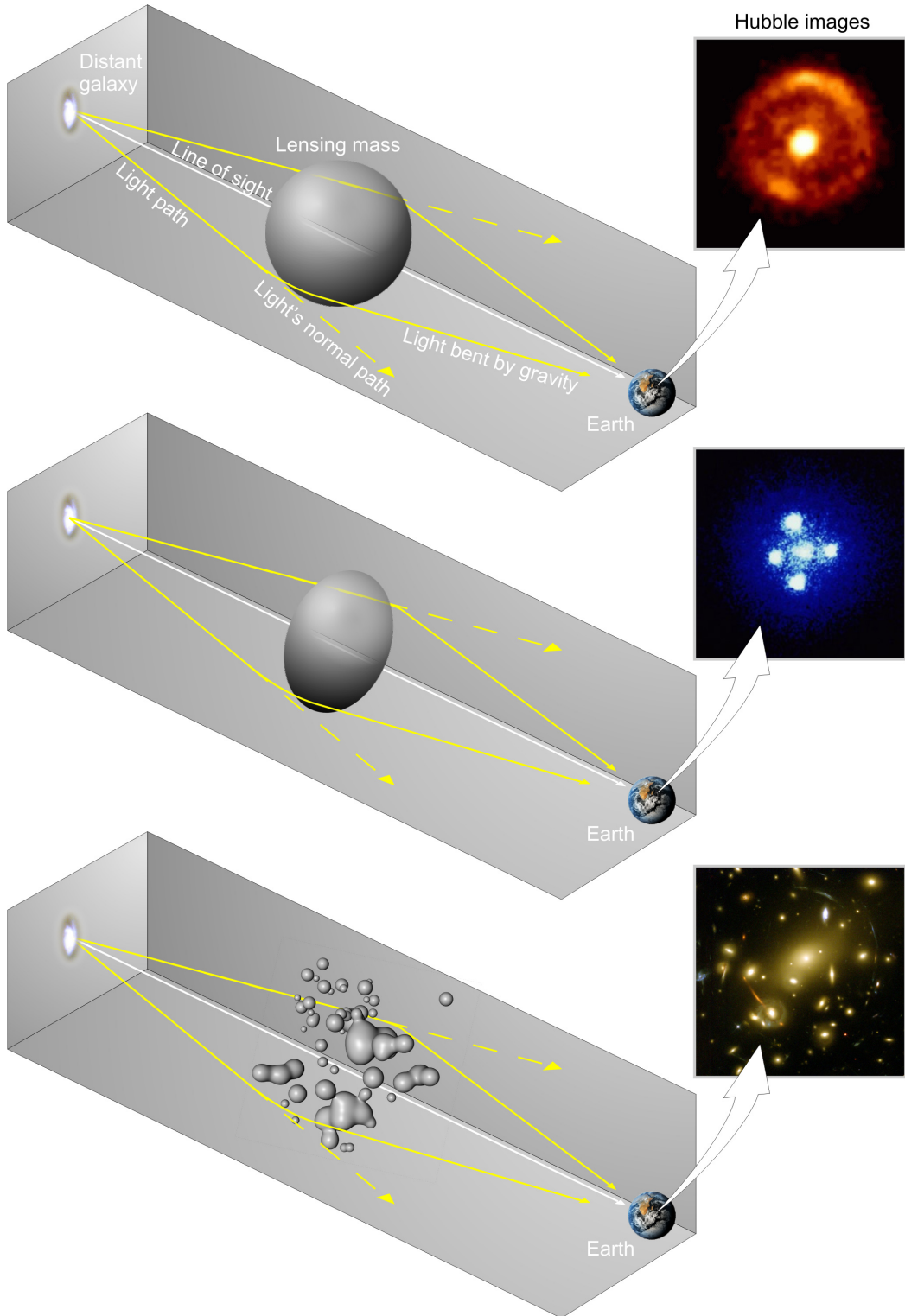


Figure 2.2 Light from distant galaxy is bent in unique ways depending on the distribution of mass between the galaxy and Earth. Yellow dashed lines indicate where the light would have gone if the matter were not present [8].

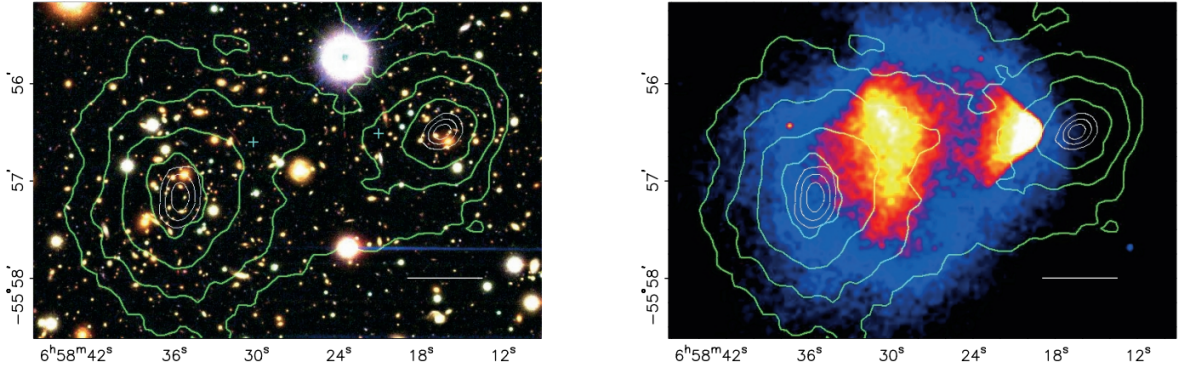


Figure 2.3 (left) Optical image of galactic cluster 1E0657-558. (right) X-ray image of the cluster with redder meaning hotter and higher baryon density. (both) Green contours are reconstruction of gravity contours from weak lensing. White rings are the best fit mass maxima at 68.3%, 95.5%, and 99.7% confidence. The matter maxima of the clusters are clearly separated from x-ray maxima. [9]

544 light, see Figure 2.2. With a sufficient understanding of light sources behind a massive object, we
 545 can reconstruct the contours of the gravitational lenses. The gradient of the contours shown in
 546 Figure 2.3 then indicates how dense the matter is and where it is.

547 The x-ray emission can then be observed from the clusters. Since these galaxies are mostly gas
 548 and are merging, then the gas should be getting hotter. If they are merging, the x-ray emissions
 549 should be the strongest where the gas is mostly moving through each other. Hence, X-ray emission
 550 maps out where the gas is in the merging galaxy cluster.

551 The lensing and x-ray observations were done on the Bullet cluster featured on Figure 2.3.
 552 The x-ray emissions do not align with the gravitational contours from lensing. The incongruence
 553 in mass density and baryon density suggests that there is a lot of matter somewhere that does
 554 not interact with light. Moreover, this dark matter cannot be baryonic [9]. The Bullet Cluster
 555 measurement did not really tell us what DM is exactly, but it did give the clue that DM also does
 556 not interact with itself very strongly. If DM did interact strongly with itself, then it would have been
 557 more aligned with the x-ray emission [9]. There have been follow-up studies of galaxy clusters with
 558 similar results. The Bullet Cluster and others like it provide a persuasive case against something
 559 possibly amiss in our gravitational theories.

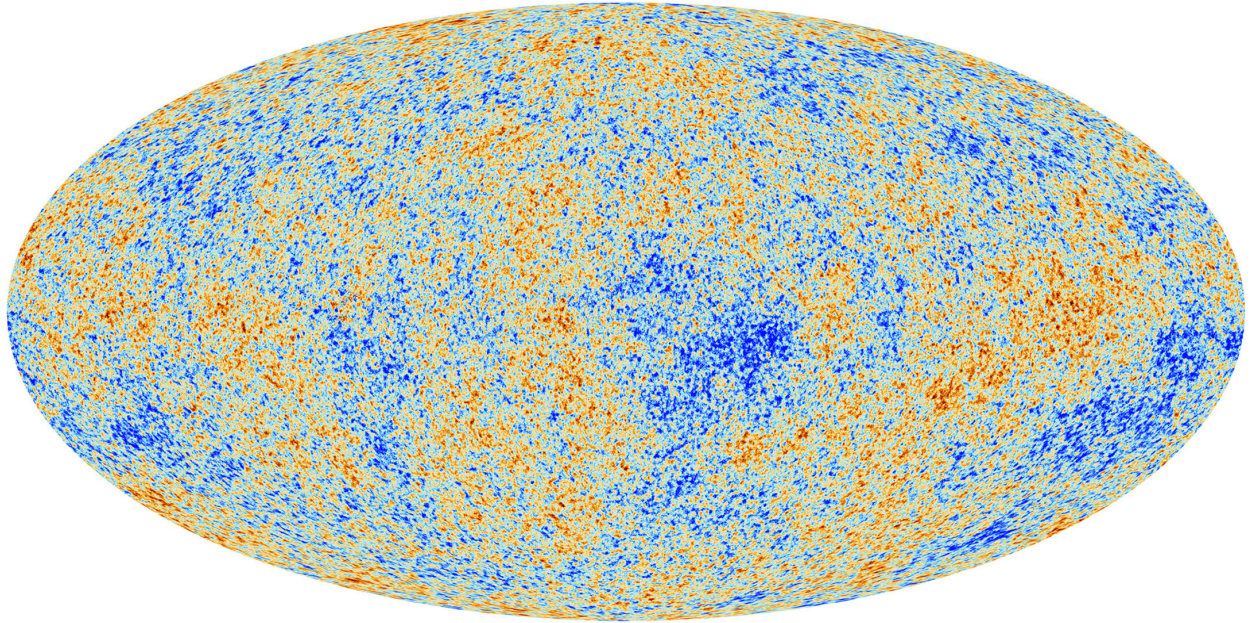


Figure 2.4 Plank CMB sky. Sky map features small variations in temperature in primordial light. These anisotropies are used to make inferences about the universe's energy budget and developmental history. [10]

560 **2.3.3 Evidence for Dark Matter: Cosmic Microwave Background**

561 The Cosmic Microwave Background (CMB) is the primordial light from the early universe
562 when Hydrogen atoms formed from the free electron and proton soup in the early universe. The
563 CMB is the earliest light we can observe; released when the universe was about 380,000 years old.
564 Then we look at how the simulated universes look like compared to what we see. Figure 2.4 is the
565 most recent CMB image from the Plank satellite after subtracting the average value and masking the
566 galactic plane [10]. Redder regions indicate a slightly hotter region in the CMB, and blue indicates
567 colder. The intensity variations are on the order of 1 in 1000 with respect to the average value.

568 The Cosmic Microwave Background shows that the universe had DM in it from an incredibly
569 early stage. To measure the DM, Dark Energy, and matter fractions of the universe from the CMB,
570 the image is analyzed into a power spectrum, which shows the amplitude of the fluctuations as
571 a function of spherical multipole moments. Λ CDM provides the best fit to the power spectra of
572 the CMB as shown in Figure 2.5. The CMB power spectrum is quite sensitive to the fraction
573 of each energy contribution in the early universe. Low l modes are dominated by variations
574 in gravitational potential. Intermediate l emerge from oscillations in photon-baryon fluid from

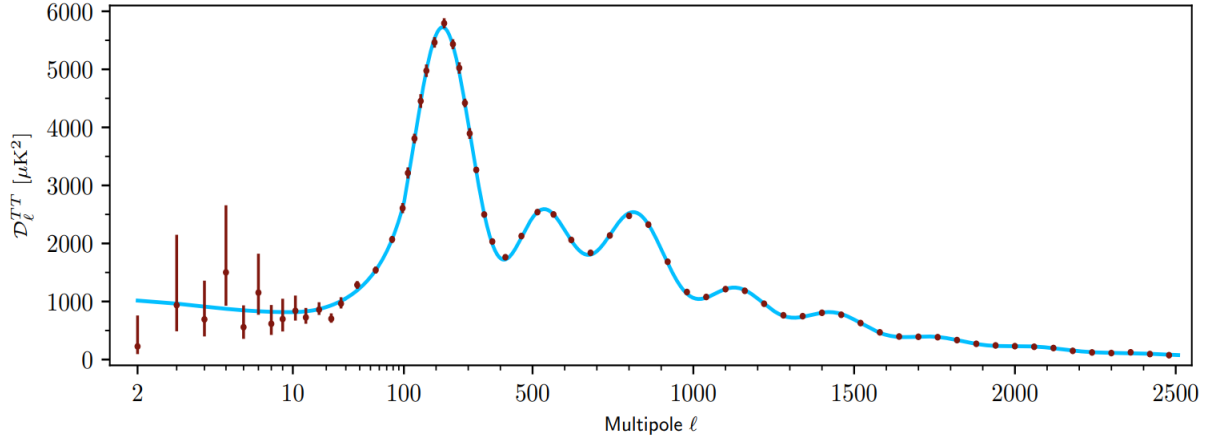


Figure 2.5 Observed Cosmic Microwave Background power spectrum as a function of multipole moment from Plank [10]. Blue line is best fit model from Λ CDM. Red points and lines are data and error, respectively.

575 competing baryon pressures and gravity. High l is a damped region from the diffusion of photons
 576 during electron-proton recombination. [1]

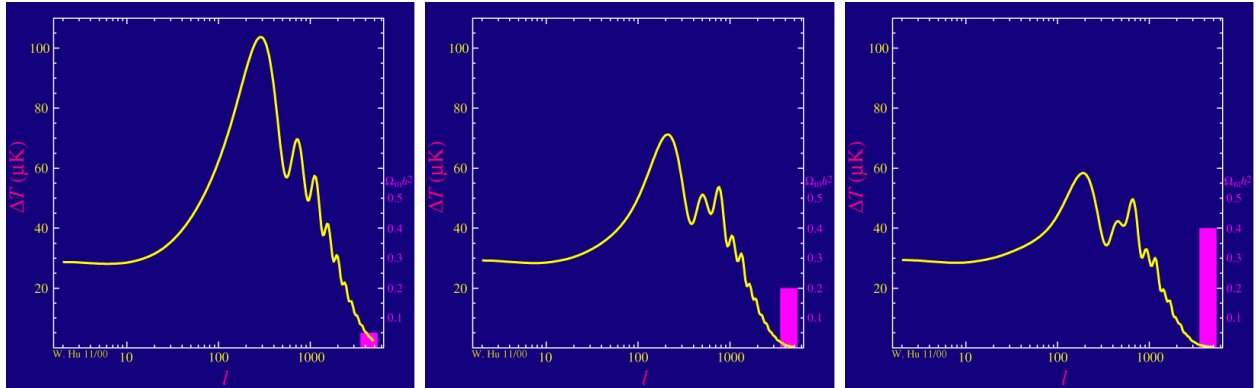


Figure 2.6 Predicted power spectra of CMB for different $\Omega_m h^2$ values for fixed baryon density from [11]. (left) Low $\Omega_m h^2$ increases the prominence of first and second peaks. (middle) $\Omega_m h^2$ is most similar to the observed power spectrum. The second and third peaks are similar in height. (right) $\Omega_m h^2$ is large which suppresses the first peak and raises the prominence of the third peak.

577 The harmonics would look quite different for a universe with less DM. Figure 2.6 demonstrates
 578 the effect $\Omega_m h^2$ has on the expected power spectrum for fixed baryon matter density. [11] Sweeping
 579 $\Omega_m h^2$ in this way clearly shows the effect dark matter has on the CMB power spectrum. The
 580 observations fit well with the Λ CDM model, and the derived fractions are as follows. The matter
 581 fraction: $\Omega_m = 0.3153$; and the baryon fraction: $\Omega_b = 0.04936$ [10]. Plank's observations also
 582 provide a measure of the Hubble constant, H_0 . H_0 especially has seen a growing tension in the

583 past decade that continues to deepened with observations from instruments like the James Webb
584 Telescope [12, 13]. As Hubble tensions deepen, we may find that perhaps Λ **CDM**, despite its
585 successes, is missing some critical physics.

586 Overall, the Newtonian motion of stars in galaxies, weak lensing from galactic clusters, and
587 power spectra from primordial light form a compelling body of research in favor of dark matter.
588 It takes another leap of theory and experimentation to make observations of DM that are non-
589 gravitational in nature. In Section 2.3, the evidence for DM implies strongly that the DM is matter
590 and not a lost parameter in the gravitational fields between massive objects. Finally, if we take one
591 axiom: that this matter has quantum behavior, such as being described by some Bohr wavelength
592 and abiding by some fermion or boson statistics; then we arrive at particle dark matter. One particle
593 DM hypothesis is the Weakly Interacting Massive Particle (WIMP). This DM candidate theory is
594 discussed further in the next section and is the focus of this thesis.

595 **2.4 Searching for Dark Matter: Particle DM**

596 Section 2.4 shows the Standard Model of particle physics and is currently the most accurate
597 model for the dynamics of fundamental particles like electrons and photons. The current status
598 of the SM does not have a viable DM candidate. When looking at the standard model, we can
599 immediately exclude any charged particle because charged particles interact strongly with light.
600 Specifically, this will rule out the following charged, fundamental particles: $e, \mu, \tau, W, u, d, s, c, t, b$
601 and their corresponding antiparticles. Recalling from Section 2.2 that DM must be long-lived and
602 stable over the age of the universe which excludes all SM particles with decay half-lives at or shorter
603 than the age of the universe. The lifetime constraint additionally eliminates the Z and H bosons.
604 Finally, the candidate DM needs to be somewhat massive. Recall from Section 2.2 that DM is cold
605 or not relativistic through the universe. This eliminates the remaining SM particles: $\nu_{e,\mu,\tau}, g, \gamma$ as
606 DM candidates. Because there are no DM candidates within the SM, the DM problem strongly
607 hints to physics beyond the SM (BSM).

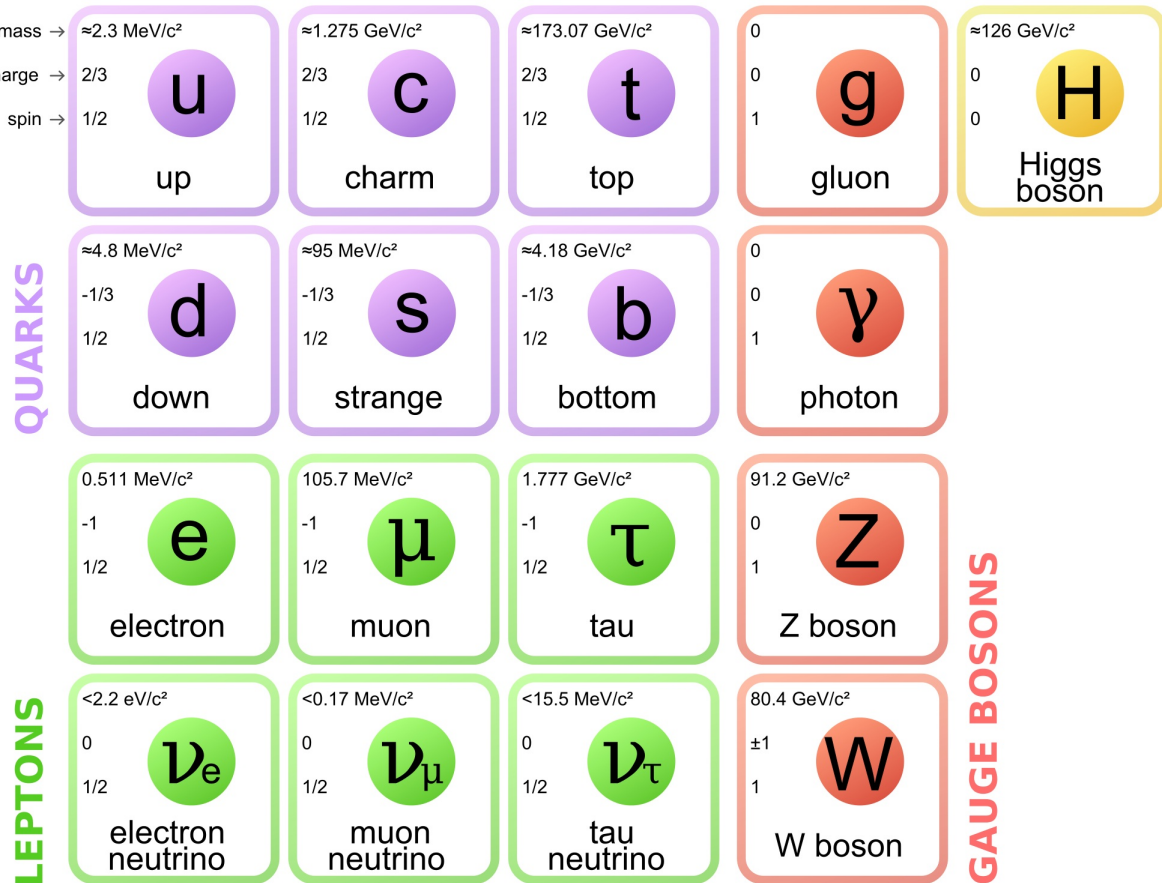


Figure 2.7 The Standard Model (SM) of particle physics. Figure taken from <http://www.quantumdiaries.org/2014/03/14/the-standard-model-a-beautiful-but-flawed-theory/>

608 2.4.1 Shake it, Break it, Make it

609 When considering DM that couples in some way with the SM, the interactions are roughly
 610 demonstrated by interaction demonstrated in Figure 2.8. The figure is a simplified Feynman
 611 diagram where the arrow of time represents the interaction modes of: **Shake it, Break it, Make it.**

612 **Shake it** refers to the direct detection of dark matter. Direct detection interactions start with
 613 a free DM particle and an SM particle. The DM and SM interact via elastic or inelastic collision
 614 and recoil away from each other. The DM remains in the dark sector and imparts some momentum
 615 onto the SM particle. The hope is that the momentum imparted onto the SM particle is sufficiently
 616 high enough to pick up with extremely sensitive instruments. Because we cannot create the DM in
 617 the lab, a direct detection experiment must wait until DM is incident on the detector. Most direct
 618 detection experiments are therefore placed in low-background environments with inert detection

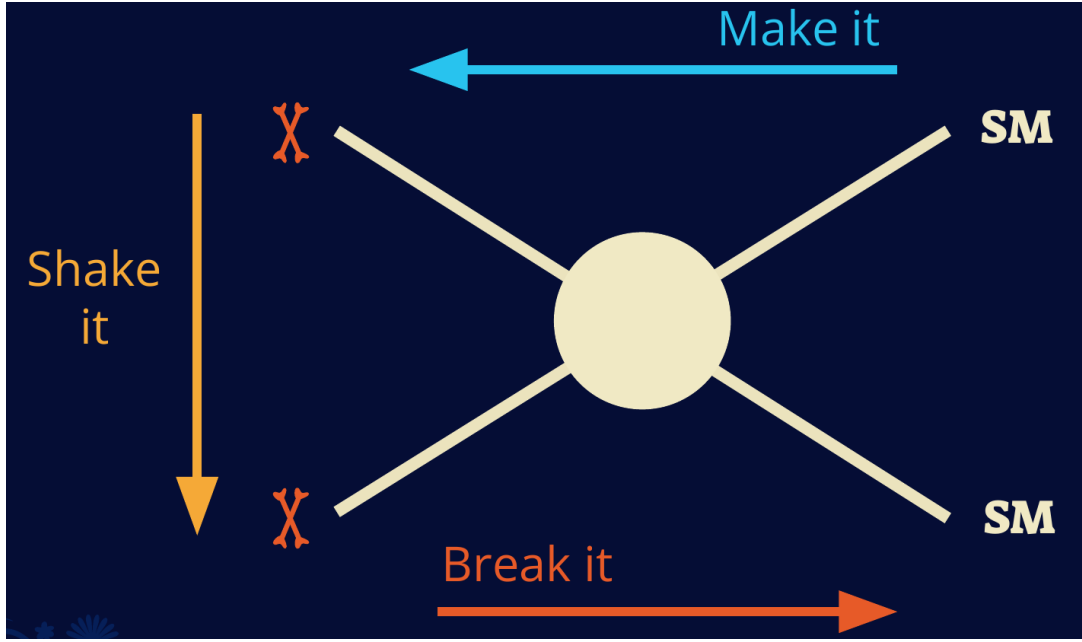


Figure 2.8 Simplified Feynman diagram demonstrating different ways DM can interact with SM particles. The 'X's refer to the DM particles whereas the SM refer to fundamental particles in the SM. The large circle in the center indicates the vertex of interaction and is purposely left vague. The colored arrows refer to different directions of time as well as their respective labels. The arrows indicate the initial and final state of the DM -SM interaction in time.

619 media like the noble gas Xenon. [14]

620 **Make it** refers to the production of DM from SM initial states. The experiment starts with
 621 particles in the SM. These SM particles are accelerated to incredibly high energies and then collide
 622 with each other. In the confluence of energy, DM hopefully emerges as a byproduct of the SM
 623 annihilation. Often it is the collider experiments that are energetic enough to hypothetically produce
 624 DM. These experiments include the world-wide collaborations ATLAS and CMS at CERN where
 625 proton collide together at extreme energies. The DM searches, however, are complex. DM likely
 626 does not interact with the detectors and lives long enough to escape the detection apparatus of
 627 CERN's colliders. This means any DM production experiment searches for an excess of events
 628 with missing momentum or energy in the events. An example event with missing transverse
 629 momentum is shown in Figure 2.9. The missing momentum with no particle tracks implies a
 630 neutral particle carried the energy out of the detector. However, there are other neutral particles
 631 in the SM, like neutrons or neutrinos, so any analysis has to account for SM signatures of missing

632 momentum. [15]

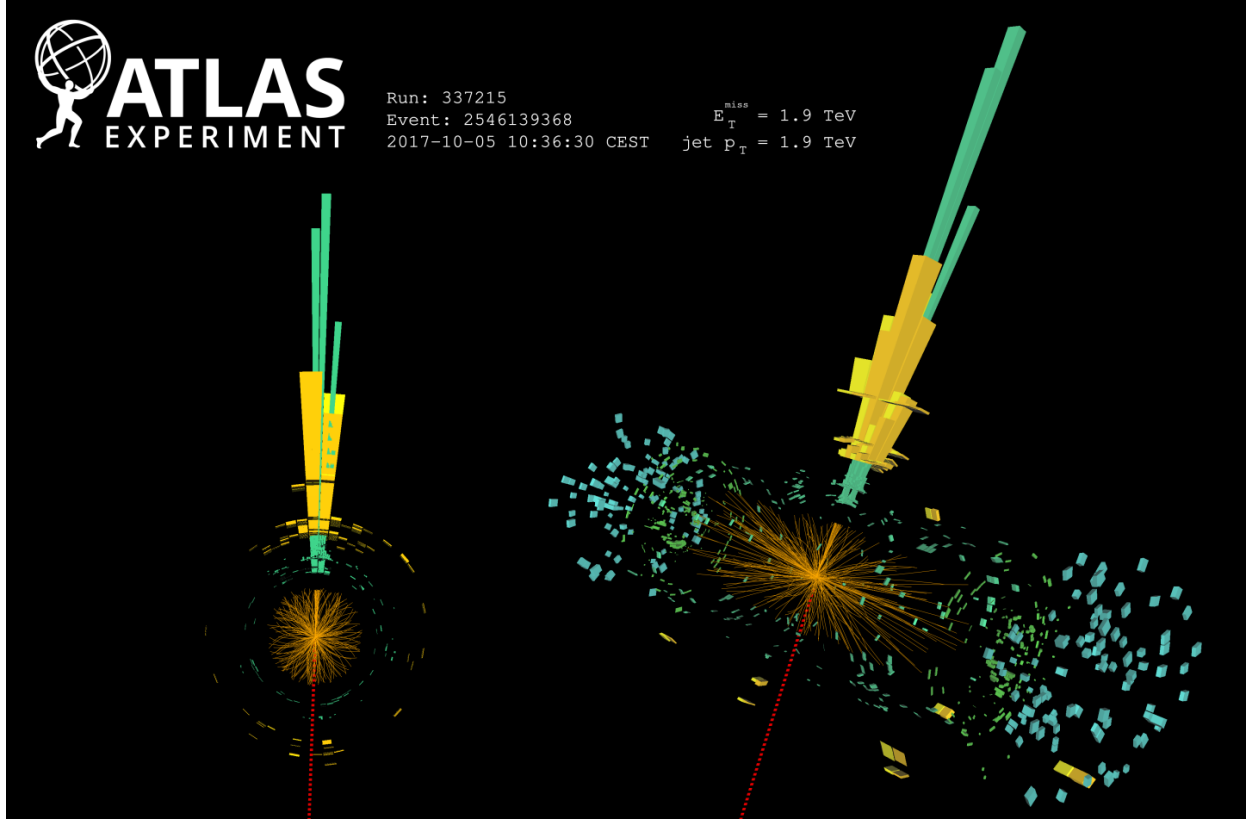


Figure 2.9 A single jet event in ATLAS detector from 2017 [16]. Jet momentum was observed to be 1.9 TeV. Missing transverse momentum was observed to be 1.9 TeV compared to the initial transverse momentum of the event was 0. Implied MET is traced by a red dashed line in event display.

633 2.4.2 Break it: Standard Model Signatures of Dark Matter through Indirect Searches

634 **Break it** refers to the creation of SM particles from the dark sector, and it is the primary focus
635 of this thesis. The interaction begins with DM or in the dark sector. The hypothesis is that this
636 DM will either annihilate with itself or decay and produce an SM byproduct. This method is
637 often referred to as the Indirect Detection of DM because we have no lab to directly control or
638 manipulate the DM. Therefore, most indirect DM searches are performed using observations of
639 known DM densities among the astrophysical sources. The strength is that we have the whole of the
640 universe and its 13.6-billion-year lifespan to use as a detector and particle accelerator. Additionally,
641 locations of dark matter are well cataloged since it was astrophysical observations that presented

642 the problem of DM in the first place.

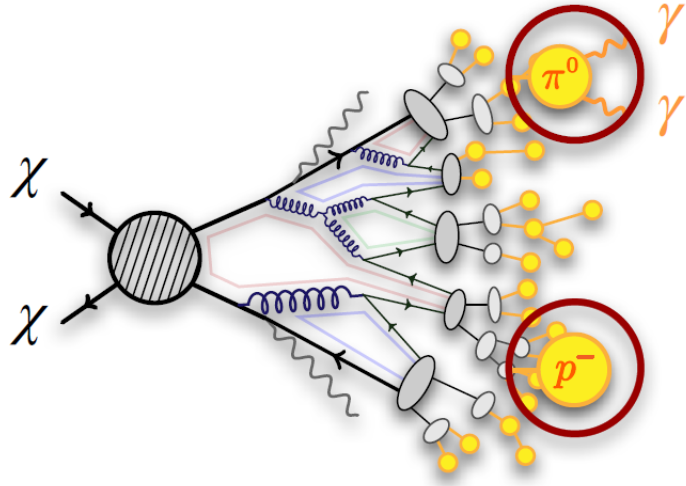


Figure 2.10 More detailed pseudo-Feynman diagram of particle cascade from dark matter annihilation into 2 quarks. The quarks hadronize and down to stable particles like γ or the anti-proton (p^-). Diagram pulled from ICRC 2021 presentation on DM annihilation search [17].

643 However, anything can happen in the universe. There are many difficult to deconvolve back-
644 grounds when searching for DM. One prominent example is the galactic center. We know the
645 galactic center has a large DM content because of stellar kinematics in our Milky Way and DM halo
646 simulations. Yet, any signal from the galactic center is challenging to parse apart from the extreme
647 environment of our supermassive black hole, unresolved sources, and diffuse emission from the
648 interstellar medium [18]. Despite the challenges, any DM model that yields evidence in the other
649 two observation methods, **Shake it or Make it** must be corroborated with indirect observations of
650 the known DM sources. Without corroborating evidence, DM observation in the lab is hard-pressed
651 to demonstrate that it is the model contributing to the DM seen at the universal scale.

652 In the case of WIMP DM, signals are described in terms of primary SM particles produced
653 from DM decay or annihilation. The SM initial state particles are then simulated down to stable
654 final states such as the γ , ν , p , or e which can traverse galactic lengths to reach Earth.

655 Figure 2.10 shows the quagmire of SM particles that emerges from SM initial states that are not
656 stable [17]. There are many SM particles with varying energies that can be produced in such an

657 interaction. For any arbitrary DM source and stable SM particle, the SM flux from DM annihilating
 658 to a neutral particle in the SM, ϕ , from a region in the sky is described by the following.

$$\frac{d\Phi_\phi}{dE_\phi} = \frac{\langle\sigma v\rangle}{8\pi m_\chi^2} \frac{dN_\phi}{dE_\phi} \times \int_{\text{source}} d\Omega \int_{l.o.s} \rho_\chi^2 dl(r, \theta') \quad (2.4)$$

659 In Equation (7.1), $\langle\sigma v\rangle$ is the velocity-weighted annihilation cross-section of DM to the SM. m_χ
 660 refers to the mass of DM, noted with Greek letter χ . $\frac{dN_\phi}{dE_\phi}$ is the N particle flux weighted by the
 661 particle energy. An example is provided in Figure 2.11 for the γ final state. The integrated terms
 662 are performed over the solid angle, $d\Omega$, and line of sight, l.o.s. ρ is the density of DM for a
 663 location (r, θ') in the sky. The terms left of the ' \times ' are often referred to as the particle physics
 664 component. The terms on the right are referred to as the astrophysical component. For decaying
 665 DM, the equation changes to...

$$\frac{d\Phi_\phi}{dE_\phi} = \frac{1}{4\pi\tau m_\chi} \frac{dN_\phi}{dE_\phi} \times \int_{\text{source}} d\Omega \int_{l.o.s} \rho_\chi dl(r, \theta') \quad (2.5)$$

666 In Equation (2.5), τ is the decay lifetime of the DM. Just as in Equation (7.1), the left and right
 667 terms are the particle physics and the astrophysical components respectively. The integrated
 668 astrophysical component of Equation (7.1) is often called the J-Factor. Whereas the integrated
 669 astrophysical component of Equation (2.5) is often called the D-Factor.

670 Exact DM $\text{DM} \rightarrow \text{SM SM}$ branching ratios are not known, so it is usually assumed to go 100%
 671 into an SM particle/anti-particle. Additionally, when a DM annihilation or decay produces one of
 672 the neutral, long-lived SM particles (ν or γ), the particle is traced back to a DM source. For DM
 673 above GeV energies, there are very few SM processes that can produce particles with such a high
 674 energy. Seeing such a signal would almost certainly be an indication of the presence of dark matter.
 675 Fortunately, the universe provides us with the largest volume and lifetime ever for a particle physics
 676 experiment.

677 2.5 Sources for Indirect Dark Matter Searches

678 The first detection of DM relied on optical observations. Since then, we have developed new
 679 techniques to find DM dense regions. As described in Section 2.3.1, many DM dense regions were
 680 through observing galactic rotation curves. Our Milky Way galaxy is among DM dense regions

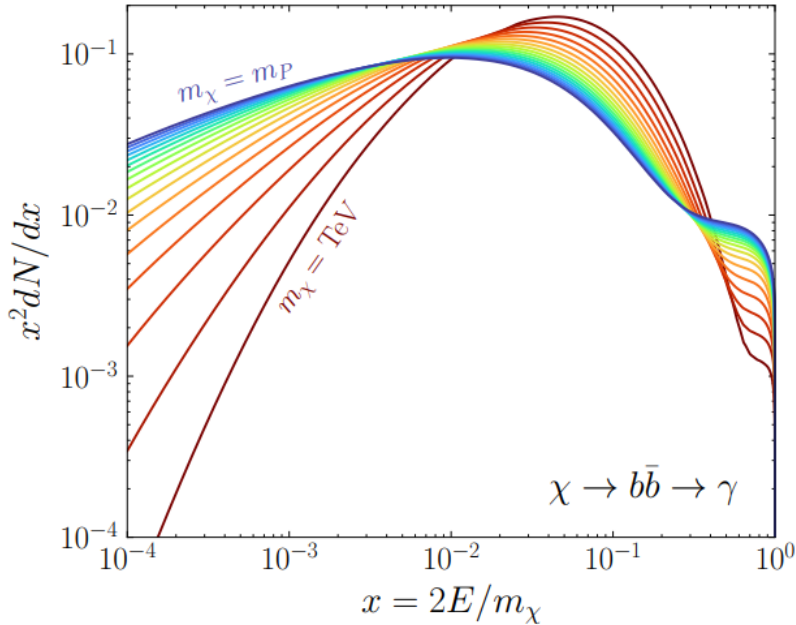


Figure 2.11 Dark Matter (DM) decay spectrum for $b\bar{b}$ initial state and γ final state. Redder spectra are for larger DM masses. Bluer spectra are light DM masses. x is a unitless factor defined as the ratio of the mass of DM, m_χ , and the final state particle energy E_γ . Figure from [19].

discovered, and it is the largest nearby DM dense region to look at. Additionally, the DM halo surrounding the Milky Way is clumpy [18]. There are regions in the DM halo of the Milky Way that have more DM than others that have captured gas over time. These sub-halos were dense enough to collapse gas and form stars. These apparent sub galaxies are known as dwarf spheroidal galaxies and are the main sources studied in this thesis. Each source type comes with different trade-offs. Galactic Center studies will be very sensitive to the assumed distribution of DM. The central DM density can vary substantially as demonstrated in Figure 2.12. At distances close to the center of the galaxy, or small r , the differences in DM densities can be 3-4 orders of magnitude. Searches toward the galactic center will therefore be quite sensitive to the assumed DM distribution.

Searches toward Dwarf Spheroidal Galaxies (dSph's) suffer from uncertainties in the DM density less than the galactic center studies. This is mostly from their diminutive size being smaller than the angular resolution of most γ -ray observatories [18]. The DM content dSph's are typically determined with the Virial theorem, Equation (2.1), and are usually majority DM [18] in mass. DSph's tend to be ideal sources to look at for DM searches. Their environments are quiet with little

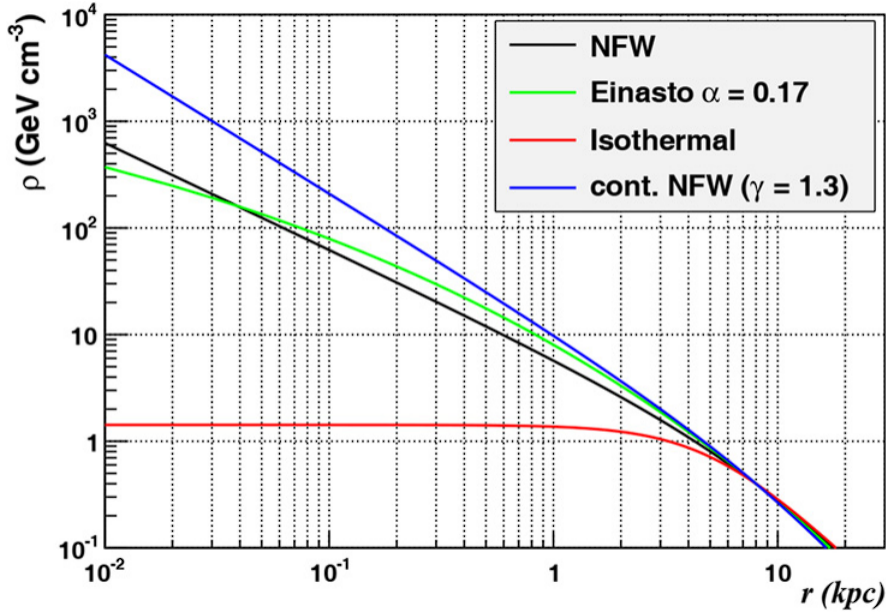


Figure 2.12 Different dark matter density profiles compared. Some models produce exceptionally large densities at small r [20].

695 astrophysical background. Unlike the galactic center, the most active components of dSph's are the
 696 stars within them versus a violent accretion disc around a black hole. All this together means that
 697 dSph's are among the best sources to look at for indirect DM searches. dSph's are the targets of
 698 focus for this thesis.

699 **2.6 Multi-Messenger Dark Matter**

700 Astrophysics entered a new phase in the past few decades that leverages our increasing sensitivity
 701 to SM channels and general relativity (GR). Up until the 21st century, astrophysical observations
 702 were performed with photons (γ) only. Astrophysics with this 'messenger' is fairly mature now.
 703 Novel observations of the universe have since only adjusted the sensitivity of the wavelength of
 704 light that is observed except at MeV energies. Gems like the CMB [10], and more have ultimately
 705 been observations of different wavelengths of light. Multi-messenger astrophysics proposes using
 706 other SM particles such the p^{+-} , or ν or gravitation waves predicted by general relativity.

707 The experiment LIGO had a revolutionary discovery in 2016 with the first detection of a binary
 708 black hole merger [21]. This opened the collective imagination to observing the universe through
 709 gravitational waves. There has also been a surge of interest in the neutrino (ν) sector. IceCube

710 demonstrated that we are sensitive to neutrinos in regions that correlate with significant photon
 711 emission like the galactic plane [22]. Neutrinos, like gravitational waves and light, travel mostly
 712 unimpeded from their source to our observatories. This makes pointing to the originating source
 713 of these messengers much easier than it is for cosmic rays which are deflected from their source by
 714 magnetic fields.

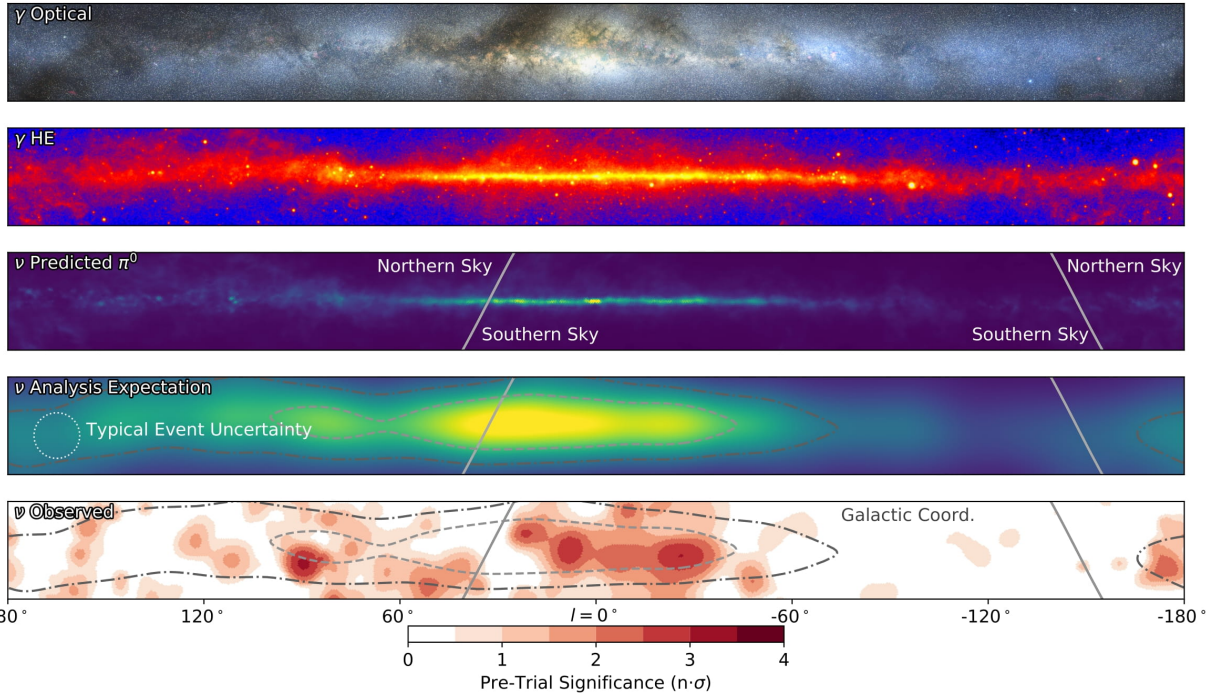


Figure 2.13 The Milky Way Galaxy in photons (γ) and neutrinos (ν) [22]. The Galactic center is at $l=0^\circ$ and is the brightest region in all panels. (top) An Optical color image of the Milky Way galaxy seen from Earth. Clouds of gas and dust obscure some light from stars. (2nd down) Integrated flux of γ -rays observed by the Fermi-LAT telescope [23]. (middle) Expected neutrino emission that corresponds with Fermi-LAT observations. (2nd up) Expected neutrino emission profile after considering detector systematics of IceCube. (bottom) Observed neutrino emission from region of the galactic plane. Substantial neutrino emission was detected.

715 The IceCube collaboration recently published a groundbreaking result of the Milky Way in
 716 neutrinos. The recent result from IceCube, shown in Figure 2.13, proves that we can make
 717 observations under different messenger regimes. The top two panels show the appearance of the
 718 galactic plane to different wavelengths of light. Some sources are more apparent in some panels,
 719 while others are not. This new channel is powerful because neutrinos are readily able to penetrate
 720 through gas and dust in the Milky Way. This new image also refines our understanding of how high

721 energy particles are produced. For example, the fit to IceCube data prefers neutrino production
 722 from the decay of π^0 [22].

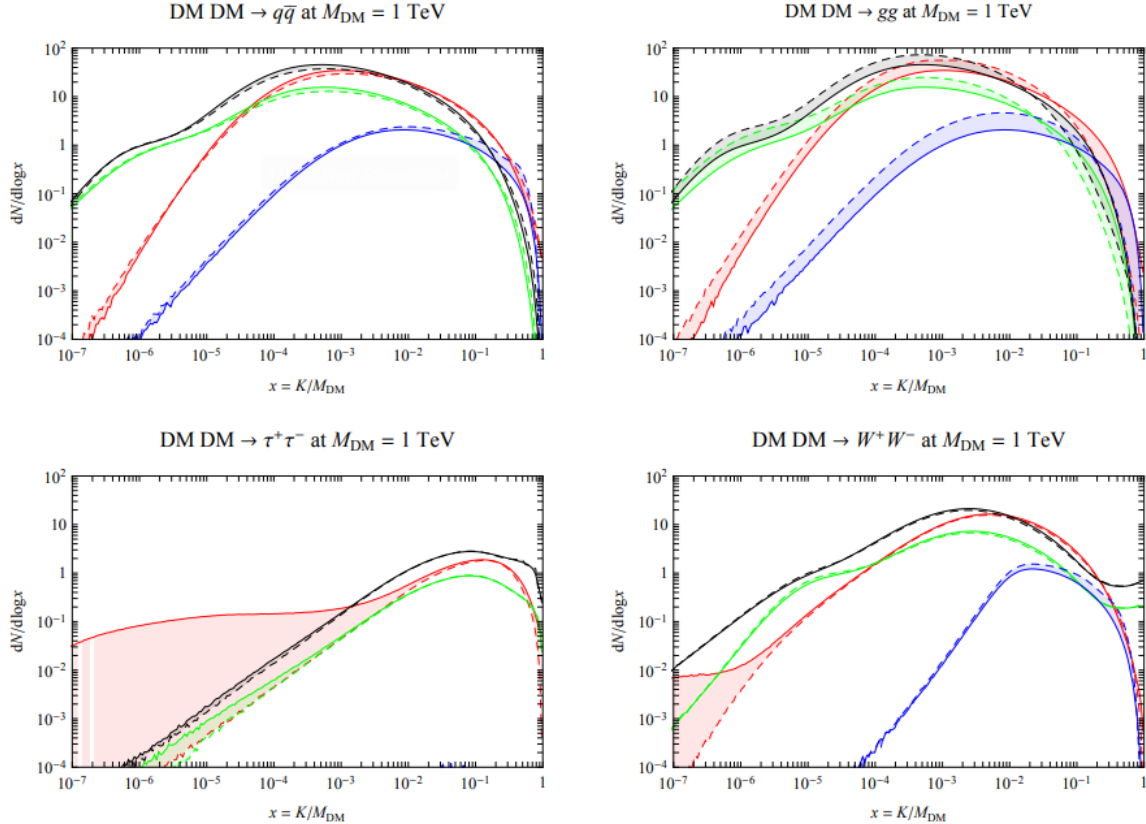


Figure 2.14 Dark Matter annihilation spectra for different final state particle and standard model annihilation channels [24]. Photons (red), e^\pm (green), \bar{p} (blue), ν (black).

723 Exposing our observations to more cosmic messengers greatly increases our sensitivity to
 724 rare processes. In the case of DM, Figure 2.14, there are many SM particles produced in DM
 725 annihilation. Among the final state fluxes are gammas and neutrinos. Charged particles are also
 726 produced however they would not likely make it to Earth since they will be deflected by magnetic
 727 fields between the source and Earth. This means observatories that can see the neutral messengers
 728 are especially good for DM searches and for combining data for a multi-messenger DM search.

729

CHAPTER 3

729 **HIGH ALTITUDE WATER CHERENKOV (HAWC) OBSERVATORY**

730 **3.1 The Detector**

731 **3.2 Events Reconstruction and Data Acquisition**

732 **3.2.1 G/H Discrimination**

733 **3.2.2 Angle**

734 **3.2.3 Energy**

735 **3.3 Remote Monitoring**

736 **3.3.1 ATHENA Database**

737 **3.3.2 HOMER**

CHAPTER 4

ICECUBE NEUTRINO OBSERVATORY

739 **4.1 The Detector**

740 **4.2 Events Reconstruction and Data Acquisition**

741 **4.2.1 Angle**

742 **4.2.2 Energy**

743 **4.3 Northern Test Site**

744 **4.3.1 PIgeon remote dark rate testing**

745 **4.3.2 Bulkhead Construction**

CHAPTER 5

746 **GLORY DUCK: MULTI-WAVELENGTH SEARCH FOR DARK MATTTER** 747 **ANNIHILATION TOWARDS DWARF SPHEROIDAL GALAXIES**

748 **5.1 Introduction**

749 The field of astrophysics now has several instruments and observatories sensitive to high energy
750 gamma-rays. The energy sensitivity for the modern gamma-ray program spans many orders of
751 magnitude. Figure 5.1 demonstrates these comparable sensitivities across energies for the five
752 experiments: Fermi-LAT, HAWC, HESS, MAGIC, and VERITAS.

753 Each of the five experiments featured in Figure 5.1 have independently searched for DM
754 annihilation from dwarf spheroidal galaxies (dSph) and set limits on annihilation cross-section of
755 WIMPs. Intriguingly, there are regions of substantial overlap in their energy sensitivities. This
756 clearly motivates an analysis that combines data from these five. Each experiment has unique
757 gamma-ray detection methods and their weaknesses and strengths can be leveraged with each other.
758 The HAWC gamma-ray observatory is extensively introduced in chapter 3, so it is not introduced
759 here. A brief description of the remaining experiments are in the following paragraphs.

760 The Large Area Telescope (LAT) is a pair conversion telescope mounted on the NASA Fermi
761 satellite in orbit \sim 550 km above the Earth [26]. LAT's field of view covers about 20% of the
762 whole sky, and it sweeps the whole sky approximately every 3 hours. LAT's gamma-ray energy
763 sensitivity ranges from 20 MeV up to 1 TeV. Previous DM searches towards dSphs using Fermi-LAT
764 are published in [27] and [28].

765 The High Energy Spectroscopic System (HESS), Major Atmospheric Gamma Imaging
766 Cherenkov (MAGIC), and Very Energetic Radiation Imaging Telescope Array System (VERI-
767 TAS) are arrays of Imaging Atmospheric Cherenkov Telescopes (IACT). These telescopes observe
768 the Cherenkov light emitted from gamma-ray showers in the Earth's atmosphere. The field of
769 view for these telescopes is no larger than 5° with energy sensitivities ranging from 30 GeV up
770 to 100 TeV [29, 30, 31]. IACTs are able to make precise observations in selected regions of the
771 sky, however can only be operated in ideal dark conditions. HESS's observations of the dwarves

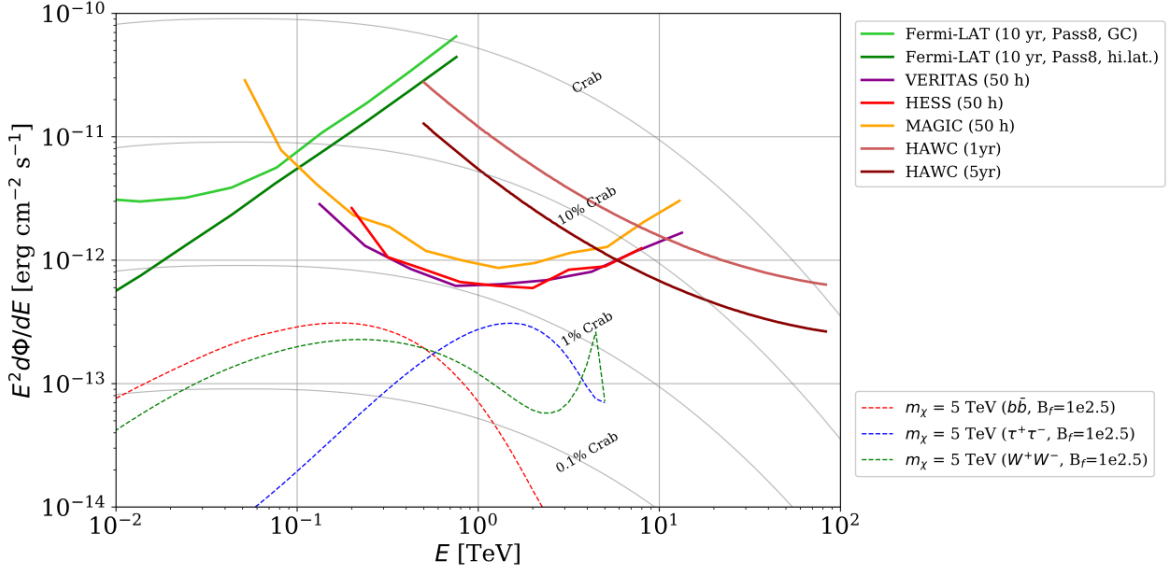


Figure 5.1 Sensitivities of five gamma-ray experiments compared to percentages of the Crab nebula's emission and dark matter annihilation. Solid lines present estimated sensitivities to power law spectra [FACT CHECK THIS] for each experiment. Green lines are Fermi-LAT sensitivities where lighter green is the sensitivity to the galactic center and dark green is its sensitivity to higher declinations. Orange, red, and purple solid lines represent the MAGIC, HESS, and VERITAS 50 hour sensitivities respectively. The maroon and brown lines are the HAWC 1 year and 5 year sensitivities. Across four decades of gamma-ray energy, these experiments have similar sensitivities on the order 10^{-12} erg $\text{cm}^{-2}\text{s}^{-1}$. The dotted lines are estimated dark matter fluxes assuming $m_\chi = 5$ TeV DM annihilating to bottom quarks (red), tau leptons (blue), and W bosons (green). Faded gray lines outline percentage flux of the Crab nebula. Figure is an augmented version of [25]

772 Sculptor and Carina were between January 2008 and December 2009. HESS's observations of
 773 Coma Berenices were taken from 2010 to 2013, and Fornax was observed in 2010 [32, 33, 34].
 774 MAGIC provided deep observations of Segue1 between 2011 and 2013 [35]. MAGIC also provides
 775 data for three additional dwarves: Coma Berenices, Draco, and Ursa Major II where observations
 776 were made in: January - June 2019 [36], March - September 2018 [36], and 2014 - 2016 [37]
 777 respectively. VERITAS provided data for Boötes I, Draco, Segue 1, and Ursa Minor from 2009 to
 778 2016 [38].

779 This chapter presents the Glory Duck analysis, the name given for the search for dark matter
 780 annihilation from dSph by combining data from the five gamma-ray observatories: Fermi-LAT,
 781 HAWC, HESS, MAGIC, and VERITAS. Specifically, the methods in analysis and modeling are
 782 presented for the HAWC gamma-ray observatory. This work will be published in the Journal of

783 Cosmology and Astroparticle Physics and presented at the International Cosmic Ray Conference
784 in 2019, 2021, and 2023 [39, 40, 41] and others.

785 **5.2 Dataset and Background**

786 This section enumerates the data analysis and background estimation methods used for HAWC's
787 study of dSphs. Section 5.2.1 and Section 5.2.2 are most useful for fellow HAWC collaborators
788 looking to replicate the Glory Duck analysis.

789 **5.2.1 Itemized HAWC files**

790 These files are only available withing HAWC's internal documentation and collaborators. They
791 are not meant for public access, and are presented here so that HAWC collaborators can reproduce
792 results accurately.

- 793 • Detector Response: `response_aerie_svn_27754_systematics_best_mc_test_noBr`
794 `oadpulse\10pctlogchargesmearing_0.63qe_25kHzNoise_run5481_curvature`
795 `0_index3.root`
- 796 • Data Map: `maps-20180119/liff/maptree_1024.root`
- 797 • Spectral Dictionary: `DM_CirrelliSpectrum_dict_gammas.npy`
- 798 • Analysis wiki: https://private.hawc-observatory.org/wiki/index.php/Glory_Duck_Multi-Experiment_Dark_Matter_Search

800 **5.2.2 Software Tools and Development**

801 This analysis was performed using HAL and 3ML [42, 43] in Python version 2. I built software
802 to implement the *A Poor Particle Physicist Cookbook for Dark Matter Indirect Detection* (PPPC)
803 [44] DM spectral model and dSphs spatial model from [45] for HAWC analysis. A NumPy version
804 of this dictionary was made for both Py2 and Py3. The code base for creating this dictionary is
805 linked on my GitLab sandbox:

- 806 • Py2: [Dictionary Generator \(Deprecated\)](#)

- 807 • Py3: [PPPC2Dict](#)

808 The analysis was performed using the f_{hit} framework as used and described in the HAWC Crab
809 paper [42]. The Python2 NumPy dictionary file for gamma-ray final states is `dmCirSpecDict.npy`.
810 The corresponding Python3 file is `DM_CirrelliSpectrum_dict_gammas.npy`. These files can
811 also be used for decay channels and the PPPC describes how [44]. All other software used for data
812 analysis, DM profile generation, and job submission to SLURM are also kept in my sandbox for
813 [the Glory Duck](#) project.

814 **5.2.3 Data Set and Background Description**

815 The HAWC data maps used for this analysis contain 1017 days of data between runs 2104
816 (2014-11-26) and 7476 (2017-12-20). They were generated from pass 4.0 reconstruction. The
817 analysis is performed using the f_{hit} energy binning scheme with bins (1-9) similar to what was done
818 for the Crab and previous HAWC dSph analysis [42, 46]. Bin 0 was excluded as it has substantial
819 hadronic contamination and poor angular resolution.

820 This analysis was done on dSphs because of their large DM mass content relative to baryonic
821 mass. We consider the following to estimate the background to this study.

- 822 • The dSphs' angular extent are small relative to HAWC's spatial resolution, so the analysis is
823 not sensitive to large or small scale anisotropies.
- 824 • The dSphs used in this analysis are off the galactic plane and therefore not contaminated by
825 diffuse emission from the galaxy.
- 826 • The dSphs are baryonically faint relative to their expected dark matter content and are not
827 expected to contain high energy gamma-ray sources.

828 Therefor we make no additional assumptions on the background from our sources and use
829 HAWC's standard direct integration method for background estimation [42]. The largest background
830 under this consideration is from an isotropic flux of cosmic rays. The contamination of this hadronic
831 flux is worse at lower energies where HAWC's gamma/hadron discrimination worse. It is possible

832 for gamma rays from DM annihilation to scatter in transit to HAWC via Inverse Compton Scattering
833 (ICS). This was investigated and its impact on the flux is negligible. Supporting information on
834 this is in Section 5.7.1

835 **5.3 Analysis**

836 The expected differential photon flux from DM-DM annihilation to standard model particles,
837 $d\Phi_\gamma/dE_\gamma$, over solid angle, Ω , is described by the familiar equation.

$$\frac{d\Phi_\gamma}{dE_\gamma} = \frac{\langle\sigma v\rangle}{8\pi m_\chi^2} \frac{dN_\gamma}{dE_\gamma} \times \int_{\text{source}} d\Omega \int_{l.o.s} dl \rho_\chi^2 J(r, \theta') \quad (5.1)$$

838 Where $\langle\sigma v\rangle$ is the velocity weighted annihilation cross-section. $\frac{dN}{dE}$ is the expected differential
839 number of photons produced at each energy per annihilation. m_χ is the rest mass of the supposed
840 DM particle. ρ_χ is the DM density. J is the astrophysical J-factor and is defined as

$$J = \int d\Omega \int_{l.o.s} dl \rho_\chi^2(r, \theta') \quad (5.2)$$

841 l is the distance to the source from Earth. r is the radial distance from the center of the source. θ' is
842 the half angle defining a cone containing the DM source. How each component is synthesized and
843 considered for HAWC's analysis is presented in the following sections. Section 5.3.1 presents the
844 particle physics model for DM annihilation. Section 5.3.2 presents the spatial distributions built
845 for each dSph.

846 **5.3.1 $\frac{dN_\gamma}{dE_\gamma}$ - Particle Physics Component**

847 For these spectra, we import the PPPC with Electroweak (EW) corrections [44]. Public versions
848 of the imported tables are provided by the [authors online](#). The spectrum is implemented as a model
849 script in astromodels for 3ML. The EW corrections were previously not considered for HAWC and
850 are significant for DM annihilating to EW coupled SM particles such as all leptons, and the γ ,
851 Z , and W bosons [46]. Figure 5.2 demonstrates the significance of EW corrections for W boson
852 annihilation. Across EW SM channels, the gamma-ray spectra become harder than spectra without
853 EW corrections. Tables from the PPPC were reformatted into Python NumPy dictionaries for
854 collaboration-wide use. A class in astromodels was developed to include the EW correction from
855 the PPPC and is aptly named `PPPCSpectra` within `DM_models.py`.

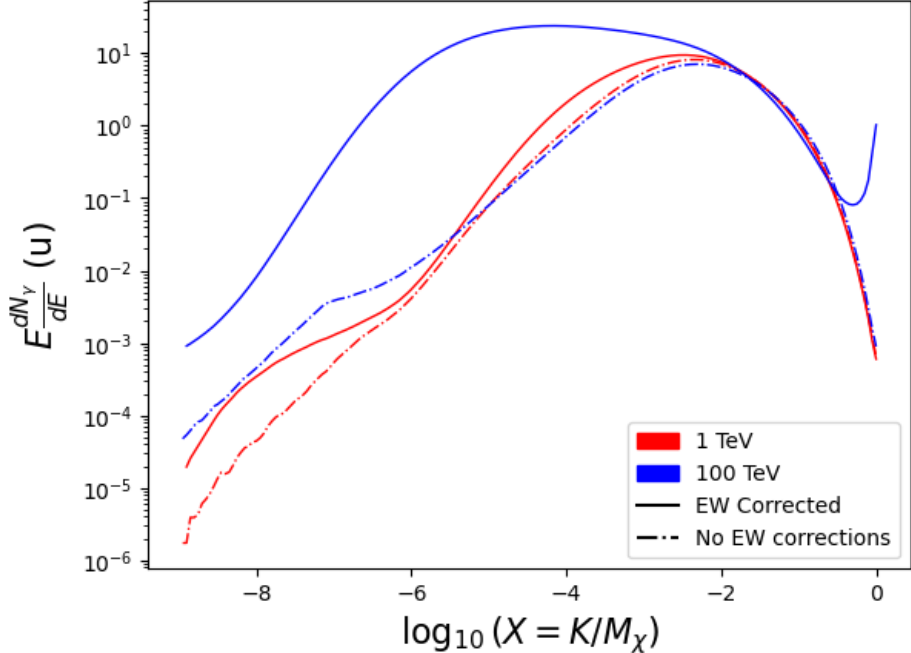


Figure 5.2 Effect of Electroweak (EW) corrections on expected DM annihilation spectrum for $\chi\chi \rightarrow W^-W^+$. Solid lines are spectral models that consider EW corrections. Dash-dot lines are spectral models without EW corrections. Red lines are models for $M_\chi = 1$ TeV. Blue lines represent models for $M_\chi = 100$ TeV. All models are sourced from the PPPC4DMID [44].

856 5.3.2 J- Astrophysical Component

857 The J-factor profiles for each source are imported from Geringer-Sameth (referred to with \mathcal{GS})
 858 [45]. \mathcal{GS} fits the Zhao DM profile to the dSphs which has a DM density described as [47]

$$\rho(r) = \frac{\rho_0}{(r/R_s)^\gamma (1 + (r/R_s)^\alpha)^{(\beta-\gamma)}}. \quad (5.3)$$

859 R_s is the scale radius and free parameter in the model. γ is the logarithmic slope in the region
 860 $r \ll R_s$. β is the logarithmic slope in the region $r \gg R_s$. α is known as the sharpness of transition
 861 where $r \approx R_s$. The classic Navarro-Frenk-White [48] (NFW) can be retrieved from Zhao by fixing
 862 $(\alpha, \beta, \gamma) = (1, 3, 1)$.

863 \mathcal{GS} best fits were pulled from the publication as $J(\theta)$, where θ is the angular separation from
 864 the center of the source. HAWC requires maps in terms of $\frac{dJ}{d\Omega}$, so the conversion from the maps
 865 was done in the following way...

866 First, convert the angular distances to solid angles

$$\Omega = 2 \cdot \pi(1 - \cos(\theta)) \quad (5.4)$$

867 which reduces with a small angle approximation to $\pi\theta^2$. Next, the central difference for both the
868 ΔJ and $\Delta\Omega$ value were calculated from the discretized $J(\theta)$ with the central difference stencil:

$$\Delta\phi_i = \phi_{i+1} - \phi_{i-1} \quad (5.5)$$

869 Where ϕ is either Ω or J . These were done separately in case the grid spacing in θ was not uniform.
870 Finally, these lists are divided so that we are left with an approximation of the $dJ/d\Omega$ profile that
871 is a function of θ . Admittedly, this is an approximation method for the map which introduces small
872 errors compared to the true profile estimate. This was checked as a systematic against the author's
873 profiling of the spatial distribution and is documented in Section 5.8.1.

874 With $\frac{dJ}{d\Omega}(\theta)$, a map is generated, first by filling in the north-east quadrant of the map. This
875 quadrant is then reflected twice, vertically then horizontally, to fill the full map. Maps are then
876 normalized by dividing the discrete 2D integral of the map. The 2D integral was a simple height
877 of bins, Newton's integral:

$$p^2 \cdot \sum_{i,j=0}^{N,M} \frac{dJ}{d\Omega}(\theta_{i,j}, \phi_{i,j}) \quad (5.6)$$

878 These maps are HEALpix maps with NSIDE 16384 and saved in the .fits format. The hyper fine
879 resolution was selected to better preserve the total expected counts after integrating Eq. (7.1) with
880 the detector response.

881 Another DM spatial distribution model from Bonnivard (\mathcal{B}) [49] was used for the Glory Duck
882 study. However, to save computational time, limits from \mathcal{GS} were scaled to \mathcal{B} instead of each
883 experiment performing a full study a second time. How these models compare is demonstrated
884 for each dSph in Figure 5.16 and Figure 5.17 Plots of these maps are provided for each source
885 in chapter A Examples of the two most impactful dSphs derived from \mathcal{GS} , Segue1 and Coma
886 Berenices are featured in Figure 5.3

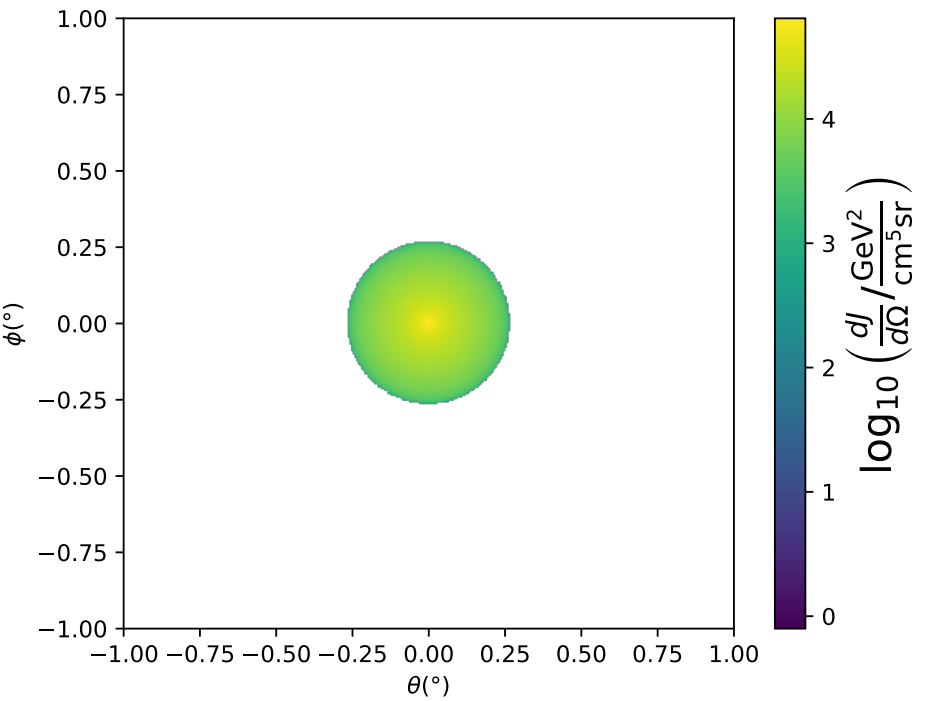
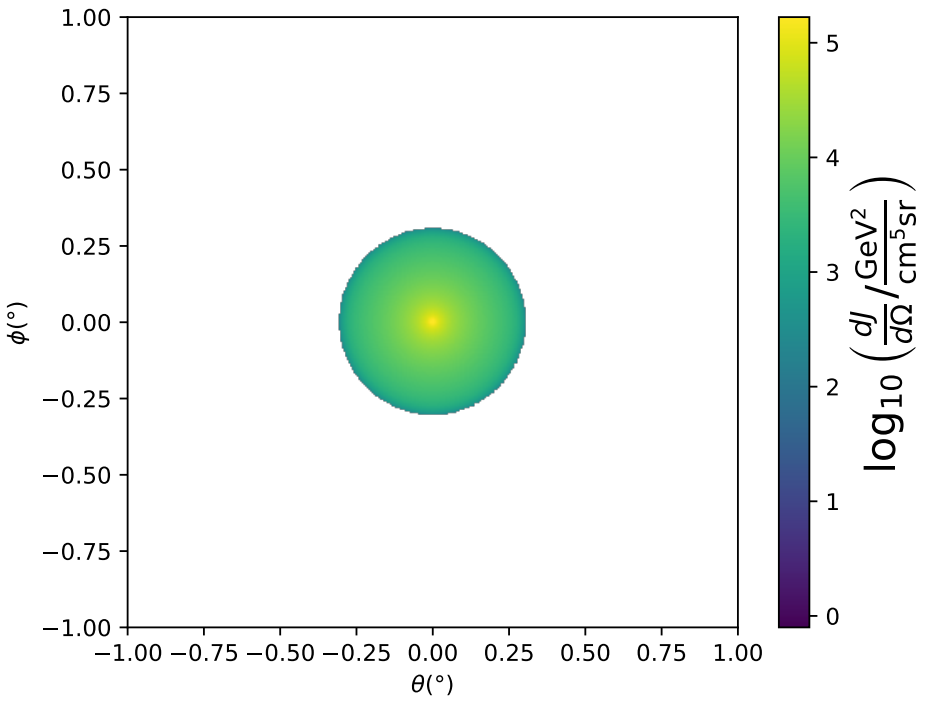


Figure 5.3 $\frac{dJ}{d\Omega}$ maps for Segue1 (top) and Coma Berenices (bottom). Origin is centered on the specific dwarf spheroidal galaxies (dSph). X and Y axes are the angular separation from the center of the dwarf. Profile is truncated at the scale radius. Plots of the remaining 11 dSph HAWC studied are linked in Fig. A.1.

887 **5.3.3 Source Selection and Annihilation Channels**

888 We use many of the dSphs presented in HAWC’s previous dSph DM search [46]. HAWC’s
889 sources for Glory Duck include Boötes I, Coma Berenices, Canes Venatici I + II, Draco, Hercules,
890 Leo I, II, + IV, Segue 1, Sextans, and Ursa Major I + II. A full description of all sources used
891 in Glory Duck is found in Table 5.1. Triangulum II was excluded from the Glory Duck analysis
892 because of large uncertainties in its J factor. Ursa Minor was excluded from HAWC’s contribution
893 to the combination because the source extension model extended Ursa Minor beyond HAWC’s field
894 of view. Ursa Minor was not expected to contribute significantly to the combined limit, so work
895 was not invested in a solution to include Ursa Minor.

896 This analysis improves on the previous HAWC dSph paper [46] in the following ways. Pre-
897 viously, the dSphs were treated and implemented as point sources. For this analysis, dSphs are
898 modeled and treated as extended source. The impact of this change with respect to the upper limit
899 is source dependent and is explored in Section 5.7.2. Previously, the particle physics model used for
900 gamma-ray spectra from DM annihilation did not have EW corrections where the PPPC includes
901 them. Finally, the gamma-ray ray dataset is much larger. The study performed here analyzes over
902 1000 days of data compared to 507.

903 The SM annihilation channels probed for the Glory Duck combination include $b\bar{b}$, $e\bar{e}$, $\mu\bar{\mu}$, $\tau\bar{\tau}$,
904 $t\bar{t}$, W^+W^- , and ZZ . A summary of all sources, with a description of each experiments’ sensitivity
905 to the source, is provided in Table 5.2.

906 **5.4 Likelihood Methods**

907 **5.4.1 HAWC Likelihood**

908 For every analysis bin in energy, f_{hit} bins (1-9), and location, we can expect N signal events and
909 B background events. The expected number of excess signal events from dark matter annihilation,
910 S , is estimated by convolving Equation (7.1) with HAWC’s energy response and pixel point spread
911 functions. I then compute the test statistic (TS) with the log-likelihood ratio test,

$$TS_{\max} = -2 \ln \left(\frac{\mathcal{L}_0}{\mathcal{L}_{\max}} \right) \quad (5.7)$$

Table 5.1 Summary of the relevant properties of the dSphs used in the present work. Column 1 lists the dSphs. Columns 2 and 3 present their heliocentric distance and galactic coordinates, respectively. Columns 4 and 5 report the J -factors of each source given from the \mathcal{GS} and \mathcal{B} independent studies and their estimated $\pm 1\sigma$ uncertainties. The values $\log_{10} J$ (\mathcal{GS} set) [45] correspond to the mean J -factor values for a source extension truncated at the outermost observed star. The values $\log_{10} J$ (\mathcal{B} set) [49] are provided for a source extension at the tidal radius of each dSph. **Bolded sources are within HAWC's field of view and provided to the Glory Duck analysis.**

Name	Distance (kpc)	l, b ($^{\circ}$)	$\log_{10} J$ (\mathcal{GS} set) $\log_{10}(\text{GeV}^2\text{cm}^{-5}\text{sr})$	$\log_{10} J$ (\mathcal{B} set) $\log_{10}(\text{GeV}^2\text{cm}^{-5}\text{sr})$
Boötes I	66	358.08, 69.62	$18.24^{+0.40}_{-0.37}$	$18.85^{+1.10}_{-0.61}$
Canes Venatici I	218	74.31, 79.82	$17.44^{+0.37}_{-0.28}$	$17.63^{+0.50}_{-0.20}$
Canes Venatici II	160	113.58, 82.70	$17.65^{+0.45}_{-0.43}$	$18.67^{+1.54}_{-0.97}$
Carina	105	260.11, -22.22	$17.92^{+0.19}_{-0.11}$	$18.02^{+0.36}_{-0.15}$
Coma Berenices	44	241.89, 83.61	$19.02^{+0.37}_{-0.41}$	$20.13^{+1.56}_{-1.08}$
Draco	76	86.37, 34.72	$19.05^{+0.22}_{-0.21}$	$19.42^{+0.92}_{-0.47}$
Fornax	147	237.10, -65.65	$17.84^{+0.11}_{-0.06}$	$17.85^{+0.11}_{-0.08}$
Hercules	132	28.73, 36.87	$16.86^{+0.74}_{-0.68}$	$17.70^{+1.08}_{-0.73}$
Leo I	254	225.99, 49.11	$17.84^{+0.20}_{-0.16}$	$17.93^{+0.65}_{-0.25}$
Leo II	233	220.17, 67.23	$17.97^{+0.20}_{-0.18}$	$18.11^{+0.71}_{-0.25}$
Leo IV	154	265.44, 56.51	$16.32^{+1.06}_{-1.70}$	$16.36^{+1.44}_{-1.65}$
Leo V	178	261.86, 58.54	$16.37^{+0.94}_{-0.87}$	$16.30^{+1.33}_{-1.16}$
Leo T	417	214.85, 43.66	$17.11^{+0.44}_{-0.39}$	$17.67^{+1.01}_{-0.56}$
Sculptor	86	287.53, -83.16	$18.57^{+0.07}_{-0.05}$	$18.63^{+0.14}_{-0.08}$
Segue I	23	220.48, 50.43	$19.36^{+0.32}_{-0.35}$	$17.52^{+2.54}_{-2.65}$
Segue II	35	149.43, -38.14	$16.21^{+1.06}_{-0.98}$	$19.50^{+1.82}_{-1.48}$
Sextans	86	243.50, 42.27	$17.92^{+0.35}_{-0.29}$	$18.04^{+0.50}_{-0.28}$
Ursa Major I	97	159.43, 54.41	$17.87^{+0.56}_{-0.33}$	$18.84^{+0.97}_{-0.43}$
Ursa Major II	32	152.46, 37.44	$19.42^{+0.44}_{-0.42}$	$20.60^{+1.46}_{-0.95}$
Ursa Minor	76	104.97, 44.80	$18.95^{+0.26}_{-0.18}$	$19.08^{+0.21}_{-0.13}$

Table 5.2 Summary of dSph observations by each experiment used in this work. A ‘-’ indicates the experiment did not observe the dSph for this study. For Fermi-LAT, the exposure at 1 GeV is given. For HAWC, $|\Delta\theta|$ is the absolute difference between the source declination and HAWC latitude. HAWC is more sensitive to sources with smaller $|\Delta\theta|$. For IACTs, we show the zenith angle range, the total exposure, the energy range, the angular radius θ of the signal or ON region, the ratio of exposures between the background-control (OFF) and signal (ON) regions (τ), and the significance of gamma-ray excess in standard deviations, σ .

Source name	Fermi-LAT	HAWC	H.E.S.S, MAGIC, VERITAS						
	Exposure (10^{11} s m 2)	$ \Delta\theta $ ($^\circ$)	IACT	Zenith ($^\circ$)	Exposure (h)	Energy range (GeV)	θ ($^\circ$)	τ	S (σ)
Boötes I	2.6	4.5	VERITAS	15 – 30	14.0	100–41000	0.10	8.6	-1.0
Canes Venatici I	2.9	14.6	–	–	–	–	–	–	–
Canes Venatici II	2.9	15.3	–	–	–	–	–	–	–
Carina	3.1	–	H.E.S.S.	27 – 46	23.7	310 – 70000	0.10	18.0	-0.3
Coma Berenices	2.7	4.9	H.E.S.S.	47 – 49	11.4	550 – 70000	0.10	14.4	-0.4
			MAGIC	5 – 37	49.5	60 – 10000	0.17	1.0	–
			MAGIC	29 – 45	52.1	70 – 10000	0.22	1.0	–
Draco	3.8	38.1	VERITAS	25 – 40	49.8	120 – 70000	0.10	9.0	-1.0
Fornax	2.7	–	H.E.S.S.	11 – 25	6.8	230 – 70000	0.10	45.5	-1.5
Hercules	2.8	6.3	–	–	–	–	–	–	–
Leo I	2.5	6.7	–	–	–	–	–	–	–
Leo II	2.6	3.1	–	–	–	–	–	–	–
Leo IV	2.4	19.5	–	–	–	–	–	–	–
Leo V	2.4	–	–	–	–	–	–	–	–
Leo T	2.6	–	–	–	–	–	–	–	–
Sculptor	2.7	–	H.E.S.S.	10 – 46	11.8	200 – 70000	0.10	19.8	-2.2
Segue I	2.5	2.9	MAGIC	13 – 37	158.0	60 – 10000	0.12	1.0	-0.5
			VERITAS	15 – 35	92.0	80 – 50000	0.10	7.6	0.7
Segue II	2.7	–	–	–	–	–	–	–	–
Sextans	2.4	20.6	–	–	–	–	–	–	–
Ursa Major I	3.4	32.9	–	–	–	–	–	–	–
Ursa Major II	4.0	44.1	MAGIC	35 – 45	94.8	120 – 10000	0.30	1.0	-2.1
Ursa Minor	4.1	–	VERITAS	35 – 45	60.4	160 – 93000	0.10	8.4	-0.1

912 where \mathcal{L}_0 is the null hypothesis, or no DM emission, likelihood. \mathcal{L}^{\max} is the best fit signal
 913 hypothesis where $\langle\sigma v\rangle$ maximizes the likelihood. We calculate the likelihood of each source and
 915 model, assuming events are Poisson distributed, with

$$\mathcal{L} = \prod_i \frac{(B_i + S_i)^{N_i} e^{-(B_i + S_i)}}{N_i!} \quad (5.8)$$

916 where S_i is the sum of expected number of signal counts. B_i is the number of background counts
 917 observed. N_i is the total number of counts.

918 I also calculate an upper limit on $\langle\sigma v\rangle$ by calculating the 95% confidence level (CL). For the
 919 CL, we define a parameter, TS_{95} , as

$$TS_{95} \equiv \sum_{\text{bins}} \left[2N \ln \left(1 + \frac{\epsilon S_{\text{ref}}}{B} \right) - 2\epsilon S_{\text{ref}} \right] \quad (5.9)$$

920 where the expected signal counts from a dSph is scaled by ϵ . S_{ref} is the expected number of excess
 921 counts in a bin from DM emission from a dSph with a corresponding annihilation cross-section,
 922 $\langle\sigma v\rangle$. We scan ϵ such that

$$2.71 = TS_{\max} - TS_{95} \quad (5.10)$$

923 HAWC's exclusive results are provided in Section 5.5.

924 5.4.2 Glory Duck Joint Likelihood

925 The joint likelihood for the 5-experiment combination was done similarly as Section 5.4.1. We
 926 calculate upper limits on $\langle\sigma v\rangle$ from the TS, Eq. (5.7), and define the likelihood ratio more generally

$$\lambda(\langle\sigma v\rangle | \mathcal{D}_{\text{dSphs}}) = \frac{\mathcal{L}(\langle\sigma v\rangle; \hat{\nu} | \mathcal{D}_{\text{dSphs}})}{\mathcal{L}(\widehat{\langle\sigma v\rangle}; \hat{\nu} | \mathcal{D}_{\text{dSphs}})} \quad (5.11)$$

927 $\mathcal{D}_{\text{dSphs}}$ is the totality of observations across experiments and dSphs. ν are the nuisance parameters
 928 which are the J factors in this study. $\widehat{\langle\sigma v\rangle}$ and $\hat{\nu}$ are the respective estimate that maximize \mathcal{L}
 929 globally. Finally, $\hat{\nu}$ is the set of nuisance parameters that maximize \mathcal{L} for a fixed value of $\langle\sigma v\rangle$.

930 The *complete* joint likelihood, \mathcal{L} that encompasses all observations from all instruments and
 931 dSphs can be factorized into *partial* functions for each dSph l (with $\mathcal{L}_{\text{dSph},l}$) and its J factor (\mathcal{J}_l):

$$\mathcal{L}(\langle\sigma v\rangle; \nu | \mathcal{D}_{\text{dSphs}}) = \prod_{l=1}^{N_{\text{dSphs}}} \mathcal{L}_{\text{dSph},l}(\langle\sigma v\rangle; J_l, \nu_l | \mathcal{D}_l) \times \mathcal{J}_l(J_l | J_{l,\text{obs}}, \sigma_{\log J_l}). \quad (5.12)$$

932 For this study, $N_{\text{dSphs}} = 20$ is the number of dSphs studied. \mathcal{D}_l are the gamma-ray observations
 933 of dSph, l . ν_l are the nuisance parameters modifying the gamma-ray observations of dSph, l ,
 934 but excludes \mathcal{J}_l . \mathcal{J}_l is the J factor for dSph, l , as defined in Equation (5.2), and it is a nuisance
 935 parameter whose value is unknown. $\log_{10} J_{l,\text{obs}}$ and $\sigma_{\log J_l}$ are obtained by fitting a log-normal
 936 function of $J_{l,\text{obs}}$ to the posterior distribution of J_l [50]. $\log_{10} J_{l,\text{obs}}$ and $\sigma_{\log J_l}$ values are provided
 937 in Table 5.1. The term \mathcal{J}_l constraining J_l is written as:

$$\mathcal{J}_l(J_l | J_{l,\text{obs}}, \sigma_{\log J_l}) = \frac{1}{\ln(10)J_{l,\text{obs}}\sqrt{2\pi}\sigma_{\log J_l}} \exp\left(-\frac{(\log_{10} J_l - \log_{10} J_{l,\text{obs}})^2}{2\sigma_{\log J_l}^2}\right). \quad (5.13)$$

938 Both the \mathcal{GS} and \mathcal{B} , displayed in Table 5.1, sets of J factors are used in this analysis. Equation (5.13)
 939 is also normalized, so it can also be interpreted as a probability density function (PDF) for $J_{l,\text{obs}}$.
 940 From Equation (7.1), we can also see that $\langle\sigma v\rangle$ and J_l are degenerate when computing $\mathcal{L}_{\text{dSph},l}$.
 941 Therefore, as noted in [51], it is sufficient to compute $\mathcal{L}_{\text{dSph},l}$ versus $\langle\sigma v\rangle$ for a fixed value of J_l .
 942 We used $J_{l,\text{obs}}(\mathcal{GS})$ reported in Tab. 5.1, in order to perform the profile of \mathcal{L} with respect to J_l .
 943 The degeneracy implies that for any $J'_l \neq J_{l,\text{obs}}$ (in practice in our case we used $J'_l = J_{l,\text{obs}}(\mathcal{B})$ to
 944 compute results from a different set of J factors):

$$\mathcal{L}_{\text{dSph},l}(\langle\sigma v\rangle; J'_l, \nu_l | \mathcal{D}_l) = \mathcal{L}_{\text{dSph},l}\left(\frac{J'_l}{J_{l,\text{obs}}} \langle\sigma v\rangle; J_{l,\text{obs}}, \nu_l | \mathcal{D}_l\right), \quad (5.14)$$

945 which is a straightforward rescaling operation that reduces the computational needs of the profiling
 946 operation since:

$$\mathcal{L}(\langle\sigma v\rangle; \hat{\nu} | \mathcal{D}_{\text{dSphs}}) = \prod_{l=1}^{N_{\text{dSphs}}} \max_{J_l} \left[\mathcal{L}_{\text{dSph},l}(\langle\sigma v\rangle; J_l, \hat{\nu}_l | \mathcal{D}_l) \times \mathcal{J}_l(J_l | J_{l,\text{obs}}, \sigma_{\log J_l}) \right]. \quad (5.15)$$

947 In addition, Eq. (5.14) enables the combination of data from different gamma-ray instruments and
 948 observed dSphs via tabulated values of $\mathcal{L}_{\text{dSph},l}$, or equivalently of λ from Eq. (5.11) as was done in
 949 this work, versus $\langle\sigma v\rangle$. $\mathcal{L}_{\text{dSph},l}$ is computed for a fixed value of J_l and profiled with respect to all
 950 instrumental nuisance parameters ν_l , these nuisance parameters are discussed in more detail below.
 951 These values are produced by each detector independently and therefore there is no need to share
 952 sensitive low-level information used to produce them, such as event lists. Figure 5.4 illustrates the
 953 multi-instrument combination technique used in this study with a comparison of the upper limit

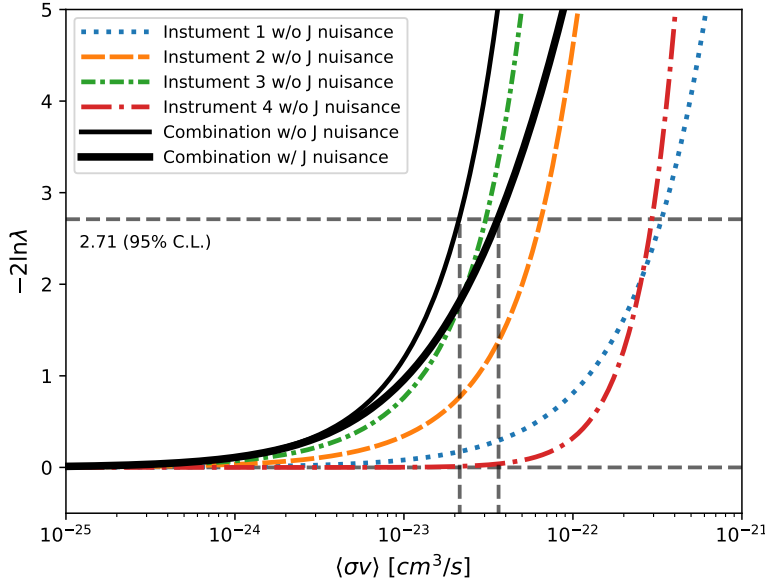


Figure 5.4 Illustration of the combination technique showing a comparison between $-2 \ln \lambda$ provided by four instruments (colored lines) from the observation of the same dSph without any J nuisance and their sum, *i.e.* the resulting combined likelihood (thin black line). According to the test statistics of Equation (5.7), the intersection of the likelihood profiles with the line $-2 \ln \lambda = 2.71$ indicates the 95% C.L. upper limit on $\langle\sigma v\rangle$. The combined likelihood (thin black line) shows a smaller value of upper limit on $\langle\sigma v\rangle$ than those derived by individual instruments. We also show how the uncertainties on the J factor effects the combined likelihood and degrade the upper limit on $\langle\sigma v\rangle$ (thick black line). All likelihood profiles are normalized so that the global minimum $\widehat{\langle\sigma v\rangle}$ is 0. We note that each profile depends on the observational conditions in which a target object was observed. The sensitivity of a given instrument can be degraded and the upper limits less constraining if the observations are performed in non-optimal conditions such as a high zenith angle or a short exposure time.

954 on $\langle\sigma v\rangle$ obtained from the combination of the observations of four experiments towards one dSph
 955 versus the upper limit from individual instruments. It also shows graphically the effect of the
 956 J -factor uncertainty on the combined observations.

957 The *partial* joint likelihood function for gamma-ray observations of each dSph ($\mathcal{L}_{\text{dSph},l}$) is
 958 written as the product of the likelihood terms describing the $N_{\text{exp},l}$ observations performed with
 959 any of our observatories:

$$\mathcal{L}_{\text{dSph},l} (\langle\sigma v\rangle; J_l, \nu_l | \mathcal{D}_l) = \prod_{k=1}^{N_{\text{exp},l}} \mathcal{L}_{lk} (\langle\sigma v\rangle; J_l, \nu_{lk} | \mathcal{D}_{lk}), \quad (5.16)$$

960 where each \mathcal{L}_{lk} term refers to an observation of the l -th dSph with associated k -th instrument

961 responses. $N_{\text{exp},l}$ varies from dSph to dSph and can be inferred from Table 5.2.

962 Each collaboration separately analyzes their data for \mathcal{D}_{lk} corresponding to dSph l and gamma-
963 ray detector k , using as many common assumptions as possible in the analysis. HAWC's treatment
964 was described earlier in Section 5.4.1 whereas the specifics of the remaining experiments is left to
965 the publication. We compute the values for the likelihood functions \mathcal{L}_{lk} (see Eq. (5.16)) for a fixed
966 value of J_l and profile over the rest of the nuisance parameters ν_{lk} . Then, values of λ from Eq. (5.11)
967 are computed as a function of $\langle\sigma v\rangle$, and shared using a common format. Results are computed for
968 seven annihilation channels, W^+W^- , ZZ , $b\bar{b}$, $t\bar{t}$, e^+e^- , $\mu^+\mu^-$, and $\tau^+\tau^-$ over 62 m_χ values between
969 5 GeV and 100 TeV provided in [44]. The $\langle\sigma v\rangle$ range is defined between 10^{-28} and $10^{-18}\text{cm}^3 \cdot \text{s}^{-1}$,
970 with 1001 logarithmically spaced values. The likelihood combination, i.e. Equation (5.12), and
971 profile over the J -factor to compute the profile likelihood ratio λ , Equation (5.11), are carried out
972 with two different public analysis software packages, namely `gLike` [52] and `LklCom` [53], that
973 provide the same results [54].

974 As mentioned previously, each experiment computes the \mathcal{L}_{lk} from Equation (5.11) differently.
975 The remainder of this section highlights the differences in this calculation across the experiments.
976 Four experiments, namely *Fermi*-LAT, H.E.S.S., HAWC and MAGIC, use a binned likelihood to
977 compute the \mathcal{L}_{lk} . For these experiments, for each observation \mathcal{D}_{lk} of a given dSph l carried out
978 using a given gamma-ray detector k , the binned likelihood function is:

$$\mathcal{L}_{lk}(\langle\sigma v\rangle; J_l, \nu_{lk} | \mathcal{D}_{lk}) = \prod_{i=1}^{N_E} \prod_{j=1}^{N_P} \left[\mathcal{P}(s_{lk,ij}(\langle\sigma v\rangle, J_l, \nu_{lk}) + b_{lk,ij}(\nu_{lk}) | N_{lk,ij}) \right] \times \mathcal{L}_{lk,\nu}(\nu_{lk} | \mathcal{D}_{\nu_{lk}}) \quad (5.17)$$

979 where N_E and N_P are the number of considered bins in reconstructed energy and arrival direction,
980 respectively; \mathcal{P} represents a Poisson PDF for the number of gamma-ray candidate events $N_{lk,ij}$
981 observed in the i -th bin in energy and j -th bin in arrival direction, when the expected number is
982 the sum of the expected mean number of signal events s_{ij} (produced by DM annihilation) and of
983 background events b_{ij} ; $\mathcal{L}_{lk,\nu}$ is the likelihood term for the extra ν_{lk} nuisance parameters that vary
984 from one instrument k to another. The expected counts for signal events s_{ij} for a given dSph l and

985 detector k is given by:

$$s_{ij}(\langle\sigma\nu\rangle, J) = \int_{E'_{\min,i}}^{E'_{\max,i}} dE' \int_{P'_{\min,j}}^{P'_{\max,j}} d\Omega' \int_0^\infty dE \int_{\Delta\Omega_{tot}} d\Omega \int_0^{T_{\text{obs}}} dt \frac{d^2\Phi(\langle\sigma\nu\rangle, J)}{dEd\Omega} \text{IRF}(E', P' | E, P, t) \quad (5.18)$$

986 where E' and E are the reconstructed and true energies, P' and P the reconstructed and true
987 arrival directions; $E'_{\min,i}$, $P'_{\min,j}$, $E'_{\max,i}$, and $P'_{\max,j}$ are their lower and upper limits of the i -th
988 energy bin and the j -th arrival direction bin; T_{obs} is the (dead-time corrected) total observation
989 time; t is the time along the observations; $d^2\Phi/dEd\Omega$ is the DM flux in the source region (see
990 Equation (7.1)); and $\text{IRF}(E', P' | E, P, t)$ is the IRF, which can be factorized as the product of the
991 effective collection area of the detector $A_{\text{eff}}(E, P, t)$, the PDFs for the energy estimator $f_E(E' | E, t)$,
992 and arrival direction $f_P(P' | E, P, t)$ estimators. Note that for Fermi-LAT, HAWC, MAGIC, and
993 VERITAS the effect of the finite angular resolution is taken into account through the convolution
994 of $d\Phi/dEd\Omega$ with f_P in Equation (5.18), whereas in the cases of H.E.S.S. f_P is approximated by a
995 delta function. This approximation has been made in order to maintain compatibility of the result
996 with what has been previously published. The difference introduced by this approximation is $< 5\%$
997 for all considered dSphs. A more comprehensive review of the differences between the analyses of
998 different instruments can be found in [25].

999 5.5 HAWC Results

1000 13 of the 20 dSphs considered for the Glory Duck analysis are within HAWC's field of view.
1001 These dSph are analyzed for emission from DM annihilation according to the likelihood method
1002 described in Section 5.4. The 13 likelihood profiles are then stacked to synthesize a combined
1003 limit on the dark matter cross-section, $\langle\sigma\nu\rangle$. This combination is done for the 7 SM annihilation
1004 channels used in the Glory Duck analysis. Figure 5.5 shows the combined limit for all annihilation
1005 channels with HAWC only observations. We also perform 300 studies of Poisson trials on the
1006 background. These trials are used to produce HAWC sensitivities with $\pm 1\sigma$ and $\pm 2\sigma$ uncertainty
1007 bands which were shared with the other collaborators for combination. The results on fitting to
1008 HAWC's Poisson trials of the DM hypothesis is shown in Figure 5.7 for all the DM annihilation
1009 channels studied for Glory Duck.

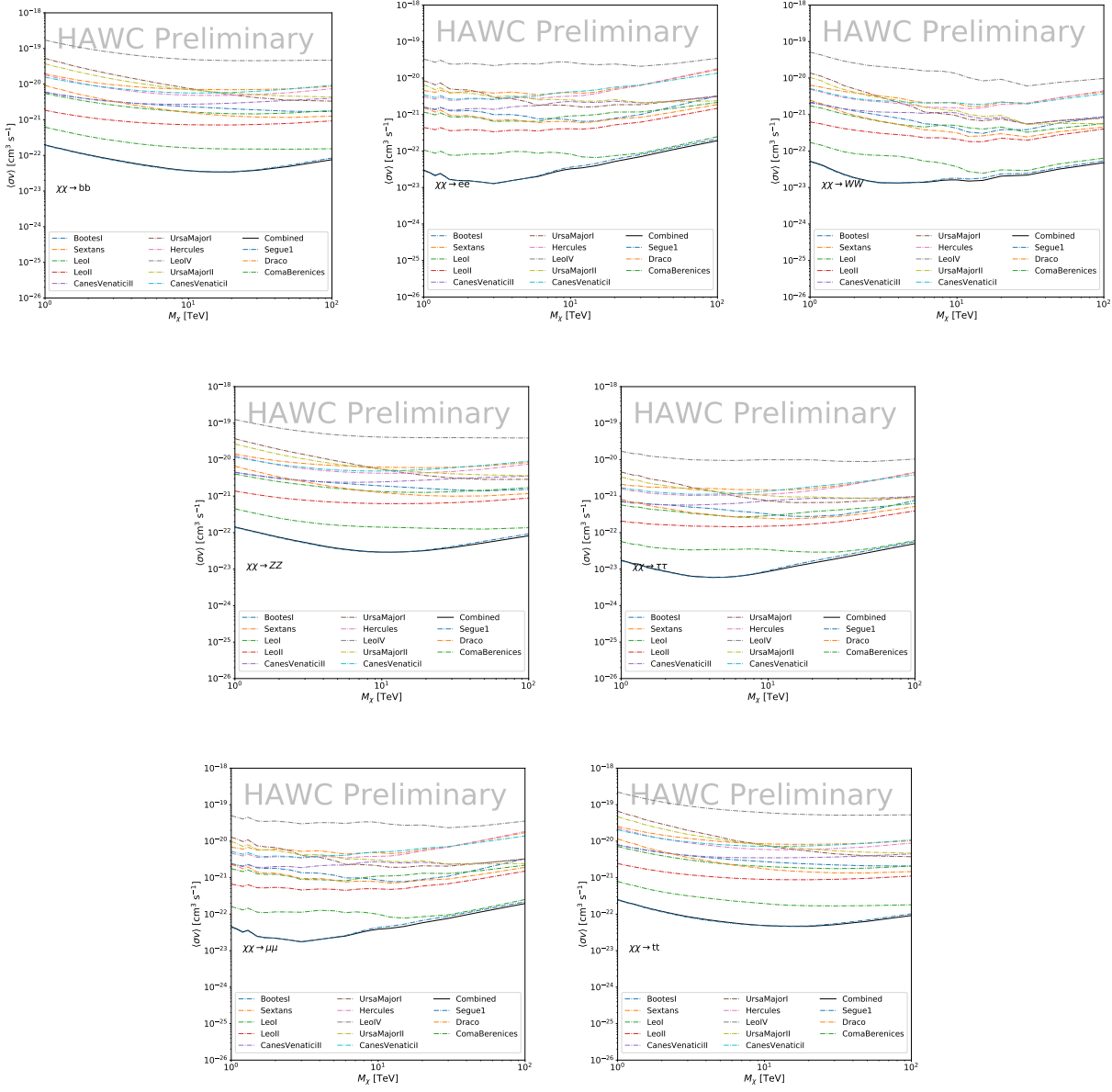


Figure 5.5

No DM was found in HAWC observations. HAWC's limits are dominated by the dSphs Segue1 and Coma Berenices. The remaining 11 dSphs do not contribute significantly to the limit because they are at high zenith and/or have much smaller J factors. Even though some remaining dSphs have large J factors, they are towards the edge of HAWC's field of view where HAWC analysis is less sensitive.

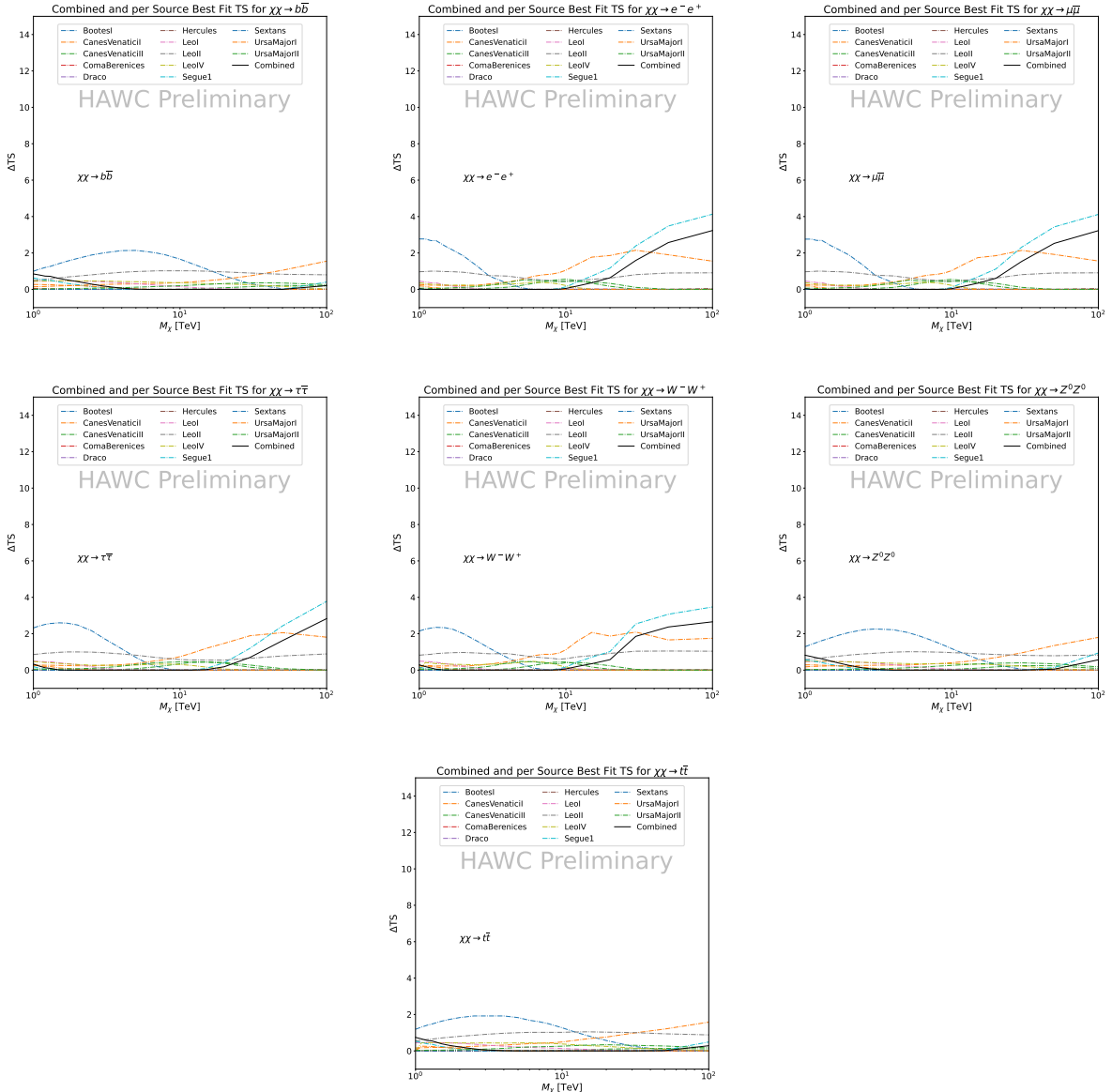


Figure 5.6 HAWC TS values for best fit $\langle\sigma v\rangle$ versus m_χ for seven SM annihilation channels with J factors from \mathcal{GS} . The solid black line shows the combined best fit TS values. The colored, dashed lines are the TS values for each of the 13 sources HAWC studied.

5.6 Glory Duck Combined Results

The crux of this analysis is that HAWC's results are combined with 4 other gamma-ray observa-

tories: Fermi-LAT, H.E.S.S., MAGIC, and VERITAS. No significant DM emission was observed by any of the five instruments. We present the upper limits on $\langle\sigma v\rangle$ assuming seven independent DM self annihilation channels, namely W^+W^- , Z^+Z^- , $b\bar{b}$, $t\bar{t}$, e^+e^- , $\mu^+\mu^-$, and $\tau^+\tau^-$. The 68%

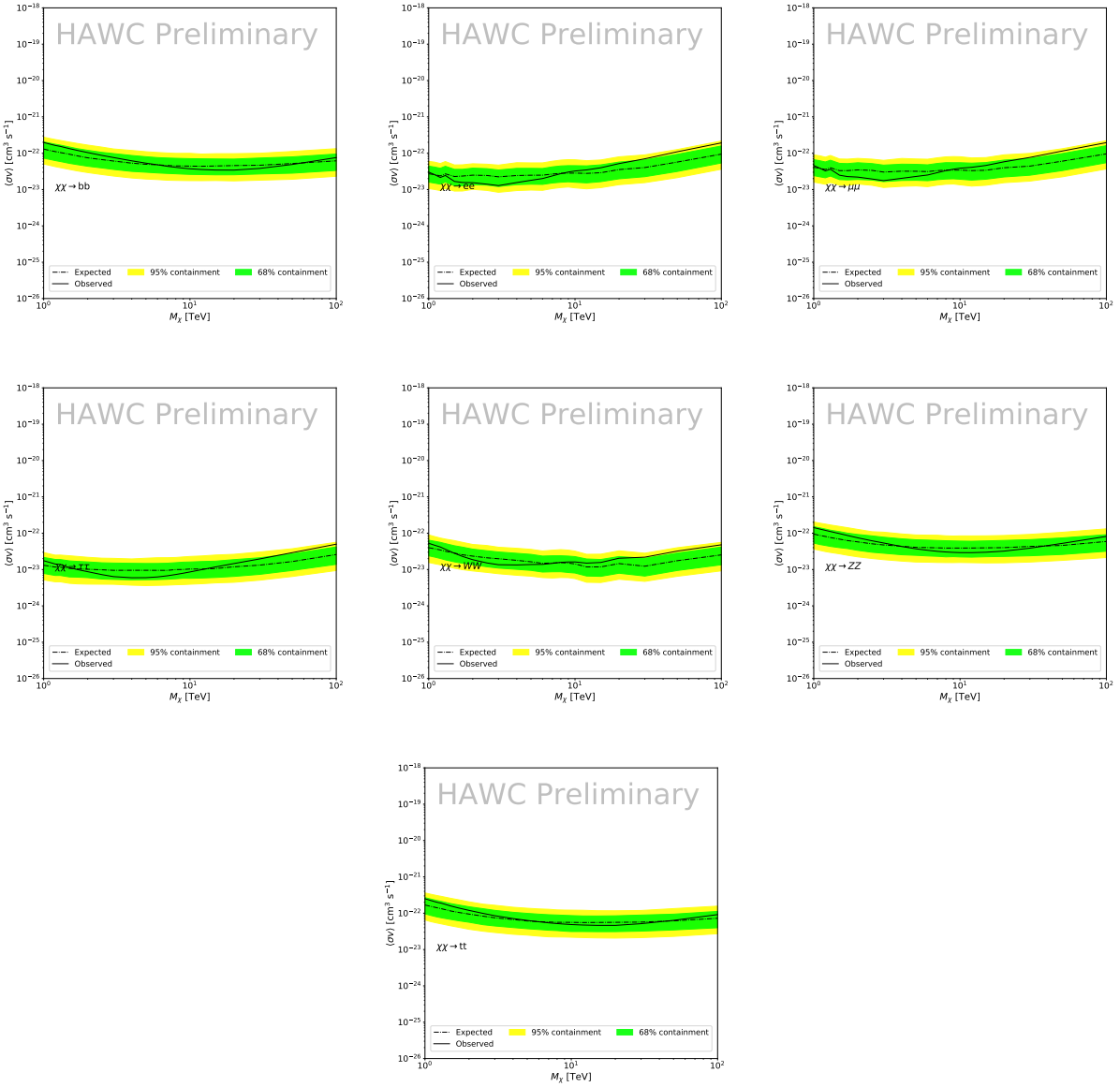


Figure 5.7 HAWC Brazil bands at 95% confidence level on $\langle\sigma v\rangle$ versus DM mass for seven annihilation channels with J -factors from \mathcal{GS} [55]. The solid line represents the combined limit from 13 dSphs. The dashed line is the expected limit. The green band is the 68% containment. The yellow band is the 95% containment.

and 95% containment bands are produced from 300 Poisson realizations of the null hypothesis corresponding to each of the combined datasets. These 300 realizations are combined identically to dSph observations. The containment bands and the median are extracted from the distribution of resulting limits on the null hypothesis. These 300 realizations are obtained either by fast simulations of the OFF observations, for H.E.S.S., MAGIC, VERITAS, and HAWC, or taken from real

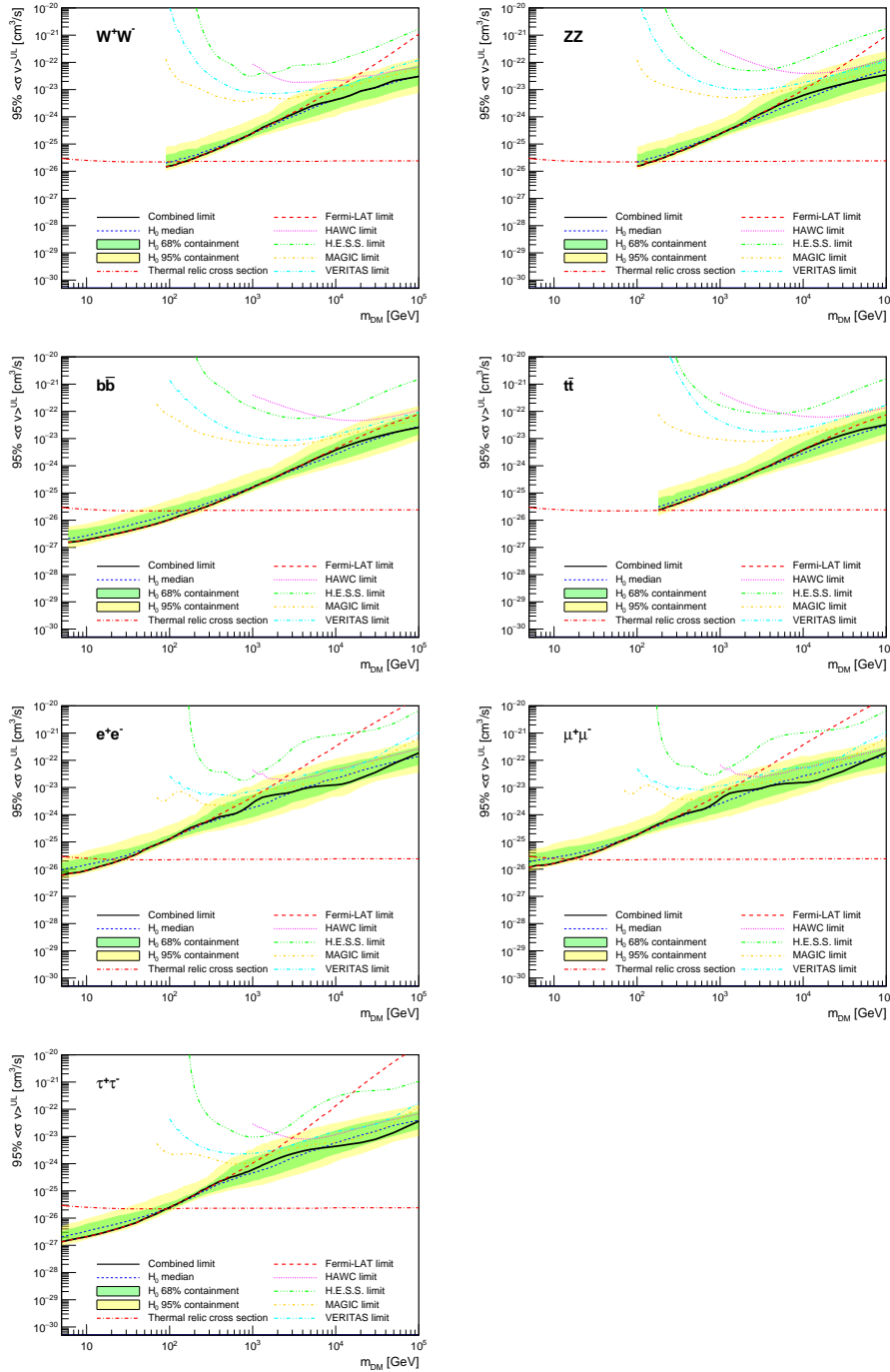


Figure 5.8 Upper limits at 95% confidence level on $\langle\sigma v\rangle$ in function of the DM mass for eight annihilation channels, using the set of J factors from Ref. [55] (\mathcal{GS} set in Table 5.1). The black solid line represents the observed combined limit, the black dashed line is the median of the null hypothesis corresponding to the expected limit, while the green and yellow bands show the 68% and 95% containment bands. Combined upper limits for each individual detector are also indicated as solid, colored lines. The value of the thermal relic cross-section in function of the DM mass is given as the red dotted-dashed line [56].

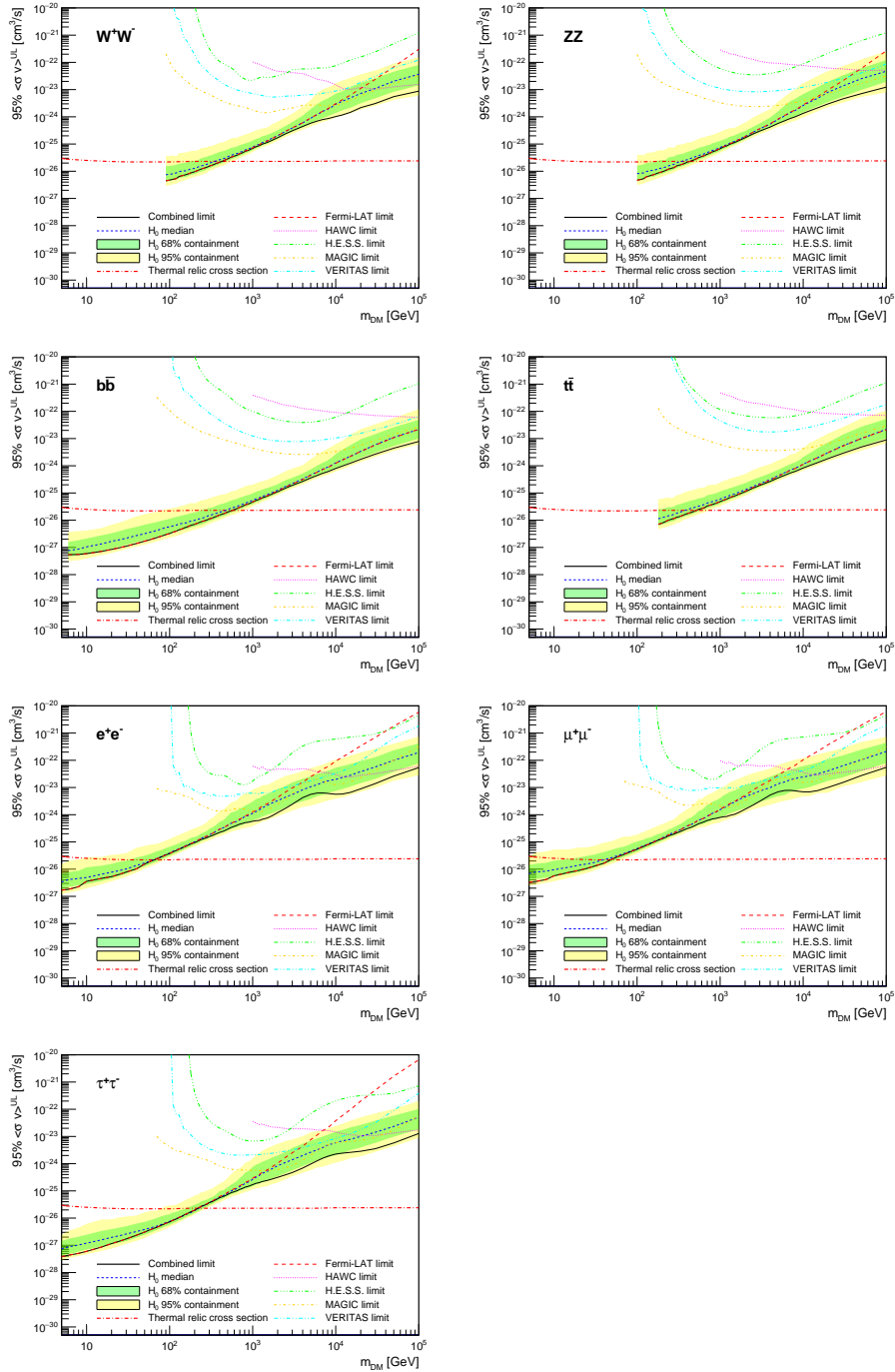


Figure 5.9 Same as Fig. 5.8, using the set of J factors from Ref. [49, 57] (\mathcal{B} set in Table 5.1).

1025 observations of empty fields of view in the case of Fermi-LAT [50, 58, 59].

1026 The obtained limits are shown in Figure 5.8 for the \mathcal{GS} set of J -factors [55] and in Figure 5.9
1027 for the \mathcal{B} set of J -factors [49, 57]. The combined limits are presented with their 68% and 95%
1028 containment bands, and are expected to be close to the median limit when no signal is present.

1029 We observe agreement with the null hypothesis for all channels, within 2σ standard deviations,
1030 between the observed limits and the expectations given by the median limits. Limits obtained from
1031 each detector are also indicated in the figures, where limits for all dSphs observed by the specific
1032 instrument have been combined.

1033 Below ~ 300 GeV, the *Fermi*-LAT dominates the DM limits for all annihilation channels. From
1034 ~ 300 GeV to ~ 2 TeV, *Fermi*-LAT continues to dominate for the hadronic and bosonic DM channels,
1035 yet the IACTs (H.E.S.S., MAGIC, and VERITAS) and *Fermi*-LAT all contribute to the limit for
1036 leptonic DM channels. For DM masses between ~ 2 TeV to ~ 10 TeV, the IACTs dominate leptonic
1037 DM annihilation channels, whereas both the *Fermi*-LAT and the IACTs dominate bosonic and
1038 hadronic DM annihilation channels. From ~ 10 TeV to ~ 100 TeV, both the IACTs and HAWC
1039 contribute significantly to the leptonic DM limit. For hadronic and bosonic DM, the IACTs and
1040 *Fermi*-LAT both contribute strongly.

1041 We notice that the limits computed using the \mathcal{B} set of J -factor are always better compared to the
1042 ones calculated with the \mathcal{GS} set. For the W^+W^- , Z^+Z^- , $b\bar{b}$, and $t\bar{t}$ channels, the ratio between the
1043 limits computed with the two sets of J -factor is varying between a factor of ~ 3 and ~ 5 depending
1044 on the energy, with the largest ratio around 10 TeV. For the channels e^+e^- , $\mu^+\mu^-$, and $\tau^+\tau^-$, the
1045 ratio lies between ~ 2 to ~ 6 , being maximum around 1 TeV. Examining Figure 5.16 and Figure 5.17
1046 in Section 5.8, these differences are explained by the fact that the \mathcal{B} set provides higher J -factors
1047 for the majority of the studied dSphs, with the notable exception of Segue I. The variation on the
1048 ratio of the limits for the two sets is due to different dSph dominating the limits depending on the
1049 energy. One set, \mathcal{B} , pushes the range of which thermal cross-section which can be excluded to
1050 higher mass. This comparison demonstrates the magnitude of systematic uncertainties associated
1051 with the choice of the J -factor calculation. The \mathcal{GS} and \mathcal{B} sets present a difference in the limits for
1052 all channels of about This difference is explained, see Figure 5.16 and Figure 5.17, by the fact that
1053 the \mathcal{B} set provides higher J -factors for all dSph except for Segue I.

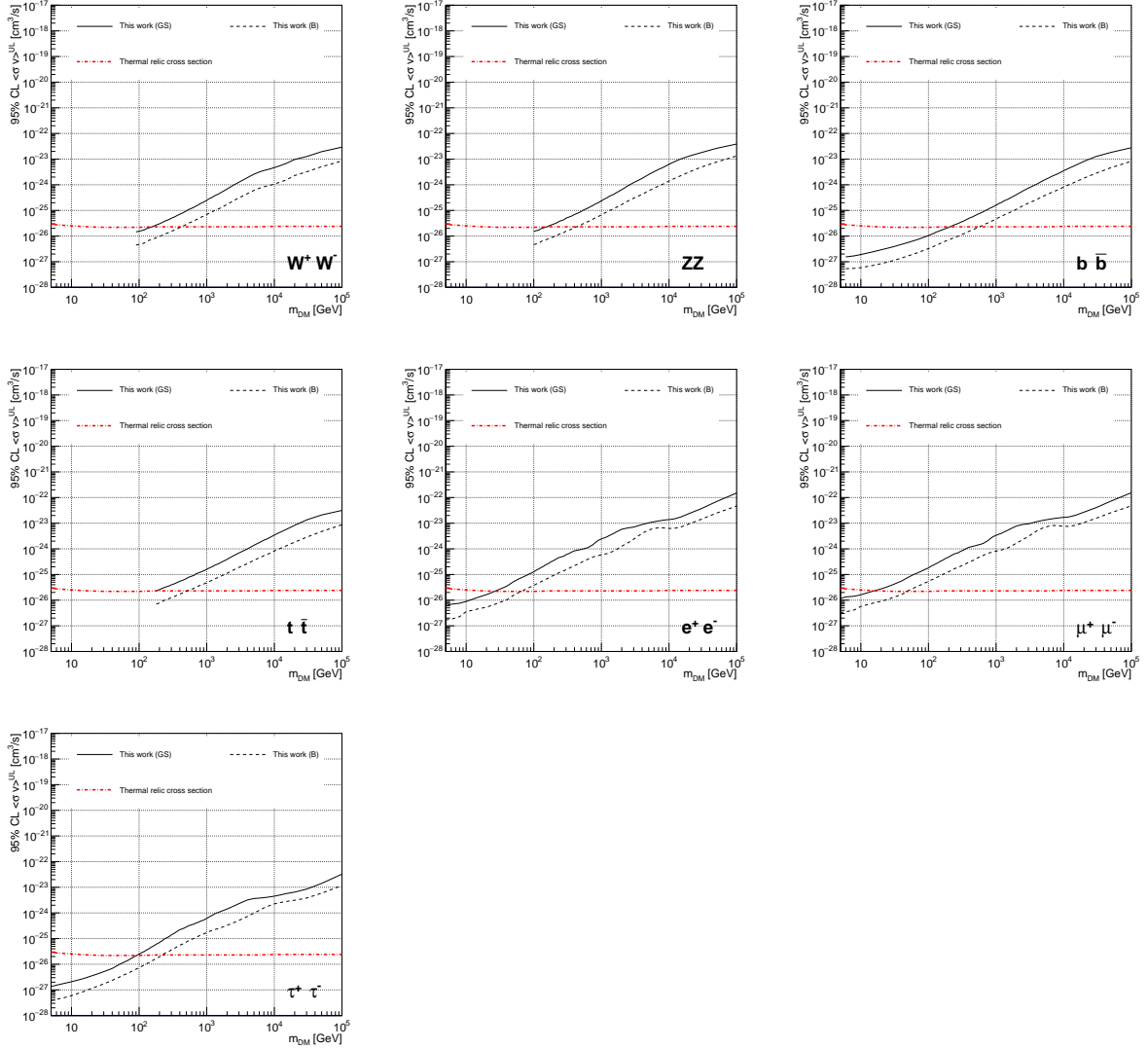


Figure 5.10 Comparisons of the combined limits at 95% confidence level for each of the eight annihilation channels when using the J factors from Ref. [55] (\mathcal{GS} set in Table 5.1), plain lines, and the J factor from Ref. [49, 57] (\mathcal{B} set in Table 5.1), dashed lines. The cross-section given by the thermal relic is also indicated [56].

1054 5.7 HAWC Systematics

1055 5.7.1 Inverse Compton Scattering

1056 The DM-DM annihilation channels produce many high energy electrons regardless of the
 1057 primary annihilation channel. These high energy electrons can produce high energy gamma-rays
 1058 through Inverse Compton Scattering (ICS). If this effect is strong, it would change the morphology
 1059 of the source and increase the total expected gamma-ray counts from any source. The PPPC [44]

1060 provides tools in Mathematica for calculating the impact of ICS for an arbitrary location in the
1061 sky for a specified annihilation channel. We calculated the change in gamma-ray counts for DM
1062 annihilation to primary $e\bar{e}$ for RA and Dec corresponding to Segue1 and Coma Berenices. These
1063 dSphs were chosen because they are the strongest contributors to the limit. $e\bar{e}$ was selected because
1064 it would have the largest number of high energy electrons. The effect was found to be on the order
1065 of 10^{-7} on the gamma-ray spectrum. As a result, this systematic is not considered in our analysis.

1066 **5.7.2 Point Source Versus Extended Source Limits**

1067 The previous DM search toward dSph approximated the dSphs as point sources [46]. In
1068 this analysis, the dSphs are implemented as extended with J-factor distributions following those
1069 produced by [55]. The resolution of the cited map is much finer than HAWC’s angular resolution.
1070 The vast majority of the J-factor distribution is represented on the central HAWC pixel of the dSph
1071 spatial map. However, the neighboring 8 pixels are not negligible and contribute to our limit.

1072 Figure 5.11 shows a substantial improvement to the limit for Segue1. Fig. 5.12 however showed
1073 identical limits. These disparities are best explained by the relative difference in their J-Factors.
1074 Both dSphs pass almost overhead the HAWC detector, however Segue1 has the larger J-Factor
1075 between the two. Adjacent pixels to the central pixel will therefore contribute to the limits. This is
1076 the case for other dSph that are closer to the zenith of the HAWC detector.

1077 Comparison plots for all sources and the combined limit can be found in the sandbox for the
1078 Glory Duck project.

1079 **5.7.3 Impact of Pointing Systematic**

1080 During the analysis it was discovered that directional reconstruction of gamma-rays had a
1081 systematic bias at large zenith angles. Slides describing this systematic can be found [here](#). Shown
1082 on the presentation is dependence on the pointing systematic on declination. New spatial profiles
1083 were generated for every dSph and limits were computed for the adjusted declination.

1084 Section 5.7.3 demonstrates the impact of this systematic for all DM annihilation channels
1085 studied by HAWC. The impact is a tiny improvement, yet mostly identical, to the combined limits.

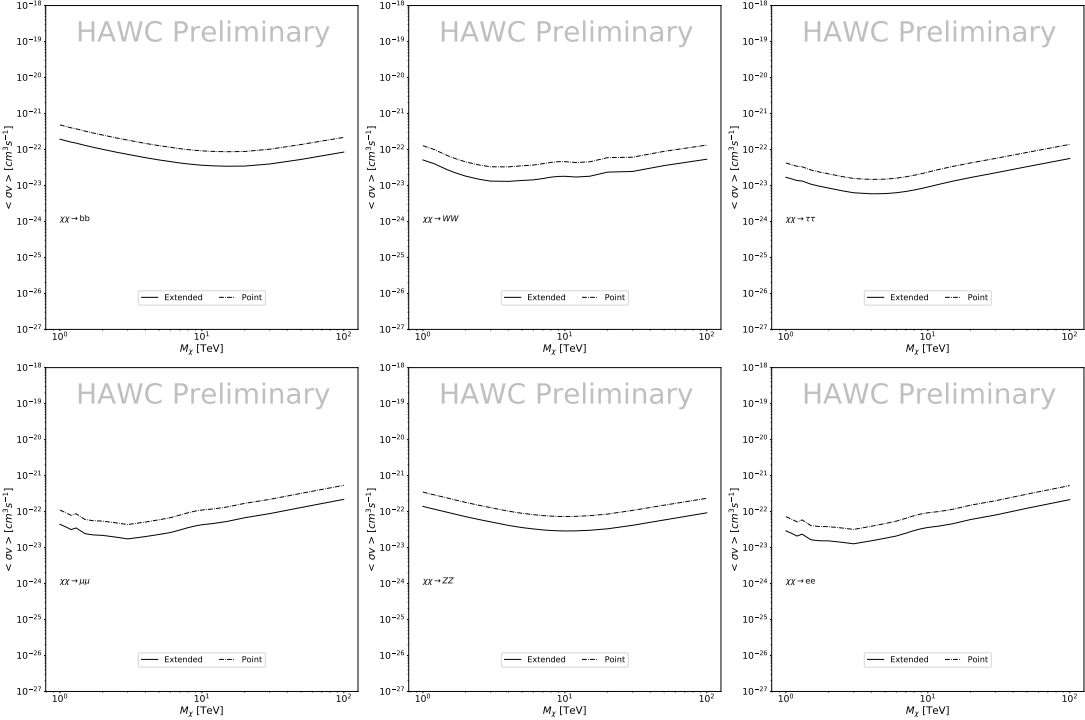


Figure 5.11 Comparisons of the combined limits at 95% confidence level for a point source analysis and extended source using [55] \mathcal{GS} J-factor distributions and PPPC [44] annihilation spectra. Shown are the limits for Segue1 which will have the most significant impact on the combined limit. 6 of the 7 DM annihilation channels are shown. Solid lines are extended source studies. Dashed lines are point source studies. Overall, the extended source analysis improves the limit by a factor of 2.

1086 5.8 J-factor distributions

1087 5.8.1 Numerical integration of \mathcal{GS} maps

1088 It was discovered well after the HAWC analysis was completed that the published tables from
 1089 \mathcal{GS} [45] quoted median J -factors were computed in a non-trivial manner. The assumption myself
 1090 and collaborators had been that the published tables represented the J -factor as a function of θ for
 1091 the best global fit model on a per-source basis. However, this is not the case. Instead, what is
 1092 published are the best fit model for each dwarf that only considers stars up to the angular separation
 1093 θ . Therefore, the model is changing for each value of θ for each dwarf. Yet, the introduced features
 1094 from unique models at each θ are much smaller than the angular resolution of HAWC. It is not
 1095 expected for these effects to impact the limits and TS greatly as a result.

1096 Median J -factor model profiles were provided by the authors. New maps were generated

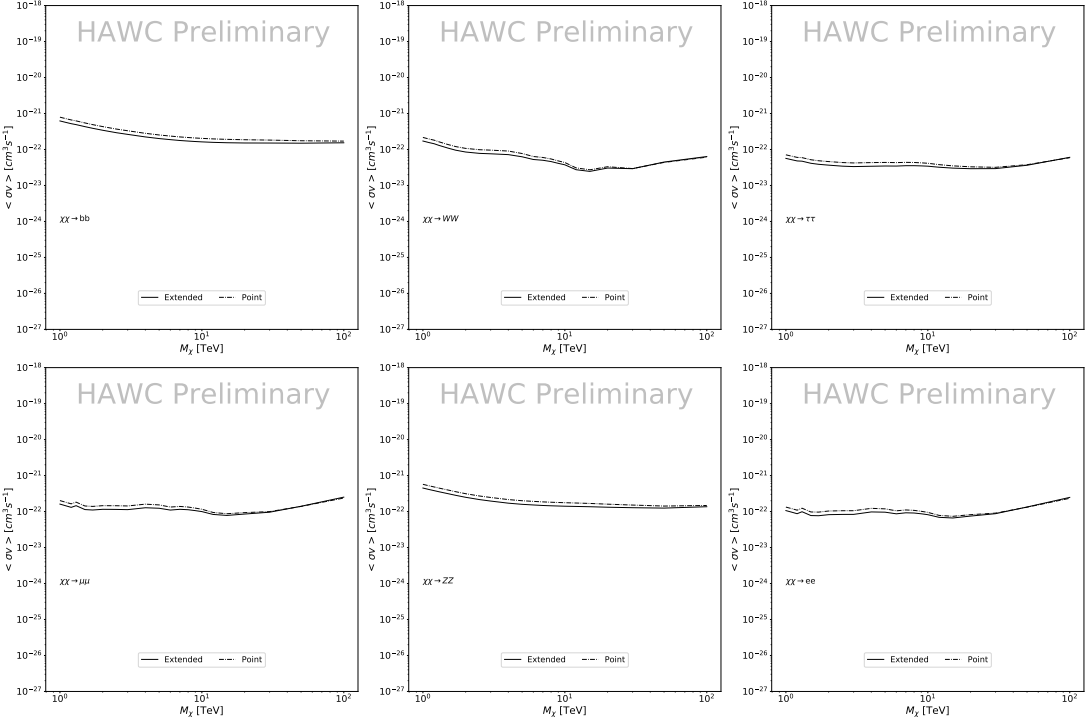


Figure 5.12 Same as Fig. 5.11 on Coma Berenices. This dSph also contributes significantly to the limit. The limits are identical in this case.

and analyzed for Segue1 and Coma Berenices. Figure 5.14 shows the differential between maps generated with the method from Section 5.8.1 and from the authors of [45]. These maps were reanalyzed for all SM DM annihilation channels. Upper limits for these channels are shown in Figure 5.15

From Figure 5.15, we can see that the impact of these model difference was no substantial. The observed impact was a fractional effect which is much smaller than the impact from selecting another DM spatial distribution model as was shown in Figure 5.10.

5.8.2 \mathcal{GS} Versus \mathcal{B} spatial models

We show in this appendix a comparison between the J -factors computed by Geringer-Sameth *et al.* [55] (the \mathcal{GS} set) and the ones computed by Bonnivard *et al.* [49, 57] (the \mathcal{B} set). The \mathcal{GS} J -factors are computed through a Jeans analysis of the kinematic stellar data of the selected dSphs, assuming a dynamic equilibrium and a spherical symmetry for the dSphs. They adopted the generalized DM density distribution, known as Zhao-Hernquist, introduced by [47], carrying

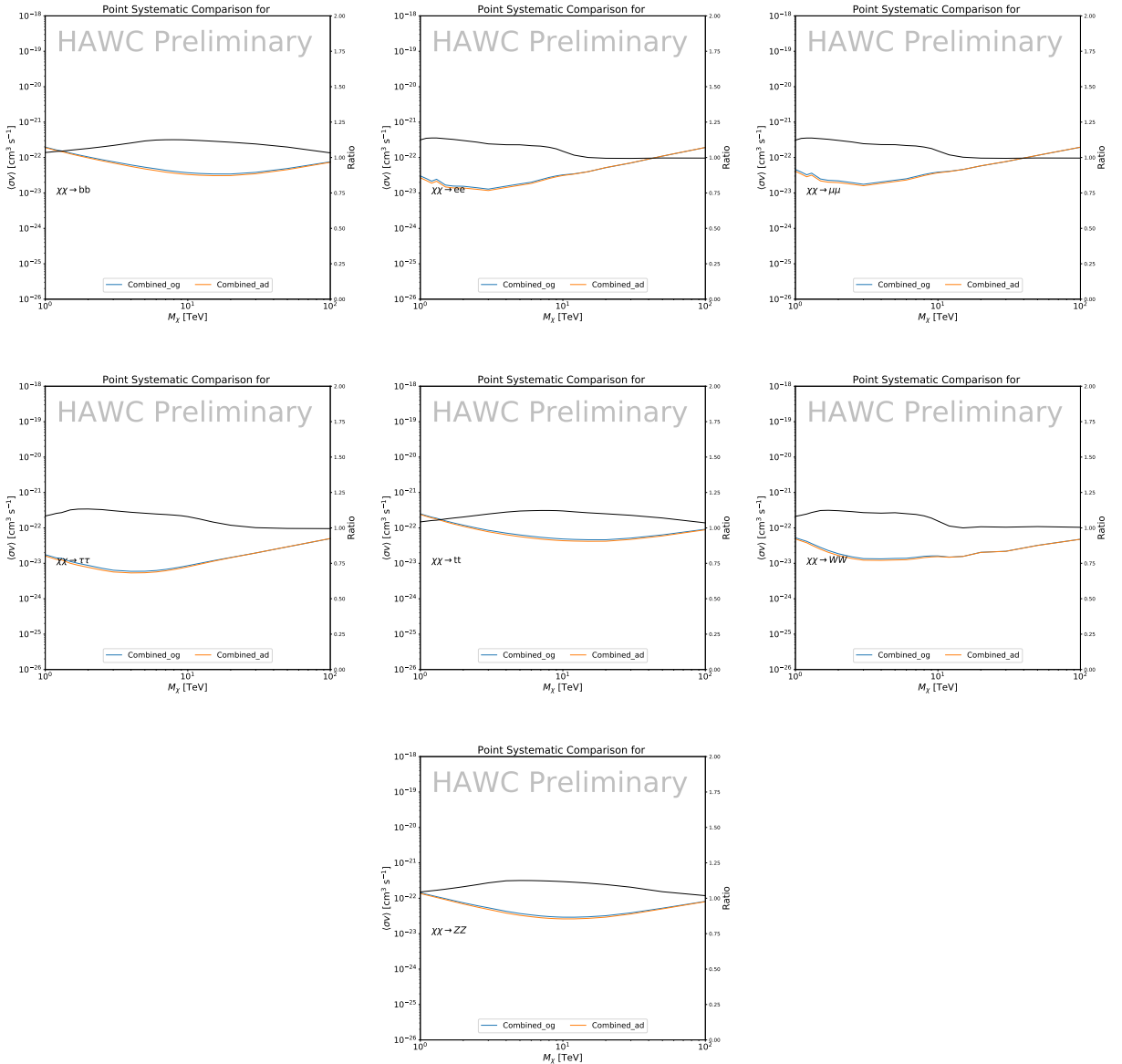


Figure 5.13 Comparison of combined limits when correcting for HAWC's pointing systematic. All DM annihilation channels are shown. The solid black line is the ratio between published limit to the declination corrected limit. The blue solid line or "Combined_og" represented the limits computed for Glory Duck. The solid orange line or "Combined_ad" represented the limits computed after correcting for the pointing systematic.

1110 three additional index parameters to describe the inner and outer slopes, and the break of the
 1111 density profile. Such a profile parametrization allows the reduction of the theoretical bias from
 1112 the choice of a specific radial dependency on the kinematic data. In other words, the increase of
 1113 free parameters with the use of the Zhao-Hernquist profile allows a better description of the mass

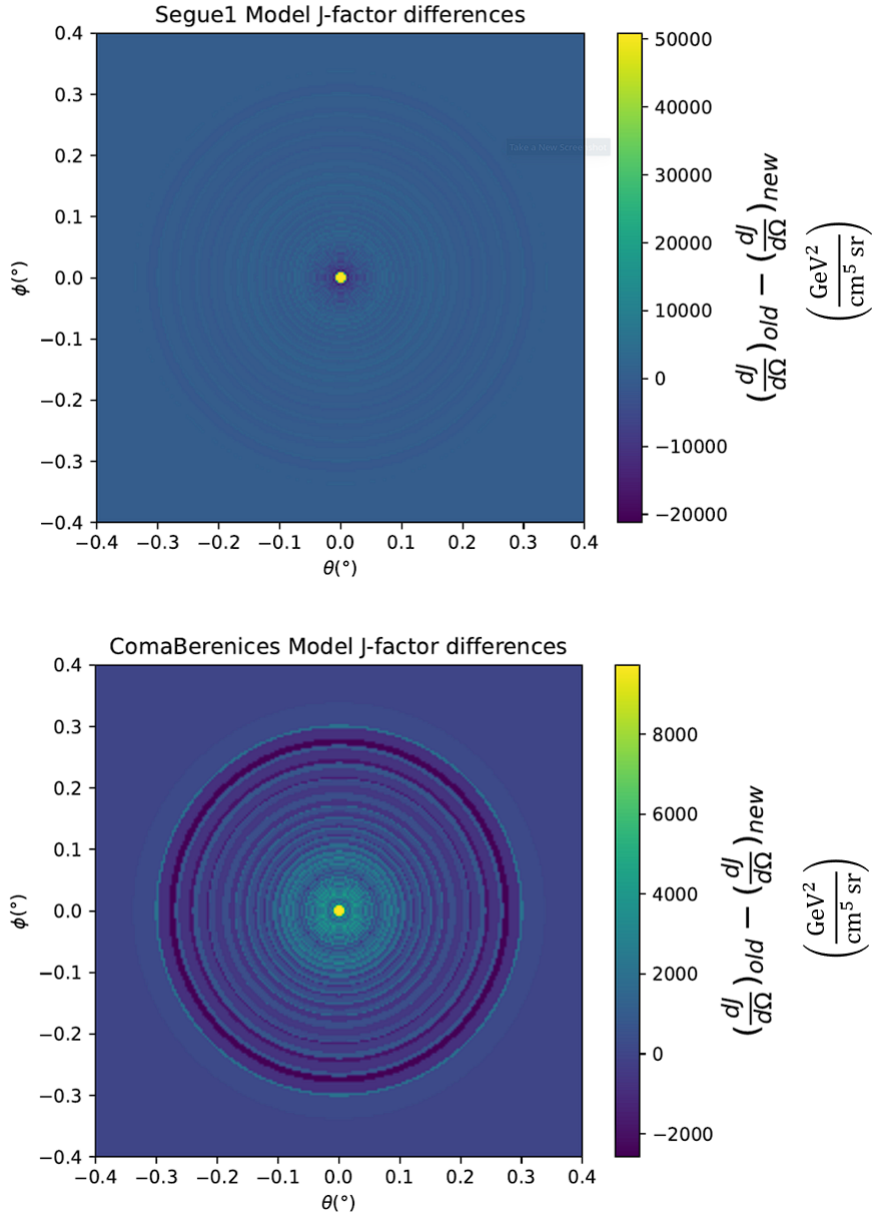


Figure 5.14 Differential map of dJ/Ω from model built in Section 5.8.1 and profiles provided directly from authors. (Top) Differential from Segue1. (bottom) Differential from Coma Berenices. Note that their scales are not the same. Segue1 shows the deepest discrepancies which is congruent with its large uncertainties. Both models show anuli where unique models become apparent.

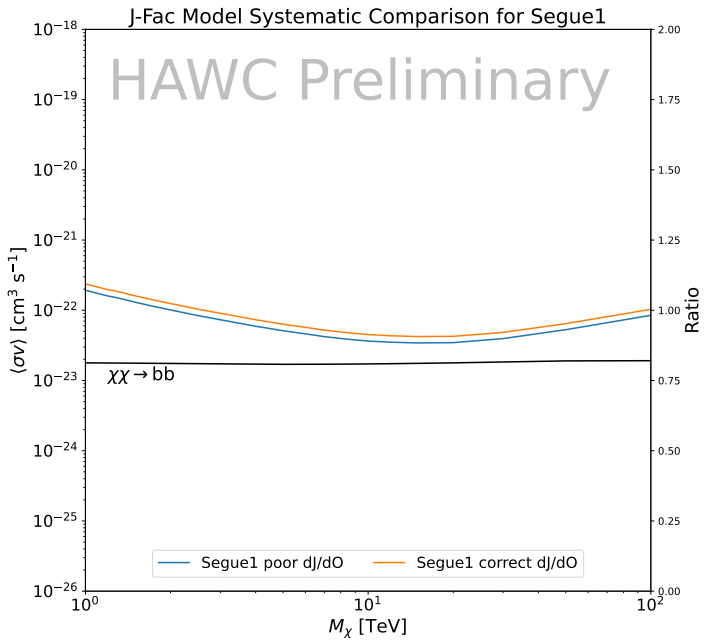
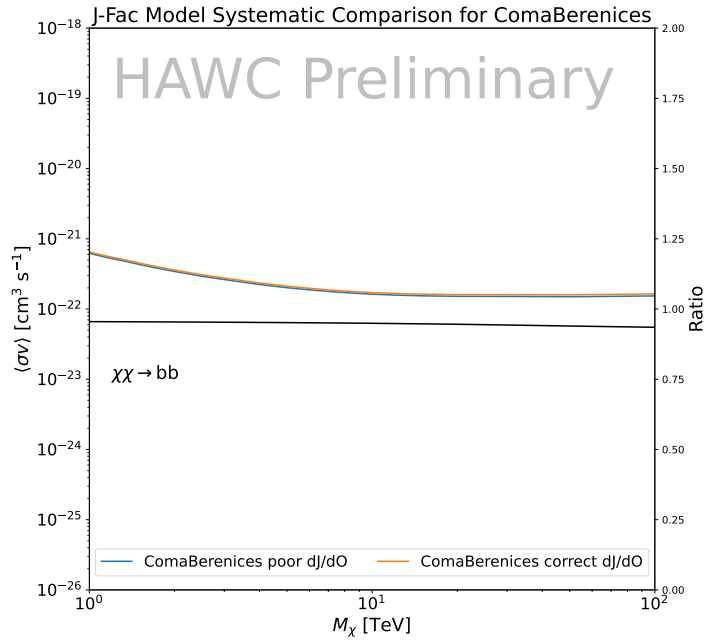


Figure 5.15 HAWC limits for Coma Berenices (top) and Segue1 (bottom) for two different map sets. Blue lines are limits calculated on maps with poor model representation. Orange lines are limits calculated on spatial profiles provided by the authors of [45]. Black line is the ratio of the poor spatial model limits to the corrected spatial models. The left y-axis measures $\langle \sigma v \rangle$ for the blue and orange lines. The right y-axis measures the ratio and is unitless.

1114 density distribution of dark matter.

1115 In addition, a constant velocity anisotropy profile and a Plummer light profile [60] for the stellar
1116 distribution were assumed. The velocity anisotropy profile depends on the radial and tangential
1117 velocity dispersion. However, its determination remains challenging since only the line-of-sight
1118 velocity dispersion can be derived from velocity measurements. Therefore, the parametrization of
1119 the anisotropy profile is obtained from simulated halos (see [61] for more details). They provide the
1120 values of the J -factors of regions extending to various angular radius up to the outermost member
1121 star.

1122 The \mathcal{B} J -factors were computed through a Jeans analysis taking into account the systematic
1123 uncertainties induced by the DM profile parametrization, the radial velocity anisotropy profile, and
1124 the triaxiality of the halo of the dwarf galaxies. They performed a more complete study of the dSph
1125 kinematics and dynamics than \mathcal{GS} for the determination of the J -factor. Conservative values of the
1126 J -factors where obtained using an Einasto DM density profile [62], a realistic anisotropy profile
1127 known as the Baes & Van Hese profile [63] which takes into account that the inner regions can be
1128 significantly non-isotropic, and a Zhao-Hernquist light profile [47].

1129 For both sets, J -factor values are provided for all dSphs as a function of the radius of the
1130 integration region [55, 49, 57]. Table 5.1 shows the heliocentric distance and Galactic coordinates
1131 of the twenty dSphs, together with the two sets of J -factor values integrated up to the outermost
1132 observed star for \mathcal{GS} and the tidal radius for \mathcal{B} . Both J -factor sets were derived through a Jeans
1133 analysis based on the same kinematic data, except for Draco where the measurements of [64] have
1134 been adopted in the computation of the \mathcal{B} value. The computations for producing the \mathcal{GS} and \mathcal{B}
1135 samples differ in the choice of the DM density, velocity anisotropy, and light profiles, for which the
1136 set \mathcal{B} takes into account some sources of systematic uncertainties.

1137 Figure 5.16 and Figure 5.17 show the comparisons for the J -factor versus the angular radius
1138 for each of the 20 dSphs used in this study. The uncertainties provided by the authors are also
1139 indicated in the figures. For the \mathcal{GS} set, the computation stops at the angular radius corresponding
1140 to the outermost observed star, while for the \mathcal{B} set, the computation stops at the angular radius

1141 corresponding to the tidal radius.

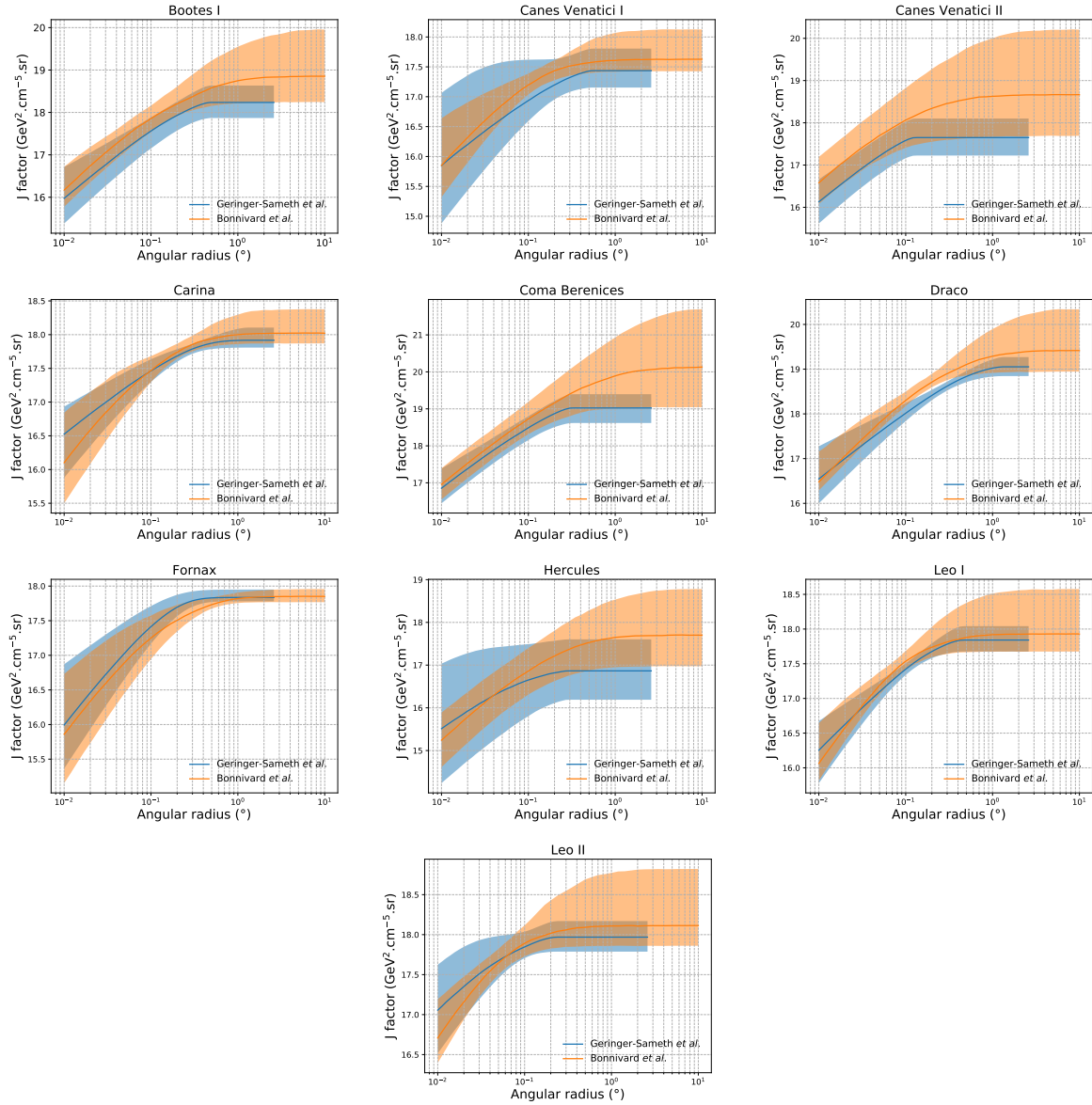


Figure 5.16 Comparisons between the J -factors versus the angular radius for the computation of J factors from Ref. [55] (\mathcal{GS} set in Table 5.1) in blue and for the computation from Ref. [49, 57] (\mathcal{B} set in Tab. 5.1). The solid lines represent the central value of the J -factors while the shaded regions correspond to the 1σ standard deviation.

1142 5.9 Discussion and Conclusions

1143 In this multi-instrument analysis, we have used observations of 20 dSphs from the gamma-ray
 1144 telescopes Fermi-LAT, H.E.S.S., MAGIC, VERITAS, and HAWC to perform a collective DM
 1145 search annihilation signals. The data were combined across sources and detectors to significantly

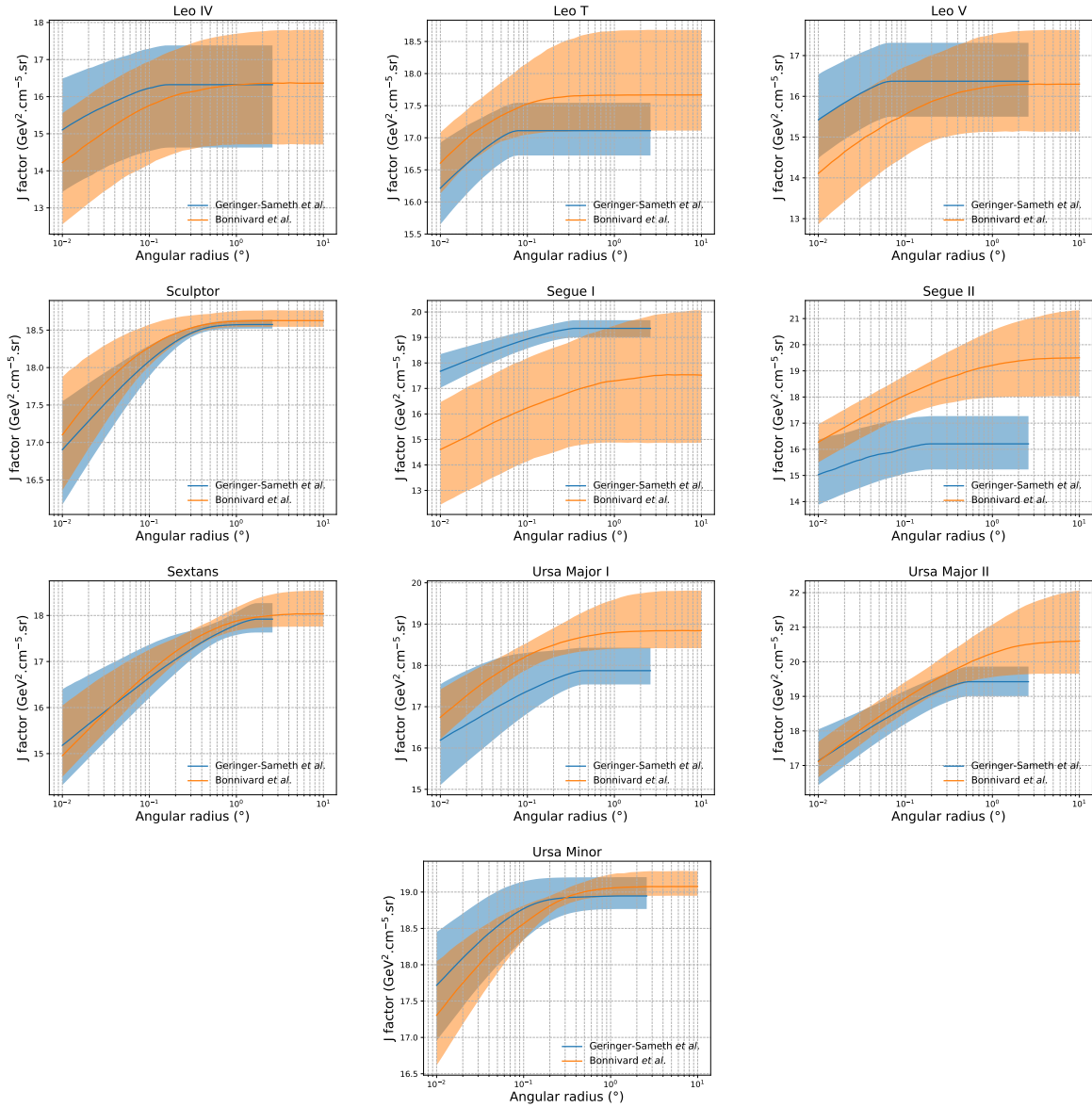


Figure 5.17 Comparisons between the J -factors versus the angular radius for the computation of J factors from Ref. [55] (\mathcal{GS} set in Tab. 5.1) in blue and for the computation from Ref. [49, 57] (\mathcal{B} set in Tab. 5.1) in orange. The solid lines represent the central value of the J -factors while the shaded regions correspond to the 1σ standard deviation.

increase the sensitivity of the search. We have observed no significant deviation from the null, no DM hypothesis, and so present our results in terms of upper limits on the annihilation cross-section for seven potential DM annihilation channels.

Fermi-LAT brings the most stringent constraints for continuum channels below approximately 1 TeV. The remaining detectors dominate at higher energies. Overall, for multi-TeV DM mass,

1151 the combined DM constraints from all five telescopes are 2-3 times stronger than any individual
1152 telescope for multi-TeV DM.

1153 Derived from observations of many dSphs, our results produce robust limits given the DM
1154 content of the dSphs is relatively well constrained. The obtained limits span the largest mass
1155 range of any WIMP DM search. Our combined analysis improves the sensitivity over previously
1156 published results from each detector which produces the most stringent limits on DM annihilation
1157 from dSphs. These results are based on deep exposures of the most promising known dSphs with
1158 the currently most sensitive gamma-ray instruments. Therefore, our results constitute a legacy of
1159 a generation of gamma-ray instruments on WIMP DM searches towards dSphs. Our results will
1160 remain the reference in the field until a new generation of more sensitive gamma-ray instruments
1161 begin operations, or until new dSphs with higher J -factors are discovered.

1162 This analysis serves as a proof of concept for future multi-instrument and multi-messenger
1163 combination analyses. With this collaborative effort, we have managed to sample over four orders
1164 in magnitude in gamma-ray energies with distinct observational techniques. Determining the nature
1165 of DM continues to be an elusive and difficult problem. Larger datasets with diverse measurement
1166 techniques could be essential to tackling the DM problem. A future collaboration using similar
1167 techniques as the ones described in this paper could grow even beyond gamma rays. The models we
1168 used for this study include annihilation channels with neutrinos in the final state. Advanced studies
1169 could aim to merge our results with those from neutrino observatories with large data sets. Efforts
1170 are already underway to add data from the IceCube, ANTARES, and KM3NeT observatories to
1171 these gamma-ray results.

1172 From this work, a selection of the best candidates for observations, according to the latest
1173 knowledge on stellar dynamics and modelling techniques for the derivation of the J -factors on
1174 the potential dSphs targets, is highly desirable at the time that new experiments are starting their
1175 dark matter programs using dSphs. Given the systematic uncertainty inherent to the derivation of
1176 the J -factors, an informed observational strategy would be to select both objects with the highest
1177 J -factors that could lead to DM signal detection, and objects with robust J -factor predictions, i.e.

1178 with kinematic measurements on many bright stars, which would strengthen the DM interpretation
1179 reliability of the observation outcome.

1180 This analysis combines data from multiple telescopes to produce strong constraints on astro-
1181 physical objects. From this perspective, these methods can be applied beyond just DM searches.
1182 Almost every astrophysical study can benefit from multi-telescope, multi-wavelength gamma-ray
1183 studies. We have enabled these telescopes to study the cosmos with greater precision and detail.
1184 Many astrophysical searches can benefit from multi-instrument gamma-ray studies, for which our
1185 analysis lays the foundation.

CHAPTER 6

1186 MULTITHREADING HAWC ANALYSES FOR DARK MATTER SEARCHES

1187 **6.1 Introduction**

1188 HAWC’s current software suite, plugins to 3ML and HAL [54, 42], do not fully utilize compu-
1189 tational advancements of recent decades. Said advancements include the proliferation of Graphical
1190 Processing Units (GPUs), and multithreading on multicore processors. The analysis described in
1191 chapter 5 took up to 3 months of wall time waiting for the full gambit of data analysis and simulation
1192 of background to compute. Additionally, with the updated 2D energy binning scheme, f_{hit} and
1193 Neural Network (NN), the time needed to compute expected to grow. Although excessive comput-
1194 ing time was, in part, from an intense use of a shared computing cluster, it was evident that there
1195 was room for improvement. In HAWC’s next generation dSph DM search, I decided to develop
1196 codes that would utilize the multicore processors on modern high performance computing clusters.
1197 The results of this work are featured in this chapter and brought a human timing improvement to
1198 computation that scales approximately as $1/N$ where N is the number of threads.

1199 **6.2 Dataset and Background**

1200 This section enumerates the data and background methods used for HAWC’s multithreaded
1201 study of dSphs. Section 6.2.1 and Section 6.2.2 are most useful for fellow HAWC collaborators
1202 looking to replicate a multithreaded dSph DM search.

1203 **6.2.1 Itemized HAWC files**

1204 These files are only available withing HAWC’s internal documentation and collaborators. They
1205 are not meant for public access, and are presented here so that HAWC collaborators can reproduce
1206 results accurately.

- 1207 • Detector Resolution: `refit-Pass5-Final-NN-detRes-zenith-dependent.root`
- 1208 • Data Map: `Pass5-Final-NN-maptree-ch103-ch1349-zenith-dependent.root`
- 1209 • Spectral Dictionary: `HDMspectra_dict_gamma.npy`

1210 **6.2.2 Software Tools and Development**

1211 This analysis was performed using HAL and 3ML [42, 43] in Python3. I built software
1212 in collaboration with Michael Martin and Letrell Harris to implement the *Dark Matter Spectra*
1213 *from the Electroweak to the Planck Scale* (HDM) [65] and dSphs spatial model from [66] for
1214 HAWC analysis. A NumPy dictionary of HDM, `HDMspectra_dict_gamma.npy`, was made for
1215 portability within the collaboration. These dictionaries were generated from the [git repository](#) [65].
1216 The analysis was performed using the Neural Network energy estimator for Pass 5.F. A description
1217 of this estimator was provided in chapter 3. [TODO: Define a subsection when it's written](#), and its
1218 key, relevant improvements are an improved energy estimation and improved sensitivities at higher
1219 zenith angles. All other software used for data analysis, DM profile generation, and job submission
1220 to SLURM are also kept in my sandbox in the [Dark Matter HAWC](#) project. The above repository
1221 also incorporates the model inputs used previously in Glory Duck, described in chapter 5, so Glory
1222 Duck remains compatible with modern software.

1223 **6.2.3 Data Set and Background Description**

1224 The HAWC data maps used for this analysis contain 2565 days of data between runs 2104 and
1225 7476. They were generated from pass 5.f reconstruction. The analysis is performed using the NN
1226 energy estimator with bin list:

1227 `B1C0Ea, B1C0Eb, B1C0Ec, B1C0Ed, B1C0Ee, B2C0Ea, B2C0Eb, B2C0Ec, B2C0Ed, B2C0Ee,`
1228 `B3C0Ea, B3C0Eb, B3C0Ec, B3C0Ed, B3C0Ee, B3C0Ef, B4C0Eb, B4C0Ec, B4C0Ed, B4C0Ee,`
1229 `B4C0Ef, B5C0Ec, B5C0Ed, B5C0Ee, B5C0Ef, B5C0Eg, B6C0Ed, B6C0Ee, B6C0Ef, B6C0Eg,`
1230 `B6C0Eh, B7C0Ee, B7C0Ef, B7C0Eg, B7C0Eh, B7C0Ei, B8C0Ee, B8C0Ef, B8C0Eg, B8C0Eh,`
1231 `B8C0Ei, B8C0Ej, B9C0Ef, B9C0Eg, B9C0Eh, B9C0Ei, B9C0Ej, B10C0Eg, B10C0Eh,`
1232 `B10C0Ei, B10C0Ej, B10C0Ek, B10C0El`

1233 Bin 0 was excluded as it has substantial hadronic contamination and poor angular resolution.

1234 Background considerations and source selection was identical to Section 5.2.3, and no additional
1235 arguments are provided here. Many of the HAWC systematics explored in Section 5.7 also apply

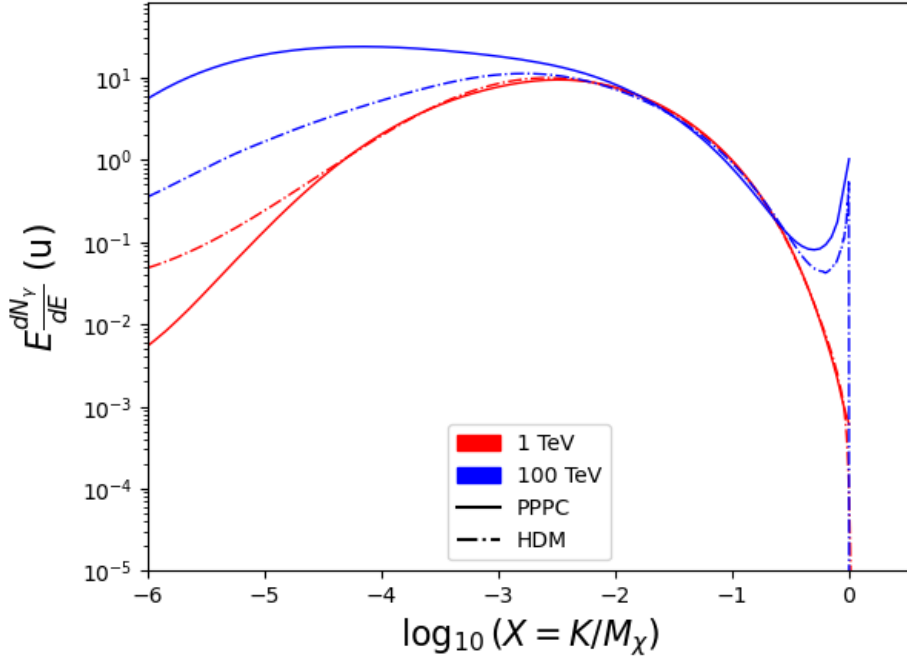


Figure 6.1 Spectral hypotheses from PPPC [44] and HDM [65] for DM annihilation: $\chi\chi \rightarrow W^-W^+$. Solid lines are spectral models with EW corrections from the PPPC. Dash-dot lines are spectral models from HDM. Red lines are models for $M_\chi = 1$ TeV. Blue lines represent models for $M_\chi = 100$ TeV.

1236 for this DM search and are not added upon here.

1237 6.3 Analysis

1238 The analysis and its systematics are almost identical to Section 5.3. Importantly, we use the
 1239 same [TODO: fix this ref](#) Equation (7.1) and Equation (5.2) for estimating the gamma-ray flux at
 1240 HAWC from our sources.

1241 6.3.1 $\frac{dN_\gamma}{dE_\gamma}$ - Particle Physics Component

1242 For these spectra, we import HDM with Electroweak (EW) corrections and additional correc-
 1243 tions for neutrinos above the EW scale [65]. The spectra are implemented as a model script in
 1244 astromodels for 3ML. A comprehensive description of EW corrections and neutrino considerations
 1245 are provided later in Sec. 8.

1246 Figure 6.1 demonstrates the impact of changes implemented in HDM on DM annihilation to W
 1247 bosons. A class in astromodels was developed to include HDM and is aptly named `HDMspectra`
 1248 within `DM_models.py`. The SM DM annihilation channels studied here are $\chi\chi \rightarrow$:

1249 e^+e^- , $\mu^+\mu^-$, $\tau^+\tau^-$, $b\bar{b}$, $t\bar{t}$, gg , W^+W^- , ZZ , $c\bar{c}$, $u\bar{u}$, $d\bar{d}$, $s\bar{s}$, $\nu_e\bar{\nu}_e$, $\nu_\mu\bar{\nu}_\mu$, $\nu_\tau\bar{\nu}_\tau$, $\gamma\gamma$, hh .

1250 For $\gamma\gamma$ and ZZ , a substantial fraction of the signal photons are expected to have $E_\gamma = m_\chi$ [65].
 1251 This introduces δ -function that is much narrower than the energy resolution of the HAWC detector.
 1252 To ensure that this feature is not lost in the likelihood fits, the 'line' feature is convolved with a
 1253 Gaussian kernel with a 1σ width of $0.05 \cdot m_\chi$ and total kernel window of $\pm 4\sigma$. This differs from
 1254 HAWC's previous line study where 30% of HAWC's energy resolution was used for the kernel [67].
 1255 The NN energy estimator's strength compared to f_{hit} at low gamma-ray energy enables narrower
 1256 kernels [65]. $\chi\chi \rightarrow \gamma\gamma$ and ZZ spectral hypotheses are shown in Figure 6.2. We did not explore
 1257 how well we reconstruct injected signal events for various kernels widths. This is a systematic
 1258 that should be tested before publication to journal. Spectral models for the remaining annihilation
 1259 channels are plotted for each m_χ in Figure B.1.

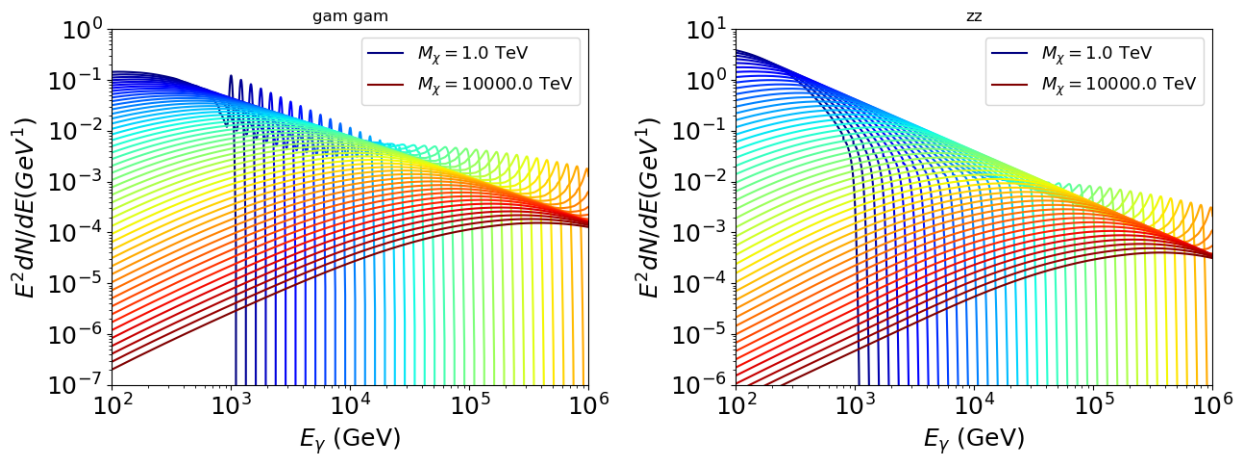


Figure 6.2 Photon spectra for $\chi\chi \rightarrow \gamma\gamma$ (left) and $\chi\chi \rightarrow ZZ$ (right) after Gaussian convolution of line features. Both spectra have δ -features at photon energies equal to the DM mass. Bluer lines are annihilation spectra with lower DM mass. Redder lines are spectra from larger DM mass. All spectral models are sourced from the Heavy Dark Matter models [65]. Axes are drawn roughly according to the energy sensitivity of HAWC.

1260 **6.3.2 J Astrophysical Components**

1261 The J-factor profiles for each source are imported from Louis Strigari et al. (referred to with
 1262 \mathcal{LS}) [66]. The \mathcal{LS} catalog fits a Navarro–Frenk–White (NFW) [48] spatial DM distributions to

1263 the dSphs which has a DM density of

$$\rho(r) = \frac{\rho_0}{\frac{r}{R_s} \left(1 + \frac{r}{R_s}\right)^2}. \quad (6.1)$$

1264 ρ_0 and the scale radius, R_s are free parameters fit for each dSph. r is the distance from the center
1265 of the dSph.

1266 Profiles in $\frac{dJ}{d\Omega}(\theta)$ up to an angular separation $\theta = 0.5^\circ$ were provided directly from the authors.
1267 Map generation from these profiles were almost identical to Section 5.3.2 except that a higher order
1268 trapezoidal integral was used for the normalization of the square, uniformly-spaced map:

$$p^2 \cdot \sum_{i=0}^N \sum_{j=0}^M w_{i,j} \frac{dJ}{d\Omega}(\theta_{i,j}, \phi_{i,j}) \quad (6.2)$$

1269 p is the angular side of one pixel in the map. $w_{i,j}$ is a weight assigned the following ways:

1270 $w_{i,j} = 1$ if $(\theta_{i,j}, \phi_{i,j})$ is fully within the region of integration

1271 $w_{i,j} = 1/2$ if $(\theta_{i,j}, \phi_{i,j})$ is on an edge of the region of integration

1272 $w_{i,j} = 1/4$ if $(\theta_{i,j}, \phi_{i,j})$ is on a corner of the region of integration

1273 Figure 6.3 shows the median and $\pm 1\sigma$ maps used as input for this DM annihilation study.

1274 6.3.3 Source Selection and Annihilation Channels

1275 HAWC's sources for this multithreaded analysis include Coma Berenices, Draco, Segue 1, and
1276 Sextans. \mathcal{LS} observed up to 43 sources in its publication, however only 4 of the best fit profiles
1277 were provided at the time this thesis was written. A full description of each source used in this
1278 analysis is found in Table 6.1.

1279 This analysis improves on chapter 5 in the following ways. Previously, the particle physics
1280 model used for gamma-ray spectra from DM annihilation was from the PPPC [44] which missed
1281 important considerations relevant for the neutrino sector. HDM is used to account for this shortfall
1282 [65]. HDM also models DM to the Planck scale which permits HAWC to probe PeV scale DM. For
1283 this study, we sample DM masses: 1 TeV - 10 PeV with 6 mass bins per decade in DM mass. In

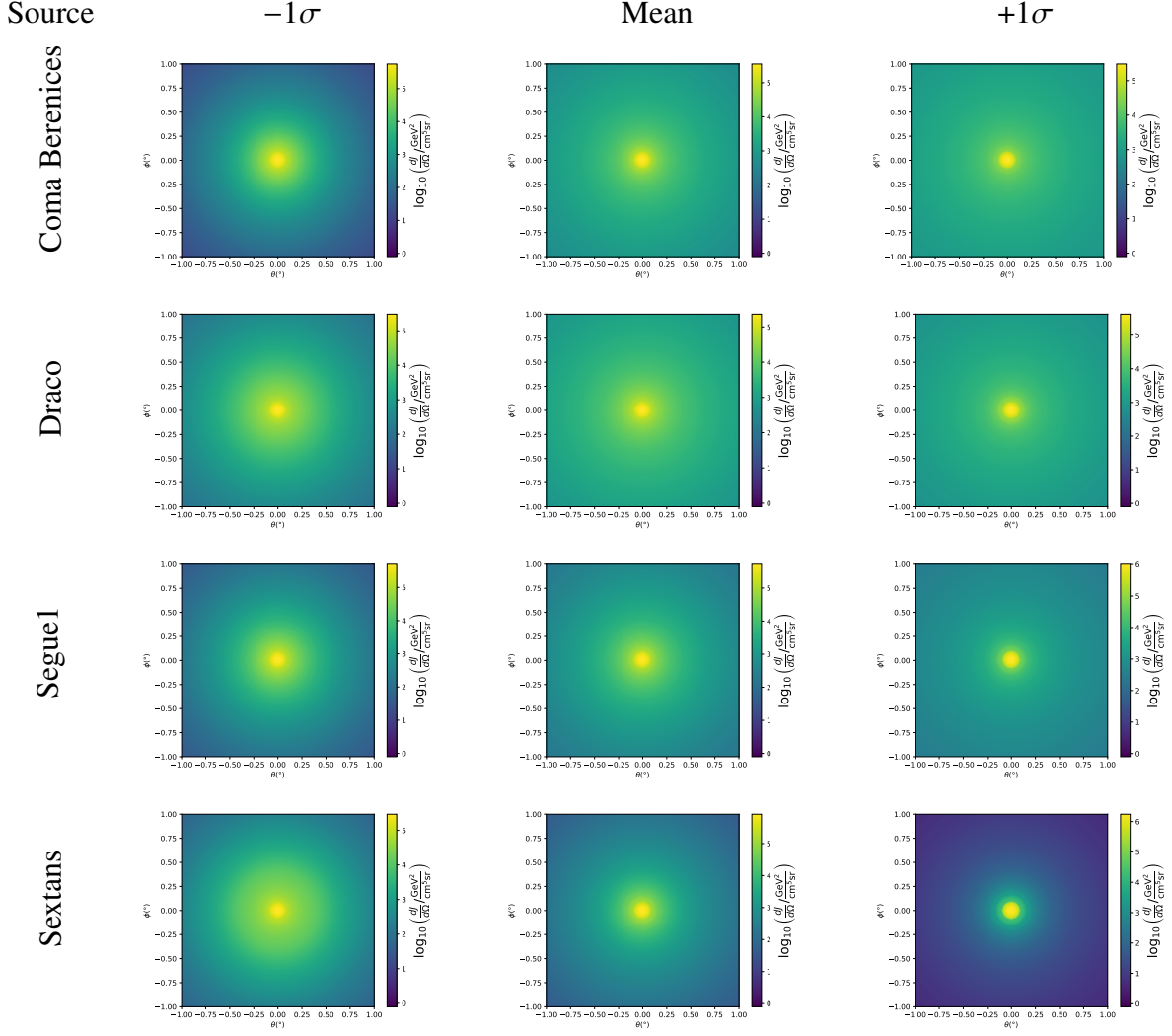


Figure 6.3 $\frac{dJ}{d\Omega}$ maps for Coma Berenices, Draco, Segue1, and Sextans. Columns are divided for the $\pm 1\sigma$ uncertainties in $dJ/d\Omega$ around the mean value from \mathcal{LS} [66]. Origin is centered on the specific dwarf spheroidal galaxies (dSph). θ and ϕ axes are the angular separation from the center of the dwarf. Profiles are truncated at 1° and flattened beyond.

1284 the case of line spectra ($\chi\chi \rightarrow \gamma\gamma$, or ZZ), we double the mass binning to 12 DM mass bins per
 1285 decade in DM mass.

1286 \mathcal{LS} provides 25 sources within HAWC's field of view. Additionally, NFW [48] DM distributions
 1287 have fewer parameters than Zhao [47], so \mathcal{LS} fits ultra-faint dwarves which expands the number of
 1288 sources. However, all sources were not provided by the authors in time for the completion of this
 1289 dissertation. Finally, the gamma-ray ray dataset is much larger. The study performed here analyzes
 1290 2565 days of data compared to 1017 days analyzed in chapter 5.

1291 **6.4 Likelihood Methods**

1292 These are identical to Section 5.4.1 and no additional changes are made to the likelihood. Bins
1293 in this analysis are expanded to include HAWC’s NN energy estimator.

1294 **6.5 Computational Methods: Multithreading**

1295 Previously, as in Section 5.3, the likelihood was minimized for one model at a time. One model
1296 in this case representing a DM annihilation channel (CHAN), DM mass (m_χ), and dSph ((SOURCE)).
1297 In an effort to conserve human and CPU time, jobs submitted for high performance computing
1298 contained a list of m_χ to iterate over for likelihood fitting. Jobs were then trivially parallelized
1299 for each permutation of the two lists: CHANS and SOURCES. The lists for CHANS and SOURCES are
1300 found in Section 6.3.1 and Table 6.1, respectively. Initially, 11 m_χ were serially sampled for one
1301 job defined by a [CHAN, SOURCE] tuple. Computing the likelihoods would take between 1.5 to 2 hrs,
1302 stochastically, for a job. We expect to compute likelihoods for data and 300 Poisson background
1303 trials. The estimated CPU time based on the above for all CHAN (N = 17) and SOURCE (M = 25)
1304 was estimated to 127,925 jobs. In total, 1,407,175 likelihood fits and profiles would be computed
1305 for the 11 mass bins we wished to study. The estimated CPU time ranged between 8k CPU days
1306 to 10k CPU days. Human time is more challenging to estimate as job allocation is stochastic and
1307 highly dependent on what other users are submitting. Yet, it is unlikely that all jobs would run
1308 simultaneously. Therefore, we can expect human time to be about as long as was seen in chapter 5

Name	Distance (kpc)	l, b ($^\circ$)	$\log_{10} J$ (\mathcal{LS} set) $\log_{10}(\text{GeV}^2 \text{cm}^{-5} \text{sr})$
Coma Berenices	44	241.89, 83.61	$19.00^{+0.36}_{-0.35}$
Draco	76	86.37, 34.72	$18.83^{+0.12}_{-0.12}$
Segue I	23	220.48, 50.43	$19.12^{+0.49}_{-0.58}$
Sextans	86	243.50, 42.27	$17.73^{+0.13}_{-0.12}$

Table 6.1 Summary of the relevant properties of the dSphs used in the present work. Column 1 lists the dSphs. Columns 2 and 3 present their heliocentric distance and galactic coordinates, respectively. Column 4 reports the J -factors of each source given from the \mathcal{LS} studies and estimated $\pm 1\sigma$ uncertainties. The values $\log_{10} J$ (\mathcal{LS} set) [66] correspond to the mean J -factor values for a source extension truncated at 0.5° .

1309 which was on the order of months to fully compute on a smaller analysis. A visual aid to describe
 1310 how jobs were organized is provided in Figure 6.4.

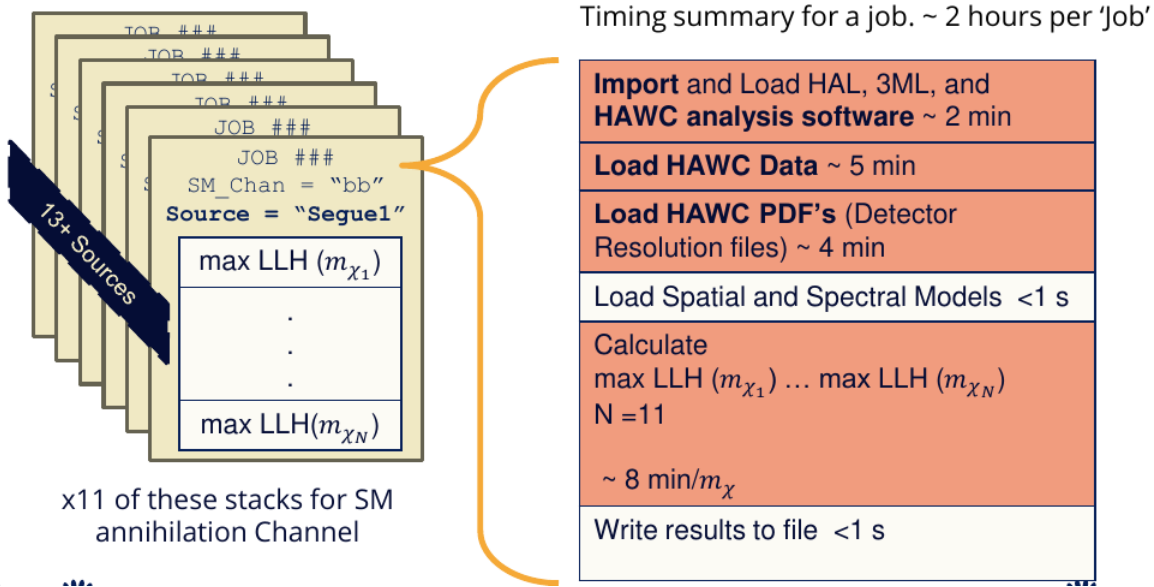


Figure 6.4 Infographic on how jobs and DM computation was organized in Section 5.3. Jobs were built for each permutation of CHANS and SOURCES shown by the left block in the figure. Each job, which took on the order 2 hrs to compute, had the following work flow: 1. Import HAWC analysis software, 2 min to run. 2. Load HAWC count maps, 5 min to run. 3. Load HAWC energy and spatial resolutions, 4 min. 5. Load DM spatial source templates and spectral models, less than 1 s. 6. Perform likelihood fit on data and model, about 8 min per DM mass. 7. Write results to file, less than 1s.

1311 The computational needs for this next generation DM analysis are extreme and is unlike other
 1312 analyses performed on HAWC. It became clear that there was a lot to gain from optimizing how
 1313 the likelihoods are computed. This section discusses how multi-threading was applied to solve and
 1314 reduce HAWC's computing of likelihoods for large parameter spaces like in DM searches.

1315 6.5.1 Relevant Foundational Information

1316 The profiling of the likelihood for HAWC is done via gradient descent where the normalization
 1317 of Equation (7.1) (linearly correlated with $\langle \sigma v \rangle$) is rescaled in the descent. Additionally, we sample
 1318 the likelihood space for a defined list of $\langle \sigma v \rangle$'s described in Section 5.4.2. The time to compute
 1319 these values is not predictable or consistent because many variables can change across the full
 1320 model-space. Comprehensively, these variables are:

1321 • m_χ : DM rest mass
 1322 • CHAN : DM annihilation channel in SM.
 1323 • SOURCE : dSph. Involves a spatial template AND coordinate in HAWC data.
 1324 • $\langle\sigma v\rangle$: Effectively the flux normalization and free parameter in the likelihood fit.
 1325 Therefore, we develop an asynchronous, functional-parallel coding pattern. Asynchronous meaning
 1326 the instructions within a function are independent and permitted to be out of sync with sibling
 1327 computations. Functional-parallel meaning that instructions are the subject of parallelization
 1328 rather than threading the likelihood computation. This is close to trivial parallelization seen in
 1329 Figure 6.4 except that we seek to consolidate the loading stages (software, data, and detector
 1330 resolution loading). Multiple asynchronous threads are expected to reduce total serial processing
 1331 time and total overhead across the entire project in addition to saving human time.

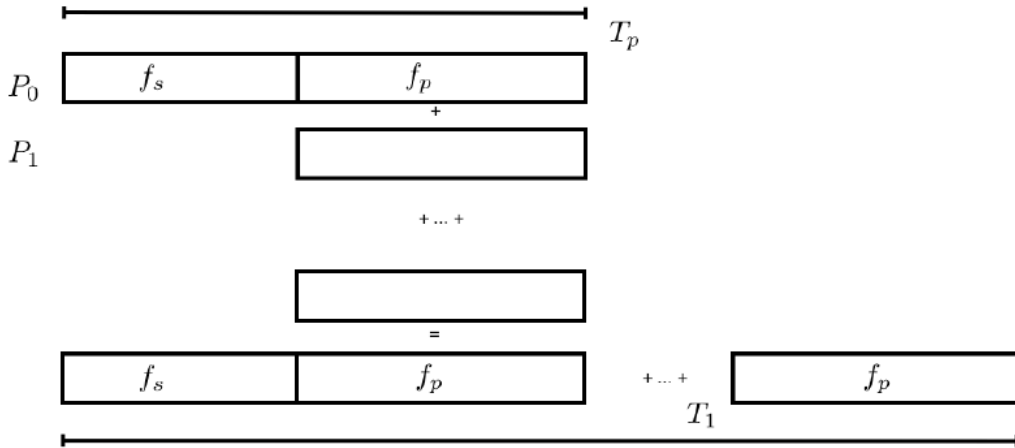


Figure 6.5 Graphic of Gustafson parallel coding pattern. f_s is the fraction of a program, in time, spent on serial computation. f_p is the fraction of computing time that is parallelizable. T_p is the total time for a parallel program to run. T_1 is the total time for a parallel program to run if only 1 processor is allocated. P_N is the N -th processor where it's row is the computation the processor performs. The Gustafson pattern is most similar to what is implemented for this analysis. Figure is pulled from [68].

1332 We need a way to measure and compare the expected speedup and efficiency gain for this
 1333 asynchronous coding pattern. I pull inspiration for timing measurement from [68] and use *Amdahl's*

1334 law with hybrid programming. Hybrid programming meaning that the computation is a mix of
 1335 distributed and shared memory programming. If we assume the code is fully parallelizable over p
 1336 processors and c threads, the ideal speedup is simply pc , and ideal run-time is $T_1/(pc)$. T_1 is the
 1337 total time for a parallel program to run if only 1 processor is allocated. However, the coding pattern
 1338 contains some amount of unavoidable serial computation, as shown in Figure 6.5. In our case, the
 1339 run time, $T_{p,c}$, is estimated to be

$$T_{p,c} = \frac{T_1}{pc} (1 + F_s(c - 1)). \quad (6.3)$$

1340 F_s is the fraction of CPU time dedicated to serial computation. The expected speedup, $S_{p,c}$, is

$$S_{p,c} \equiv \frac{T_1}{T_{p,c}} = \frac{pc}{1 + F_s(c - 1)}. \quad (6.4)$$

1341 From Equation (6.4), we can see that the speed-up scales with p/F_s . We are free to minimize F_s
 1342 asymptotically by enlarging the total models that are submitted to the thread pool, thereby shrinking
 1343 the CPU fraction dedicated to serial operation. We are also free to define exactly how many threads
 1344 and processors we utilize, yet eventually hit a hard cap at the hardware available on our computing
 1345 cluster. HAWC uses Intel Xeon™processors with 48 cores and 96 threads. We see that a successful
 1346 code will scale well as the expected speedup is inversely correlated with F_s . As the total number
 1347 of models sampled grows, the speedup will also.

1348 6.5.2 Implementation

1349 The multithreaded code was written in Python3 and is documented in the `dark_matter_hawc`
 1350 [repository](#) within the script named `mpu_analysis.py`. A version of the script as of April 25
 1351 **TODO: make sure to update on this date** is also provided in Section B.2. It has many dependencies
 1352 including the HAWC analysis software. Figure 6.6 displays the workflow of a job with 3 threads.
 1353 Within a job, SOURCE is kept fixed and CHANS remains 17 elements long. More m_χ are sampled
 1354 from 11 bins up to 49 (for $\gamma\gamma$ and ZZ) and 25 (for remaining CHANS) which amounts to 12 or 6
 1355 mass bins per decade. m_χ and CHANS are permuted into a 473 element list which is split evenly
 1356 across N threads where N is [2, 8, 16]. For each m_χ -CHAN tuple, 1001 $\langle\sigma v\rangle$ values are sampled in

Timing summary for a multi-threaded job.

Import and Load HAL, 3ML, and HAWC analysis software ~ 2 min		
Load HAWC Data ~ 5 min		
Load HAWC PDF's (Detector Resolution files) ~ 4 min		
Load Spatial Model < 1s		
Load Spectra Models <1 s	Load Spectra Models <1 s	Load Spectra Models <1 s
Calculate max LLH (Chan_0, m_{χ_1}) ... max LLH (Chan_?, m_{χ_N}) N = TOTAL/N_THREADS ~ 8 min/Spec_model	Calculate max LLH (Chan_?, m_{χ_1}) ... max LLH (Chan_?, m_{χ_N}) N = TOTAL/N_THREADS ~ 8 min/Spec_model	Calculate max LLH (Chan_?, m_{χ_1}) ... max LLH (Chan_?, m_{χ_N}) N = TOTAL/N_THREADS ~ 8 min/Spec_model
Write results to file <1 s	Write results to file <1 s	Write results to file <1 s
Join Threads and terminate < 1s		

Figure 6.6 Task chart for one multithreaded job developed for this project. Green blocks indicate a shared resource across the threads AND computation performed serially. Red blocks indicate functional parallel processing within each thread. 3 threads are represented here, yet many more can be employed during the full analysis. Jobs are defined by the SOURCE as these require unique maps to be loaded into the likelihood estimator. The m_{χ} , CHAN, and $\langle \sigma v \rangle$ variables are entered into the thread pool and allocated as evenly as possible across the threads.

- 1357 the likelihood, and the value of $\langle \sigma v \rangle$ that maximizes the likelihood is found. Although rare, fits
 1358 that failed are handled on a case by case basis.

1359 6.5.3 Performance

M Tasks	$T_{p,c}$ (hr:min:s)			
	$T_{1,1}$	$T_{1,2}$	$T_{1,8}$	$T_{1,16}$
50	1:40:37.5	0:52:43.7	0:19:13.8	0:13:44.0
74	2:22:30.0	1:15:00.6	0:25:21.3	0:15:49.8
100	(3:07:51.9)	1:40:10.5	0:30:44.4	0:20:01.4
200	(6:02:20.6)	-	1:00:32.0	0:30:35.0
473	(13:58:40.3)	-	2:01:41.4	1:07:53.2

Table 6.2 Timing summaries for analyses for serial and multithreaded processes. M tasks is the number of functional-parallel tasks ran for the computation. $T_{p,c}$ is a single run time in hours:minutes:seconds for runs utilizing p nodes and c threads. Runs are run interactively on the same computer to maximize consistency. Empty entries are indicated with '-'. (·) entries are estimated entries extrapolated from data earlier in the column.

- 1360 We see a significant reduction to wall time needed for our dSph analyses to run. Table 6.2

1361 shows the timing summaries for analyses of different sizes and thread counts. Additionally, the
 1362 efficiency gained when consolidating the serial loading of data is also apparent in our ability to
 1363 study many more tasks in about the same amount of wall time as a smaller serial computation. Trials
 1364 represented in the table were run on an AMD Opteron® processor 6344 with 48 cores, 2 threads per
 1365 core; 2.6 GHz clock. This is not the same architecture used for analysis on the HAWC computing
 1366 cluster however they are similar enough that results shown here are reasonably representative of
 1367 computing on the HAWC computing cluster. I use Tab. 6.2 for the inferences and conclusions in
 1368 the following paragraphs.

1369 First, we want to find T_s , the time of serial computation. From Fig. 6.5, the timing for our
 1370 coding pattern can be written as

$$T_s + Mt_p = T_{1,1}^M. \quad (6.5)$$

1371 M is the number of functional-parallel tasks (represented as column 1 of Tab. 6.2), and t_p is the
 1372 average time to complete a single parallel task. $T_{1,1}^M$ is the total time for a parallel program to run if
 1373 only 1 processor is allocated for M parallel task. With two runs of different M (M_1 and M_2), we
 1374 can use a system of equations to compute

$$T_s = 803.1\text{s} \text{ and } t_p = 104.6\text{s} \quad (6.6)$$

1375 Now, we have specific estimation for the fraction of serial computing time, F_s :

$$F_s = \frac{803.1}{803.1 + 104.6 \cdot M}. \quad (6.7)$$

1376 The maximum M for this study is 473 which evaluates to: $F_s = 0.016$ or 1.6% of computing time.
 1377 Table 6.3 shows the resulting speedups.

1378 We see a speedup that generally exceeds expectations from Eq. (6.4) for real trail runs. We also
 1379 see that there are diminishing returns as the number of threads increases. For small jobs with large c ,
 1380 both the expected and observed speedup are significantly smaller than c . One thing not considered
 1381 in Eq. (6.4) is the time incurred via communication latency. Communication latency increases
 1382 with the number of threads and contributes to diminishing returns. Additionally, these values are

M Tasks	F_s	$S_{1,2}$	$S_{1,8}$	$S_{1,16}$
50	1.33 E-1	1.90 [1.76]	5.23 [4.14]	6.35 [5.34]
74	9.40 E-2	1.90 [1.83]	5.62 [4.82]	9.00 [6.64]
100	7.13 E-2	1.88 [1.87]	6.11 [5.34]	9.38 [7.73]
200	3.70 E-2	- [1.93]	5.98 [6.36]	11.85 [10.29]
473	1.60 E-2	- [1.97]	6.89 [7.20]	12.35 [12.91]

Table 6.3 Speed up summaries for analyses for serial and multithreaded processes. M tasks is the number of functional-parallel tasks ran for the computation. $S_{p,c}$ is a single speedup comparison for runs utilizing p nodes and c threads. [·] are the estimated speedups calculated from Tab. 6.2, Eq. (6.7), and Eq. (6.4). Empty entries are indicated with '-'.

1383 for single runs and do not consider the stochastic variation expected in a shared high performance
 1384 computing resource. Therefor, these results are not strictly conclusive, yet demonstrate the merits
 1385 of multi-threading. We see very clearly that there is a lot to gain, and this new coding pattern will
 1386 expand HAWC's analysis capabilities.

1387 6.6 Analysis Results

1388 3 of the 43 $\mathcal{L}\mathcal{S}$ dSphs considered for the multithreaded analysis. These dSph are analyzed
 1389 for emission from DM annihilation according to the likelihood method described in Section 5.4.
 1390 The three likelihood profiles are then stacked to synthesize a combined limit on the dark matter
 1391 annihilation cross-section, $\langle\sigma v\rangle$. This combination is done each of the 17 SM annihilation channels.
 1392 Figure 6.7 and Fig. 6.8 show the combined limits for all annihilation channels with HAWC's
 1393 observations. Test statistics of the best fit $\langle\sigma v\rangle$ values for each m_χ and CHAN are shown in Fig. 6.9
 1394 and Fig. 6.10. We also compare these limits to HAWC's Glory Duck limits shown in Section 5.5.
 1395 The comparison to Glory Duck are featured in Fig. 6.11 for all the DM annihilation channels studied
 1396 for Glory Duck. A full comparison is provided in the appendix in Fig. B.2, Fig. B.3, and Fig. B.4.
 1397 Here, we show updated limits for $\chi\chi \rightarrow b\bar{b}, e\bar{e}, \mu\bar{\mu}, \tau\bar{\tau}, t\bar{t}, W^+W^-$, $\gamma\gamma$ and ZZ . For the first time
 1398 ever, we show limits for $\chi\chi \rightarrow c\bar{c}, s\bar{s}, u\bar{u}, d\bar{d}, \nu_e\bar{\nu}_e, \nu_\mu\bar{\nu}_\mu, \nu_\tau\bar{\nu}_\tau, gg$, and hh .

1399 No DM was found in HAWC observations. The largest excess found in HAWC data was for DM
 1400 annihilating to W -bosons or $\nu_e\bar{\nu}_e$ for $m_\chi = 10$ TeV at significance 2.11σ and 2.14σ respectively.
 1401 HAWC's limits and excesses are dominated by Segue1. Coma Berenices shows excesses at higher
 1402 DM mass, yet no similar excesses were observed in Segue1 or Sextans. Sextans did not contribute

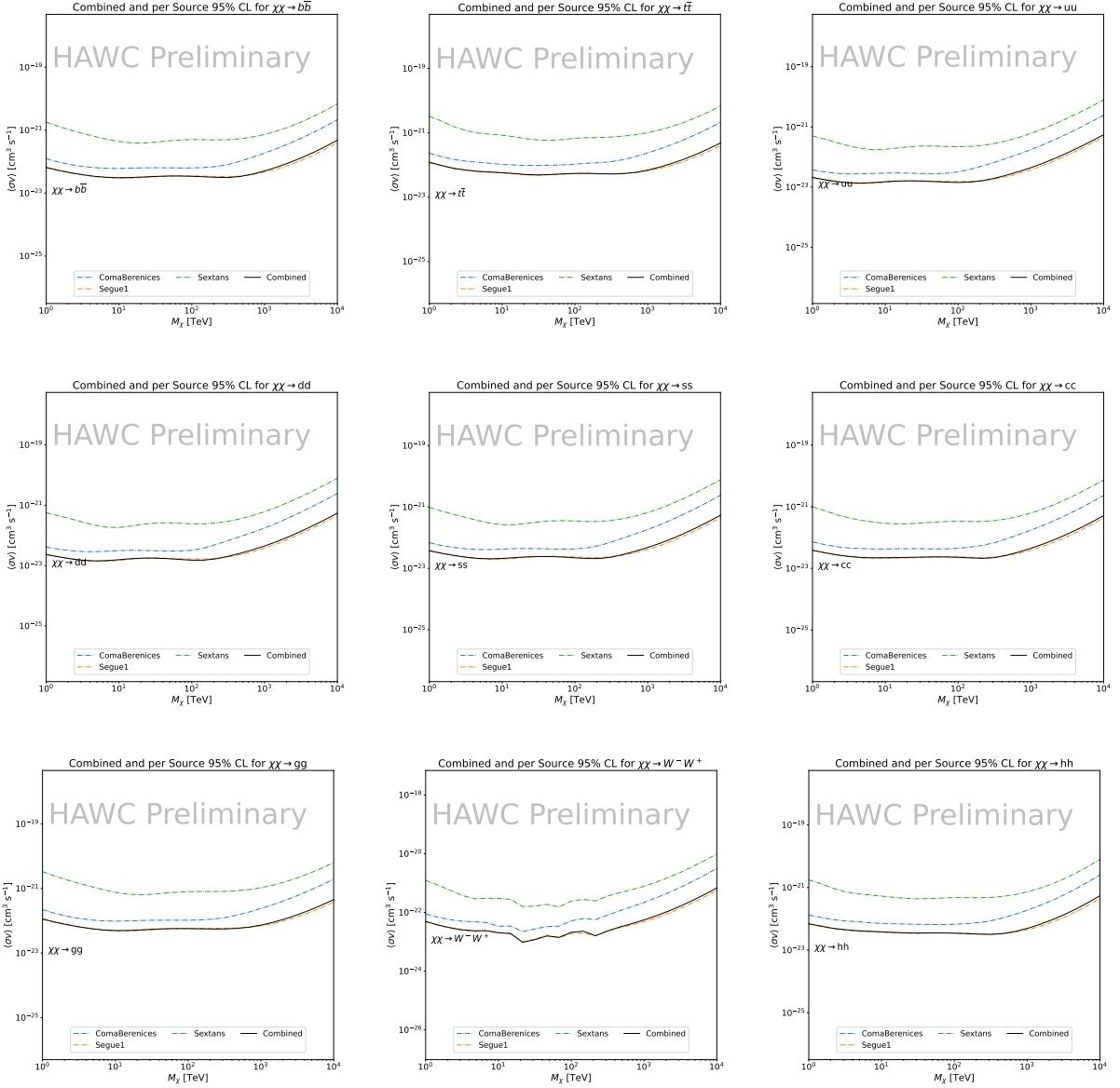


Figure 6.7 HAWC upper limits at 95% confidence level on $\langle\sigma v\rangle$ versus m_χ for $\chi\chi \rightarrow b\bar{b}$, $t\bar{t}$, $u\bar{u}$, $d\bar{d}$, $s\bar{s}$, $c\bar{c}$, gg , W^+W^- , and hh . Limits are with $\mathcal{L}\mathcal{S}$ J -factors [66]. The solid line represents the observed combined limit. Dashed lines represent limits from individual dSphs.

1403 significantly to signal excesses or the combined limit as it is at high zenith. Draco was not included
 1404 as the PDF of some of our analysis bins were wider than what is reasonable for a point source
 1405 analysis. Draco is at a high zenith for HAWC, so the effort required to include it was not justified
 1406 by the benefits.

1407 We did not generate background trials in time of writing this thesis. These are not shown and

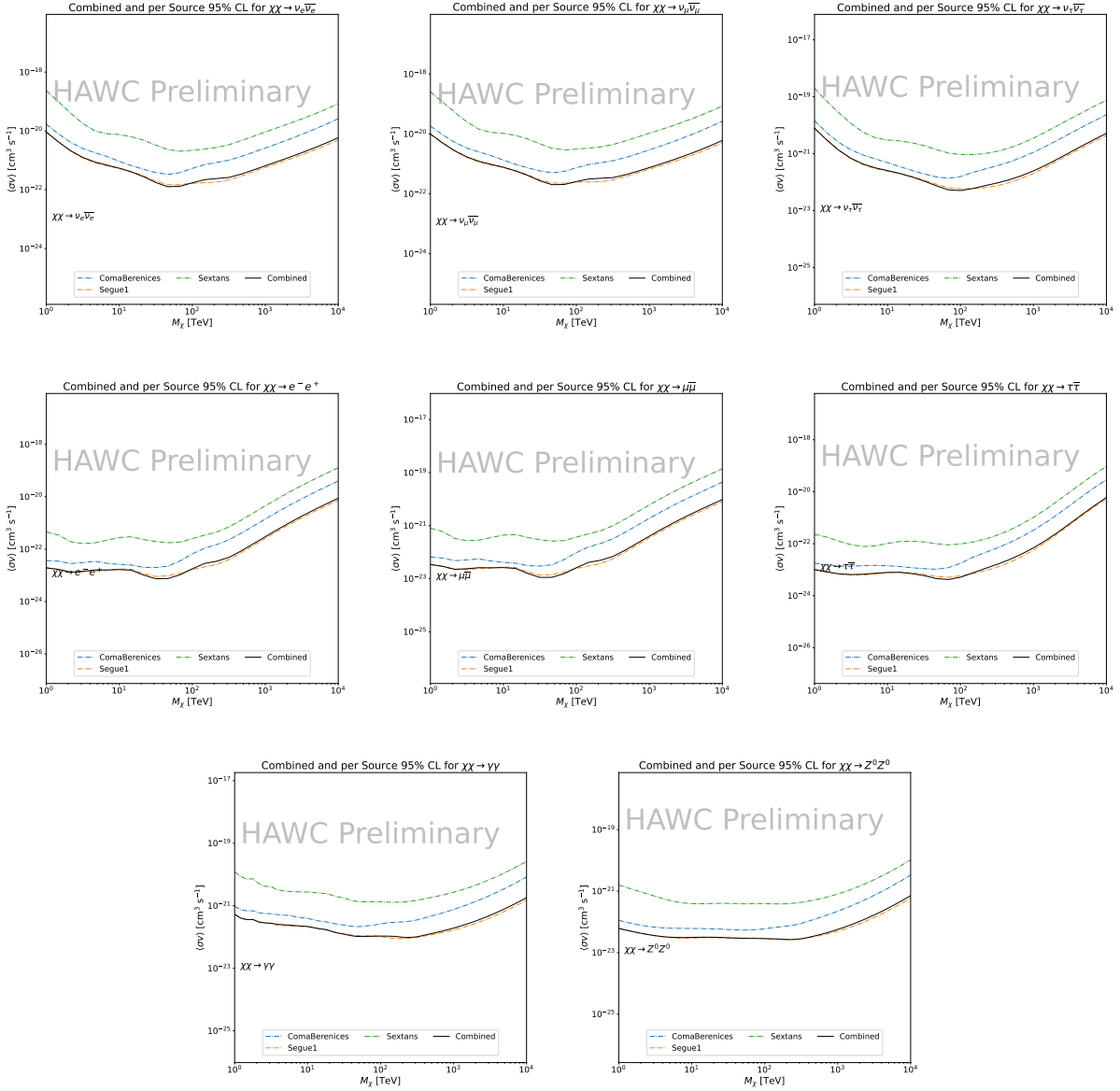


Figure 6.8 HAWC upper limits at 95% confidence level on $\langle\sigma v\rangle$ versus m_χ for $\chi\chi \rightarrow \nu_e \bar{\nu}_e$, $\nu_\mu \bar{\nu}_\mu$, $\nu_\tau \bar{\nu}_\tau$, $e \bar{e}$, $\mu \bar{\mu}$, $\tau \bar{\tau}$, $\gamma\gamma$ and ZZ . Limits use $\mathcal{L}S$ J -factors [66]. The solid line represents the observed combined limit. Dashed lines represent limits from individual dSphs.

1408 are an immediate next step for this analysis before publication.

1409 When comparing these results to Section 5.5, we see an overall decrease to the confidence limit
1410 therefore improvement to HAWC's expected sensitivity. This improvement is generally stronger
1411 than a doubling of data, or a factor $\sqrt{2}$ decrease. The comparison is somewhat complex and
1412 dependent on the dSph and SM annihilation channel. Figure 6.11 shows the comparisons of limits

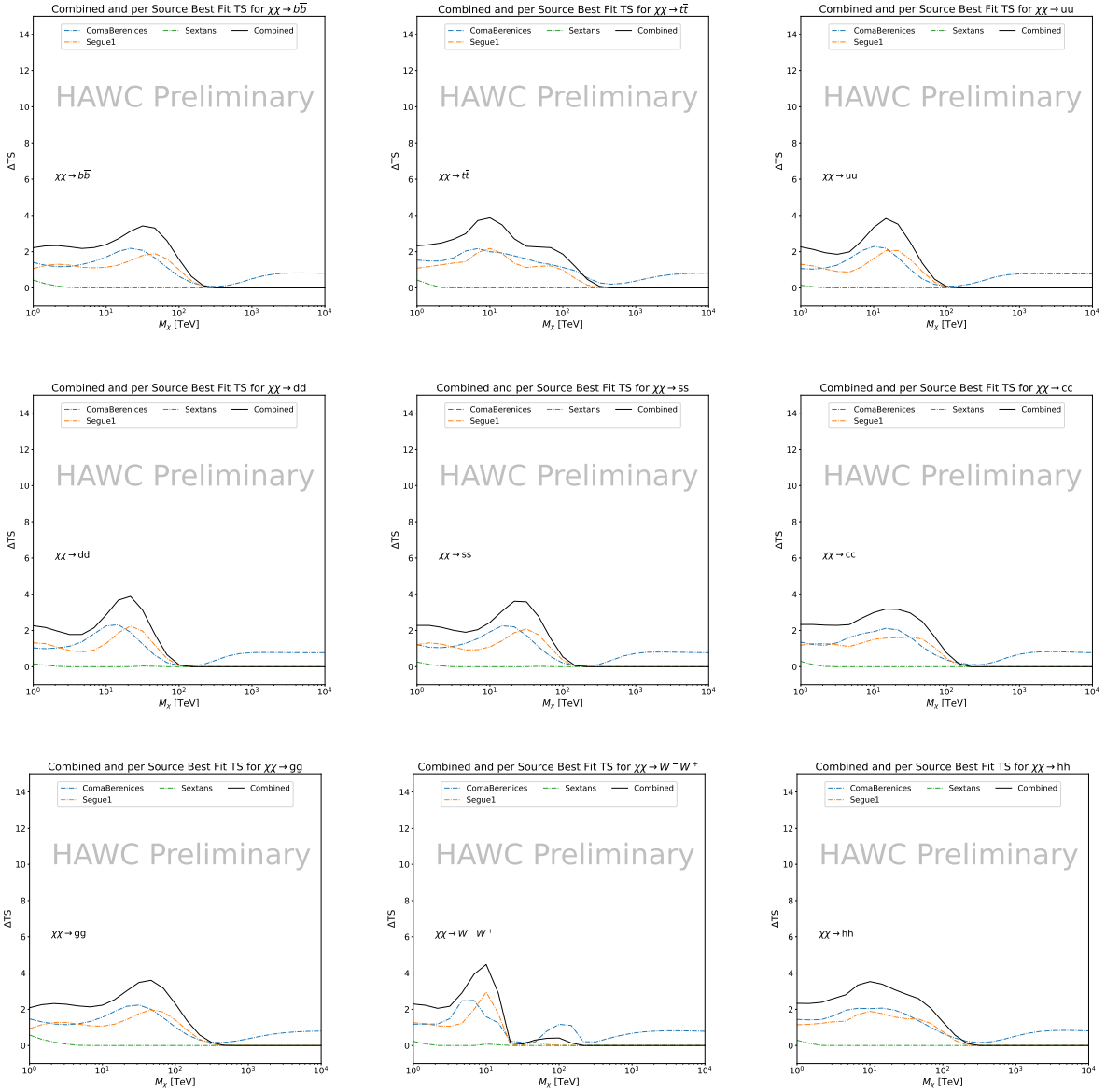


Figure 6.9 HAWC TS values for best fit $\langle\sigma v\rangle$ versus m_χ for SM annihilation channels: $\chi\chi \rightarrow b\bar{b}$, $t\bar{t}$, $u\bar{u}$, $d\bar{d}$, $s\bar{s}$, $c\bar{c}$, gg , W^-W^+ , and hh . Limits use \mathcal{LS} J -factors. The solid black line shows the combined best fit TS values. The colored, dashed lines are the TS values from each dSph.

1413 calculated for this analysis and Glory Duck (Section 5.5). Segue 1 and Coma Berenices are low
 1414 zenith where improvements to HAWC's analysis come only from energy estimation. Differences
 1415 between these two are dominantly from their differences in J -factor, half-light radii of the dSphs,
 1416 and the particle physics inputs. Substantial gains in HAWC's analysis methods (pass 5.F) were
 1417 made at high zenith which is important for sources like Sextans. The HDM particle physics model

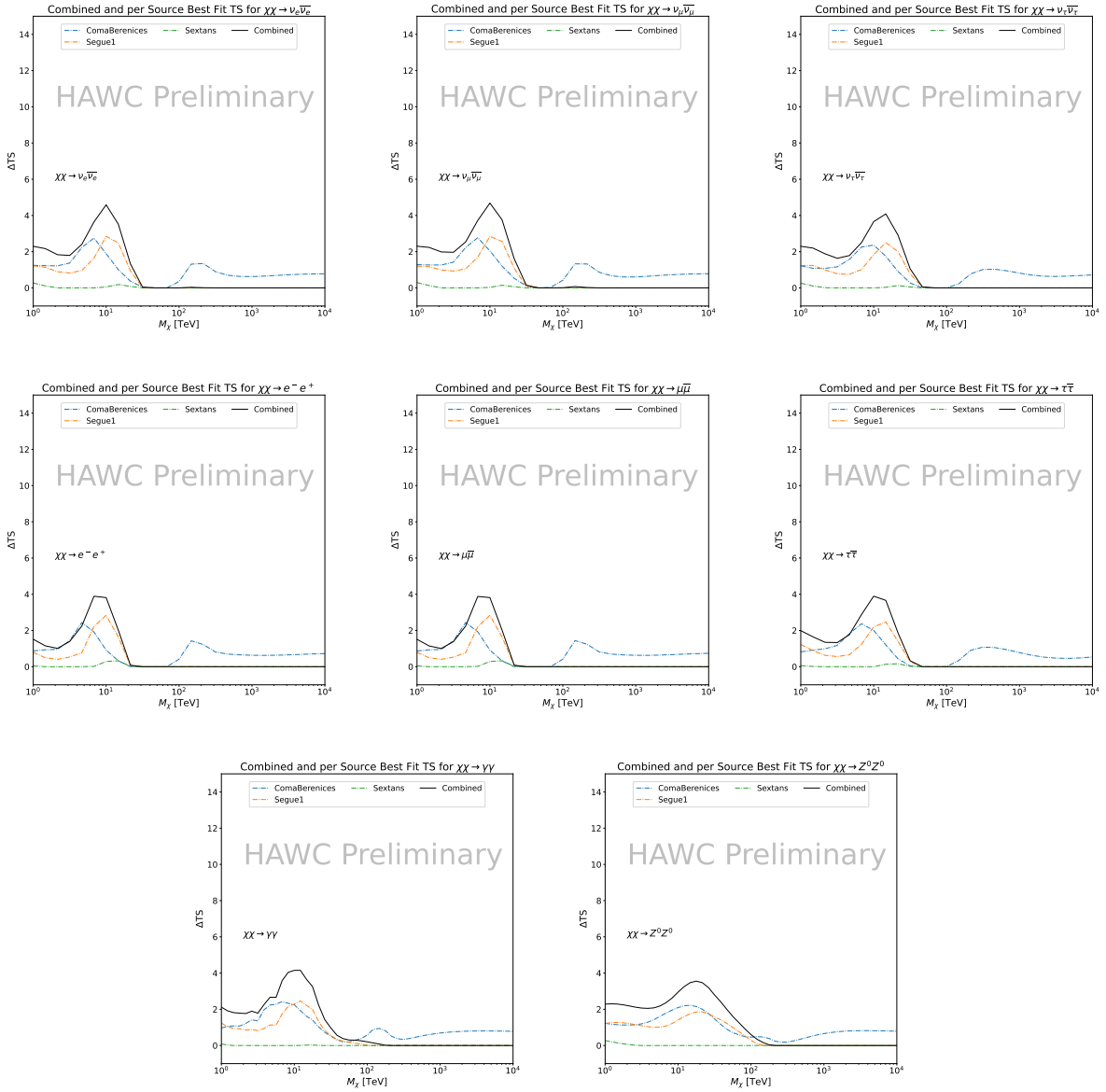


Figure 6.10 HAWC TS values for best fit $\langle\sigma v\rangle$ versus m_χ for SM annihilation channels: $\chi\chi \rightarrow \nu_e \bar{\nu}_e$, $\nu_\mu \bar{\nu}_\mu$, $\nu_\tau \bar{\nu}_\tau$, $e^- e^+$, $\mu \bar{\mu}$, $\tau \bar{\tau}$, $\gamma\gamma$ and ZZ . Limits use \mathcal{LS} J -factors. The solid black line shows the combined best fit TS values. The colored, dashed lines are the TS values from each dSph.

1418 produces almost identical spectra to the PPPC for $\chi\chi \rightarrow e^- e^+$. This channel can be used to
 1419 compare limits between dSph spatial models. Overhead sources see minimal improvement to the
 1420 limits, while high zenith sources see an order of magnitude improvement for all DM masses. Softer
 1421 SM annihilation channels see broad improvements to the limit compared to harder channels.

1422 **6.7 Systematics**

1423 Systematics to this analysis are identical to what was performed earlier in Glory Duck, Sec-
1424 tion 5.7. We are also sensitive to the choice in spatial template, and this was explored in Section 5.7.2
1425 and Section 5.8.2.

1426 **6.8 Conclusion and Discussion**

1427 In this multithreaded analysis, we have used observations of 3 dSphs from HAWC to perform
1428 a collective DM annihilation search towards dSphs. The data were combined across sources
1429 to significantly increase the sensitivity of the search. Advanced computational techniques were
1430 deployed to accelerate wall-time spent analyzing by an order of magnitude. We have observed
1431 no significant deviation from the null, no DM hypothesis, and so present our results in terms of
1432 upper limits on the velocity-weighted cross-section, $\langle\sigma v\rangle$, for seventeen potential DM annihilation
1433 channels across four decades of DM mass.

1434 This analysis serves as a proof of concept for multithreaded HAWC analyses with large parameter
1435 spaces. Larger datasets with fast techniques will be essential to tackling the DM problem. The
1436 models we used for this study include annihilation channels with neutrinos in the final state.
1437 Advanced studies could aim to merge our results with those from neutrino observatories with large
1438 data sets.

1439 A full HAWC analysis will include systematic studies of the J -factor distributions. Additionally,
1440 because of the timing reduction, the study can be doubled in size to include DM decay. We have not
1441 yet received the remaining spatial profiles to the \mathcal{LS} catalog, and limits can be quickly computed
1442 once these are received. Finally, statistical studies with Poisson variation of HAWC's background
1443 are essential to a comprehensive understanding of our observed excesses.

Segue1

Coma Berenices

Sextans

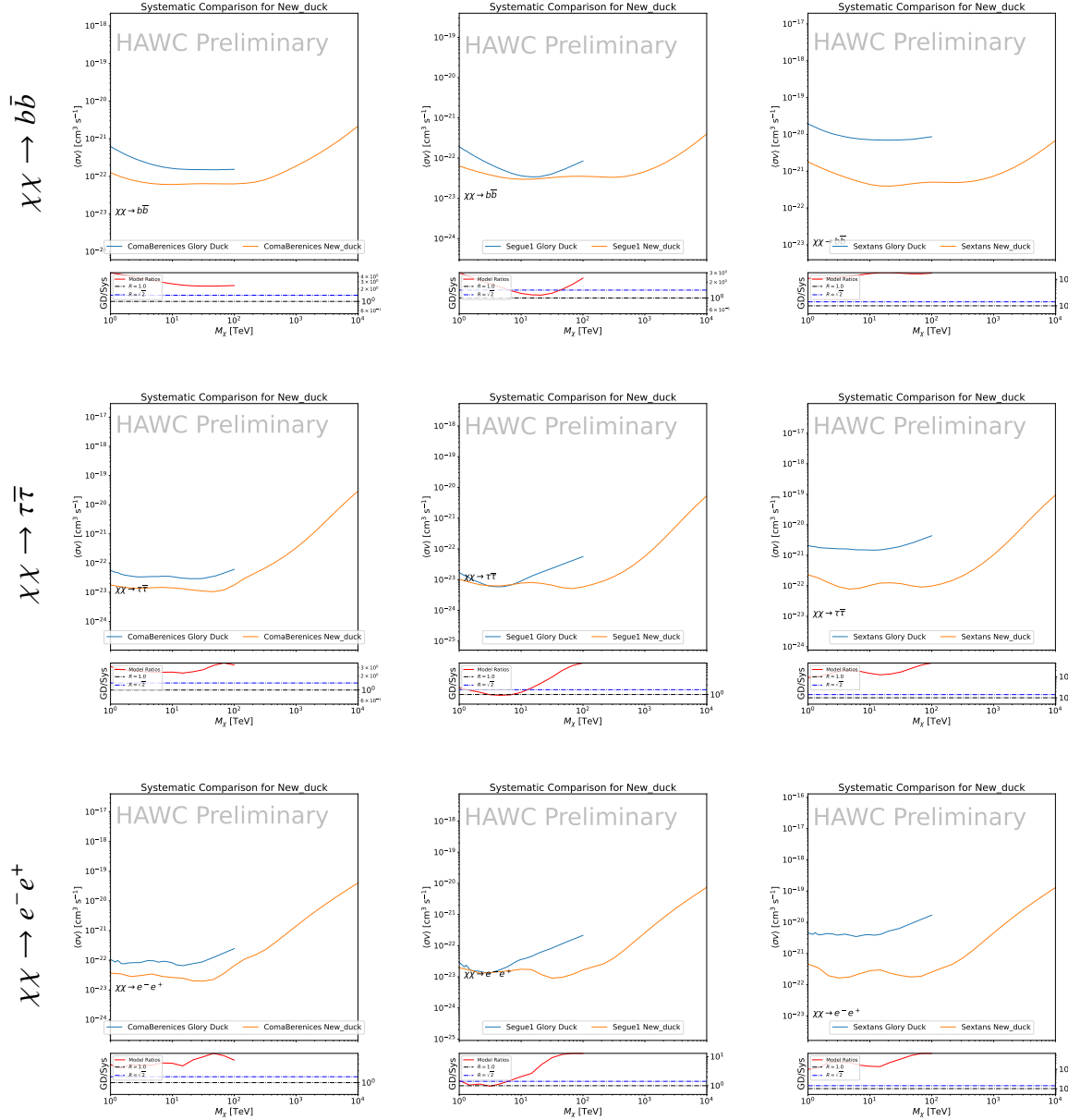


Figure 6.11 Comparison of HAWC limits from this analysis to Glory Duck (Fig. 5.5) for 3 dSphs and 3 DM annihilation channels: $b\bar{b}$, $\tau\bar{\tau}$, and e^-e^+ . Each sector shows the 95% confidence limit from Glory Duck (blue line) and this analysis (orange line) in the top plot. The lower plot features the ratio in log scale of Glory Duck to this analysis in a red solid line. Horizontal dashed lines are for ratios of 1.0 (black) and $\sqrt{2}$ (blue). Ratios larger than 1.0 are for limits smaller, or stricter, than Glory Duck. Ratios larger than $\sqrt{2}$ indicates limits are stricter than a simple doubling of the Glory Duck data.

CHAPTER 7

1444 HEAVY DARK MATTER ANNIHILATION SEARCH WITH ICECUBE'S NORTH SKY 1445 TRACK DATA

1446 7.1 Introduction

1447 Neutrinos are another astrophysical messenger than can travel long distances without significant
1448 attenuation or deflection. Uniquely, they interact less readily than photons especially above PeV
1449 energies. Neutrinos thereofre provide another window through which we can perform dark matter
1450 searches. Neutrinos come in three flavors which triples the multiplicity of the particles we are
1451 searching for.

1452 The previous Icecube DM annihilation analysis towards dwarf galaxies was performed in 2013
1453 [69]. This is in spite of the potentially crucial sensitivity afforded from neutrino spectral lines [70].
1454 A lot has changed in IceCube since its previous DM annihilation search such as, additional strings,
1455 more sophisticated analysis methods, and more accurate theory modeling. It has come time for
1456 IceCube to make a DM dSph contribution.

1457 As I have shown previously in Sec. 5 and Sec. 6, we can build a fast and robust analysis
1458 that shares tools with the field. The hope being that IceCube can eventually combine data with
1459 gamma-ray observatories.

1460 IceCube is sensitive to annihilating DM to the DM ranges above 1 TeV and can produce
1461 competitive results relative to gamma-ray observatories in spectral models that produce sharp
1462 neutrino features. The goal of this analysis is to perform a DM annihilation search using the
1463 Northern Sky Tracks datasets. The search will only be towards dwarf spheroidal galaxies (dSph)
1464 for the strengths mentioned in Section 5.3.3. These sources are treated as point sources for IceCube
1465 with little loss to sensitivity or model dependence on how the DM is distributed. DM masses from
1466 500 GeV to 100 PeV are considered for this analysis. Several DM annihilation channels available
1467 from the HDMspectra are studied in this analysis. This chapter presents the analysis work for IC3
1468 for DM searches toward dSphs.

1469 **7.2 Dataset and Background**

1470 This section enumerates the data and background methods used for IceCube's study of dSphs.

1471 Section 7.2.1 and Section 7.2.2 are most useful for fellow IceCube collaborators looking to replicate

1472 this analysis.

1473 **7.2.1 Itemized IceCube files**

1474 These files are only available withing IceCube's internal documentation and collaborators. They

1475 are not meant for public access, and are presented here so that IceCube collaborators can reproduce

1476 results accurately.

- 1477 • Software Environment: CVMFS Py3-v4.1.1

- 1478 • Data Sample: Northern Tracks NY86v5p1

- 1479 • Analysis Software: csky ([nu_dark_matter](#))

1480 • Analysis wiki: https://wiki.icecube.wisc.edu/index.php/Dark_Matter_Annihilation_Search_towards_dwarf_spheroidals_with_NST_and_DNN_Cascades

- 1482 • Project repository

1483 **7.2.2 Software Tools and Development**

1484 This analysis was performed inside IceCube's CVMFS (3.4.1.1) software environment using

1485 csky for likelihood calculations. Csky at first did not come with dark matter spectral models

1486 nor could accomodate custom flux models. We developed these capacities for single source and

1487 stacked source studies for this analysis. The analysis code is held in a separate repository from

1488 csky. The [nu_dark_matter branch of csky](#) manages the input of custom dark matter spectra and

1489 accompanied DM astrophysical source then calculates likelihoods with a selected data sample. The

1490 [IceCube Dark Matter dSph repository](#) manages the generation of spectral models for neutrinos,

1491 physics parameter extraction from n_{sig} , J -factor per source inputs, and bookkeeping for the large

1492 parameter space. The project repository required a secondary software environment for neutrino

1493 oscillations. How to launch and run those calculations are documented in the project repository
1494 and the Docker image is additionally saved in Section C.1

1495 7.2.3 Data Set and Background Description

1496 For this analysis, I use the Northern Sky Tracks (NST) Sample (Version V005-P01). The sample
1497 contains up-going track-like events, usually from ν_μ and ν_τ with a superior angular resolution
1498 compared to the cascade dataset. This sample covers 10.4 years of data (IC86_2011-2021). The
1499 accepted neutrino energy range used for the analysis is unique from most other IceCube searches
1500 because DM spectra are hard with large contributions close to $E_\nu = m_\chi$. Therefore the sampled
1501 energy range is $1 < \log(E_\nu/\text{GeV}) < 9.51$ with step size 0.125.

1502 The strength of a dwarf analysis is that there is no additional background consideration beyond
1503 nominal, baseline background estimations (see Section 5.2.3). For NST, the nominal contribu-
1504 tion comes from atmospheric neutrinos and isotropic astrophysical neutrinos. We estimate the
1505 background by scrambling NST data along Right Ascension.

1506 7.3 Analysis

1507 The expected differential neutrino flux from DM-DM annihilation to standard model particles,
1508 $d\Phi_\nu/dE_\nu$, over solid angle, Ω is described by the familiar equation.

$$\frac{d\Phi_\nu}{dE_\nu} = \frac{\langle\sigma v\rangle}{8\pi m_\chi^2} \frac{dN_\nu}{dE_\nu} \times \int_{\text{source}} d\Omega \int_{l.o.s} \rho_\chi^2 dl(r, \theta') \quad (7.1)$$

1509 This is identical to past examples, Eq. (7.1) except that there are 3 neutrino flavors, so there are a
1510 corresponding 3 flux equations. Section 5.3 has a complete description of each term in Eq. (7.1).
1511 Additionally, neutrinos oscillate between flavors which needs to be considered for the expected
1512 neutrino flux at Earth. Section 7.3.1 presents the particle physics model and processing for DM
1513 annihilation. Section 7.3.2 presents the spatial distributions built for each dSph.

1514 7.3.1 $\frac{dN_\nu}{dE_\nu}$ - Particle Physics Component

1515 Neutrino spectra from heavy dark matter annihilation were generated using HDMSSpectra [65]
1516 and χ arrov [71]. HDMSSpectra has tables for the decay and annihilation of heavy dark matter
1517 for different dark matter masses and SM primary annihilation channels. The simulation includes

1518 electroweak radiative corrections and higher order loop corrections with quarks. This publication
1519 also pushes the simulated DM mass to the Plank scale (1 EeV), however this study will not explore
1520 that high.

1521 An important feature in the spectra is that neutrino line channels will be accompanied with
1522 a low energy tail [65]. Thus the earth will not fully attenuate a heavy DM line-like signal from
1523 high declination sources where the neutrino flux must first traverse through the Earth. The DM
1524 annihilation channels that feature lines include all leptonic channels. ($\nu_{e,\mu,\tau}$, e , μ , and τ) We use the
1525 `Xarov` software to propagate and oscillate the neutrinos from the source to Earth. Because these
1526 sources are quite large in absolute terms, and also far (order 10 kpc or more), the resulting flavor
1527 spectra are the averages of the transition probabilities [71]:

$$P(\nu_\alpha \rightarrow \nu_\beta) \approx \begin{bmatrix} 0.55 & 0.18 & 0.27 \\ 0.18 & 0.44 & 0.38 \\ 0.27 & 0.38 & 0.35 \end{bmatrix} \quad (7.2)$$

1528 Examples of the spectra before and after propagation are shown in Fig. 7.1.

1529 When calculating the expected contribution to n_s , only ν_μ , ν_τ are considered as NST's effective
1530 area to ν_e is negligible [72]. Therefore the expected composite neutrino spectrum is sum of the two
1531 flavors: $\nu_\mu + \nu_\tau$. The spectral tables are then converted to splines to condense information, enable
1532 random sampling of the spectra, and reduce computing times. The spectral splines are finally
1533 implemented as a DM class in csky.

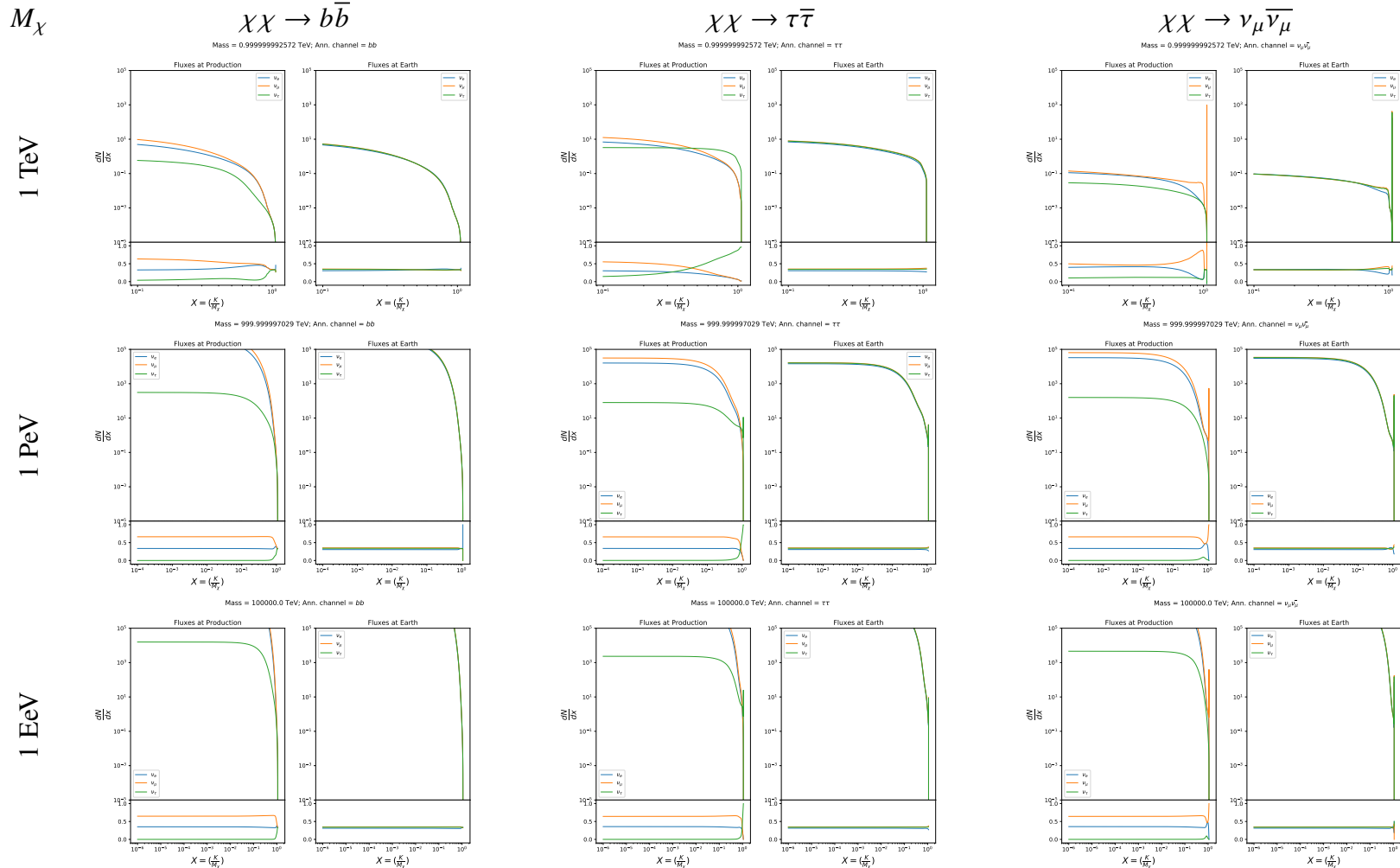


Figure 7.1 Neutrino spectra at production (left panels) and after oscillation at Earth (right panels). Blue, orange, and green lines are the ν_e , ν_μ , and ν_τ spectra respectively. Top panels show the spectra in $\frac{dN}{dE}$. Lower panels plot the flavor ratio to $\nu_e + \nu_\mu + \nu_\tau$. SM annihilation channels $b\bar{b}$, $\tau\bar{\tau}$, and $\nu_\mu\bar{\nu}_\mu$ are shown for $M_\chi = 1 \text{ PeV}$, TeV , and EeV .

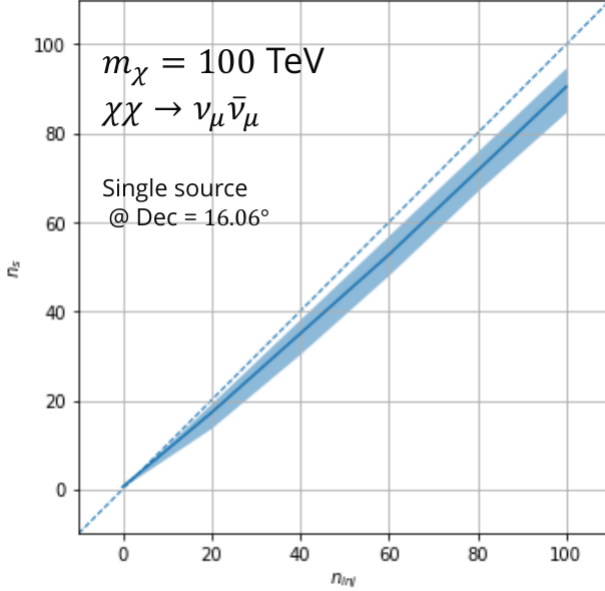


Figure 7.2 Signal recovery for 100 TeV DM annihilation into $\nu_\mu \bar{\nu}_\mu$ for a source at Dec = 16.06°. n_{inj} is the number of injected signal events in simulation. n_s is the number of reconstructed signal events from the simulation. Although the uncertainties are small and tight, the reconstructed n_s are systematically underestimated.

7.3.1.1 Treatment of Neutrino Line Features

All DM annihilation channels into leptons $\chi\chi \rightarrow [\nu_{e,\mu,\tau}, e, \mu, \tau]$ develop a prominent and narrow spectral line feature. For all neutrino flavors, this line is visible and prominent in all m_χ studied in this analysis. For charged leptons, the feature only really shows up at the larger DM mass models and varies between the flavors. Examples for lines in the annihilation spectra with neutrinos or charged leptons primary annihilation products are provided in Fig. 7.1.

The neutrino line feature is so narrow relative the sampled energy range that the random sampling of the spectra and likelihood fitting rarely capture the line in computation. As a result, often the best fit to simulation of background will always floor to TS = 0 and the signal recovery systematically underestimates the signal (see Fig. 7.2).

To remedy this, a similar approach to the IceCube's decay analysis [73]. Two smoothing kernels were tested (Gaussian, uniform) to widen the line feature. The widths were tuned such that the signal recovery approached unity for DM mass 100 TeV to 1 PeV for a source at Segue 1's declination, 16.06°. Near horizon was chosen in order to isolate loss in signal recovery from too narrow a line versus from Earth's attenuation of very high energy neutrinos. The convolution also

1549 needed to as close as possible preserve the integrated counts of neutrinos. The optimized kernel
 1550 window for all lines is summarized as:

- 1551 • Guassian kernel with 2σ width = $3.5E-3 \cdot m_\chi$
 1552 • Minimum energy included in convolution = $\text{MIN}[0.995 \cdot m_\chi, E(\nu_{\text{line}}) - 4\sigma]$
 1553 • Maximum energy included in convolution = $\text{MAX}[1.005 \cdot m_\chi, E(\nu_{\text{line}}) + 4\sigma]$

1554 where $E(\nu_{\text{line}})$ is the neutrino energy where the neutrino line is at the maximum.

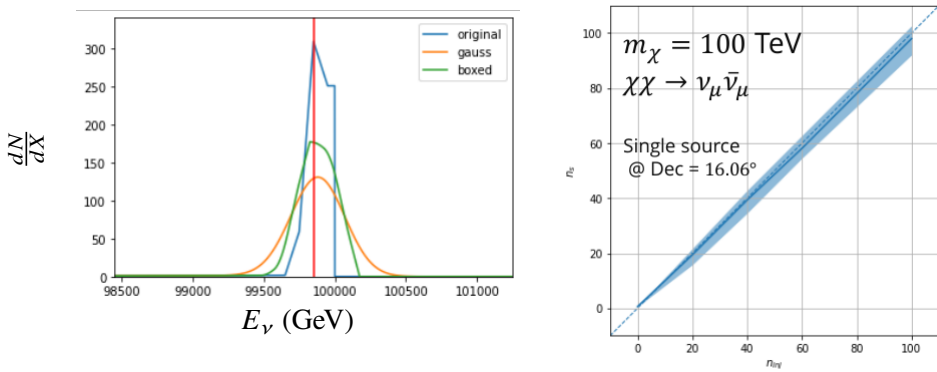


Figure 7.3 Left panel shows the two kernels overlaying the original spectrum from χaronv after propagation to Earth [71]. The vertical red line indicates where the original neutrino line is maximized. Blue line is the output from χaronv . Green line is the spectrum after convolution with a flat kernel. Orange line is the spectrum after Gaussian convolution. Right panel shows the signal recovery of the spectral model using the Gaussian kernel with parameters enumerated above.

1555 These parameters broadly improved the signal recovery of the line spectra. An example is in
 1556 Fig. 7.3. Signal recovery studies for are expanded upon in Section 7.6.

1557 7.3.1.2 Spline Fitting

1558 In an effort to reduce computational work, memory burden, and align with point source methods
 1559 used for NGC1068 [74], spectral splines were created and adopted for estimating the neutrino flux
 1560 for the different spectral models. Software was written to generate, book keep, and calculate values
 1561 on the splines.

1562 When using splines, one has to be careful of the goodness to fit. The spline software used here,
 1563 Photospline [75], uses the penalized spline technique. Through the penlized technique, poor fits

1564 are penalized according to the accuracy of the nominal value, and the smoothness of the first and
 1565 second derivatives. The B-spline construction however does not penalize on the integral of the fit
 1566 distribution which is critical in low signal studies, such as DM searches. There are additional caveats
 1567 when testing the goodness to fit to the MC generated above for all DM annihilation channels.

- 1568 • The splines must be Log10(*) in Energy and dN/dE to account for the exponential nature of
 1569 the flux.
- 1570 • The fidelity of the fit matters more at $E_\nu \approx m_\chi$ where the model uncertainties are minimal
 1571 and physical considerations (like the cut-off) are most important.
- 1572 • The fidelity of the fit matters less at low E_ν as the model uncertainties are large AND
 1573 IceCube's sensitivity diminishes significantly below 500 GeV.
- 1574 • Total integrated counts should be well preserved.

1575 The resulting cost function was built to evaluate the goodness of spline fits to account for the above
 1576 considerations.

$$e_i = x_i \cdot \left(\frac{dN_i}{dE_i} - 10^{\hat{e}_i} \right) \quad (7.3)$$

1577 Where \hat{e}_i is the spline estimator's value for x_i . $x_i = E_{\nu_i}/m_\chi$. $\frac{dN_i}{dE_i}$ is the flux value from MC. I then
 1578 take the RMS of the error distribution and the resulting value, err, is used to evaluate the fidelity of
 1579 the spectral spline.

$$\text{err} = \sqrt{\frac{1}{x_{\max} - x_{\min}} \int_{x_{\min}}^{x_{\max}} e^2 dx} \quad (7.4)$$

1580 Each SM channel had unique tolerances for 'err'. Channels with very hard cut-offs had looser
 1581 tolerance for err because a significant error would be generated from single counts over/underes-
 1582 timated at the cut-off. Soft channels do not share this issue, so the tolerance is much stricter. All
 1583 annihilation channels from HDM are modeled well below IceCube's NST sensitivity. We do not
 1584 think it is necessary to evaluate the spline fits below 100 GeV [72] and use this value as the default
 1585 lower cut-off. Yet, HDM's model uncertainties at $E_\nu < 10^{-6} \cdot m_\chi$ span an order of magnitude
 1586 [65]. We also choose not to evaluate the splines below this critical value if it is within IceCube's

$\chi\chi \rightarrow$	GOOD	OK	FAIL	Limits of err calc [X_{min}, X_{max}]
$Z^0 Z^0, W^+ W^-$	1.0E-3	1.0E-3, 1.0E-2	1.0E-2	MAX[100GeV/ m_χ , 10^{-6}], 1.0
$t\bar{t}, hh$	1.0E-5	1.0E-5, 1.0E-4	1.0E-4	MAX[100GeV/ m_χ , 10^{-6}], 1.0
$b\bar{b}, d\bar{d}, u\bar{u}$	9.0E-7	9.0E-7, 9.0E-6	9.0E-6	MAX[100GeV/ m_χ , 10^{-6}], 1.0
$\nu\bar{\nu}_{e,\mu,\tau}$	1.0E-3	1.0E-3, 1.0E-2	1.0E-2	MAX[100GeV/ m_χ , 10^{-6}], MIN[0.995, ($E_n(\nu_{line}) - 4\sigma$)/ M_χ]
$e\bar{e}, \mu\bar{\mu}, \tau\bar{\tau}$	1.0E-3	1.0E-3, 1.0E-2	1.0E-2	MAX[100GeV/ m_χ , 10^{-6}], MIN[0.995, ($E_n(\nu_{line}) - 4\sigma$)/ M_χ]

Table 7.1 Spline err tolerances used for input in particle physics component to Eq. (7.1). Column 1 is the DM annihilation channel being fit. Columns 2, 3, and 4 are the tolerances for "GOOD" (pass), "OK" requires inspection, and "FAIL" (tune and refit) respectively. Column 5 has the X ranges over which the error is evaluated. MAX/MIN [·, ·] takes the maximum or minimum of the two enclosed values.

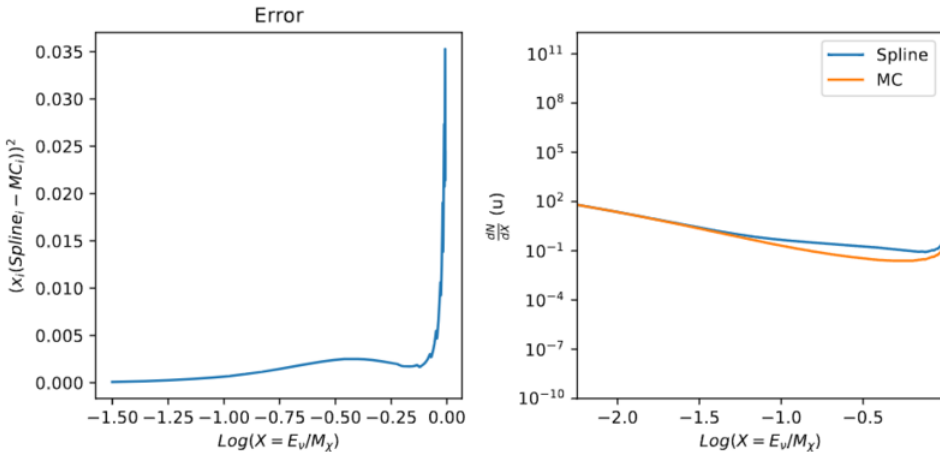


Figure 7.4 Example spline that failed the fit. Failed splines are corrected on a case by case basis unless the SM channel has a systematic problem fitting the splines. In this case, I made a bookkeeping error and loaded the incorrect spectral model

1587 sensitivity. Finally, the smoothing of the spectral lines in leptonic annihilation channels are ignored
 1588 for evaluating the fit. We used the lower limit of the kernel mask as the upper limit of evaluation.
 1589 Table 7.1 summarizes the tolerances for the DM annihilation channels used for this analysis.

1590 The errors are then plotted in two ways. First, FAIL and OK are directly plotted with e_i as a
 1591 function of x, and the full spline and MC. An example of a single failure is provided in Fig. 7.4
 1592 Second, a summary plot of all the splines is plotted and colors coded. Figure C.1 are the spline
 1593 summaries as of writing this thesis. The goal broadly is to eliminate all red and inspect yellow
 1594 statuses.

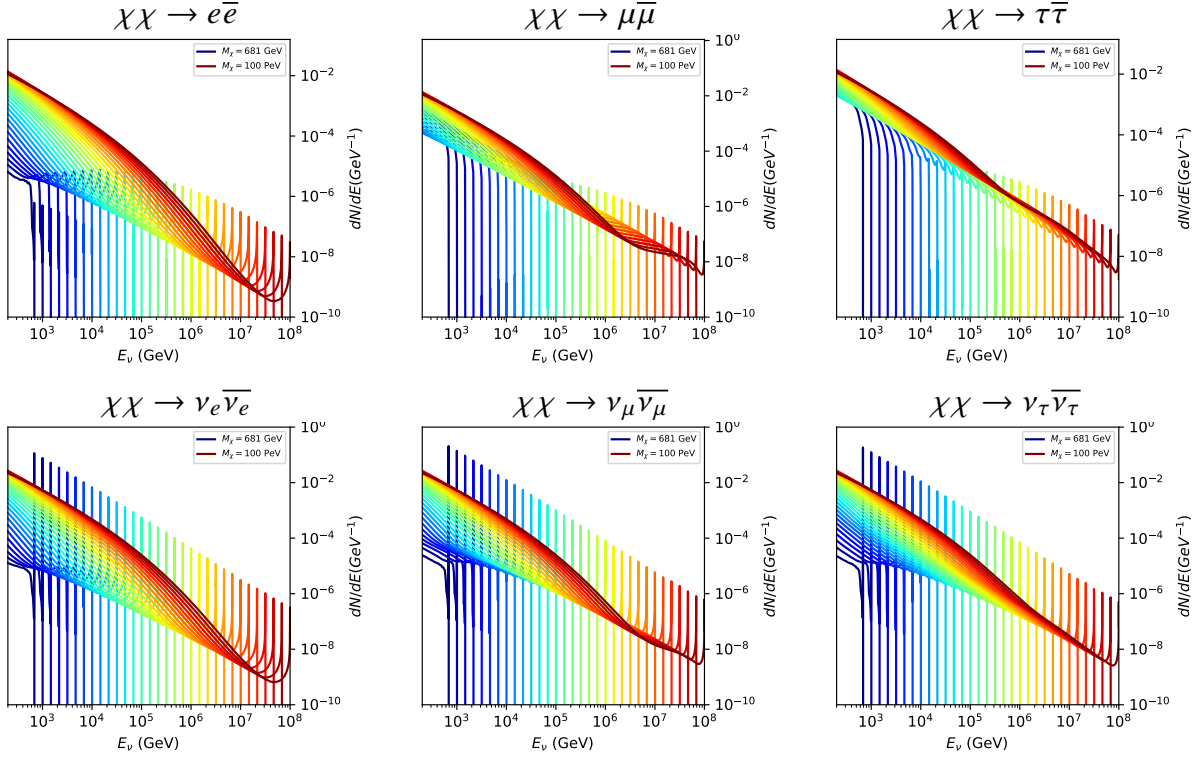


Figure 7.5 Summary of input spectral models that were smoothed with Gaussian kernel. Spectral models are for $\chi\chi \rightarrow e\bar{e}$, $\mu\bar{\mu}\tau\bar{\tau}$, $\nu_e\bar{\nu}_e$, $\nu_\mu\bar{\nu}_\mu$, and $\nu_\tau\bar{\nu}_\tau$. These spectra are the composite ($\nu_\mu + \nu_\tau$) of neutrino flavors. Every spectral model used for this analysis is featured as a colored solid line. Bluer lines are for lower DM mass spectral models. DM masses range from 681 GeV to 100 PeV. HDM [65], χ arov [71], and Photospline [75] are used to generate these spectra. Energy (x-axis) was chosen to roughly represent the energy sensitivity of NST.

1595 The ν_e spectra at Earth are not considered in this analysis, so no work was done to refine the
 1596 spline fits for this flavor. A Final inspection of the splines by eye to verify that the spline fitting did
 1597 not introduce spurious features into the distribution that would corrupt the likelihood fitting.

1598 7.3.1.3 Composite Neutrino Spectra

1599 With all of the previously mentioned pieces, we are ready to fully assemble a comprehensive
 1600 description of the particle physics term dN/dE in Eq. (7.1).

$$\frac{dN_\nu}{dE_{\nu_\oplus}} = \left(\frac{dN_{\nu_e}}{dE_{\nu_e}} + \frac{dN_{\nu_\mu}}{dE_{\nu_\mu}} + \frac{dN_{\nu_\tau}}{dE_{\nu_\tau}} \right)_{\text{src}} \cdot \mathbf{P}(\nu_\alpha \rightarrow \nu_\beta) \quad (7.5)$$

1601 Figure 7.5 shows the spectral models that required Gaussian smoothing, the leptonic annihilation
 1602 channels. The remaining models where the only processing was spline fitting are documented in
 1603 Section C.3. Notice that the different neutrino flavors are unique, especially in their low energy

1604 tails. Therefore, this analysis will be sensitive to DM annihilating to the distinct neutrino flavors.

1605 **7.3.2 *J*- Astrophysical Component**

1606 For this analysis, we re-adopt the \mathcal{GS} model used in Sec. 5 for dSph from [45]. These
1607 models are based on a modified Navarro-Frenk-White (NFW) profile where the indices of the NFW
1608 (traditionally 1,3,1) are allowed to float. The angular width of these sources is much smaller than
1609 the angular resolution of IceCube NST [74]. We therefore treat these sources as point sources in
1610 this analysis, and forgo generating maps. These sources and the \mathcal{GS} model have already been
1611 discussed at length in Section 5.3.2 and is not repeated here. IceCube uses identical sources to
1612 Tab. 5.1 except we analyze source with declinations above 0.0 degrees.

1613 **7.3.3 Source Selection and Annihilation Channels**

1614 We use all of the dSphs presented in IceCube’s previous dSph DM search [69]. IceCube’s
1615 sources for these simulation studies include Bootes I, Canes Venatici I, Canes Venatici II, Coma
1616 Berenices, Draco, Hercules, Leo I, Leo II, Leo V, Leo T, Segue 1, Segue 2, Ursa Major I, Ursa
1617 Major II, and Ursa Minor. A full description of all sources used is in Table 5.1. Sources with
1618 declinations less than 0.0 are excluded from this analysis.

1619 This analysis improves on the previous IceCube dSph paper [69] in the following ways. Pre-
1620 viously, the IceCube detector was not yet completed to the 86 string configuration. Many more
1621 dSphs will be observed, from 4 to 15. Previously, the particle physics model used for neutrino-ray
1622 spectra from DM annihilation did not have EW corrections where they are now included [65]. The
1623 spectral models also predict substantial differences between the neutrino flavors, so this analysis
1624 will be the first DM dwarf analysis to discriminate between primary neutrino flavors. The study
1625 performed here studies 10.4 years of data.

1626 The SM annihilation channels probed for this study include $\chi\chi \rightarrow$

1627 $b\bar{b}, t\bar{t}, u\bar{u}, d\bar{d}, e\bar{e}, \mu\bar{\mu}, \tau\bar{\tau}, ZZ, W^+W^-, \nu_e\bar{\nu}_e, \nu_\mu\bar{\nu}_\mu$, and $\nu_\tau\bar{\nu}_\tau$

1628 **7.4 Likelihood Methods**

1629 I use the Point-Source search likelihood which is widely used in IceCube analyses. The
1630 likelihood function is defined as the following:

$$L(n_s) = \prod_{i=1}^N \left[\frac{n_s}{N} S_i + \left(1 - \frac{n_s}{N}\right) B_i \right] \quad (7.6)$$

1631 where i is an event index, S and B are the signal PDF and background PDF respectively. For a joint
1632 analysis where the sources are stacked the likelihood is expanded in the simplified way:

$$L(n_s) = \prod_{i=1}^{N_{\text{sources}}} L_i(n_s) \quad (7.7)$$

1633 Where L_i is the likelihood from the i -th source in the stacked analysis. The Test Statistic (TS)
1634 definition remains the same as Eq. (5.7)

1635 **7.5 Background Simulation**

1636 Before we look at data, we must first analyze background and signal injection to validate our
1637 analysis. This is in part because the TS distributions are not expected to behave according to a
1638 chi-squared distribution with 1 degree of freedom. TS distributions can also vary significantly
1639 between DM mass and annihilation models. Therefor, Wilks' theorem may not be applicable to the
1640 analysis. Instead, a critical value is defined from a large number of background trials. We study the
1641 TS distributions first for each source, then for the stacked analysis. The following sections show
1642 the results of the likelihood fitting for a suite of background trials.

1643 I assume that TS values are physical: $\text{TS} \geq 0$. η denotes the fraction of positive TS values
1644 above the threshold and written in the legend of the TS distributions. $\epsilon[x]$ indicate the fraction
1645 of events where $\text{TS} < x$. For TS plots shown here, the decimal values of x are 1.0e-2 and 1.0e-3.
1646 Each subplot represents a simulation of 100,000 data-scrambled background trials. ?? show the
1647 background TS distributions obtained from Segue 1, a source with little Earth attenuation and
1648 large J -factor, and Ursa Major II, similarly large J -fator but significantly more Earth attenuation,
1649 assuming that dark matter annihilates into $b\bar{b}$, $\tau\bar{\tau}$, and $\nu_\mu\bar{\nu}_\mu$. I show the TS distributions of a
1650 stacked study of 15 sources for all DM annihilation channels.

1651 **7.5.1 TS per Source**

1652 Figure 7.6 to Figure 7.11 present the TS distributions for Segue 1 and Ursa Major II for 100,000
1653 trials. More studies for all annihilation channels and remaining 13 sources were also performed
1654 and are documented in IceCube’s internal wiki.

1655 Although it was not expected, almost every distribution produced follows a χ^2 distribution with
1656 1 degree of freedom. This is important for future assumptions made in Sec. 8 and may justify
1657 statistical calculations assuming Wilk’s theorem is valid.

1658 **7.5.2 Stacked TS**

1659 Figure 7.12 to Figure 7.22 present the TS distributions for a stacked study of 15 sources with
1660 \mathcal{GS} J -factors on 100,000 trials. The presentation of these plots are identical to the single source
1661 distributions in Section 7.5.1.

1662 Each subplot, except the final, is the TS distribution for a specific DM mass listed in the subplot.
1663 The final subplot plots the all DM spectral models used as input for the TS distribution calculations
1664 with bluer lines indicating lower DM mass and redder indicating higher DM mass.

1665 **7.6 Signal Recovery**

1666 We also wish to understand how well the analysis is able to reconstruct signal neutrinos. In
1667 order to test this, we inject neutrinos from our spectral models randomly then attempt to discern the
1668 number of signal neutrinos in the data. Figure 7.23 and Figure 7.24 show this study for $\chi\chi \rightarrow b\bar{b}$,
1669 $t\bar{t}$, and $\nu_\mu\bar{\nu}_\mu$ for a stacked analysis of 15 sources. We see that the analysis is conservative at smaller
1670 m_χ , yet improves at larger m_χ . We also see that the uncertainty around the reconstructed signal
1671 events shrinks for the neutrino annihilation spectra.

1672 **7.6.1 Sensitivities**

1673 In IceCube, we usually define the 90% confidence level (CL), as the minimum number of signal
1674 events (n_s) required to have a Type I error rate smaller than 0.5 and Type II error rate of 0.1. We
1675 compute n_s from the following equation

$$n_s = T_{live} \int_0^{\Delta\Omega} d\Omega \int_{E_{min}}^{E_{max}} dE_\nu A_{eff}(\hat{n}, E_\nu) \frac{d\Phi_\nu}{d\Omega dE_\nu}(\hat{n}, E_\nu), \quad (7.8)$$

1676 to extract the sensitivity on the dark matter annihilation cross-section. T_{live} is the detector livetime,
1677 A_{eff} is the effective area of the detector, and $E_{\text{min}}, E_{\text{max}}$ are the minimum, maximum energies of
1678 the expected neutrinos, respectively.

1679 Sensitivities are calculated for each source individually as if they were the only source and as a
1680 stack over 1000 trials. From Eq. (7.8) and Eq. (7.1) we can compute the $\langle \sigma v \rangle$ at a 90% confidence
1681 level. Figure 7.25 and Fig. 7.26 show the sensitivities for some DM annihilation channels. Not
1682 all channels computed successfully in time for the writing of this dissertation. Among channels
1683 missing include two neutrino flavors: e and τ .

1684 7.7 Systematics

1685 Lol What Systematics. Beside signal recovery we don't have many additional studies for here.
1686 The current analysis plan is to compare these sensitivities to another J -factor catalog such as \mathcal{LS}
1687 [66]. Additionally, we set out to perform a standard suite of IceCube systematic studies which
1688 include: **TODO: THE BIG 4: ICE MODEL ETC**

1689 7.8 Conclusions

1690 We built many things for this analysis. We utilized advanced computing techniques like
1691 parallel programming and spline fitting of particle physics Monte Carlo to greatly expand and
1692 refine IceCube's sensitivity to DM annihilation from dSphs. We imported updated astrophysical
1693 and particle physics models that better represent what we believe neutrino signals from DM
1694 annihilation should look like. We, for the first time, build an analysis that is sensitivity to PeV DM
1695 annihilation.

1696 When we compare to previous IceCube publications of dSphs [69], we see an order of magnitude
1697 improvement to our sensitivity. This analysis has been working group approved within IceCube and
1698 has begun the unblinding process. This processes did not complete in time for this dissertation.
1699 Therefor we do not show data for this thesis and is the clear next step.

1700 The test statistic distributions in this analysis also demonstrate more characteristic behaviour
1701 compared to previous DM analyses. With a 10 year dataset, we finally have enough statistics to
1702 almost trivially combine with other photon observatories, such as HAWC. The first ground work for

1703 a multi-messenger DM search is provided with concluding remarks in Sec. 8.

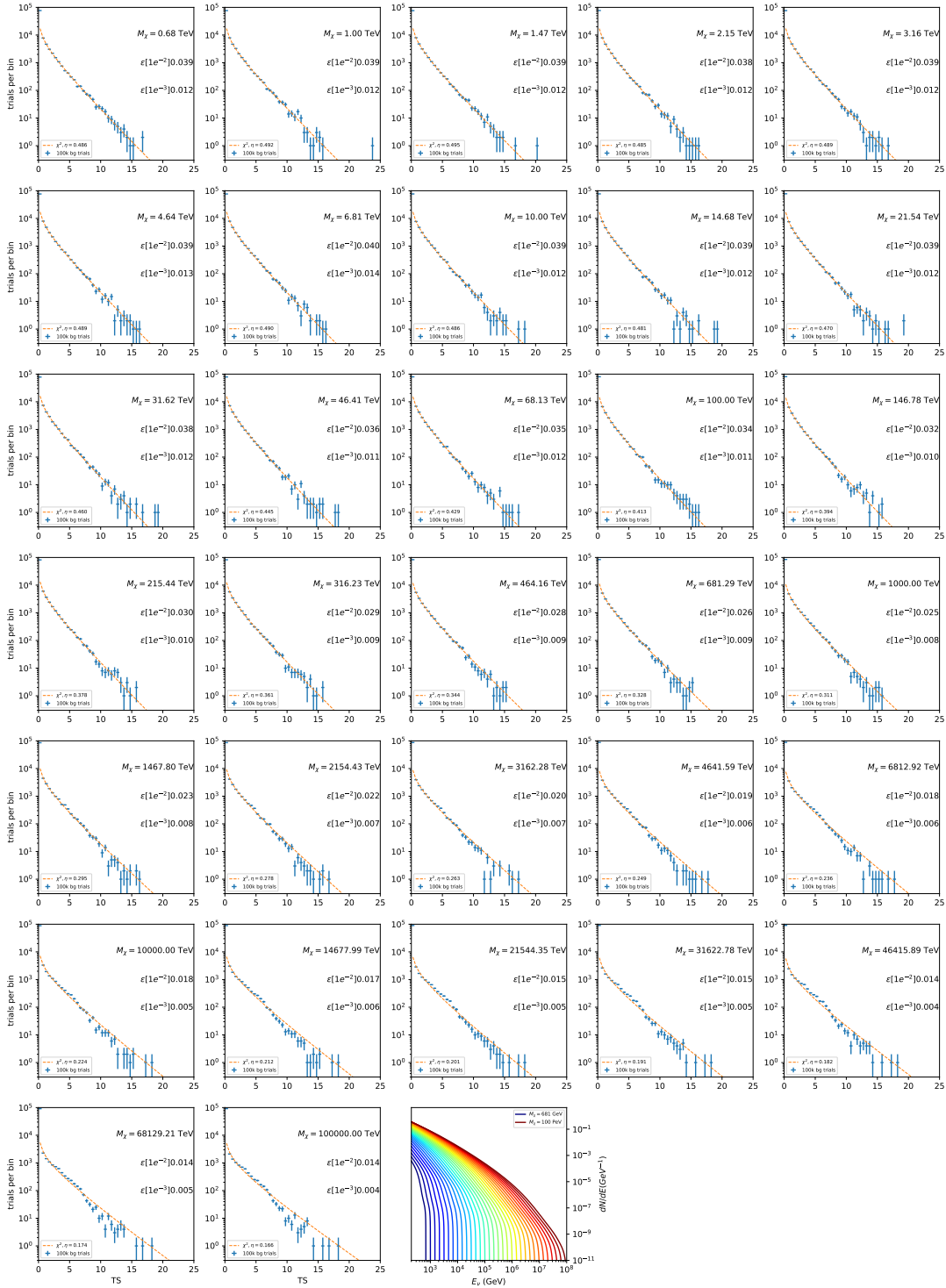


Figure 7.6 Test statistic (TS) distributions for Segue 1 and $\chi\chi \rightarrow b\bar{b}$. Each subplot, except the final, is the TS distribution for a specific DM mass listed in the subplot. Orange dashed lines are the traces for a χ^2 distribution with 1 degree of freedom. $\epsilon[\cdot]$ is the fraction of trials smaller than the bracketed value. The final subplot plots the all DM spectral models, similar to Fig. 7.5, used as input for the TS distributions.

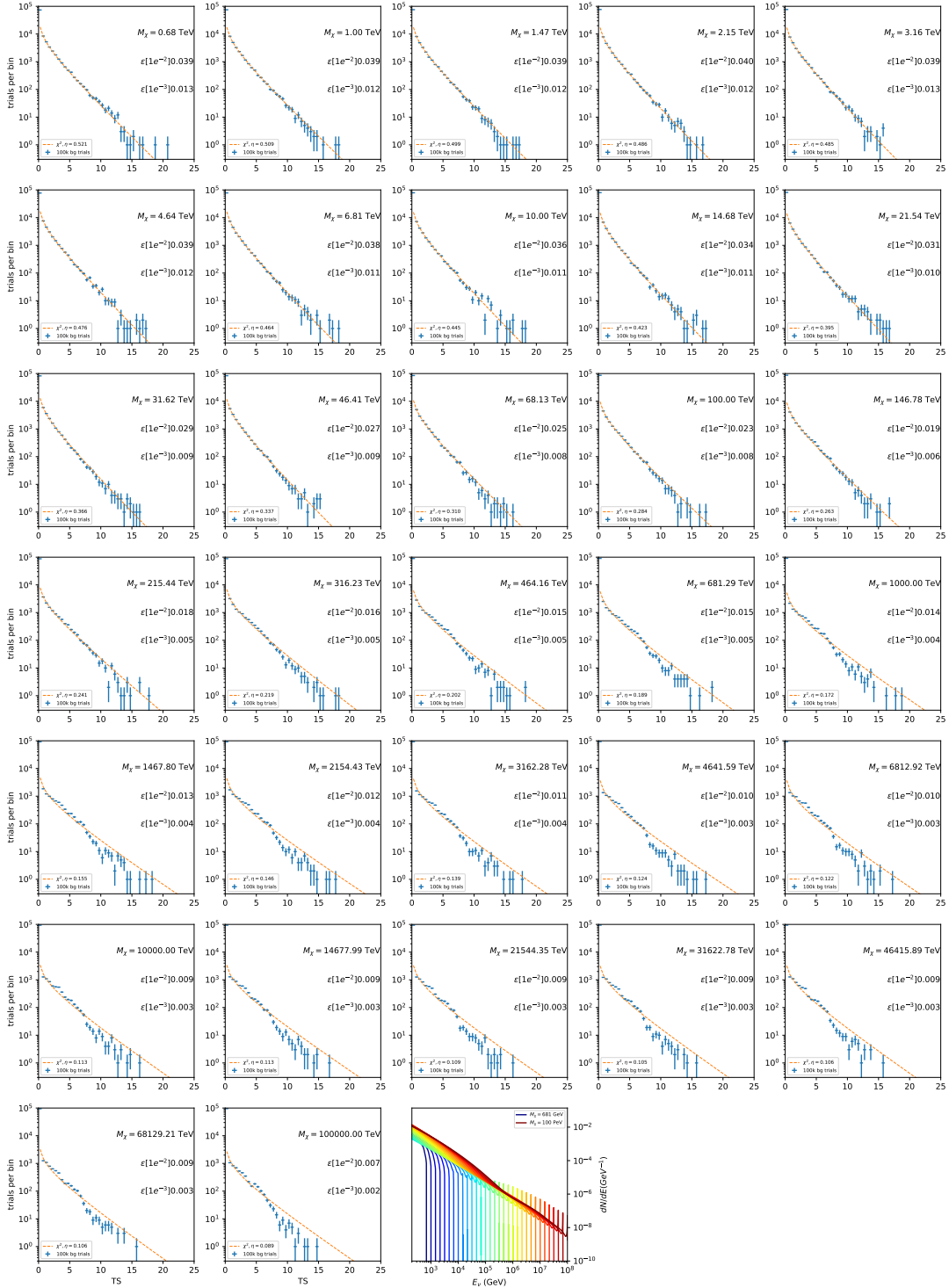


Figure 7.7 Same as Fig. 7.6 for Segue 1 $\chi\chi \rightarrow \tau\bar{\tau}$.

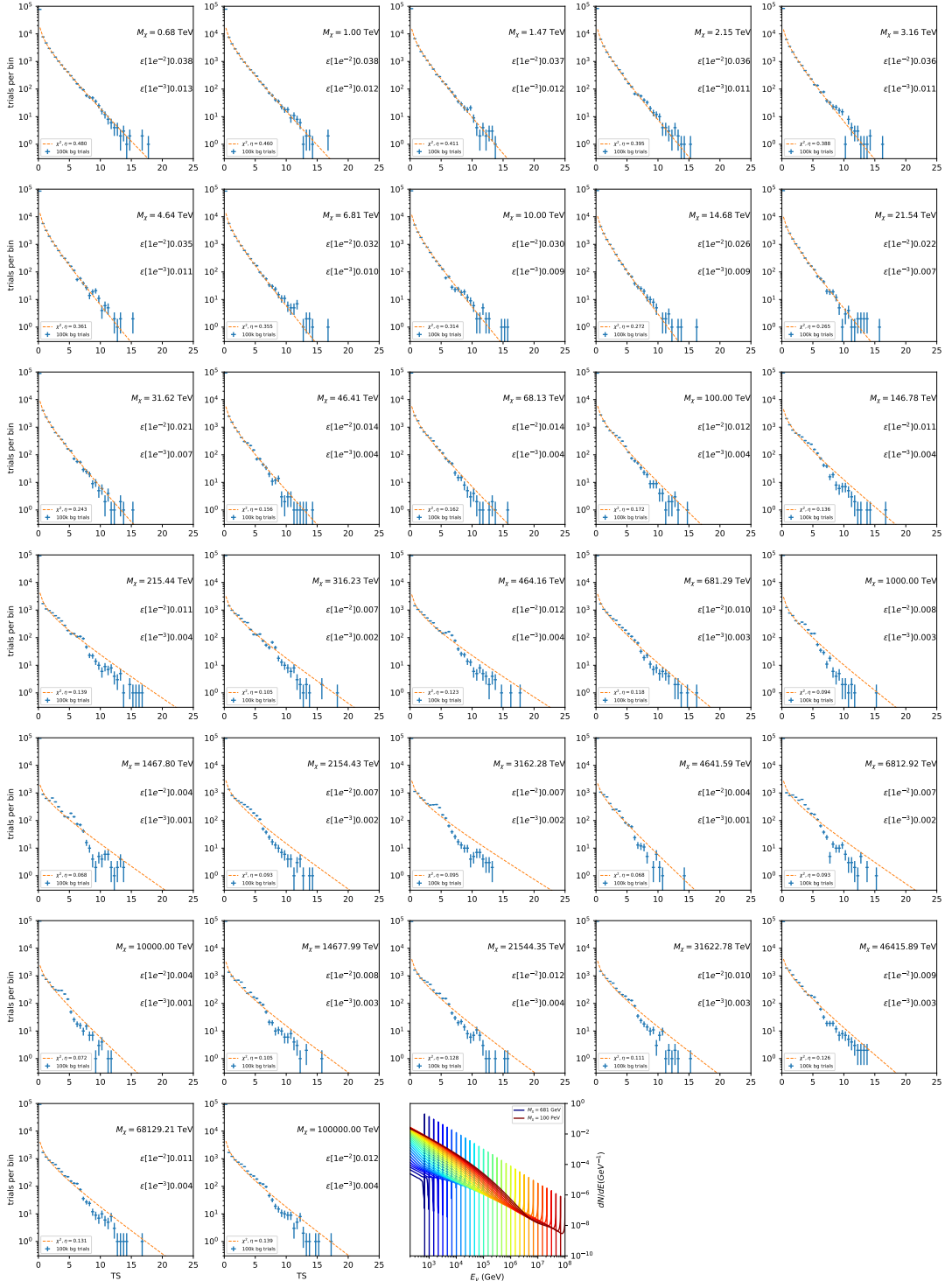


Figure 7.8 Same as Fig. 7.6 for Segue 1 $\chi\chi \rightarrow \nu_\mu\bar{\nu}_\mu$.

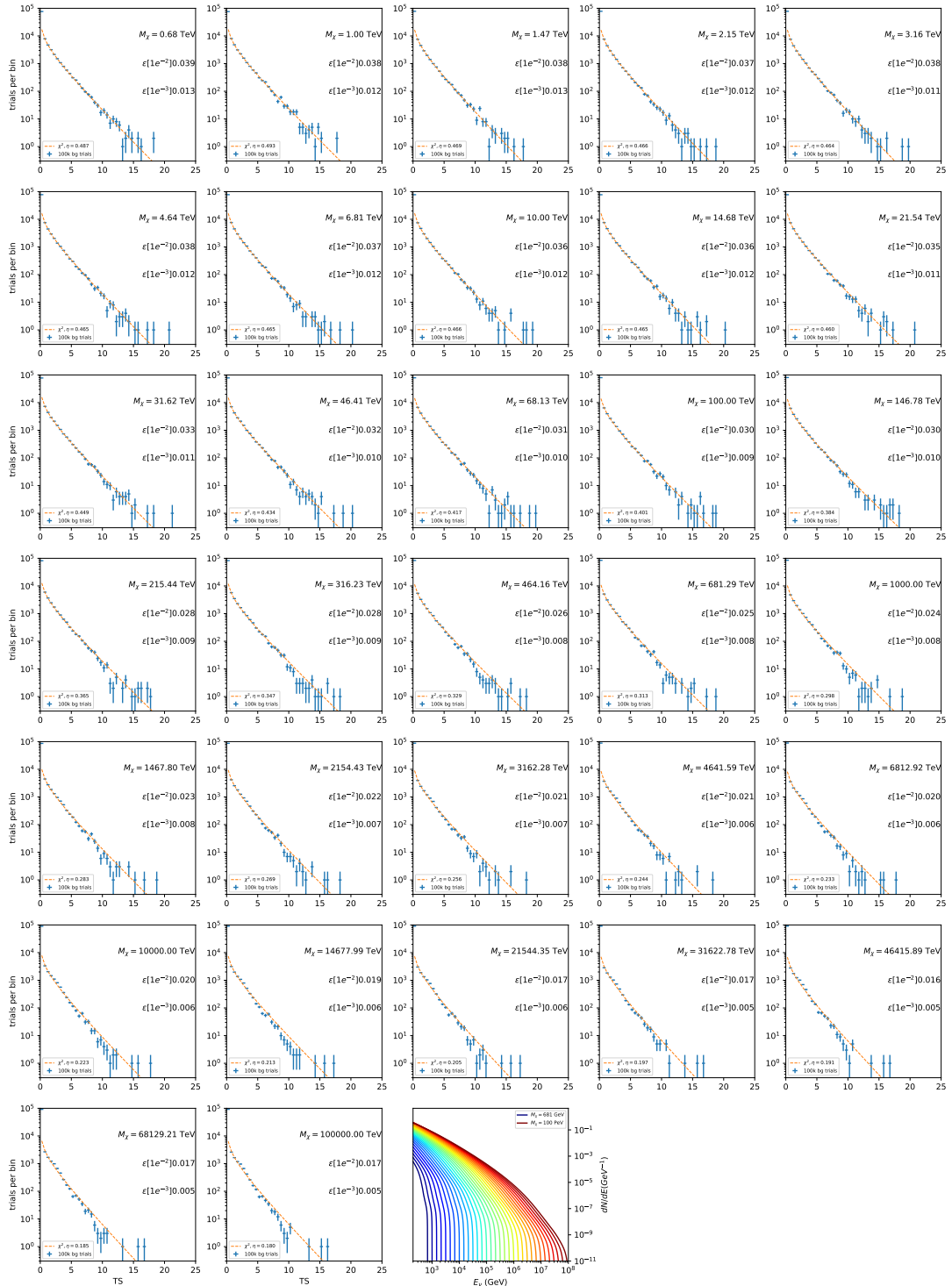


Figure 7.9 Same as Fig. 7.6 for Ursa Major II 1 $\chi\chi \rightarrow b\bar{b}$.

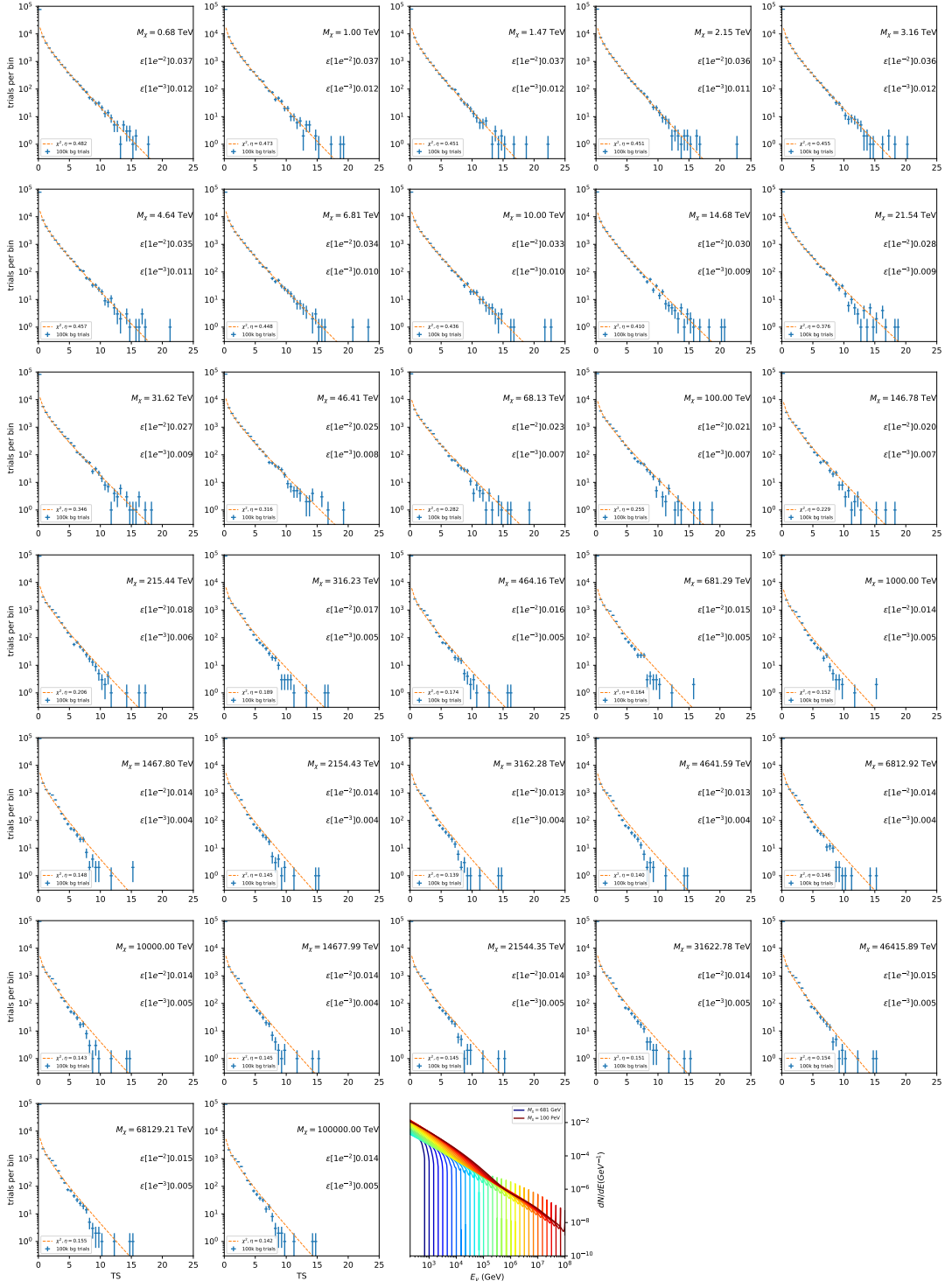


Figure 7.10 Same as Fig. 7.6 for Ursus Major II 1 $\chi\chi \rightarrow \tau\bar{\tau}$.

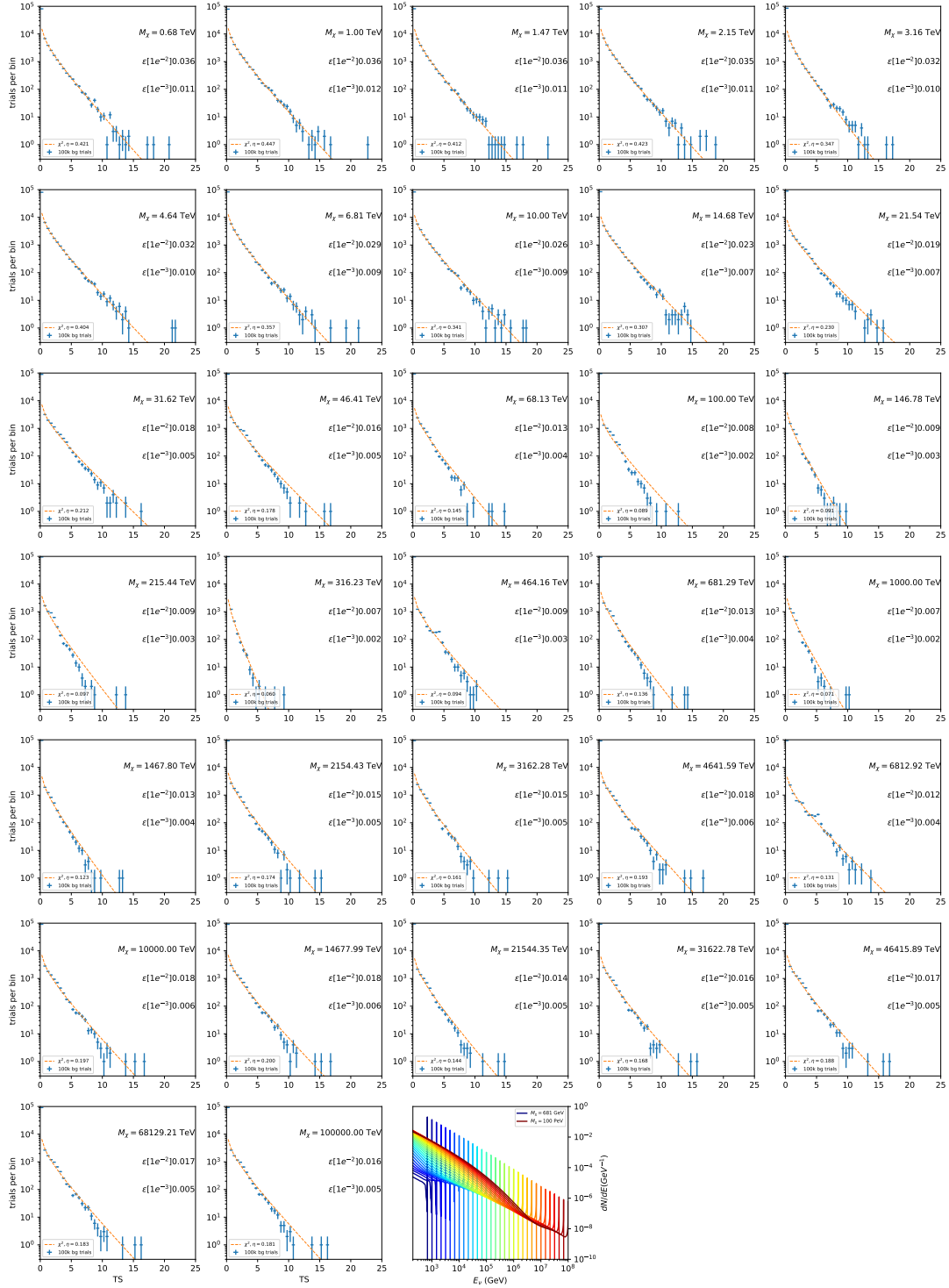


Figure 7.11 Same as Fig. 7.6 for Ursus Major II 1 $\chi\chi \rightarrow \nu_\mu\bar{\nu}_\mu$.

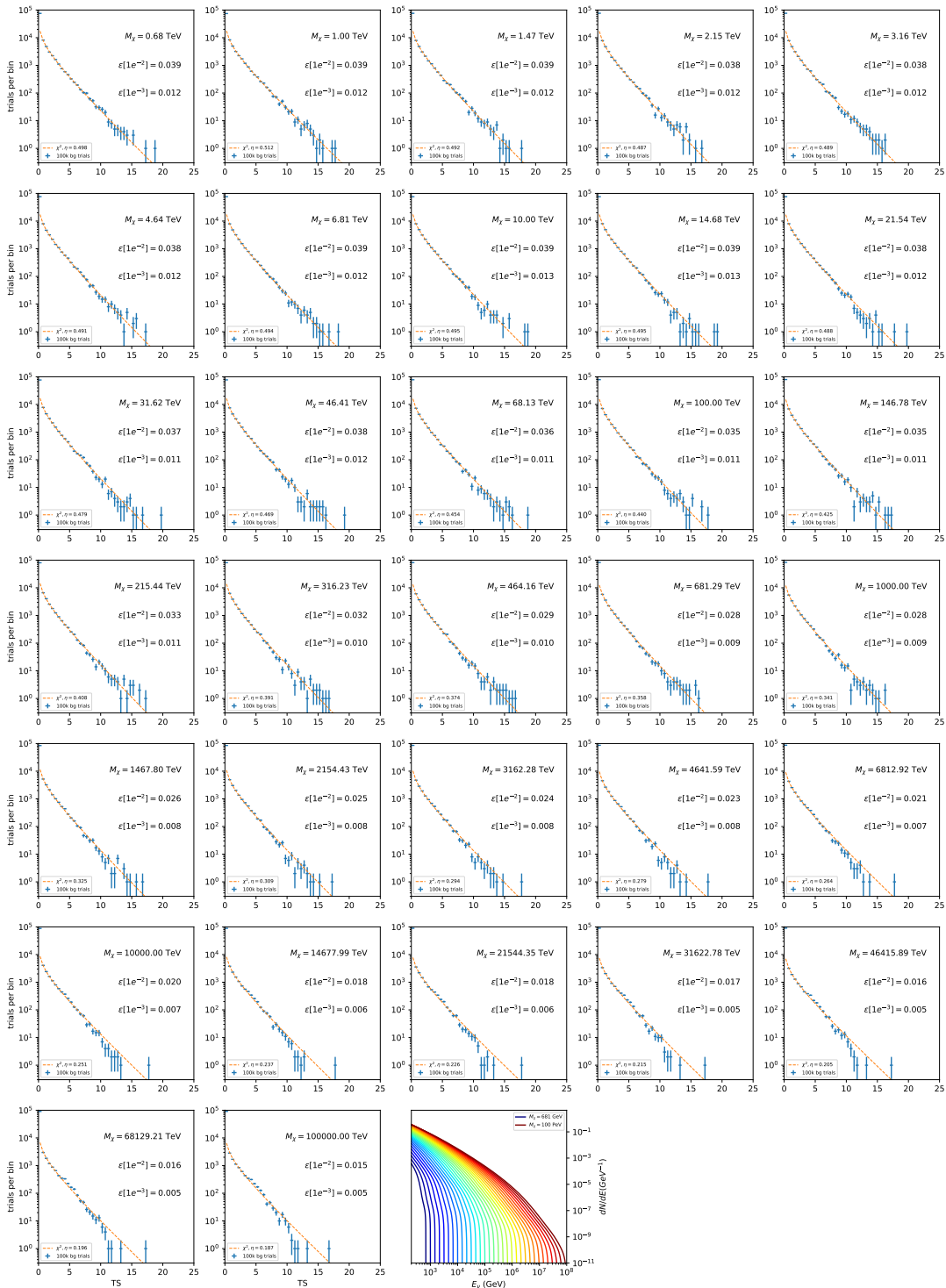


Figure 7.12 Same as Fig. 7.6 for 15, $\mathcal{G}\mathcal{S}$ J-factor, stacked sources and $\chi\chi \rightarrow b\bar{b}$.

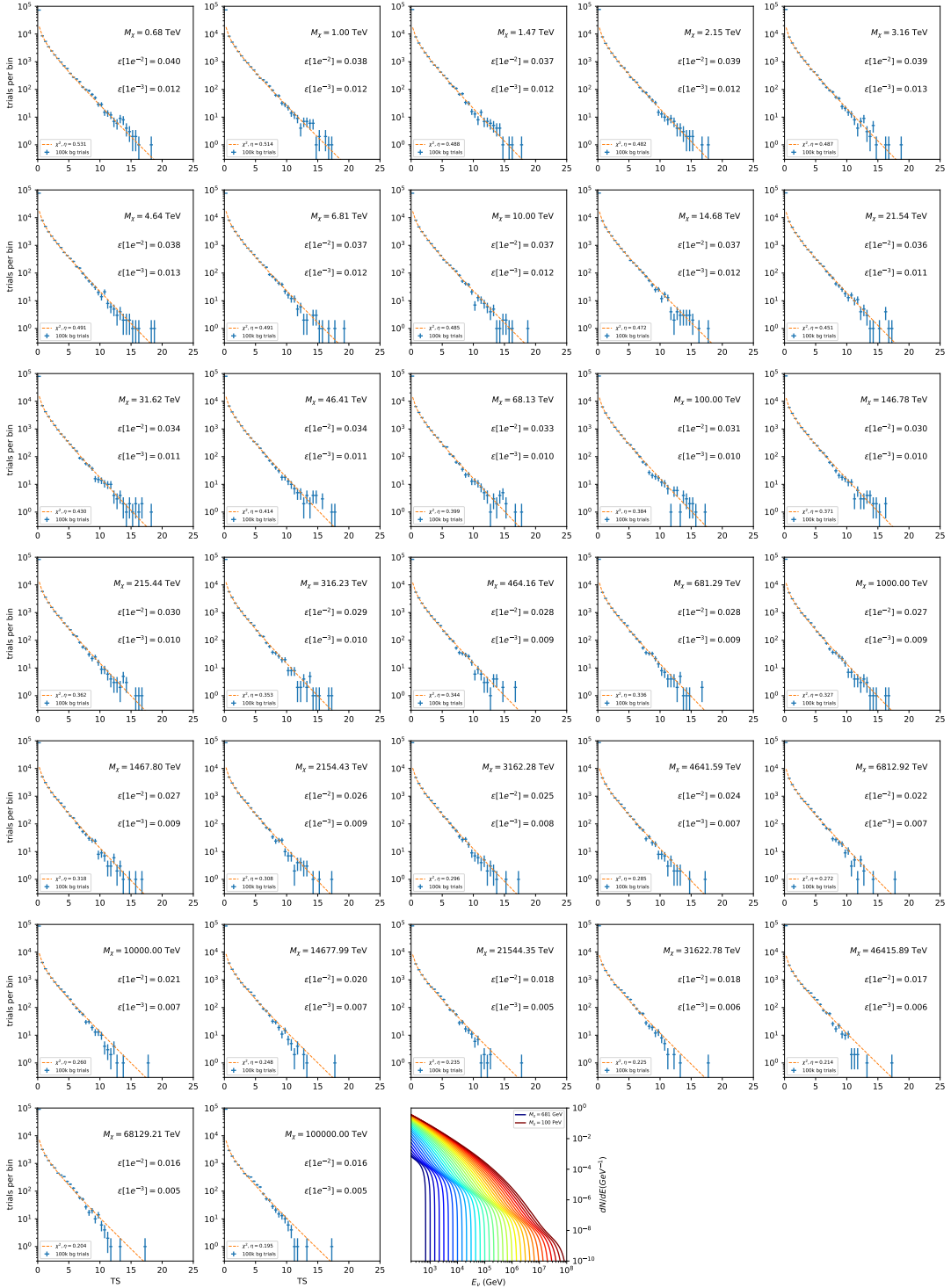


Figure 7.13 Same as Fig. 7.6 for 15, GS J-factor, stacked sources and $\chi\chi \rightarrow t\bar{t}$.

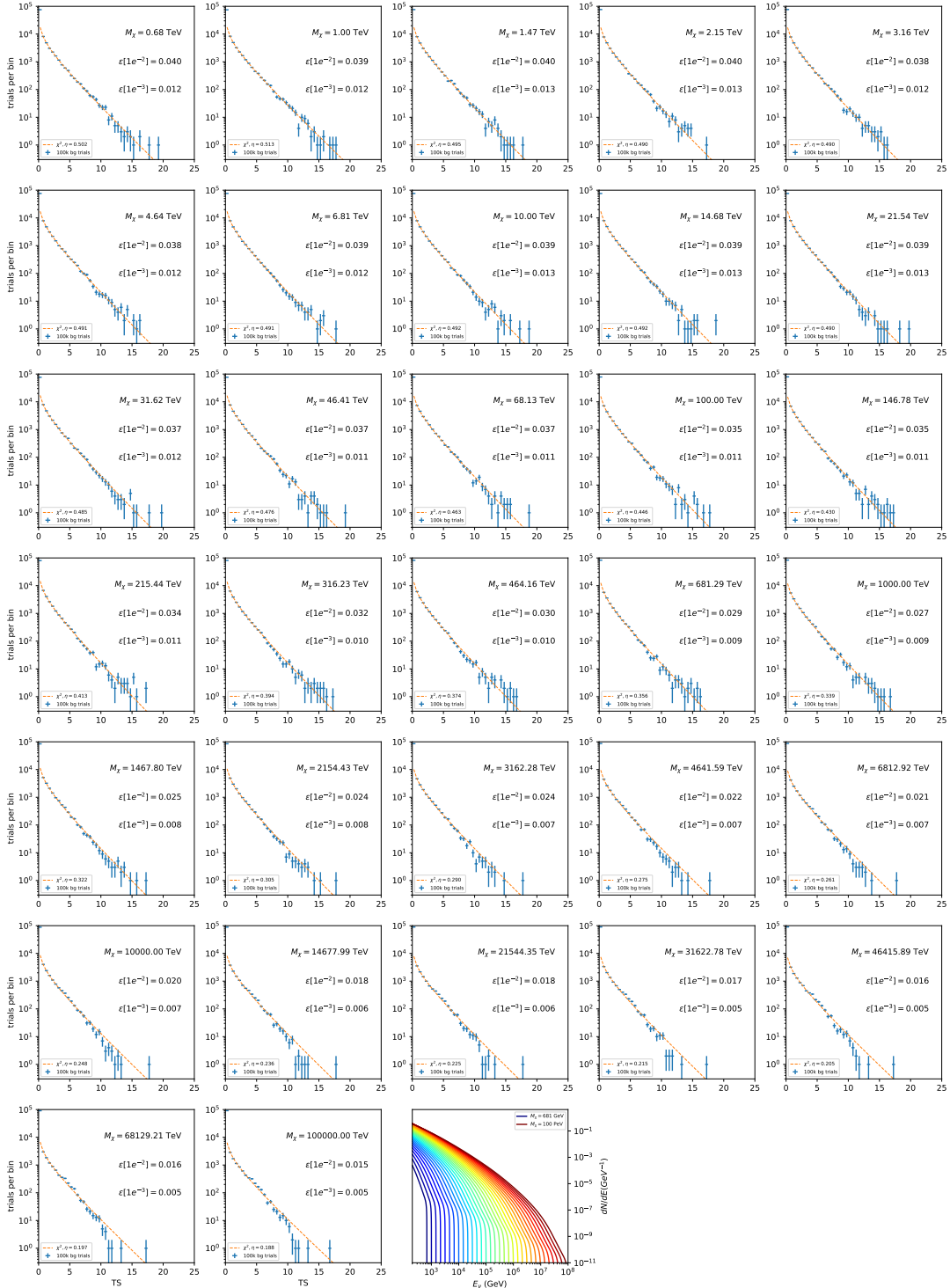


Figure 7.14 Same as Fig. 7.6 for 15, \mathcal{GS} J-factor, stacked sources and $\chi\chi \rightarrow u\bar{u}$.

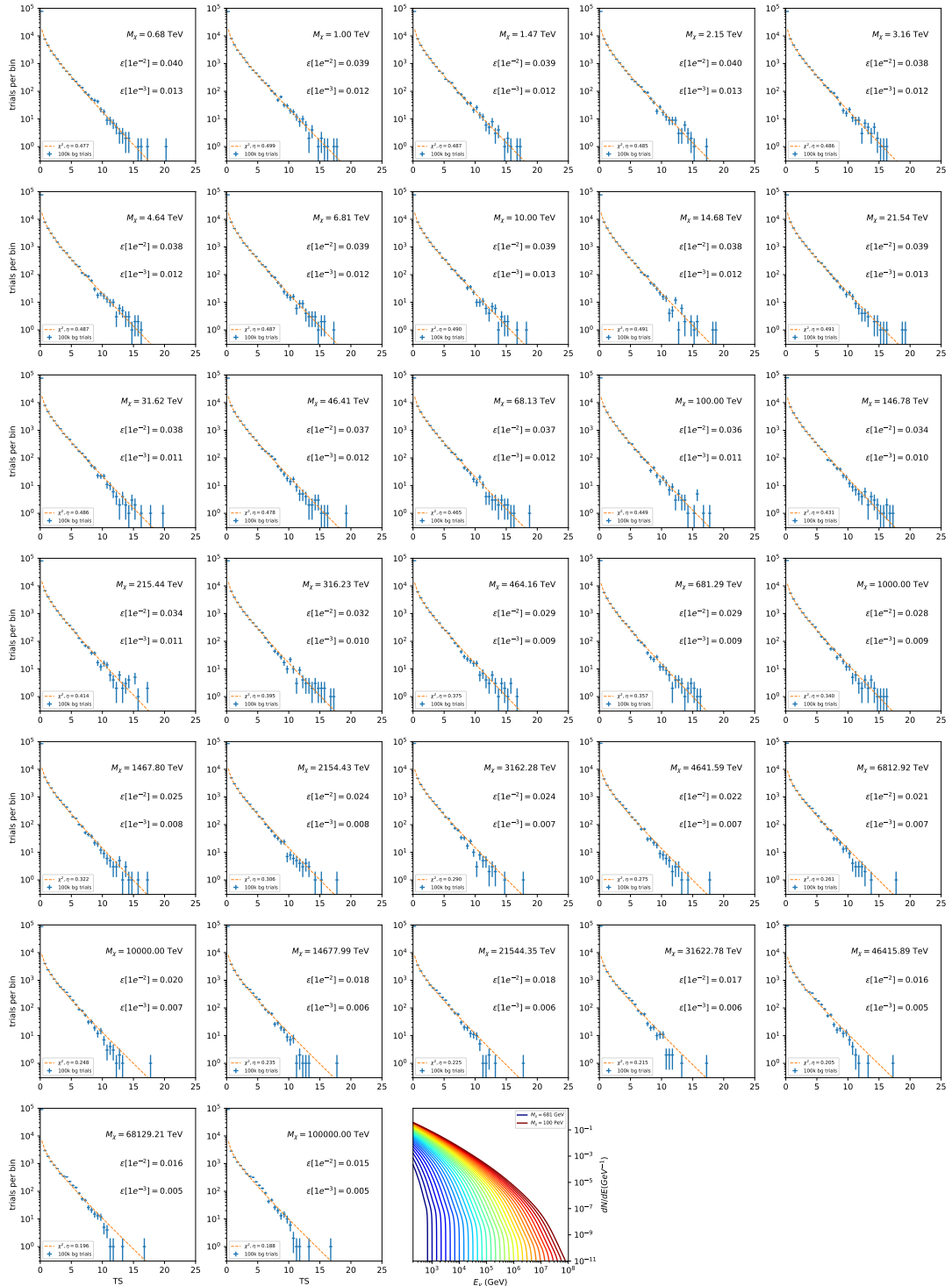


Figure 7.15 Same as Fig. 7.6 for 15, \mathcal{GS} J-factor, stacked sources and $\chi\chi \rightarrow d\bar{d}$.

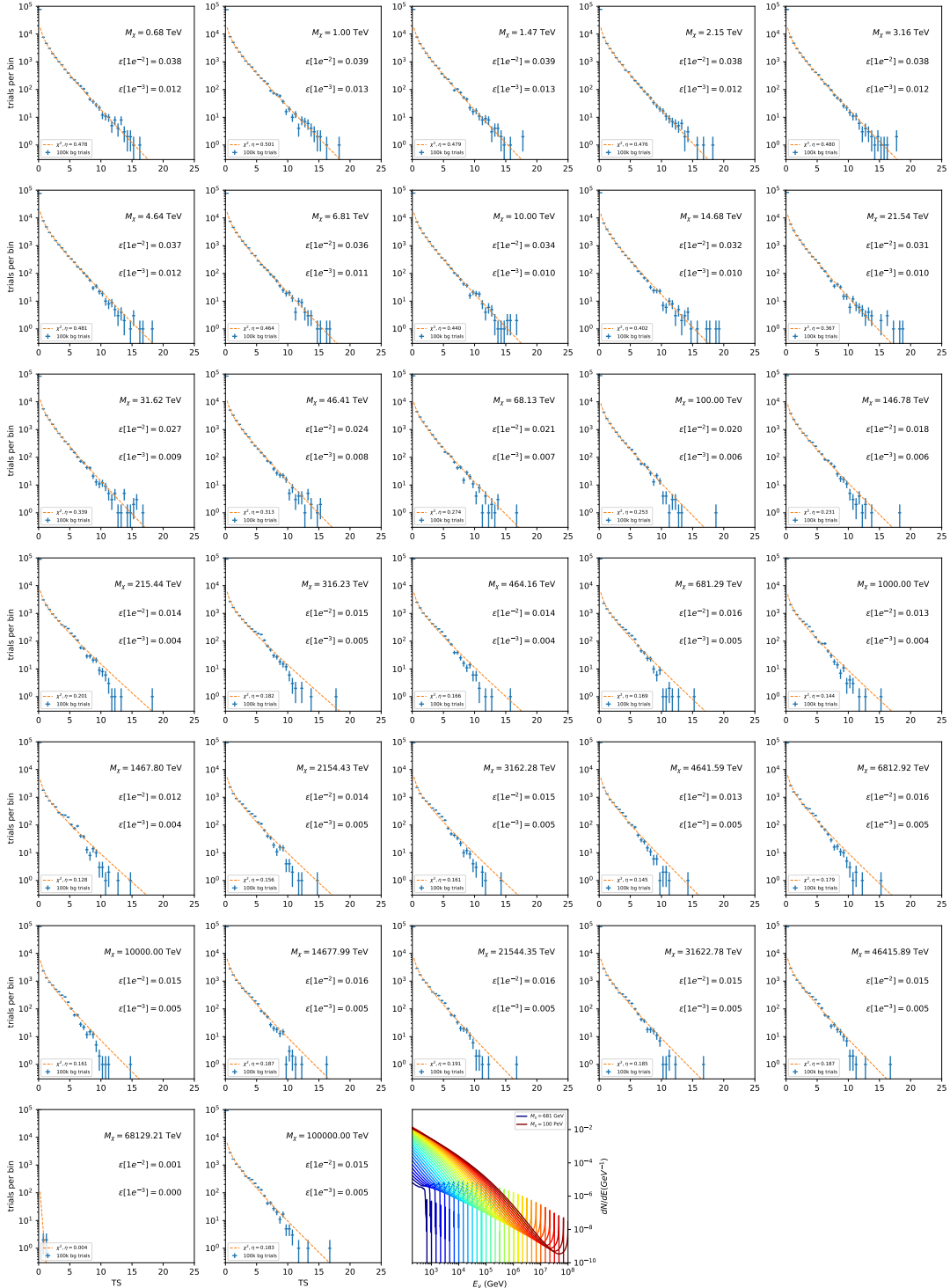


Figure 7.16 Same as Fig. 7.6 for 15, $\mathcal{G}\mathcal{S}$ J-factor, stacked sources and $\chi\chi \rightarrow e\bar{e}$.

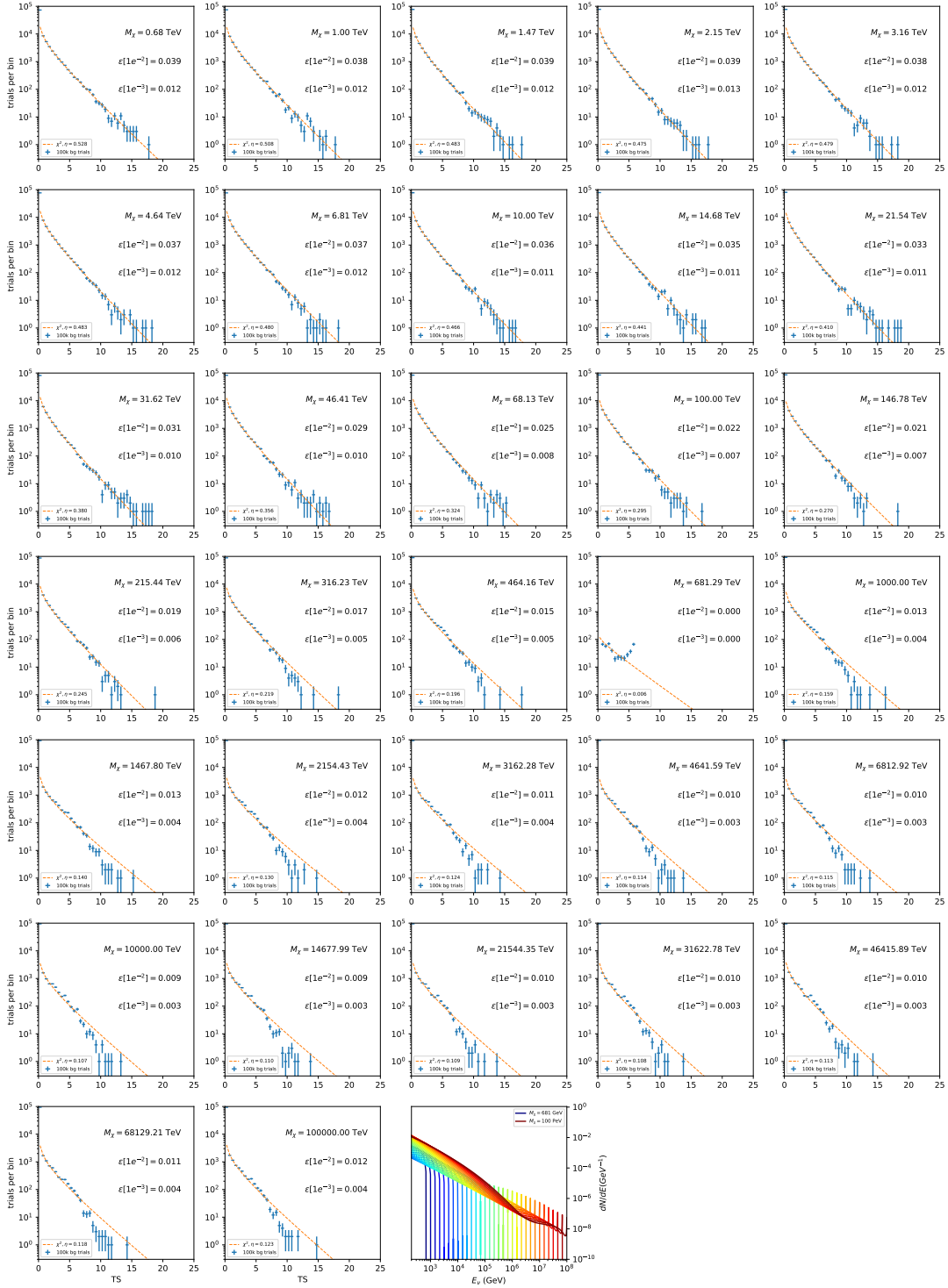


Figure 7.17 Same as Fig. 7.6 for 15, \mathcal{GS} J -factor, stacked sources and $\chi\chi \rightarrow \mu\bar{\mu}$.

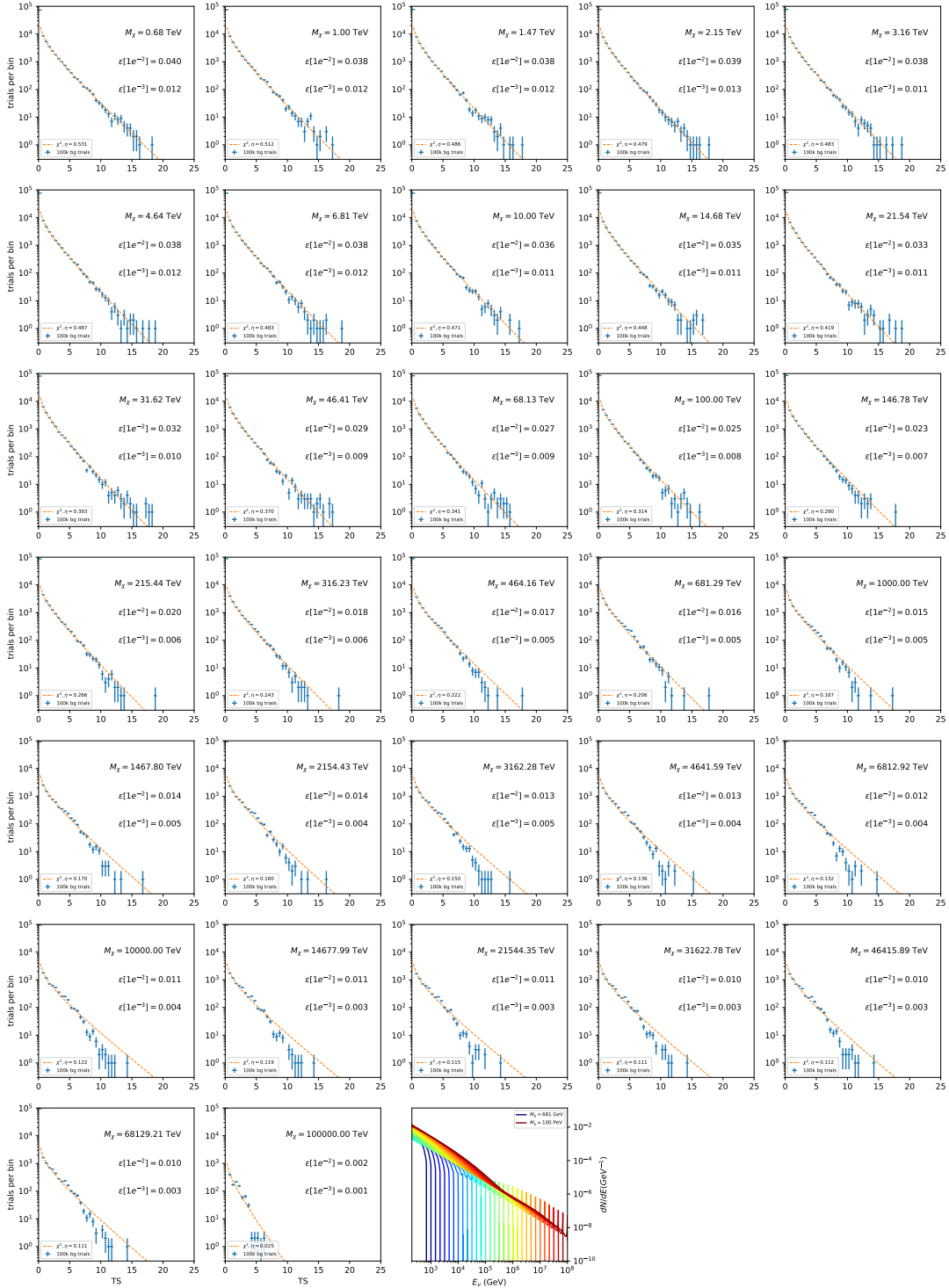


Figure 7.18 Same as Fig. 7.6 for 15, \mathcal{GS} J-factor, stacked sources and $\chi\chi \rightarrow \tau\bar{\tau}$.

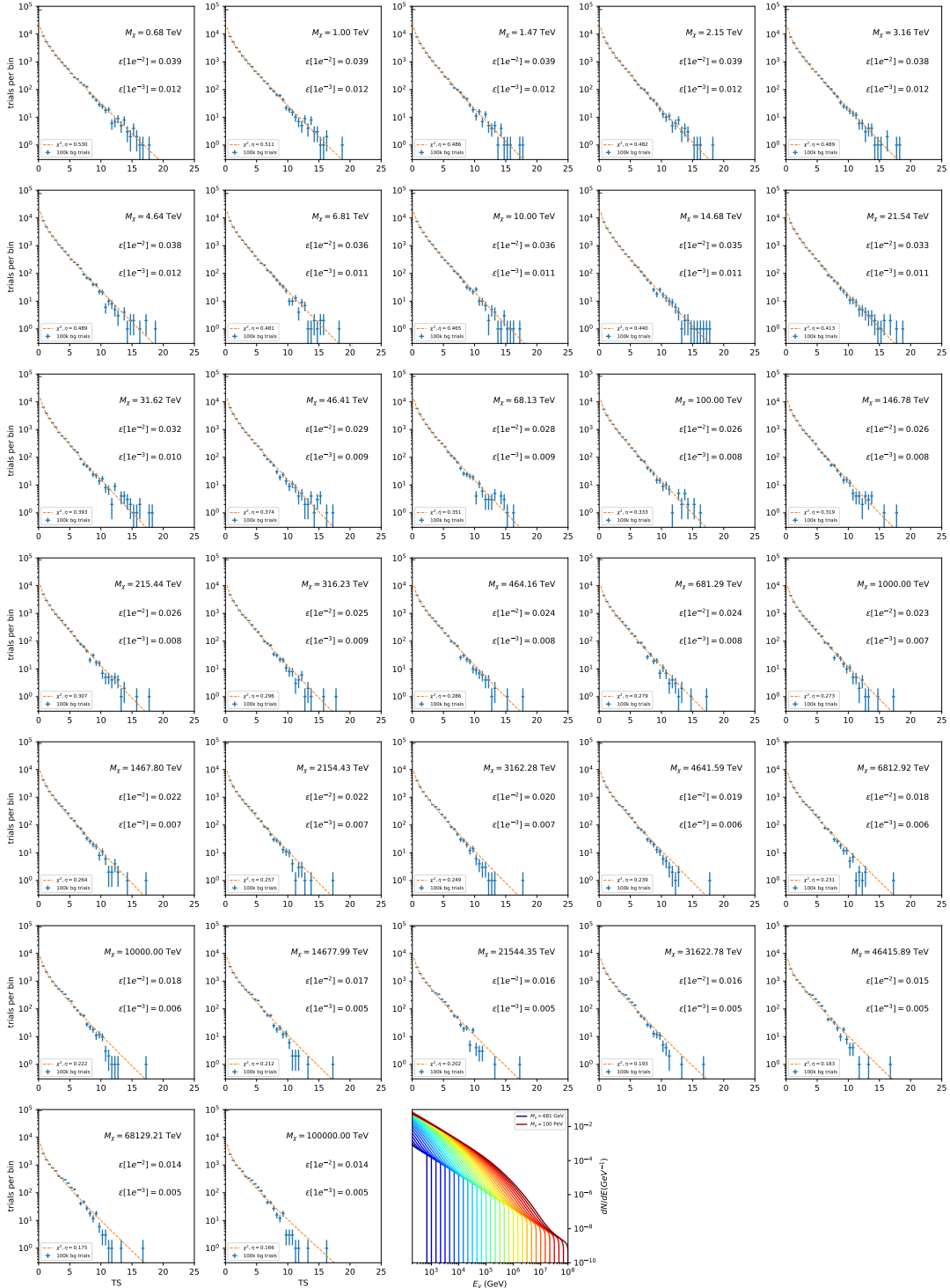


Figure 7.19 Same as Fig. 7.6 for 15, \mathcal{GS} J-factor, stacked sources and $\chi\chi \rightarrow W^+W^-$.

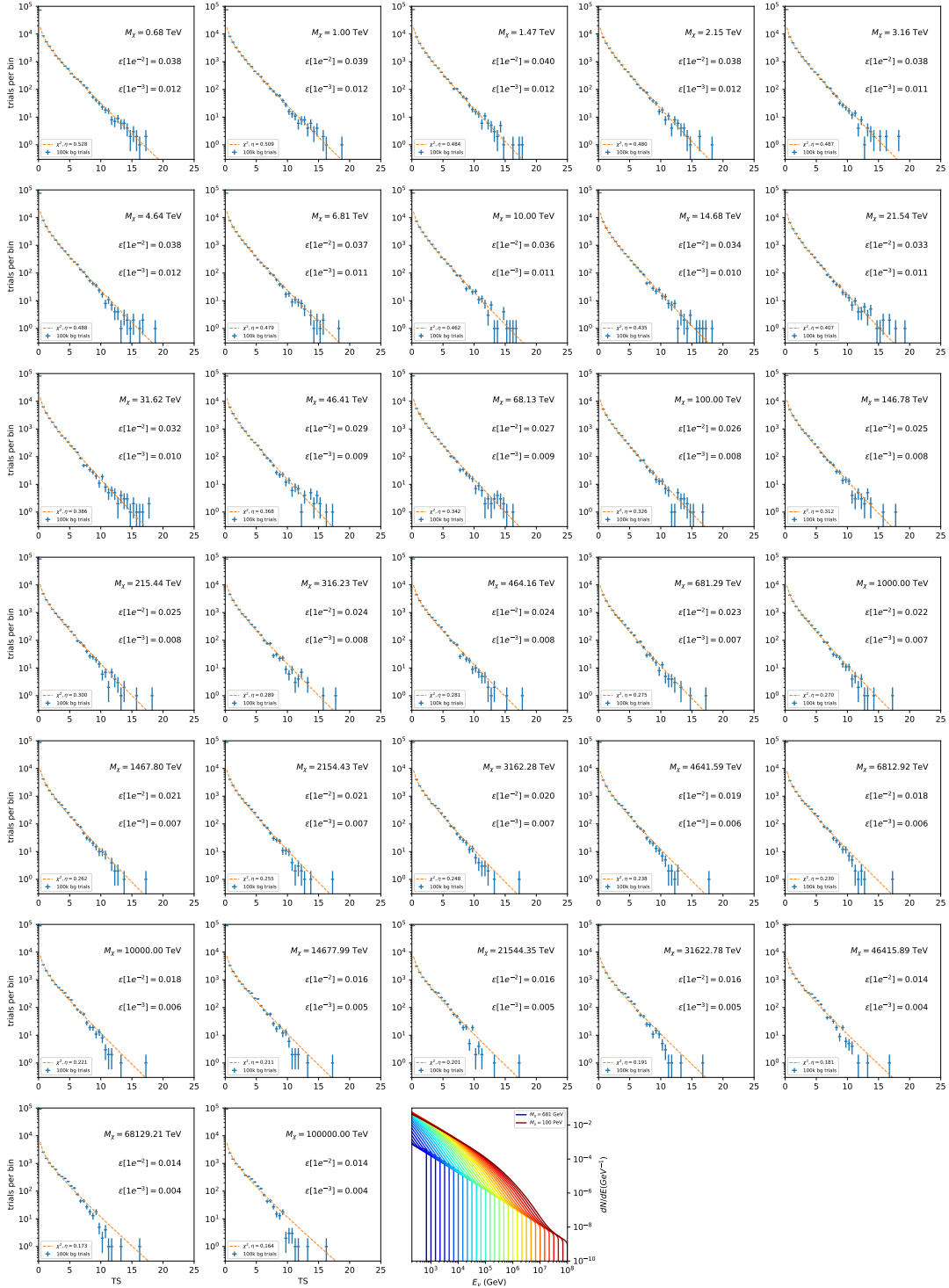


Figure 7.20 Same as Fig. 7.6 for 15, \mathcal{GS} J-factor, stacked sources and $\chi\chi \rightarrow ZZ$.

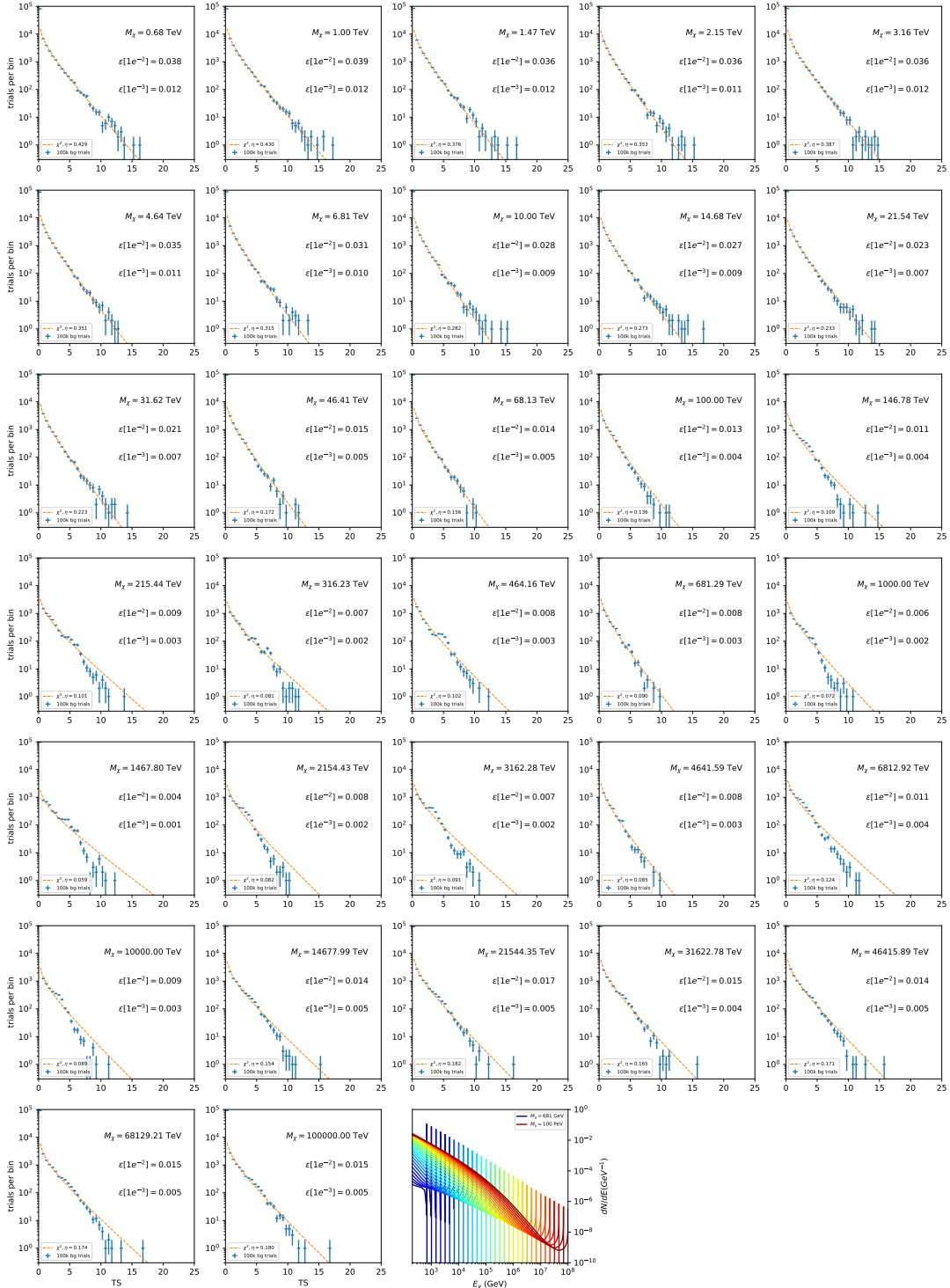


Figure 7.21 Same as Fig. 7.6 for 15, \mathcal{GS} J -factor, stacked sources and $\chi\chi \rightarrow \nu_e \bar{\nu}_e$.

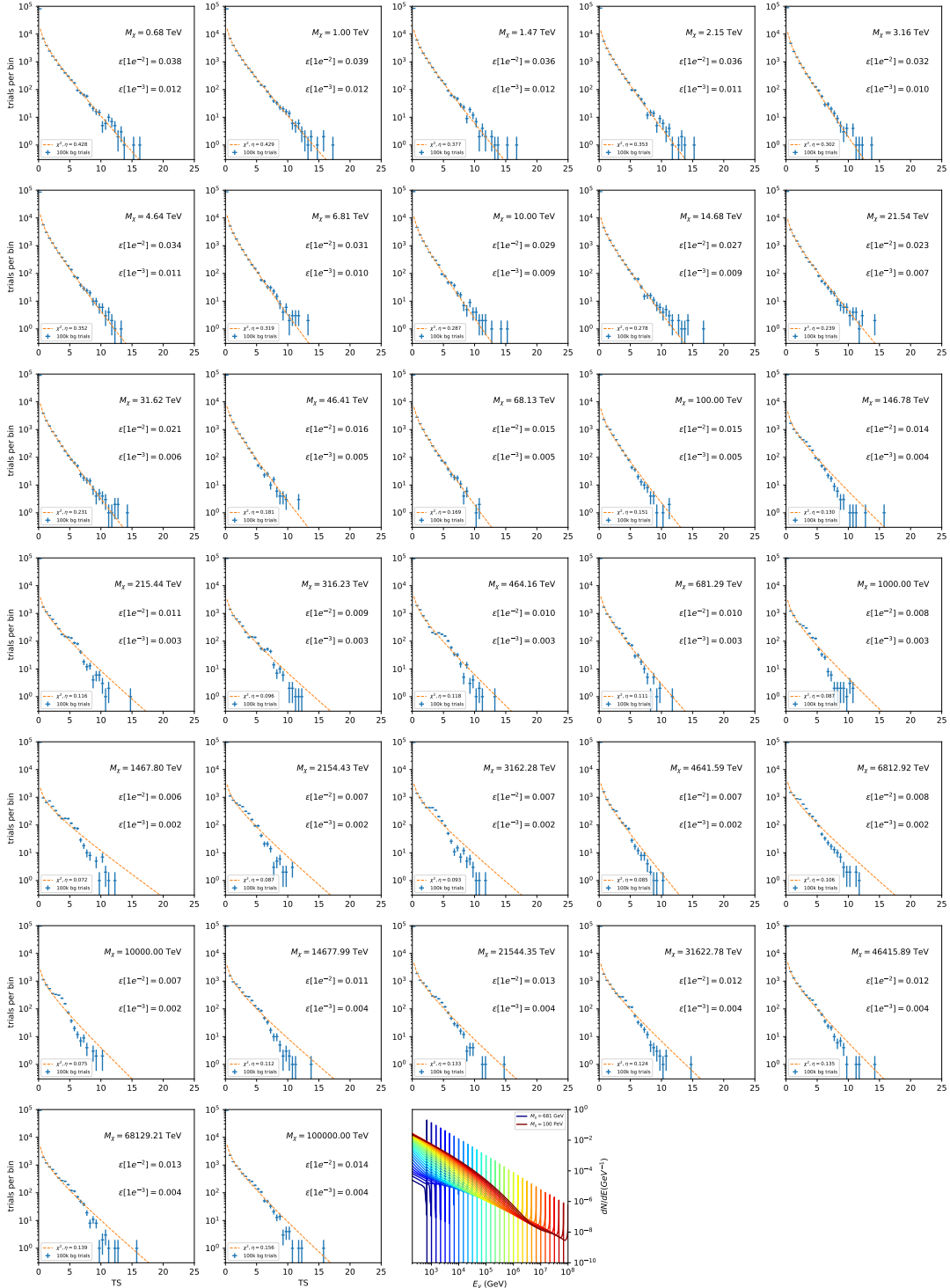


Figure 7.22 Same as Fig. 7.6 for 15, GS J-factor, stacked sources and $\chi\chi \rightarrow \nu_\mu \bar{\nu}_\mu$.

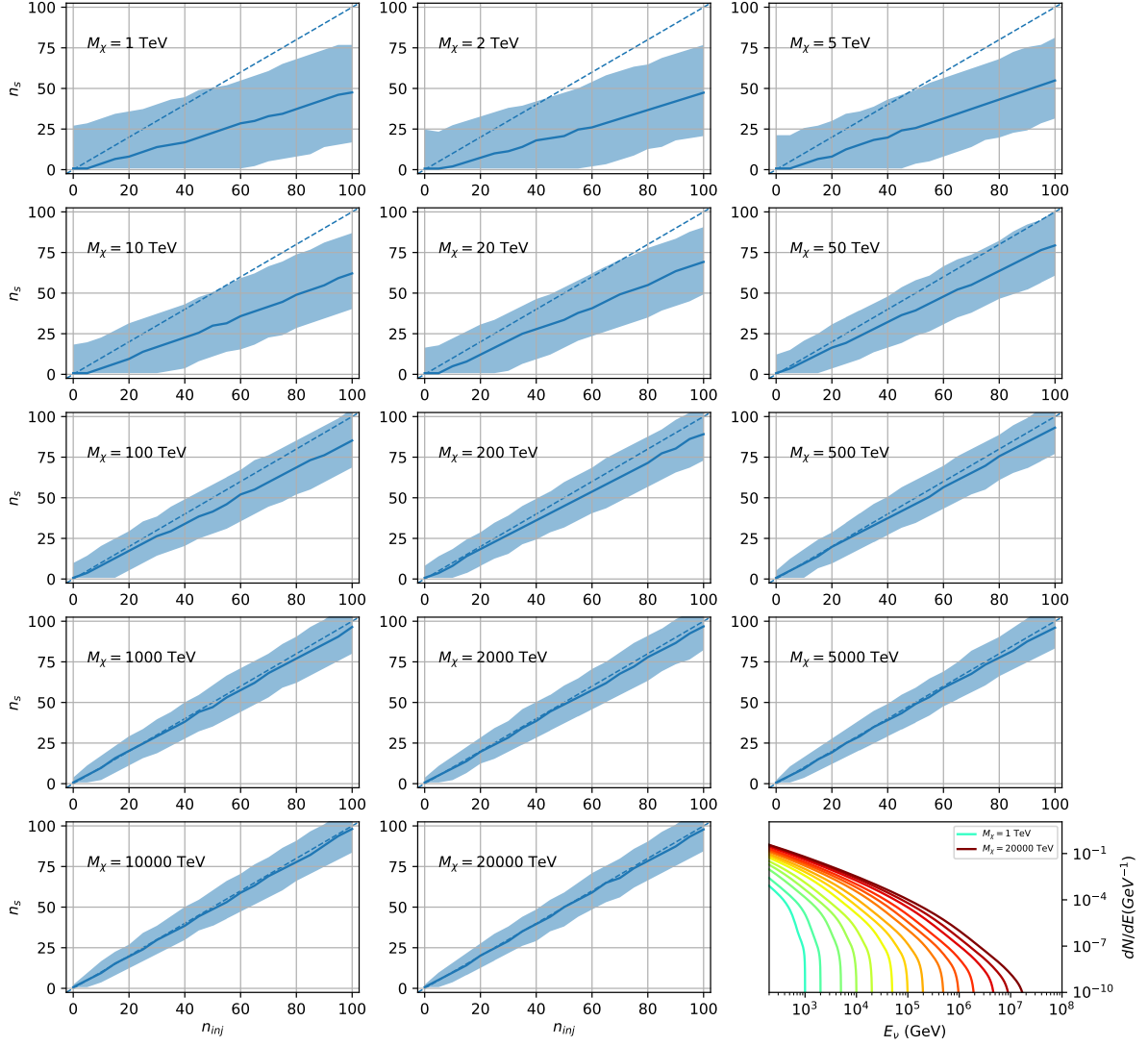


Figure 7.23 Signal Recovery study for an analysis with 15 stacked sources using the \mathcal{GS} J -factors [45]. Each panel block represents 14 studies for DM mass ranging between 1 TeV and 20 PeV and one annihilation channel. Panel block is for $t\bar{t}$. Each panel block features every spectral model used as input in the bottom-right subpanel. The remaining panels show n_{inj} as the number of signal events injected into background simulation. Whereas, n_s is the number of signal events recovered from analyzing the injected simulation. Blue line represents the median values of 100 simulations. Light blue bands show the 1σ statistical uncertainty around the median.

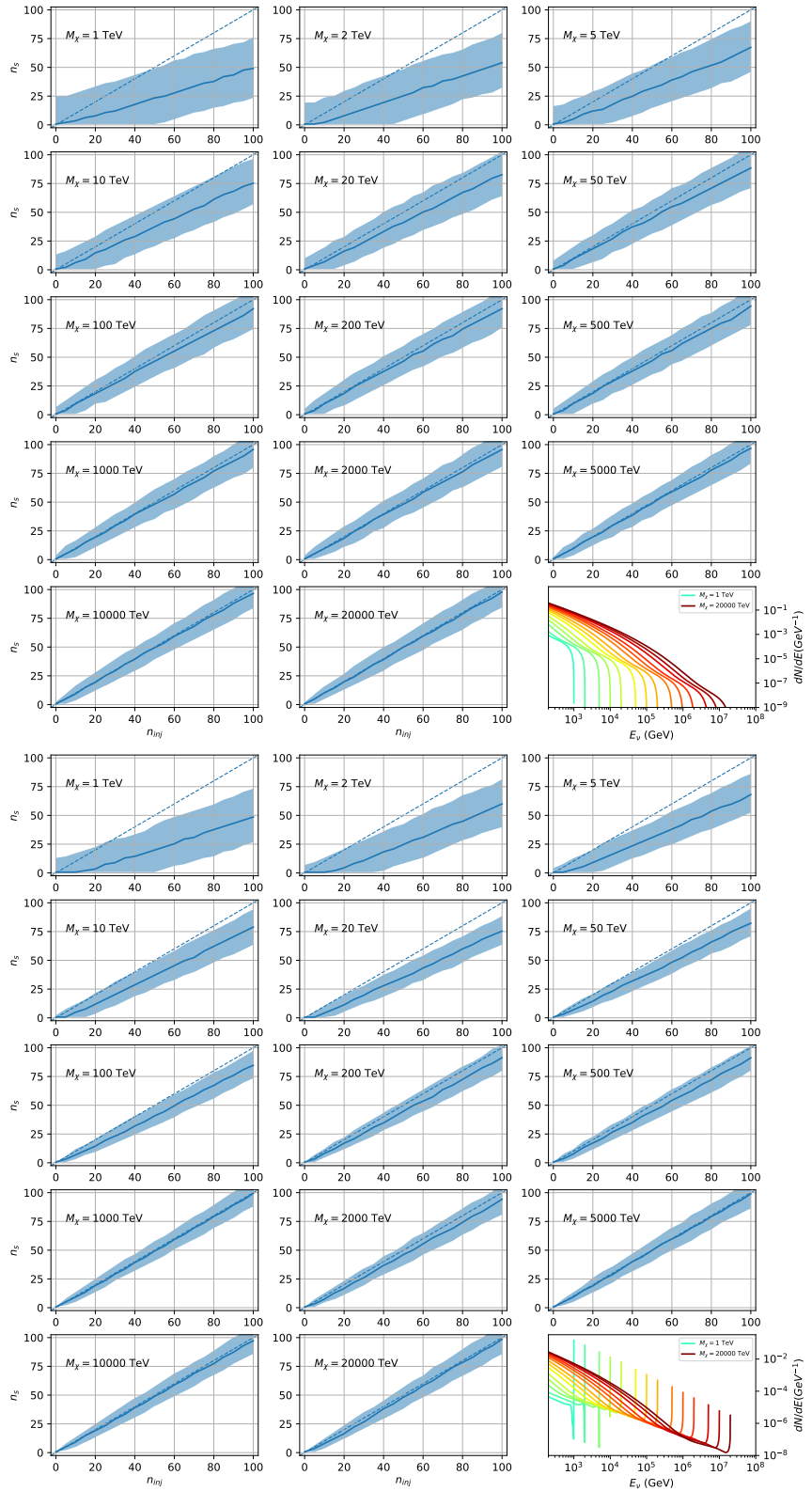


Figure 7.24 Same as Fig. 7.23 but for $\chi\chi \rightarrow b\bar{b}$ (top) and $\nu_\mu\bar{\nu}_\mu$ (bottom).

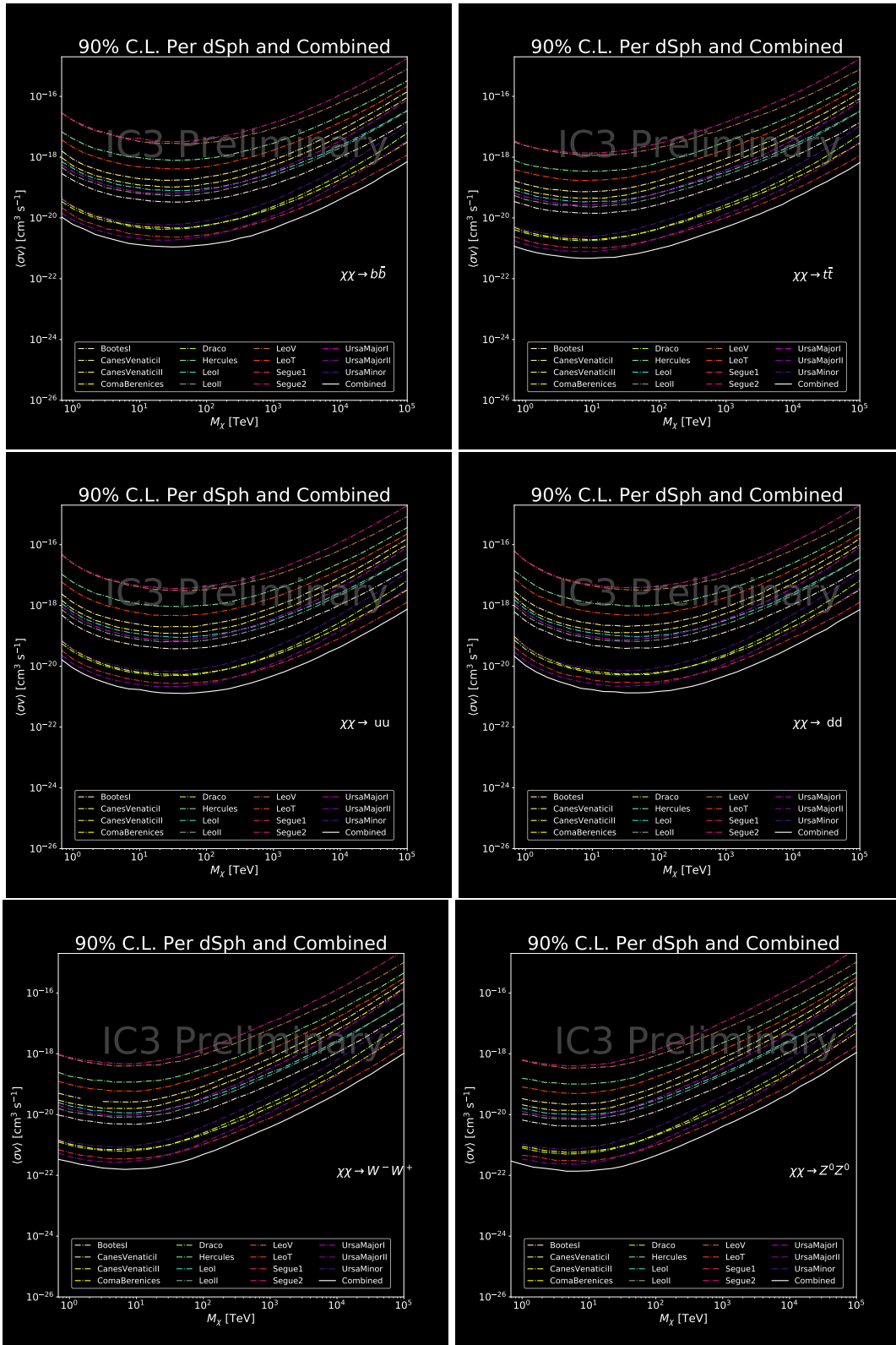


Figure 7.25 Words. I prent Icecibe Sensitivities weeee

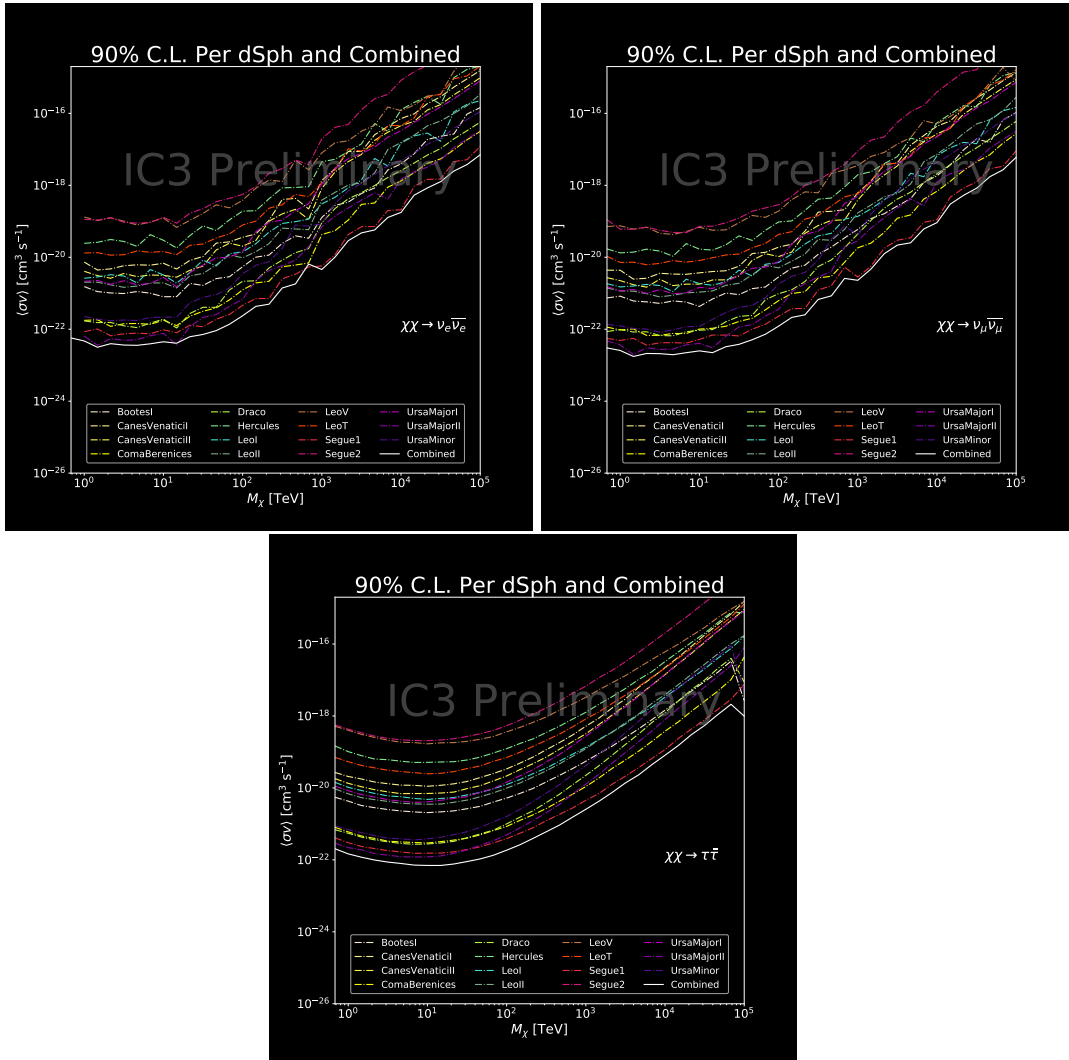


Figure 7.26 Words. I predict Icecibe Sensitivities weeee

CHAPTER 8

NU DUCK

1704

MULTI-EXPERIMENT SUPPLEMENTARY FIGURES

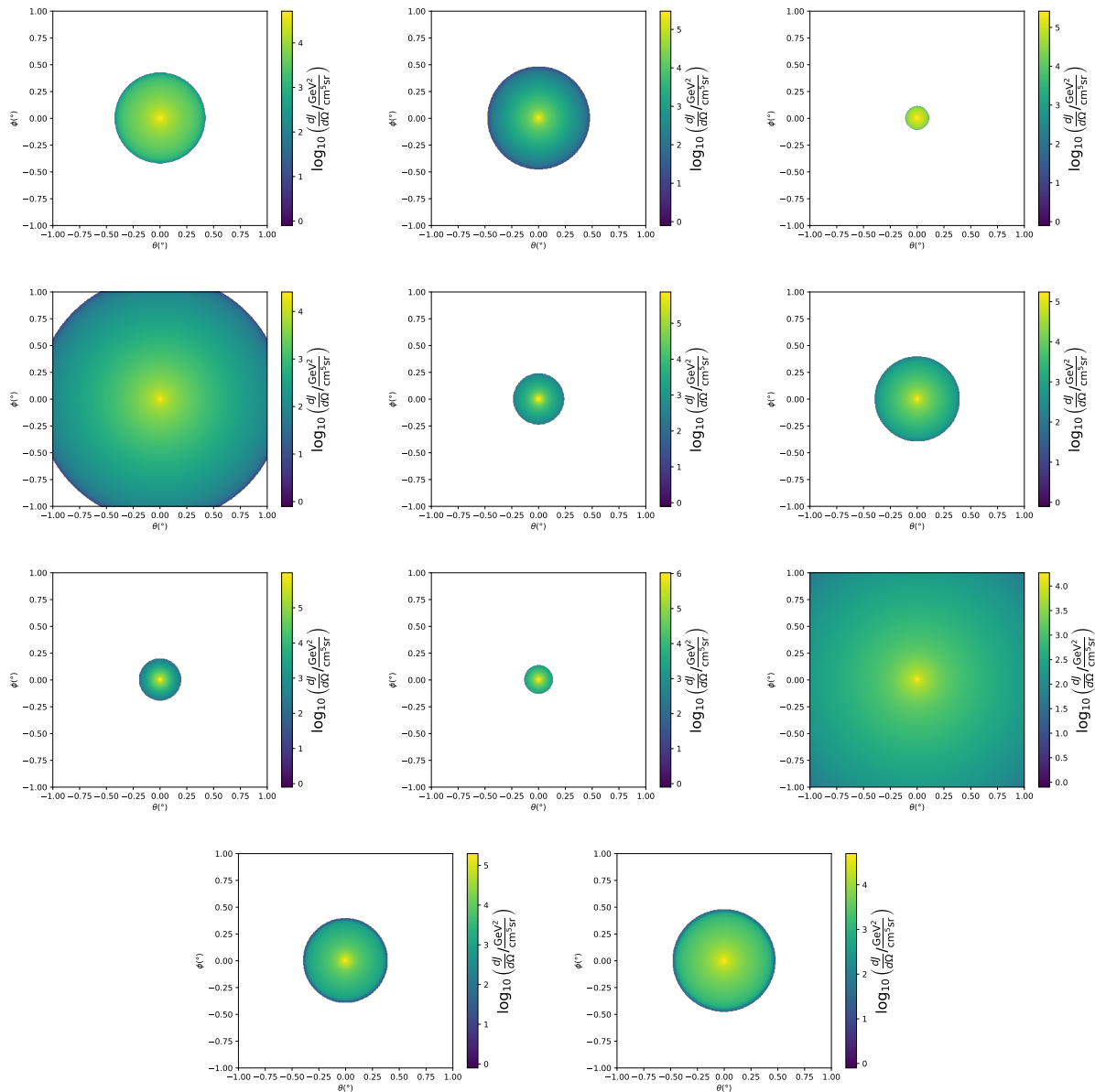


Figure A.1 Sister figure to Figure 5.3. Sources in the first row from left to right: Bootes I, Canes Venatici I, II. In second row: Draco, Hercules, Leo I. In the first row: Leo II, Leo IV, Sextans. In the final row: Ursa Major I, Ursa Major II.

APPENDIX B

1706 MULTITHREADING DARK MATTER ANALYSES SUPPLEMENTARY MATERIAL

1707 B.1 Remaining Spectral Models

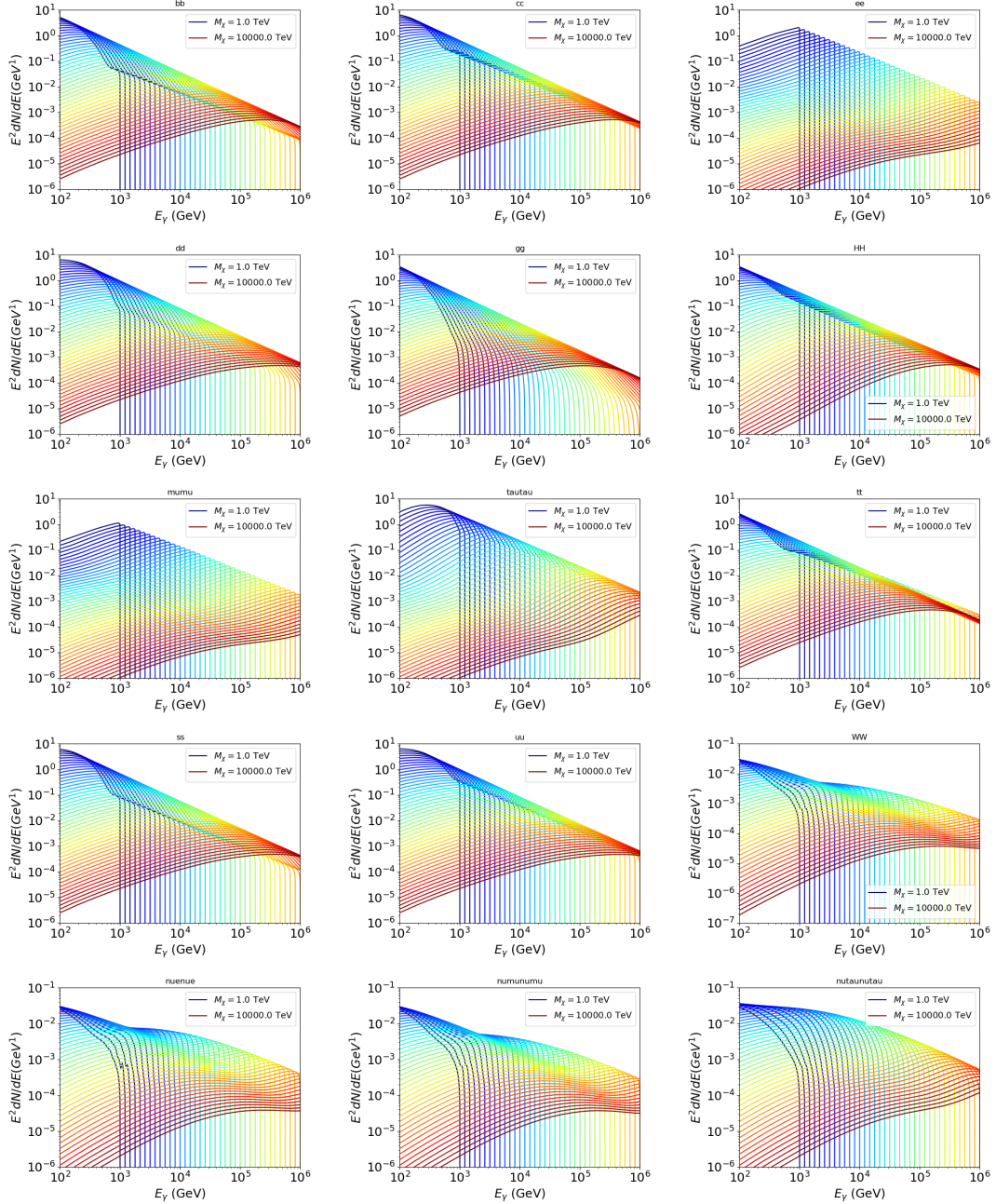


Figure B.1 Sister figure to Figure 6.2 for remaining SM primary annihilation channels studied for this thesis. These did not require any post generation smoothing and so are directly pulled from [65] with a binning scheme most helpful for a HAWC analysis.

1708 **B.2 mpu_analysis.py**

```
17091 import warnings
17102 with warnings.catch_warnings():
17113     warnings.simplefilter("ignore")
17124 # Python base libraries
17135 import os
17146 import sys
17157 import time
17168 # Import general libraries with namespace
17179 import matplotlib
17180 # Necessary for computing on cluster
17191 matplotlib.use("agg")
17202 import numpy as np
17213 import multiprocessing as mp
17224 # Import HAWC software
17235 sys.path.insert(1, os.path.join(os.environ['HOME'], 'hawc_software', 'threeML-
1724     analysis-scripts', 'fitModel'))
17256 from analysis_modules import *
17267 from threeML import *
17278 from hawc_hal import HAL, HealpixConeROI
17289 from threeML.minimizer.minimization import FitFailed
17290 # Import Dark Matter HAWC Libraries
17301 import analysis_utils as au
17312 import spectra as spec
17323 import sources as srcs
17334
17345 #* READ ONLY PATHS This block will change eventually
17356 MASS_LIST = './plotting/studies/nd/masses.txt'
17367 CHAN_LIST = './plotting/studies/nd/chans.txt'
17378
17389 #* WRITE PATHS, default location is to scratch
17390 OUT_PATH = os.path.join(os.environ["SCRATCH"], os.environ["USER"], 'New_duck')
```

```

17401 print('Our out path is going to be {}'.format(OUT_PATH))
17412
17423 # Define parallel Function. Can also be run serially
17434 def some_mass_fit(sigVs, datalist, shape, dSph, jfactor, mass_chan,
17445                 progress=None, log_file='', queue=None, i_job=0):
17456
17467     if progress is None:
17478         progress = [0]
17489     else: # Create log files for each thread
17490         log_file = log_file.replace('.log', '_ThreadNo_')
17501         log_file = log_file + str(i_job) + ".log"
17512         sys.stdout = open(log_file, "w")
17523
17534     fits = []
17545
17556     try:
17567         for m_c in mass_chan:
17578             print(f'Mass chan tuple: {m_c}')
17589             mass = int(m_c[0])
17590             ch = m_c[1]
17601             # Build path to output files
17612             outPath = os.path.join(OUT_PATH, ch, dSph)
17623             au.ut.ensure_dir(outPath)
17634
17645             if progress[i_job] < 0:
17656                 # If the master gets a Keyboard interrupt, commit suicide.
17667                 break
17678
17689                 ### Start Model Building for DM mass and SM channel #####
17690             spectrum = spec.DM_models.HDMSpectra()
17701             spectrum.set_channel(ch)
17712
17723             myDwarf = ExtendedSource(dSph, spatial_shape=shape,

```

```

17734                     spectral_shape=spectrum)
17745
17756             spectrum.J = jfactor * u.GeV**2 / u.cm**5
17767             spectrum.sigmav = 1e-24 * u.cm**3 / u.s
17778             spectrum.set_dm_mass(mass * u.GeV)
17789
17790             spectrum.sigmav.bounds = (1e-30, 1e-12)
17801             model = Model(myDwarf)
17812             ##### End model Building #####
17823
17834             jl = JointLikelihood(model, datalist, verbose=False)
17845
17856             try:
17867                 result, lhdf = jl.fit(compute_covariance=False)
17878                 ts = -2.* (jl.minus_log_like_profile(1e-30) - jl.
1788 _current_minimum)
17899                 # Also profile the LLH vs sv
17900                 ll = jl.get_contours(spectrum.sigmav, sigVs[0],
17911                               sigVs[-1], len(sigVs),
17922                               progress=False, log=['False'])
17933
17944                 sigv_ll = au.ut.calc_95_from_profile(ll[0], ll[2])
17955                 # Write results to file
17966                 outFileLL = outPath+f"/LL_{dSph}_{ch}_mass{int(mass)}_GD.txt"
17977                 np.savetxt(outFileLL, (sigVs, ll[2]),
17988                               delimiter='\t', header='sigV\tLL\n')
17999
18000                 with open(outPath+f"/results_{dSph}_{ch}_mass{int(mass)}_GD.
1801 txt", "w") as results_file:
18021                     results_file.write("mDM [GeV]\tsigV_95\tsigV_B.F.\n")
18032
18043                     results_file.write("%i\t%.5E\t%.5E\t%.5E"%(mass, sigv_ll,
18054                                         ts, result.value[0]))

```

```

18065         # End write to file
18076     except FitFailed: # Don't kill all threads if a fit fails
18087         print("Fit failed. Go back and calculate this spectral model
1809 later")
18108         fits.append((ch, mass, -1, -1))
18119         with open(log_file+'.fail', 'w') as f_file:
18120             f_file.write(f'{ch}, {mass}\n')
18131
18142         progress[i_job] += 1
18153         matplotlib.pyplot.close() # Prevent leaky memory
18164
18175         fits.append((ch, mass, result.value[0], ts))
18186         progress[i_job] += 1
18197         matplotlib.pyplot.close()
18208     except KeyboardInterrupt:
18219         progress[i_job] = -1
18220
18231     fits = np.array(fits)
18242     if queue is None:
18253         return fits
18264     else:
18275         queue.put((i_job, fits))
18286
18297 def main(args):
18308     masses = np.loadtxt(MASS_LIST, dtype=int)
18319     chans = np.loadtxt(CHAN_LIST, delimiter=',', dtype=str)
18320     mass_chan = au.ut.permute_lists(chans, masses)
18331
18342     print(f"DM masses for this study are: {masses}")
18353     print(f"SM Channels for this study are XX -> {chans}")
18364     print(mass_chan)
18375
18386 # extract information from input argument

```

```

18397 dSph = args.dSph
18408 data_mngr = au.ut.Data_Selector('P5_NN_2D')
18419 dm_profile = srcts.Spatial_DM(args.catalog, dSph, args.sigma, args.decay)
18420
18431     ### Extract Source Information ####
18442 if dm_profile.get_dec() < -22.0 or dm_profile.get_dec() > 62.0:
18453     raise ValueError("HAWC can't see this source D: Exitting now...")
18464
18475 print(f'{dSph} information')
18486 print(f'jfac: {dm_profile.get_factor()}\tRA: {dm_profile.get_ra()}\tDec: {dm_profile.get_dec()}\n')
1849
18507
18518 shape = SpatialTemplate_2D(fits_file=dm_profile.get_src_fits())
18529     ### Finish Extract Source Information ####
18530
18541     ### LOAD HAWC DATA ####
18552 roi = HealpixConeROI(data_radius=2.0, model_radius=8.0,
18563                         ra=dm_profile.get_ra(), dec=dm_profile.get_dec())
18574 bins = choose_bins.analysis_bins(args, dec=dm_profile.get_dec())
18585
18596 hawc = HAL(dSph, data_mngr.get_datmap(), data_mngr.get_detres(), roi)
18607 hawc.set_active_measurements(bin_list=bins)
18618 datalist = DataList(hawc)
18629     ### FINISH LOAD HAWC DATA ####
18630
18641 # set up SigV sampling. This sample is somewhat standardized
18652 sigVs = np.logspace(-28,-18, 1001, endpoint=True) # NOTE This will change
1866 with HDM
18673
18684 if args.n_threads == 1:
18695     # No need to start || programming just iterate over the masses
18706 kw_arg = dict(sigVs=sigVs, datalist=datalist, shape=shape, dSph=dSph,
18717                         jfactor=dm_profile.get_factor(), mass_chan=mass_chan,

```

```

18728                 log_file=args.log)
18729             some_mass_fit(**kw_arg)
18730         else:
18731             # I Really want to suppress TQMD output
18732             from tqdm import tqdm
18733             from functools import partialmethod
18734             tqdm.__init__ = partialmethod(tqdm.__init__, disable=True)
18735
18806             x = np.array_split(mass_chan, args.n_threads)
18817             n_jobs = len(x)
18828
18839             print("Thread jobs summary by mass and SM channel")
18840             for xi in x:
18851                 print(f'{xi}')
18862
18873             queue = mp.Queue()
18884             progress = mp.Array('i', np.zeros(n_jobs, dtype=int))
18895
18906             # Define task pool that will be split amongsts threads
18917             kw_args = [dict(sigVs=sigVs, datalist=datalist, shape=shape,
18928                             dSph=dSph, jfactor=dm_profile.get_factor(),
18939                             mass_chan=mass_chan, progress=progress,
18940                             queue=queue, i_job=i, log_file=args.log)
18951                 for i, mass_chan in enumerate(x)]
18962
18973             # Define each process
18984             procs = [mp.Process(target=some_mass_fit, kwargs=kw_args[i]) \
18995                 for i in range(n_jobs)]
19006
19017             ### Start MASTER Thread only code block ###
19028             # Begin running all child threads
19039             for proc in procs: proc.start()
19040

```

```

19051     try:
19062         # In this case, the master does nothing except monitor progress of
1907         the threads
19083         # In an ideal world, the master thread also does some computation.
19094         n_complete = np.sum(progress)
19105         while_count = 0
19116
19127         while n_complete < len(mass_chan):
19138
19149             if np.any(np.asarray(progress) < 0):
19150                 # This was no threads are stranded when killing the script
19161                 raise KeyboardInterrupt()
19172             if while_count%1000 == 0:
19183                 print(f"{np.sum(progress)} of {len(mass_chan)} finished")
19194
19205             n_complete = np.sum(progress)
19216             time.sleep(.25)
19227             while_count += 1
19238
19249         except KeyboardInterrupt:
19250             # signal to jobs that it's time to stop
19261                 for i in range(n_jobs):
19272                     progress[i] = -2
19283                     print('\nKeyboardInterrupt: terminating early.')
19294             ### End MASTER Thread only code block ###
19305
19316             fitss = [queue.get() for proc in procs]
19327             print(fitss)
19338             print(f'Thread statuses: {progress[:]}')
19349
19350             # putting results in a file
19361
19372             print("QUACK! All Done!")

```

```

19383
19394
19405 if __name__ == '__main__':
19416     import argparse
19427
19438     p = argparse.ArgumentParser(description="Run a DM annihilation analysis on
1944         a dwarf spheroidal for a specific SM channel for DM masses [1 TeV to 10
1945         PeV]")
19469
19470     # Dwarf spatial modeling arguements
19481     p.add_argument("-ds", "--dSph", type=str,
19492             help="dwarf spheroidal galaxy to be studied", required=
1950             True)
19513     p.add_argument("-cat", "--catalog", type=str, choices=['GS15', 'LS20'],
19524             default='LS20', help="source catalog used")
19535     p.add_argument("-sig", "--sigma", type=int, choices=[-1, 0, 1], default=0,
19546             help="Spatial model uncertainty. 0 corresponds to the
1955 median. +/-1 correspond to the +/-1sigma uncertainty respectively.")
19567
19578     # Arguements for the energy estimators
19589     p.add_argument("-e", "--estimator", type=str,
19590             choices=['P5_NHIT', 'P5_NN_2D'],
19601             default="P5_NN_2D", required=False,
19612             help="The energy estimator choice. Options are: P5_NHIT,
1962 P5_NN_2D. GP not supported (yet).")
19633     p.add_argument("--use-bins", default=None, nargs="*",
19644             help="Bins to use for the analysis", dest="use_bins")
19655     p.add_argument('--select_bins_by_energy', default=None, nargs="*",
19666             help="Does nothing. May fill in later once better
1967 understood")
19687     p.add_argument('--select_bins_by_fhit', default=None, nargs="*",
19698             help="Also does nothing see above")
19709     p.add_argument( '-ex', "--exclude", default=None, nargs="*",

```

```

19750         help="Exclude Bins", dest="exclude")

19751

19752 # Computing and logging arguements.

19753 p.add_argument('-nt', '--n_threads', type=int, default=1,
19754                     help='Maximum number of threads spawned by script. Default
19755 is 4')

19756 p.add_argument('-log', '--log', type=str, required=True,
19757                     help='Name for log files. Especially needed for threads')

19758

19759 p.add_argument('--decay', action="store_true",
19760                     help='Set spectral DM hypothesis to decay')

19761

19762 args = p.parse_args()

19763 print(args.decay)

19764 if args.exclude is None: # default exclude bins 0 and 1
19765     args.exclude = ['B0C0Ea', 'B0C0Eb', 'B0C0Ec', 'B0C0Ed', 'B0C0Ee']

19766

19767 if args.decay: OUT_PATH += '_dec'
19768 else: OUT_PATH += '_ann'

19769 OUT_PATH = OUT_PATH + '_' + args.catalog
19770 if args.sigma != 0: OUT_PATH += f'_{args.sigma}sig'

19771

19772 main(args)

```

1995 B.3 Comparison with Glory Duck

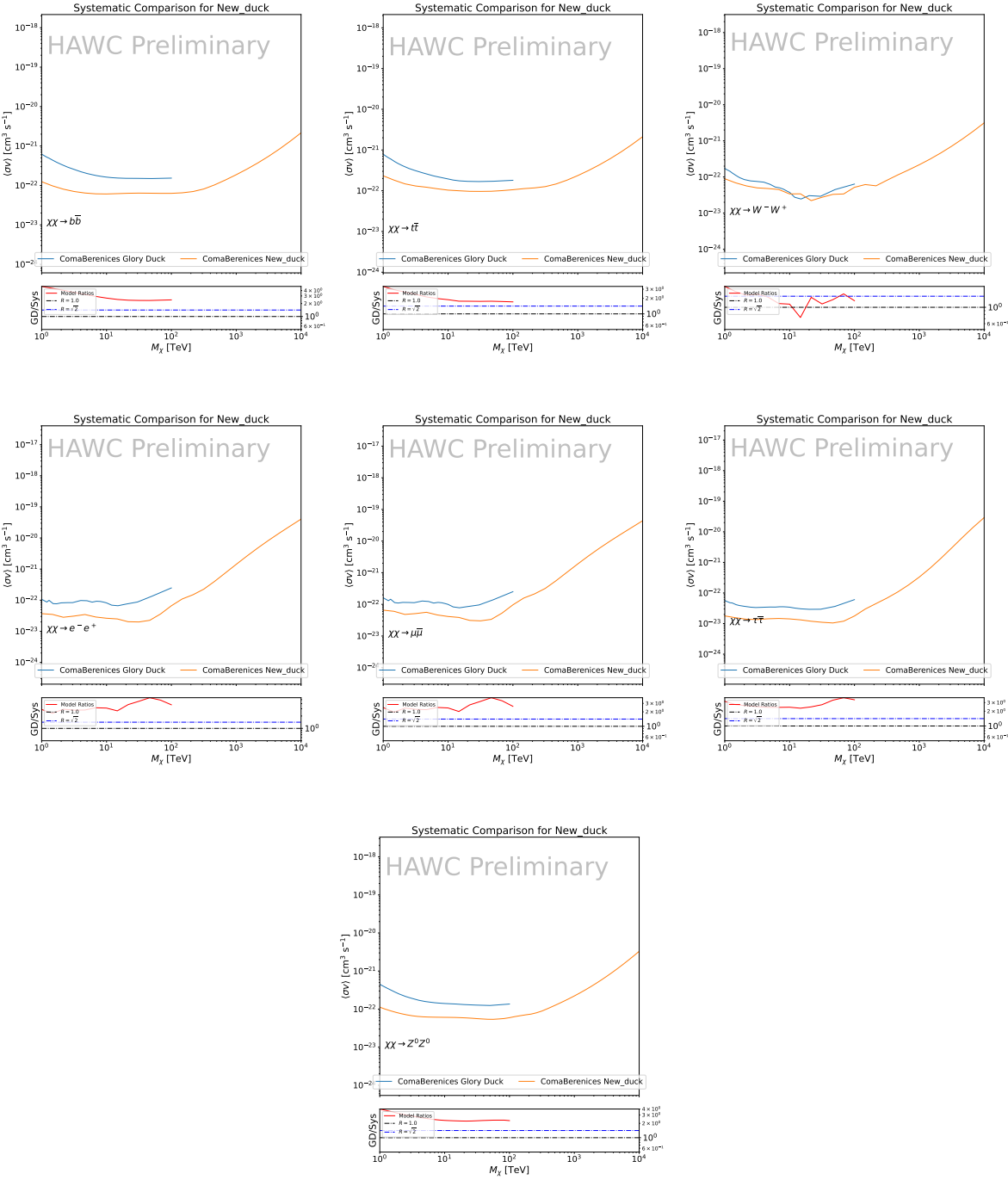


Figure B.2 TODO: fill this out

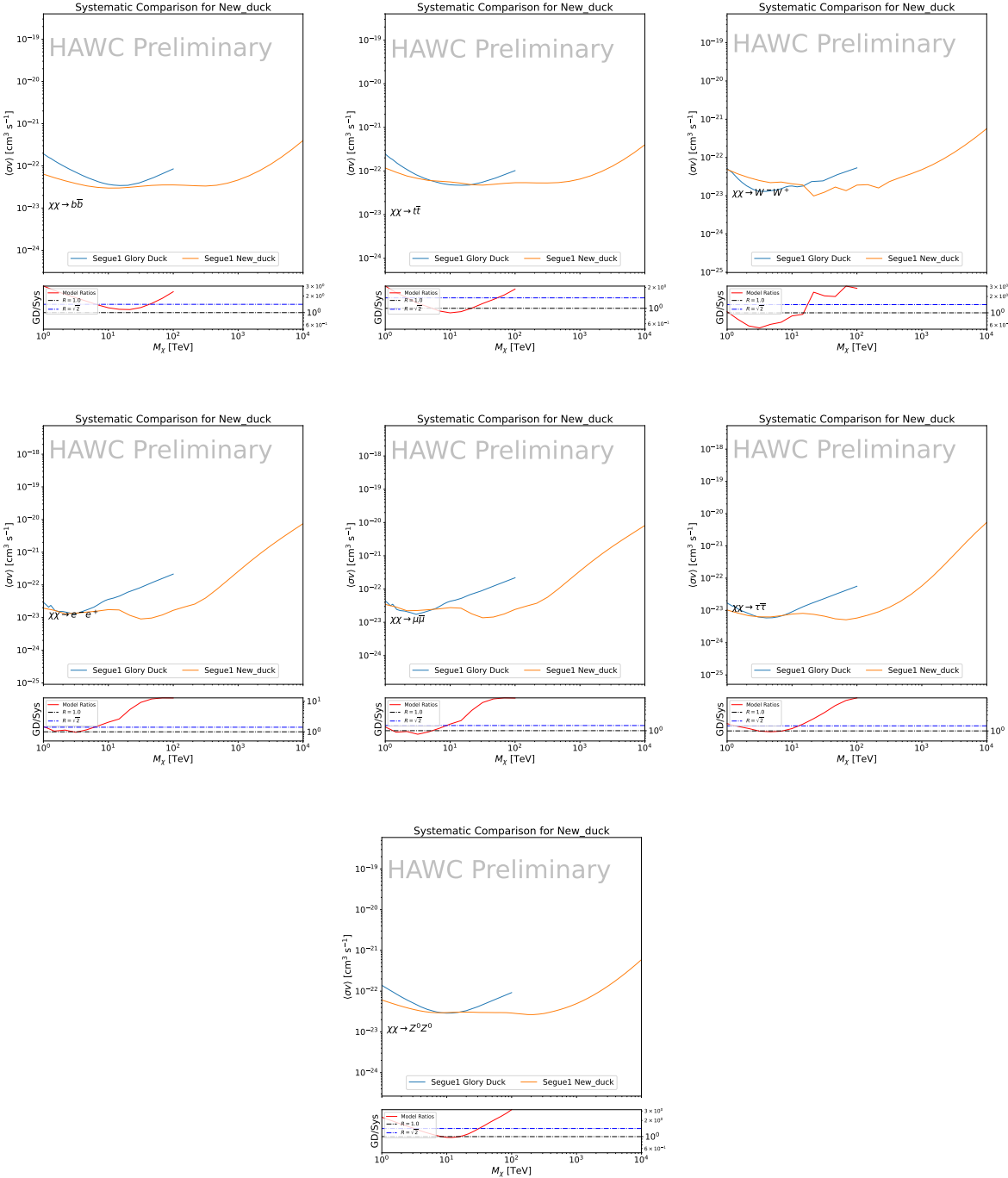


Figure B.3 TODO: fill this out

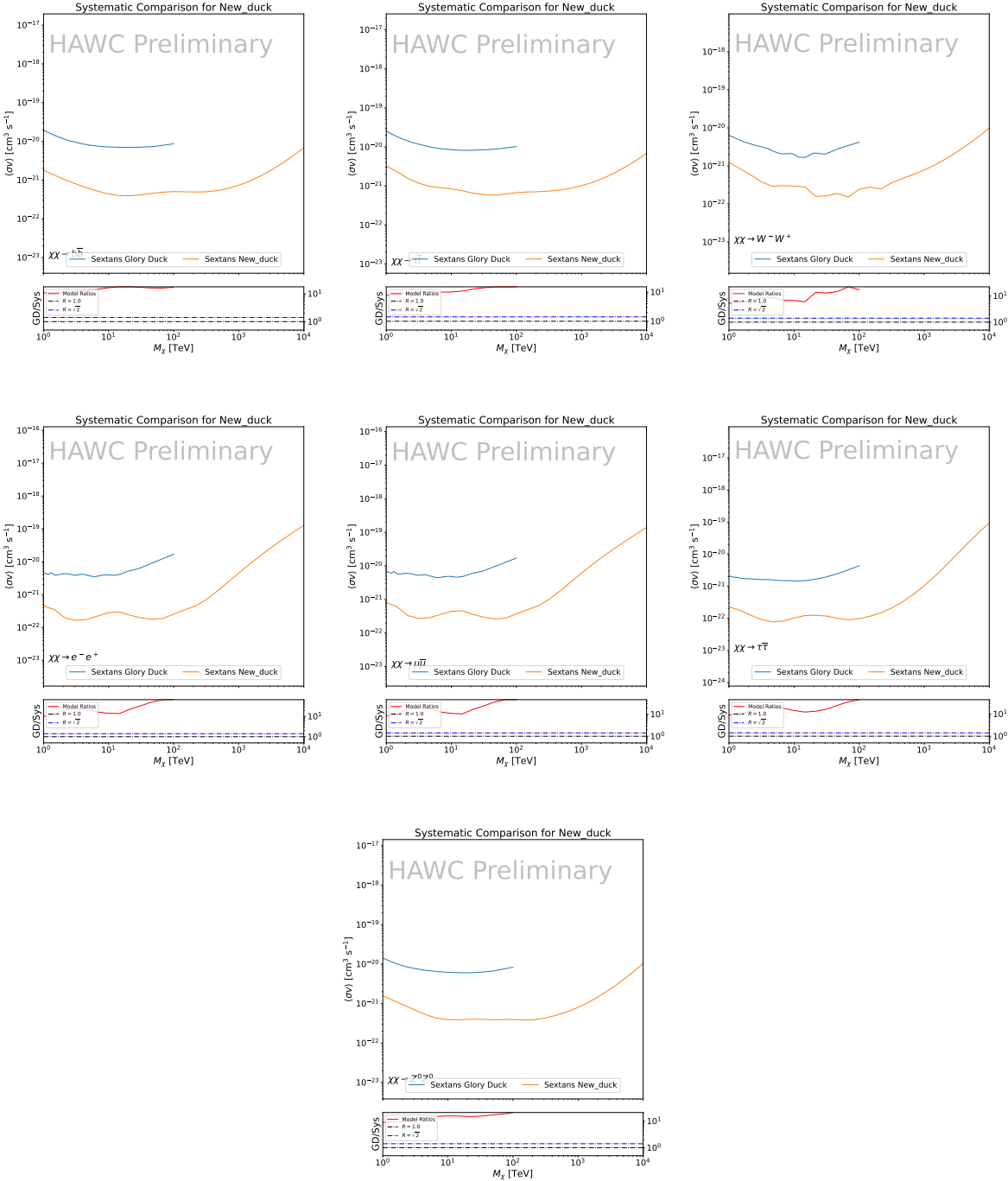


Figure B.4 TODO: fill this out

APPENDIX C

1996 ICECUBE HEAVY DARK MATTER ANALYSIS SUPPLEMENTARY MATERIAL

1997 C.1 Docker Image for Oscillating Neutrino Spectra

```
19981 FROM ubuntu:18.04
19992
20003 # Execute commands to install software packages
20014 RUN apt -y update
20025
20036     # Install utility programs
20047 RUN apt -y install vim wget git cmake
20058
20069 ARG DEBIAN_FRONTEND=noninteractive
20070
20081     # Install python
20092 RUN apt -y install python python-dev python-pip libjpeg-dev zlib1g-dev
20103
20114     # We need Python2 for installing Charon.
20125 RUN apt -y install python-numpy python-sympy python-matplotlib \
20136             python-sympy python-h5py python-astropy python-ipython
20147
20158     # Install dependencies of Charon : SQuIDS, NuSQuIDS
20169 RUN apt -y install libgsl-dev libgslcblas0 libgsl23 gsl-bin pkg-config
20170     # Install SQuIDS
20181 RUN mkdir /home/SQuIDS /home/SQuIDS_install
20192 WORKDIR /home/SQuIDS
20203 RUN git clone https://github.com/jsalvado/SQuIDS.git
20214 WORKDIR /home/SQuIDS/SQuIDS
20225 RUN git checkout 7ad9ba7c6ad06d1f0fa8418f937ebf1a403fef90
20236     # Before executing "make install" an environmental variable has to be set.
20247 ENV PKG_CONFIG_PATH=/home/SQuIDS/SQuIDS/lib
20258 RUN ./configure --prefix=../SQuIDS_install \
```

```

20269  && make
20270 RUN make install
20281
20292 # Set up an environmental variable that is required to install nuSQuIDS..
20303 ENV SQuIDS=/home/SQuIDS/SQuIDS
20314 ENV LD_LIBRARY_PATH=$SQuIDS/lib:$LD_LIBRARY_PATH
20325
20336 # Install NuSQuIDS
20347 RUN mkdir /home/nuSQuIDS
20358 WORKDIR /home/nuSQuIDS
20369 RUN git clone https://github.com/qrliu/nuSQuIDS.git
20370 WORKDIR /home/nuSQuIDS/nuSQuIDS
20381 RUN git checkout 072d8ef740e2fc7330f1fabaea94f0f4540c46f9
20392 RUN apt -y install libhdf5-dev hdf5-tools
20403 RUN apt -y install libboost1.65-all-dev
20414 RUN ./configure --with-squids=$SQuIDS --with-python-bindings --prefix=../
2042     nuSQuIDS_install \
20435     && make \
20446     && make install
20457
20468 # Set up an environmental variable for nuSQuIDS.
20479 ENV nuSQuIDS=/home/nuSQuIDS/nuSQuIDS
20480 ENV LD_LIBRARY_PATH=$nuSQuIDS/lib:$LD_LIBRARY_PATH
20491
20502 # Build the python bindings
20513 WORKDIR /home/nuSQuIDS/nuSQuIDS/resources/python/src
20524 RUN make
20535
20546 # Set up an environmental variable for the python bindings.
20557 ENV PYTHONPATH=$nuSQuIDS/resources/python/bindings/:$PYTHONPATH
20568
20579 # Install Charon in the /home/Charon/charon directory.
20580 RUN mkdir /home/Charon

```

```
20591 WORKDIR /home/Charon
20602 RUN git clone https://github.com/icecube/charon.git \
20613     && apt -y install unzip python-scipy
20624 WORKDIR charon
20635 RUN git checkout c531efe4e01dc364a60d1c83f950f04526ccd771
20646 RUN unzip ./charon/xsec/xsec.zip -d charon/xsec/ \
20657
20668 # Download neutrino spectra tables in the /home/Charon/charon/data directory
2067 .
20689 && mkdir ./charon/data
20690 WORKDIR ./charon/data
20701 RUN wget --no-check-certificate https://icecube.wisc.edu/~qliu/charon/
2071     SpectraEW.hdf5 \
20722 && wget --no-check-certificate https://icecube.wisc.edu/~qliu/charon/
2073     Spectra_PYTHIA.hdf5 \
20743 && wget --no-check-certificate https://icecube.wisc.edu/~qliu/charon/
2075     Spectra_noEW.hdf5
20764
20775 WORKDIR ../..
20786 RUN python setup.py install
20797 WORKDIR /home
```

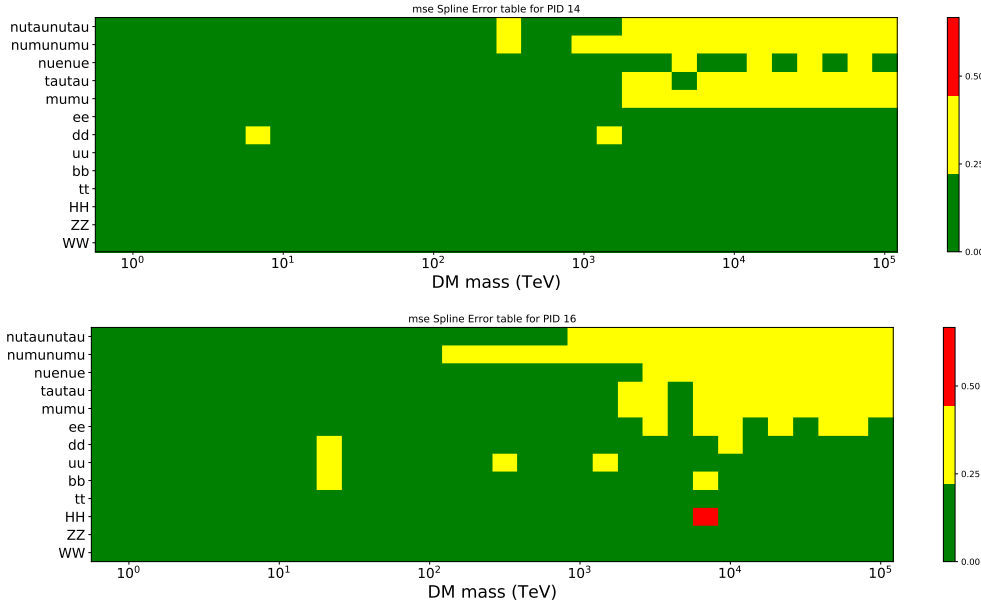


Figure C.1 Current status of spline tables according to constraints defined by Tab. 7.1. Green splines are splines that passed under the GOOD tolerance. Yellow are splines that are OK. Red are splines that FAIL. All yellow splines were inspected individually before running the analysis. Splines were made for the μ (PID 14; top panel) flavor and τ (PID 16; bottom panel) neutrino flavors.

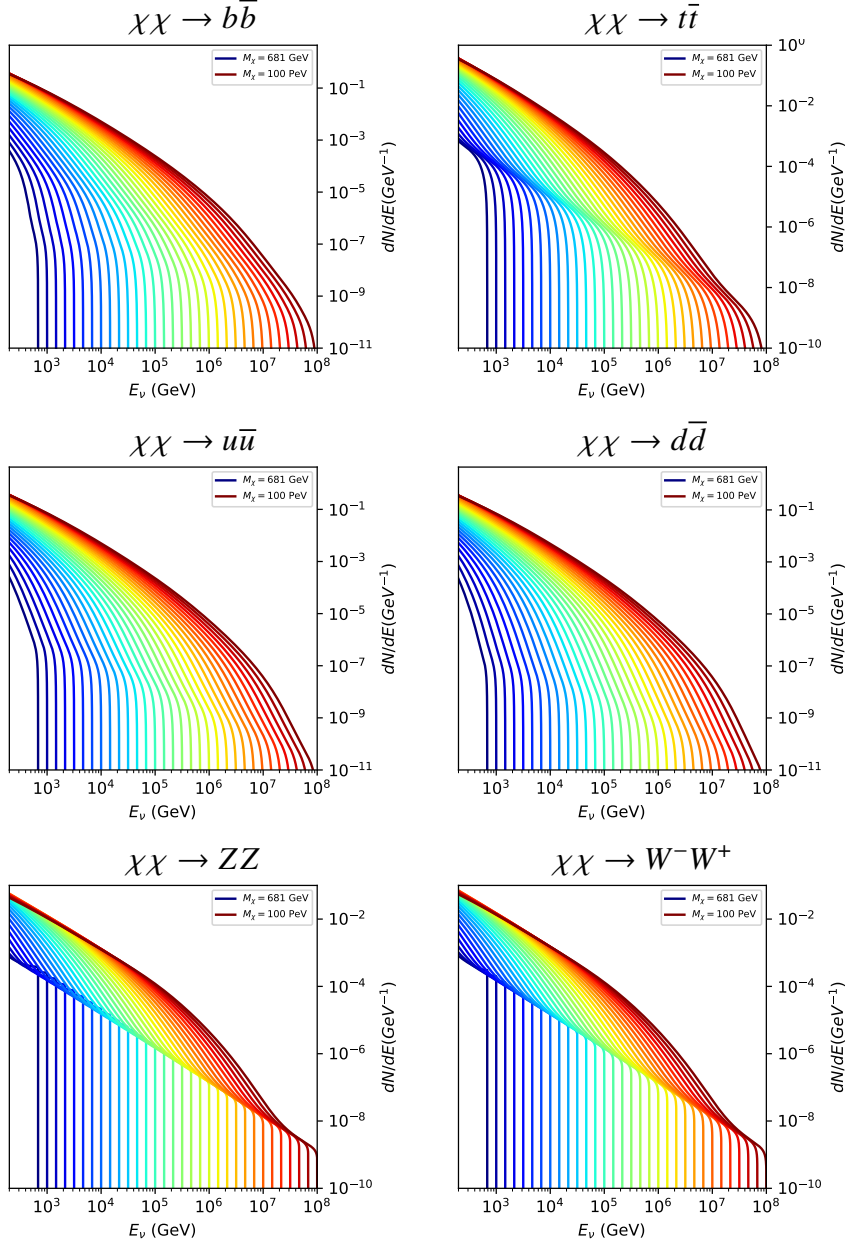


Figure C.2 Sister figure to Fig. 7.5 for annihilation channels that did not require kernel smoothing. These spectra are the composite ($\nu_\mu + \nu_\tau$) of neutrino flavors. Every spectral model used for this analysis is featured as a colored solid line. Bluer lines are for lower DM mass spectral models. DM masses range from 681 GeV to 100 PeV.

2082 C.4 Segue 1 And Ursa Major II Signal Recovery



Figure C.3 TODO: Fill this out eventually. I think I want all the plots generated first[NEEDS A SOURCE][FACT CHECK THIS]

BIBLIOGRAPHY

- 2084 [1] Anne M. Green. “Dark matter in astrophysics/cosmology”. In: *SciPost Phys. Lect.*
 2085 *Notes* (2022), p. 37. doi: [10.21468/SciPostPhysLectNotes.37](https://doi.org/10.21468/SciPostPhysLectNotes.37). URL: <https://scipost.org/10.21468/SciPostPhysLectNotes.37>.
- 2087 [2] Bing-Lin Young. “A survey of dark matter and related topics in cosmology”. In: *Frontiers*
 2088 *of Physics* 12 (Oct. 2016). doi: <https://doi.org/10.1007/s11467-016-0583-4>.
 2089 URL: <https://doi.org/10.1007/s11467-016-0583-4>.
- 2090 [3] Gianfranco Bertone, Dan Hooper, and Joseph Silk. “Particle dark matter: evidence,
 2091 candidates and constraints”. In: *Physics Reports* 405.5 (2005), pp. 279–390. ISSN:
 2092 0370-1573. doi: <https://doi.org/10.1016/j.physrep.2004.08.031>. URL:
 2093 <https://www.sciencedirect.com/science/article/pii/S0370157304003515>.
- 2094 [4] Gianfranco Bertone and Dan Hooper. “History of dark matter”. In: *Rev. Mod. Phys.*
 2095 90 (4 Aug. 2018), p. 045002. doi: [10.1103/RevModPhys.90.045002](https://doi.org/10.1103/RevModPhys.90.045002). URL: <https://link.aps.org/doi/10.1103/RevModPhys.90.045002>.
- 2097 [5] Fritz Zwicky. “The Redshift of Extragalactic Nebulae”. In: *Helvetica Physica Acta* 6.
 2098 (1933), pp. 110–127. doi: [10.5169/seals-110267](https://doi.org/10.5169/seals-110267).
- 2099 [6] Vera C. Rubin and Jr. Ford W. Kent. “Rotation of the Andromeda Nebula from a
 2100 Spectroscopic Survey of Emission Regions”. In: *ApJ* 159 (Feb. 1970), p. 379. doi:
 2101 [10.1086/150317](https://doi.org/10.1086/150317).
- 2102 [7] K. G. Begeman, A. H. Broeils, and R. H. Sanders. “Extended rotation curves of spiral galax-
 2103 ies: dark haloes and modified dynamics”. In: *Monthly Notices of the Royal Astronomical So-*
 2104 *ciety* 249.3 (Apr. 1991), pp. 523–537. ISSN: 0035-8711. doi: [10.1093/mnras/249.3.523](https://doi.org/10.1093/mnras/249.3.523).
 2105 eprint: <https://academic.oup.com/mnras/article-pdf/249/3/523/18160929/mnras249-0523.pdf>. URL: <https://doi.org/10.1093/mnras/249.3.523>.
- 2107 [8] *Different types of gravitational lenses*. website. Feb. 2004. URL: <https://esahubble.org/images/heic0404b/>.
- 2109 [9] Douglas Clowe et al. “A Direct Empirical Proof of the Existence of Dark Matter”. In: *apjl*
 2110 648.2 (Sept. 2006), pp. L109–L113. doi: [10.1086/508162](https://doi.org/10.1086/508162). arXiv: [astro-ph/0608407](https://arxiv.org/abs/astro-ph/0608407)
 2111 [[astro-ph](https://arxiv.org/abs/astro-ph/0608407)].
- 2112 [10] Planck Collaboration and N. et. al. Aghanim. “Planck 2018 results I. Overview and the
 2113 cosmological legacy of Planck”. In: *A&A* 641 (2020). doi: [10.1051/0004-6361/201833880](https://doi.org/10.1051/0004-6361/201833880). URL: <https://doi.org/10.1051/0004-6361/201833880>.
- 2115 [11] Wayne Hu. *Matter Density Animation*. web. 2024. URL: <http://background.uchicago.edu/~whu/animbut/anim2.html>.

- 2117 [12] Wenlong Yuan et al. “A First Look at Cepheids in a Type Ia Supernova Host with JWST”. in:
2118 *The Astrophysical Journal Letters* 940.1 (Nov. 2022). doi: [10.3847/2041-8213/ac9b27](https://doi.org/10.3847/2041-8213/ac9b27).
2119 URL: <https://dx.doi.org/10.3847/2041-8213/ac9b27>.
- 2120 [13] Wendy L. Freedman. “Measurements of the Hubble Constant: Tensions in Perspective”. In:
2121 *The Astrophysical Journal* 919.1 (Sept. 2021), p. 16. doi: [10.3847/1538-4357/ac0e95](https://doi.org/10.3847/1538-4357/ac0e95).
2122 URL: <https://dx.doi.org/10.3847/1538-4357/ac0e95>.
- 2123 [14] Jodi Cooley. “Dark Matter direct detection of classical WIMPs”. In: *SciPost Phys. Lect.*
2124 *Notes* (2022), p. 55. doi: [10.21468/SciPostPhysLectNotes.55](https://doi.org/10.21468/SciPostPhysLectNotes.55). URL: <https://scipost.org/10.21468/SciPostPhysLectNotes.55>.
- 2126 [15] “Search for new phenomena in events with an energetic jet and missing transverse momentum
2127 in pp collisions at $\sqrt{s} = 13$ TeV with the ATLAS detector”. In: *Phys. Rev. D* 103
2128 (11 July 2021), p. 112006. doi: [10.1103/PhysRevD.103.112006](https://doi.org/10.1103/PhysRevD.103.112006). URL: <https://link.aps.org/doi/10.1103/PhysRevD.103.112006>.
- 2130 [16] *Jetting into the dark side: a precision search for dark matter*. website. July 2020. URL:
2131 <https://atlas.cern/updates/briefing/precision-search-dark-matter>.
- 2132 [17] Celine Armand et. al. “Combined dark matter searches towards dwarf spheroidal galaxies
2133 with Fermi-LAT, HAWC, H.E.S.S., MAGIC, and VERITAS”. in: *Proceedings of Science*.
2134 Vol. 395. Mar. 2022. doi: <https://doi.org/10.22323/1.395.0528>.
- 2135 [18] Tracy R. Slatyer. “Les Houches Lectures on Indirect Detection of Dark Matter”. In: *SciPost*
2136 *Phys. Lect. Notes* (2022), p. 53. doi: [10.21468/SciPostPhysLectNotes.53](https://doi.org/10.21468/SciPostPhysLectNotes.53). URL:
2137 <https://scipost.org/10.21468/SciPostPhysLectNotes.53>.
- 2138 [19] Christian W Bauer, Nicholas L. Rodd, and Bryan R. Webber. “Dark matter spectra from
2139 the electroweak to the Planck scale”. In: *Journal of High Energy Physics* 2021.1029-8479
2140 (June 2021). doi: [https://doi.org/10.1007/JHEP06\(2021\)121](https://doi.org/10.1007/JHEP06(2021)121).
- 2141 [20] Riccardo Catena and Piero Ullio. “A novel determination of the local dark matter density”.
2142 In: *Journal of Cosmology and Astroparticle Physics* 2010.08 (Aug. 2010), p. 004. doi:
2143 [10.1088/1475-7516/2010/08/004](https://doi.org/10.1088/1475-7516/2010/08/004). URL: <https://dx.doi.org/10.1088/1475-7516/2010/08/004>.
- 2145 [21] B. P. Abbott et al. “Observation of Gravitational Waves from a Binary Black Hole Merger”.
2146 In: *Phys. Rev. Lett.* 116 (6 Feb. 2016), p. 061102. doi: [10.1103/PhysRevLett.116.061102](https://doi.org/10.1103/PhysRevLett.116.061102). URL: <https://link.aps.org/doi/10.1103/PhysRevLett.116.061102>.
- 2148 [22] R. Abbasi et. al. “Observation of high-energy neutrinos from the Galactic plane”. In: *Science*
2149 380.6652 (June 2023), pp. 1338–1343.
- 2150 [23] NASA Goddard Space Flight Center. *Fermi’s 12-year view of the gamma-ray sky*. website.

- 2151 2022. URL: <https://svs.gsfc.nasa.gov/14090>.
- 2152 [24] Marco Cirelli et al. “PPPC 4 DM ID: a poor particle physicist cookbook for dark matter
2153 indirect detection”. In: *Journal of Cosmology and Astroparticle Physics* 2011.03 (Mar.
2154 2011), p. 051. doi: [10.1088/1475-7516/2011/03/051](https://doi.org/10.1088/1475-7516/2011/03/051). URL: <https://dx.doi.org/10.1088/1475-7516/2011/03/051>.
- 2156 [25] Javier Rico. “Gamma-Ray Dark Matter Searches in Milky Way Satellites—A Comparative
2157 Review of Data Analysis Methods and Current Results”. In: *Galaxies* 8.1 (Mar. 2020), p. 25.
2158 doi: [10.3390/galaxies8010025](https://doi.org/10.3390/galaxies8010025). arXiv: [2003.13482](https://arxiv.org/abs/2003.13482) [astro-ph.HE].
- 2159 [26] W. B. Atwood et al. “The Large Area Telescope on the Fermi Gamma-Ray Space Telescope
2160 Mission”. In: *apj* 697.2 (June 2009), pp. 1071–1102. doi: [10.1088/0004-637X/697/2/1071](https://doi.org/10.1088/0004-637X/697/2/1071). arXiv: [0902.1089](https://arxiv.org/abs/0902.1089) [astro-ph.IM].
- 2162 [27] M. Ackermann et al. “Searching for Dark Matter Annihilation from Milky Way Dwarf
2163 Spheroidal Galaxies with Six Years of Fermi Large Area Telescope Data”. In: *prl* 115.23,
2164 231301 (Dec. 2015), p. 231301. doi: [10.1103/PhysRevLett.115.231301](https://doi.org/10.1103/PhysRevLett.115.231301). arXiv:
2165 [1503.02641](https://arxiv.org/abs/1503.02641) [astro-ph.HE].
- 2166 [28] Mattia Di Mauro, Martin Stref, and Francesca Calore. “Investigating the effect of Milky
2167 Way dwarf spheroidal galaxies extension on dark matter searches with Fermi-LAT data”.
2168 In: *Phys. Rev. D* 106 (12 Dec. 2022), p. 123032. doi: [10.1103/PhysRevD.106.123032](https://doi.org/10.1103/PhysRevD.106.123032).
2169 URL: <https://link.aps.org/doi/10.1103/PhysRevD.106.123032>.
- 2170 [29] F. et al. Aharonian. “Observations of the Crab Nebula with H.E.S.S.”. In: *Astron. Astrophys.*
2171 457 (2006), pp. 899–915. doi: [10.1051/0004-6361:20065351](https://doi.org/10.1051/0004-6361:20065351). arXiv: [astro-ph/0607333](https://arxiv.org/abs/astro-ph/0607333).
- 2173 [30] J. Albert et al. “VHE γ -Ray Observation of the Crab Nebula and its Pulsar with the MAGIC
2174 Telescope”. In: *The Astrophysical Journal* 674.2 (Feb. 2008), p. 1037. doi: [10.1086/525270](https://doi.org/10.1086/525270). URL: <https://dx.doi.org/10.1086/525270>.
- 2176 [31] N. Park. “Performance of the VERITAS experiment”. In: *Proceedings, 34th International
2177 Cosmic Ray Conference (ICRC2015): The Hague, The Netherlands, July, 30th July - 6th
2178 August*. Vol. 34. 2015, p. 771. arXiv: [1508.07070](https://arxiv.org/abs/1508.07070) [astro-ph.IM].
- 2179 [32] A. Abramowski et al. “H.E.S.S. constraints on Dark Matter annihilations towards the Sculptor
2180 and Carina Dwarf Galaxies”. In: *Astropart. Phys.* 34 (2011), pp. 608–616. doi: [10.1016/j.astropartphys.2010.12.006](https://doi.org/10.1016/j.astropartphys.2010.12.006). arXiv: [1012.5602](https://arxiv.org/abs/1012.5602) [astro-ph.HE].
- 2182 [33] A. Abramowski et al. “Search for dark matter annihilation signatures in H.E.S.S. observations
2183 of Dwarf Spheroidal Galaxies”. In: *Phys. Rev. D* 90 (2014), p. 112012. doi: [10.1103/PhysRevD.90.112012](https://doi.org/10.1103/PhysRevD.90.112012). arXiv: [1410.2589](https://arxiv.org/abs/1410.2589) [astro-ph.HE].

- 2185 [34] H. Abdalla et al. “Searches for gamma-ray lines and ‘pure WIMP’ spectra from Dark
2186 Matter annihilations in dwarf galaxies with H.E.S.S”. in: *JCAP* 11 (2018), p. 037. doi:
2187 [10.1088/1475-7516/2018/11/037](https://doi.org/10.1088/1475-7516/2018/11/037). arXiv: [1810.00995 \[astro-ph.HE\]](https://arxiv.org/abs/1810.00995).
- 2188 [35] J. Aleksić et al. “Optimized dark matter searches in deep observations of Segue 1 with
2189 MAGIC”. in: *JCAP* 1402 (2014), p. 008. doi: [10.1088/1475-7516/2014/02/008](https://doi.org/10.1088/1475-7516/2014/02/008).
2190 arXiv: [1312.1535 \[hep-ph\]](https://arxiv.org/abs/1312.1535).
- 2191 [36] V.A. Acciari et al. “Combined searches for dark matter in dwarf spheroidal galaxies observed
2192 with the MAGIC telescopes, including new data from Coma Berenices and Draco”. In: *Physics of the Dark Universe* (2021), p. 100912. ISSN: 2212-6864. doi: <https://doi.org/10.1016/j.dark.2021.100912>. URL: <https://www.sciencedirect.com/science/article/pii/S2212686421001370>.
- 2196 [37] M. L. Ahnen et al. “Indirect dark matter searches in the dwarf satellite galaxy Ursa Major II
2197 with the MAGIC Telescopes”. In: *JCAP* 1803.03 (2018), p. 009. doi: [10.1088/1475-7516/2018/03/009](https://doi.org/10.1088/1475-7516/2018/03/009). arXiv: [1712.03095 \[astro-ph.HE\]](https://arxiv.org/abs/1712.03095).
- 2199 [38] S. et al. Archambault. “Dark matter constraints from a joint analysis of dwarf Spheroidal
2200 galaxy observations with VERITAS”. in: *prd* 95.8 (Apr. 2017). doi: [10.1103/PhysRevD.95.082001](https://doi.org/10.1103/PhysRevD.95.082001). arXiv: [1703.04937 \[astro-ph.HE\]](https://arxiv.org/abs/1703.04937).
- 2202 [39] Louise Oakes et al. “Combined Dark Matter searches towards dwarf spheroidal galaxies with
2203 Fermi-LAT, HAWC, HESS, MAGIC and VERITAS”. in: *Proceedings of Science*. 2019.
- 2204 [40] Celine Armand et al. on behalf of the Fermi-LAT, HAWC, HESS, MAGIC, VERITAS.
2205 “Combined Dark Matter searches towards dwarf spheroidal galaxies with Fermi-LAT,
2206 HAWC, HESS, MAGIC and VERITAS”. in: *Proceedings of Science*. 2021.
- 2207 [41] Daniel Kerszberg et al. on behalf of the Fermi-LAT, HAWC, HESS, MAGIC, and VER-
2208 TIAS collaborations. “Search for dark matter annihilation with a combined analysis of
2209 dwarf spheroidal galaxies from Fermi-LAT, HAWC, H.E.S.S., MAGIC and VERITAS”. in:
2210 *Proceedings of Science*. 2023.
- 2211 [42] A. U. Abeysekara et al. “Observation of the Crab Nebula with the HAWC Gamma-Ray
2212 Observatory”. In: *The Astrophysical Journal* 843.1 (June 2017), p. 39. doi: [10.3847/1538-4357/aa7555](https://doi.org/10.3847/1538-4357/aa7555). URL: <https://doi.org/10.3847/1538-4357/aa7555>.
- 2214 [43] Giacomo Vianello et al. *The Multi-Mission Maximum Likelihood framework (3ML)*. 2015.
2215 arXiv: [1507.08343 \[astro-ph.HE\]](https://arxiv.org/abs/1507.08343).
- 2216 [44] Marco Cirelli et al. “PPPC 4 DM ID: a poor particle physicist cookbook for dark matter
2217 indirect detection”. In: *Journal of Cosmology and Astroparticle Physics* 2011.03 (Mar.
2218 2011). ISSN: 1475-7516. doi: [10.1088/1475-7516/2011/03/051](https://doi.org/10.1088/1475-7516/2011/03/051). URL: <http://dx.doi.org/10.1088/1475-7516/2011/03/051>.

- 2220 [45] Alex Geringer-Sameth, Savvas M. Koushiappas, and Matthew Walker. “DWARF GALAXY
2221 ANNIHILATION AND DECAY EMISSION PROFILES FOR DARK MATTER EXPERI-
2222 MENTS”. In: *The Astrophysical Journal* 801.2 (Mar. 2015), p. 74. ISSN: 1538-4357. doi:
2223 [10.1088/0004-637x/801/2/74](https://doi.org/10.1088/0004-637x/801/2/74). URL: <http://dx.doi.org/10.1088/0004-637X/801/2/74>.
- 2225 [46] A. Albert et al. “Dark Matter Limits from Dwarf Spheroidal Galaxies with the HAWC
2226 Gamma-Ray Observatory”. In: *The Astrophysical Journal* 853.2 (Feb. 2018), p. 154. ISSN:
2227 1538-4357. doi: [10.3847/1538-4357/aaa6d8](https://doi.org/10.3847/1538-4357/aaa6d8). URL: <http://dx.doi.org/10.3847/1538-4357/aaa6d8>.
- 2229 [47] HongSheng Zhao. “Analytical models for galactic nuclei”. In: *Mon. Not. Roy. Astron. Soc.*
2230 278 (1996), pp. 488–496. doi: [10.1093/mnras/278.2.488](https://doi.org/10.1093/mnras/278.2.488). arXiv: [astro-ph/9509122](https://arxiv.org/abs/astro-ph/9509122)
2231 [[astro-ph](#)].
- 2232 [48] Julio F. Navarro, Carlos S. Frenk, and Simon D. M. White. “The Structure of Cold Dark
2233 Matter Halos”. In: *ApJ* 462 (May 1996), p. 563. doi: [10.1086/177173](https://doi.org/10.1086/177173). eprint:
2234 [astro-ph/9508025](https://arxiv.org/abs/astro-ph/9508025) ([astro-ph](#)).
- 2235 [49] V. Bonnivard et al. “Spherical Jeans analysis for dark matter indirect detection in dwarf
2236 spheroidal galaxies - Impact of physical parameters and triaxiality”. In: *Mon. Not. Roy.
2237 Astron. Soc.* 446 (2015), pp. 3002–3021. doi: [10.1093/mnras/stu2296](https://doi.org/10.1093/mnras/stu2296). arXiv:
2238 [1407.7822](https://arxiv.org/abs/1407.7822) [[astro-ph.HE](#)].
- 2239 [50] M. Ackermann et al. “Searching for Dark Matter Annihilation from Milky Way Dwarf
2240 Spheroidal Galaxies with Six Years of Fermi Large Area Telescope Data”. In: *prl* 115.23,
2241 231301 (Dec. 2015), p. 231301. doi: [10.1103/PhysRevLett.115.231301](https://doi.org/10.1103/PhysRevLett.115.231301). arXiv:
2242 [1503.02641](https://arxiv.org/abs/1503.02641) [[astro-ph.HE](#)].
- 2243 [51] M. L. Ahnen et al. “Limits to Dark Matter Annihilation Cross-Section from a Combined
2244 Analysis of MAGIC and Fermi-LAT Observations of Dwarf Satellite Galaxies”. In: *JCAP*
2245 1602.02 (2016), p. 039. doi: [10.1088/1475-7516/2016/02/039](https://doi.org/10.1088/1475-7516/2016/02/039). arXiv: [1601.06590](https://arxiv.org/abs/1601.06590)
2246 [[astro-ph.HE](#)].
- 2247 [52] Javier Rico et al. *gLike: numerical maximization of heterogeneous joint
2248 likelihood functions of a common free parameter plus nuisance parameters*.
2249 <https://doi.org/10.5281/zenodo.4601451>. Version v00.09.03. Mar. 2021. doi: [10.5281/zenodo.4601451](https://doi.org/10.5281/zenodo.4601451). URL: <https://doi.org/10.5281/zenodo.4601451>.
- 2251 [53] Tjark Miener and Daniel Nieto. *LklCom: Combining likelihoods from different experiments*.
2252 <https://doi.org/10.5281/zenodo.4597500>. Version v0.5.3. Mar. 2021. doi: [10.5281/zenodo.4597500](https://doi.org/10.5281/zenodo.4597500). URL: <https://doi.org/10.5281/zenodo.4597500>.
- 2254 [54] T. Miener et al. “Open-source Analysis Tools for Multi-instrument Dark Matter Searches”.
2255 In: *arXiv e-prints*, arXiv:2112.01818 (Dec. 2021), arXiv:2112.01818. arXiv: [2112.01818](https://arxiv.org/abs/2112.01818)

- 2256 [astro-ph.IM].
- 2257 [55] Alex Geringer-Sameth and Matthew Koushiappas Savvas M. and Walker. “Dwarf galaxy
2258 annihilation and decay emission profiles for dark matter experiments”. In: *Astrophys.*
2259 *J.* 801.2 (2015), p. 74. doi: [10.1088/0004-637X/801/2/74](https://doi.org/10.1088/0004-637X/801/2/74). arXiv: [1408.0002](https://arxiv.org/abs/1408.0002)
2260 [astro-ph.CO].
- 2261 [56] Gianfranco Bertone, Dan Hooper, and Joseph Silk. “Particle dark matter: evidence, can-
2262 didates and constraints”. In: *Physics Reports* 405.5-6 (Jan. 2005), pp. 279–390. ISSN:
2263 0370-1573. doi: [10.1016/j.physrep.2004.08.031](https://doi.org/10.1016/j.physrep.2004.08.031). URL: <http://dx.doi.org/10.1016/j.physrep.2004.08.031>.
- 2265 [57] V. Bonnivard et al. “Dark matter annihilation and decay in dwarf spheroidal galaxies: The
2266 classical and ultrafaint dSphs”. In: *Mon. Not. Roy. Astron. Soc.* 453.1 (2015), pp. 849–867.
2267 doi: [10.1093/mnras/stv1601](https://doi.org/10.1093/mnras/stv1601). arXiv: [1504.02048](https://arxiv.org/abs/1504.02048) [astro-ph.HE].
- 2268 [58] A. et al. Albert. “Searching for Dark Matter Annihilation in Recently Discovered Milky Way
2269 Satellites with Fermi-LAT”. in: *Astrophys. J.* 834.2 (2017), p. 110. doi: [10.3847/1538-4357/834/2/110](https://doi.org/10.3847/1538-4357/834/2/110). arXiv: [1611.03184](https://arxiv.org/abs/1611.03184) [astro-ph.HE].
- 2271 [59] Mattia Di Mauro and Martin Wolfgang Winkler. “Multimessenger constraints on the dark
2272 matter interpretation of the Fermi-LAT Galactic Center excess”. In: *prd* 103.12, 123005
2273 (June 2021), p. 123005. doi: [10.1103/PhysRevD.103.123005](https://doi.org/10.1103/PhysRevD.103.123005). arXiv: [2101.11027](https://arxiv.org/abs/2101.11027)
2274 [astro-ph.HE].
- 2275 [60] H. C. Plummer. “On the Problem of Distribution in Globular Star Clusters: (Plate 8.)”
2276 In: *Monthly Notices of the Royal Astronomical Society* 71.5 (Mar. 1911), pp. 460–470.
2277 ISSN: 0035-8711. doi: [10.1093/mnras/71.5.460](https://doi.org/10.1093/mnras/71.5.460). eprint: <https://academic.oup.com/mnras/article-pdf/71/5/460/2937497/mnras71-0460.pdf>. URL:
2279 <https://doi.org/10.1093/mnras/71.5.460>.
- 2280 [61] Daniel R. Hunter. “Derivation of the anisotropy profile, constraints on the local velocity
2281 dispersion, and implications for direct detection”. In: *JCAP* 02 (2014), p. 023. doi:
2282 [10.1088/1475-7516/2014/02/023](https://doi.org/10.1088/1475-7516/2014/02/023). arXiv: [1311.0256](https://arxiv.org/abs/1311.0256) [astro-ph.CO].
- 2283 [62] Barun Kumar Dhar and Liliya L. R. Williams. “Surface mass density of the Einasto family
2284 of dark matter haloes: are they Sersic-like?” In: *Mon. Not. Roy. Astron. Soc.* (2010). doi:
2285 [10.1111/j.1365-2966.2010.16446.x](https://doi.org/10.1111/j.1365-2966.2010.16446.x).
- 2286 [63] M. Baes and E. Van Hese. “Dynamical models with a general anisotropy profile”. In:
2287 *Astron. Astrophys.* 471 (2007), p. 419. doi: [10.1051/0004-6361:20077672](https://doi.org/10.1051/0004-6361:20077672). arXiv:
2288 [0705.4109](https://arxiv.org/abs/0705.4109) [astro-ph].
- 2289 [64] Matthew G. Walker, Edward W. Olszewski, and Mario Mateo. “Bayesian analysis of re-
2290 solved stellar spectra: application to MMT/Hectochelle observations of the Draco dwarf

- 2291 spheroidal”. In: *mnras* 448.3 (Apr. 2015), pp. 2717–2732. doi: [10.1093/mnras/stv099](https://doi.org/10.1093/mnras/stv099).
2292 arXiv: [1503.02589 \[astro-ph.GA\]](https://arxiv.org/abs/1503.02589).
- 2293 [65] Nicholas L. Rodd et al. “Dark matter spectra from the electroweak to the Planck scale”. In:
2294 *J. High Energy Physics* 121.10.1007 (June 2021).
- 2295 [66] Pace, Andrew B and Strigari, Louis E. “Scaling relations for dark matter annihilation and
2296 decay profiles in dwarf spheroidal galaxies”. In: *Monthly Notices of the Royal Astronomical
2297 Society* 482.3 (Oct. 2018), pp. 3480–3496. ISSN: 0035-8711. doi: [10.1093/mnras/sty2839](https://doi.org/10.1093/mnras/sty2839).
- 2299 [67] Albert, A. et al. “Search for gamma-ray spectral lines from dark matter annihilation in
2300 dwarf galaxies with the High-Altitude Water Cherenkov observatory”. In: *Phys. Rev. D* 101 (10 May 2020), p. 103001. doi: [10.1103/PhysRevD.101.103001](https://doi.org/10.1103/PhysRevD.101.103001). URL:
2301 <https://link.aps.org/doi/10.1103/PhysRevD.101.103001>.
- 2302
2303 [68] Victor Eijkhout and Edmund Show and Robert van de Geijn. *The Science of Computing. The Art of High Performance Computing*. Vol. 3. Open Copy published under CC-BY 4.0 license, 2023, pp. 63–66.
- 2304
2305
2306 [69] Aartsen, M. et al. “IceCube search for dark matter annihilation in nearby galaxies and galaxy
2307 clusters”. In: *Phys. Rev. D* 88 (12 Dec. 2013), p. 122001. doi: [10.1103/PhysRevD.88.122001](https://doi.org/10.1103/PhysRevD.88.122001). URL: <https://link.aps.org/doi/10.1103/PhysRevD.88.122001>.
- 2308
2309 [70] Pearl Sandick et al. “Sensitivity of the IceCube neutrino detector to dark matter annihilating
2310 in dwarf galaxies”. In: *Phys. Rev. D* 81 (8 Apr. 2010), p. 083506. doi: [10.1103/PhysRevD.81.083506](https://doi.org/10.1103/PhysRevD.81.083506). URL: <https://link.aps.org/doi/10.1103/PhysRevD.81.083506>.
- 2311
2312 [71] Qinrui Liu and Jeffrey Lazar and Carlos A. Argüelles and Ali Kheirandish. “ χ aro: a tool
2313 for neutrino flux generation from WIMPs”. In: *Journal of Cosmology and Astroparticle
2314 Physics* 2020.10 (Oct. 2020), p. 043. doi: [10.1088/1475-7516/2020/10/043](https://doi.org/10.1088/1475-7516/2020/10/043). URL:
2315 <https://dx.doi.org/10.1088/1475-7516/2020/10/043>.
- 2316 [72] Tessa Cerver. “Time Integrated searches for Astrophysical Neutrino Sources using the
2317 IceCube Detector and Gender in Physics studies for the Genera Project”. In: *UNIVERSITE
2318 DE GEN`EVE* (2019), pp. 57–64.
- 2319 [73] Minjin Jeong on behalf of the IceCube Collaboration. “Search for Dark Matter Decay in
2320 Nearby Galaxy Clusters and Galaxies with IceCube”. In: *Proceedings of Science* 444.38
2321 (2023).
- 2322 [74] IceCube Collaboration. “Evidence for neutrino emission from the nearby active galaxy NGC
2323 1068”. In: *Science* 378.6619 (2022).
- 2324 [75] Nathan Whitehorn and Jakob van Santen. *Photospline*. IceCube: GitHub.